GEOLOGICAL CONTROL ON PERMEABILITY HETEROGENEITY IN DEEPLY BURIED DOLOMITE ROCKS

A Dissertation

by

QIFEI HUANG

Submitted to the Office of Graduate and Professional Studies of
Texas A&M University
in partial fulfillment of the requirements for the degree of

DOCTOR OF PHILOSOPHY

Chair of Committee,	Yuefeng Sun
Committee Members,	Walter B. Ayers
	Benchun Duan
	Zoya Heidari
	Michael C. Pope
Head of Department,	Michael C. Pope

May 2017

Major Subject: Geology

ABSTRACT

Geological deposition and diagenesis in carbonate rocks are strongly affected by sea level fluctuation, which can result in significant heterogeneity in pore types, elastic properties, and permeability. In this dissertation research, the mechanism of dolomitization of deeply buried carbonate reservoirs in Sichuan Basin, China is investigated in comparison with shallow carbonate microbialite in Alabama, USA. Based on rock physics, geological factors controlling elastic properties and permeability heterogeneity of carbonate rocks are further studied quantitatively, integrating core, well log and seismic data.

Core and log measurements were first integrated to estimate pore type variation within the Feixianguan carbonate reservoirs in Sichuan Basin, China. The results show that cementation factor (m) from Archie's equation and frame flexibility factor (γ_μ) from a rock physics model are the most effective pore structure indicators for distinguishing diagenetic pore types of the recrystallized rocks, and thus, for classifying permeability-porosity relationships.

The variation of γ_μ is then applied to correlate pore type variations with sea level cyclicities of different orders. The results show that a general trend of γ_μ curve correlates with eustatic sea level cycle, while the two prominent changes of the curve differentiated the three relative sea level cycles by recognizing the episodic subaerial dissolution. Each cycle is characterized by the initial development of moldic porosity ($\gamma_\mu < 4$) followed by intercrystalline porosity ($\gamma_\mu > 4$) with decreasing pore size and increasing γ_μ. The pore

type evolution corresponds to the process of seepage refluxing associated with sea level regression. Further integrated analysis of γ_μ variation, and δ^{18} O and δ^{13} C isotopes, cathodoluminescence images, confirms that reflux dolomitization played a key role in the studied Feixianguan Formation. Dolomitization started at shallow tidal flat or lagoon in the form of protodolomite by microbial dolomitization, which continued to grow following the seepage reflux of sea water. After the burial, the early dolomite was further recrystallized. Seismic inversion is also applied to estimate permeability, using the different permeability-porosity relations constrained by γ_μ from the core and log analysis. The results shows strong heterogeneity in the spatial distribution of permeability and can be used to guide field production.

DEDICATION

To my parents Bihua He and Shungang Huang, husband Luchen Li, and daughter Claire Li, who have encouraged and supported me unconditionally throughout the study.

ACKNOWLEDGMENTS

I would like to thank my committee chair, Dr. Yuefeng Sun, and my committee members, Dr. Ayers, Dr. Duan, Dr. Heidari and Dr. Pope, for their encouragement and help during my Ph.D. program. I also want to thank my friends, colleagues, and the department faculty and staff for all the support during my time at the Department of Geology & Geophysics, Texas A&M University. Thanks also go to the Berge-Hughes Center, ConocoPhillips, Marathon, Newfield, Saudi Aramco, and Williford Scholarship for financial support. I'm grateful for Dr. Mancini and Dr. Pope for access to the data from Little Cedar Creek Field, the Zhongyuan Oil Field of Sinopec for the dataset from Puguang Gas Field, and Occidental Petroleum Corporation for providing summer internships. Gratitude also goes to many people who have helped me in the Puguang Project, especially Dr. Qifeng Dou, who helped me set up the project and process the data. Among all the people who have helped me during my Ph.D. program, I am extremely thankful for the guidance from Dr. Sun, who has helped tremendously throughout my research. He is such a great advisor that not only cares about your progress in research but also guides you towards right thinking. He also cares about all his students and tries to help whenever is needed. I believe everything he taught me will benefit me a lot in the future. Last but not least, I would like to thank my parents, husbands, and daughter, for all the support to pursue my graduate degree.

CONTRIBUTORS AND FUNDING SOURCES

Contributors

This work was supervised by a dissertation committee consisting of Dr. Yuefeng Sun, Dr. Benchun Duan, and Dr. Michael Pope of the Department of Geology & Geophysics, Dr. Walt Ayers of the Department of Petroleum Engineering, and Dr. Zoya Heidari of the Department of Petroleum Engineering at the University of Texas-Austin.

Data used in this study are provided by two resources: 1. SINOPEC, China, and Dr. Earnest Mancini from the University of Alabama, to support academic research of 2. the Reservoir Geophysics Program in the Department of Geology and Geophysics, Texas A&M University.

All work for the dissertation was completed independently by the student.

Funding sources

Graduate study was supported by several funding sources consisting of fellowships from ConocoPhillips, Marathon, Newfield, and Saudi Aramco, Williford Scholarship, and the teaching assistantships from the Department of Geology & Geophysics.

NOMENCLATURE

AI = acoustic impedance

AVO = amplitude versus offset

Den = density

EI= elastic impedance

FF = formation factor

FZI = flow zone index

HST = high-stand system tract

LCCF = little cedar creek field

MICP = mercury injection capillary pressure

NPHI = neutron porosity

NMR = nuclear magnetic resonance

PI = poisson impedance

PR = poisson's ratio

PSI = pore structure indicator

SB = sequence boundary

SEM=scanning electron microscope

SI = shear impedance

SPI = secondary porosity indicator

TCF = trillion cubic feet

TST = transgressive system tract

m = cementation factor

ρ = density

κ = permeability (md)

ϕ = porosity

ϕ_p = primary medium porosity from Wyllie's equation

ϕ_s = spherical porosity

ϕ_B = bulk porosity calculated from density-neutron logs

σ = interfacial tension

P_d = displacement capillary pressure

Pc_{10} = maximum pore throat size at 10% mercury injection

Pc_{50} = maximum pore throat size at 50% mercury injection

P_{10} =capillary pressure at 10% of mercury injection

P_{50} = capillary pressure at 50% of mercury injection

P_c = capillary pressure (psi)

R_d = deep resistivity

R_s = shallow resistivity

R_t = resistivity

R_{wa} = apparent water resistivity

S_{Hg} = Hg saturation

$S_{\min}$ = irreducible water saturation

S_{w} = water saturation

V_p = compressional wave velocity

V_s = shear wave velocity

V_{st} = Stoneley wave velocity

V_m = matrix velocity

V_f = fluid velocity

K = bulk modulus

K_d= dry frame bulk modulus

K_s= solid bulk modulus

μ = shear modulus

μ_d= dry frame shear modulus

μ_s= solid shear modulus

γ = frame flexibility factor

γ_μ = shear frame flexibility factor

S = pore shape factor

TABLE OF CONTENTS

Page

Page

Page

LIST OF FIGURES

Page

Page

Page

Page

Page

Page

Page

Page

CHAPTER I

INTRODUCTION

I.1 Motivations

Carbonate rock most commonly originates from calcareous organisms. Its production has a strong reliance on climatic conditions, such as temperature, salinity and water circulation that favor biological activity. Therefore, carbonate rock contains very useful records for reconstruction of paleoclimate and prediction of sea level fluctuations. Carbonate minerals are sensitive to chemical reaction and thus are susceptible to diagenetic modification. Diagenesis can lead to strong heterogeneity, which makes the prediction of rock properties difficult. Dolomitization is one of the most significant diagenetic processes in carbonate rocks, even completely obliterating depositional rock fabrics. Due to its dependence on depositional porosity for the circulation of dolomitizing fluid, dolomitization may be indicative of carbonate facies and thus sea level change. However, the origins of dolomite are controversial. When integrated with geochemistry data, the textural relationships of different dolomite crystals are useful for deducing their origins (Moss and Tucker, 1996). In this study, quantification of carbonate texture, such as pore structure, was investigated initially using core and logs. Next, the relationship between pore structure variation, dolomitization and sea level change were studied. Finally, spatial distributions of pore structure and permeability were estimated by seismic inversion. This integrated study shows potential to assist in the study of paleoclimatology, and regional hydrology, and may be applied to carbonate

reservoir characterization for worldwide exploration and exploitation of hydrocarbon resources.

The study of sedimentary records, particularly carbonate rocks, is important for the paleoclimate reconstruction. It is more informative of past long-term sea level fluctuations than conventional methods of diatom and pollen analysis, carbon dating, tide gauge recording, and oxygen isotopes. The characteristic deposition of sediments during sea level changes produces repeatable facies patterns and depositional sequences (Sarg, 1988; Eberli and Ginsburg, 1989). In siliciclastic rocks, cyclic deposition of deltaic, incised fluvial, and open marine sediments indicates relative sea-level changes. Compared to siliciclastic rocks, carbonate rocks provide even better indications of climate change, because carbonate production relies strongly on the temperature, as well as water salinity and circulation. Low-frequency relative sea level changes may be indicated by unconformities formed after sea level fall and by flooding surfaces formed following sea level rise. High-frequency sea level changes can be predicted by investigating variations of carbonate facies, such as shallowing-upward cycles in shallow water carbonates (Grotzinger, 1986; Strasser, 1988; Fischer, 1991). Therefore, seismic and well log data, with their wide applications for mapping sedimentary facies, reservoir properties, unconformities, and flooding surfaces, are useful tools for the study of sea level changes (Coe, 2003). For instance, in the late 1970s, Peter Vail and colleagues from Exxon Production Research assembled a global sea-level chart for the Mesozoic and Cenozoic, showing (at the resolution of about 1 Ma) how they interpreted global sea-level to have changed through time (e.g. Vail and Mitchum, 1979).

Dolomitization of carbonate rocks may indicate sea level change, due to the strong dependence on the depositional porosity and permeability that are controlled by facies. However, the mechanisms of dolomitization are controversial (Adams and Rhodes, 1960; Badiozamani, 1973; Churcher and Majid, 1989; Lucia et al., 2003; Saller and Dickson, 2011). Dolomite has limited occurrences in Recent marine water, and the laboratory synthesis of dolomite under normal condition is very difficult without microbial mediation. Extensive dolomitization is often found in ancient platform carbonates after long-term circulation of diagenetic fluid. As dolomitization requires sufficient flow of magnesium-rich fluid, the study of dolomitization requires an understanding of the regional hydrological setting, which sometimes can be very difficult. Many dolomitization models were proposed through the years, including mixing zone dolomitization, reflux dolomitization, etc. (Saller and Dickson, 2011). However, the mystery of dolomitization still exists, as the chemical and hydrological conditions of dolomite formation are poorly understood, and multiple genetic interpretations are allowed from the petrographic and geochemical data (Machel, 2004).

Even though studying carbonate rocks, particular dolomite, is challenging, it is very useful for the understanding of paleoclimate and sea level fluctuation. Also, such study can be very beneficial for the exploration of hydrocarbons, lead, and zinc (Warren, 2000).

Marine carbonate rocks are important conventional hydrocarbon reservoirs. More than 60% of the global hydrocarbon reserves occur in carbonate rocks, and most of the

hydrocarbon production from the Middle East is from carbonate reservoirs. The high productivity in carbonate rocks occurs because they are highly susceptibility to diagenesis, which helps produce and preserve pores after burial (Bathurst, 1972). Dolomitization and dissolution are the most important diagenetic processes for enhancement of reservoir quality. Approximately 80% of the hydrocarbon reservoirs in North American carbonate rocks are in dolomite, and up to 50% of the conventional carbonate reservoirs around the world are dolomites (Zengler et al., 1980). Compared to limestone, dolomite is more likely to be naturally fractured, which further helps dissolution and dolomitization.

Stratigraphic traps in carbonate rocks are relatively easy to locate, as their sedimentary facies follow patterns that are mappable and predictable. However, carbonate rocks with varied rock textures cause strong heterogeneity in reservoir performance and exhibit complex permeability and porosity relationships. Carbonate rocks that have similar porosity may have permeability differences that vary by orders of magnitude (e.g. Lucia, 1995). Reservoirs with isolated moldic or vuggy pores have very different production compared with reservoirs dominant by intercrystalline pores. Commonly, significant amounts of hydrocarbon are left behind in the isolated pores after water flooding of a carbonate reservoir (Green and Willhite, 1999). The problems are how to effectively describe reservoir heterogeneity, predict reservoir performance and recover residual oil. Most of the commonly applied methods of reservoir characterization are either qualitative discrimination of high permeability pores from low permeability pores or are limited to laboratory study. More quantitative and applicable

characterization of rock texture is needed for more accurate prediction of permeability from porosity data. Rock physics parameters with strong physical meaning are necessary for this purpose. In addition, appropriate rock physics parameters can help extract information about carbonate rock fabrics from seismic data, which is crucial to understanding the spatial distribution of the porosity and permeability in complex carbonate reservoirs. Additionally, accurate prediction of pore-scale heterogeneity is necessary for reservoir management. The study of pore structure variation is crucial for better fluid prediction from seismic AVO inversion, as the effect of fluid can sometimes disguise by the influence of pore structure.

I.2 Objectives of the research

Understanding carbonate deposition and diagenesis is important from many perspectives. It not only helps clarify paleoclimate and sea level change but also can directly influence hydrocarbon exploration. Therefore, the overall objective of this study is to understand geological controls on carbonate rock heterogeneity, with its applications to paleoclimatology, sea level fluctuation, and reservoir management. This research is divided into three parts.

Chapter II focuses on quantitative characterization of carbonate pore structure based on core and log measurements. Evaluation of mercury injection curves and resistivity, velocity, neutron-density logs were applied to understand the heterogeneity in the Feixianguan dolomite rocks. The objective was to understand the limitations and

advantages of different rock physics approaches and have a more accurate prediction of pore type and permeability.

Chapter III focused on deciphering the genesis of different pore structure and revealing the potential correlation between pore structure and sea level. The objective was to understand the geological controls on carbonate heterogeneity. The pore structure indicator derived from Chapter II was used to characterize the texture relationships between different types of dolomite. The origins of the dolomite were interpreted based on these relationships.

Chapter IV focused on seismic prediction of carbonate pore structure and permeability. The objectives were to understand the spatial distribution of reservoir and to validate the geological interpretation in Chapter III from a larger scope of observation. The rock physics model introduced in Chapter II will be used to guide seismic inversion.

The integrated study of the relations among pore structure, diagenesis, and sea level change may help find other giant carbonate reservoirs worldwide and potentially assist the study of regional paleo-hydrology and climate change.

I.3 Datasets and geological background

I.3.1 Datasets

The dataset used for this study is from a very deep carbonate formation in Puguang Gas Field, Sichuan, China, which has diversified diagenetic rock textures. A comparative study of a shallow carbonate formation from the Little Cedar Creek Oil

Field, Alabama, USA is included in Appendix H, which are dominated by the preserved depositional rock textures.

From the Puguang Gas Field, conventional well log data from 54 wells were obtained, including gamma ray (GR), resistivity, sonic velocities, density, etc.. 15 of the 54 wells have shear wave velocity logs. Core measurements such as core permeability, core porosity, thin sections, and capillary pressure were available for 1,499 samples from 4 wells. The locations of wells are shown in Figure 1.1. Some wells also contain SEM images and cathodoluminescence images. The thin sections were impregnated with epoxy to better illustrate the pore space, in red color. Two cored wells, Well1 and Well2, were used most in this study and have a complete suite of core analysis and well log data, including 820 core measurements of porosity and permeability and 55 thin sections for Well 1 and 720 core measurements of porosity and permeability and 266 thin sections for Well 2. The measurements of core porosity and permeability were accomplished by helium injection. Permeability values present the Klinkenberg-corrected nitrogen permeability measured under a confining pressure of 20 bars. High quality, seismic angle gathers, and post-stack volumes were also supplied. The 3D seismic data provided were from a seismic survey with an offset range of 4500-5200 meters for the zone of interest. The prestack gathers used for seismic inversion in this study were processed including depth migration with high signal-to-noise ratio. The frequency range is between 8 and 64 Hz. The largest angle used for inversion in this study is 21 degrees.

I.3.2 Geological background

Puguang gas field is located in the northern folded area of Sichuan Basin, China. Discovered in 2009, this field was proven with large gas reserves in dolomite at a depth greater than 5,000 m (Hao et al., 2009; Wang et al., 2010). Gas in the Lower Triassic reservoir is trapped in a NNE-trending, fault-bounded anticline (Figure 1.1) in the northern folded area of Sichuan Basin. Top seals of the reservoir are evaporites and tight dolomite (Cai et al., 2004). Production comes from ooilite grainstone that was deposited in the marginal shoal of an ancient carbonate platform (Ma et al., 2007). These Permian-Triassic ooid grains were deposited during a global warming that resulted in a high productivity of organic carbonates.

Carbonate shoals were deposited at the shelf margin during falling sea level (Ma et al., 2008a, 2008b). At the end of Permian, the carbonate build-ups grew at a slower rate than sea level rise and were drowned. Following a subsequent sea level drop, carbonate shoals developed. The oolitic grainstone was deposited at a location where groundwater and seawater were mixing, and excessive evaporation was occurring on the surface; thus, conditions were favorable for the dolomitization of limestones (Adams and Rhodes, 1960; Badiozamani, 1973; Machel, 2004). In the studied reservoir, dolomitization and related dissolution greatly improved the porosity and permeability (Ma et al., 2007). However, the degree to which the grainstones were altered by these diagenetic processes varies spatially (Sun et al., 2015). The ooids are deposited at a positive relief on the platform leads tend to be more exposed and affected by selective meteoric dissolution followed by selective dolomitization. In contrast, ooids at lower

positions are more influenced by the reflux of evaporated sea water, where both grains and rock matrix are unselectively dolomitized. Therefore, moldic pores at geographically higher positions and intercrystalline pores at lower positions compose the two most important but distinctive pore types for the studied reservoir (Sun et al., 2015). Both may have high porosity and hold hydrocarbons. However, intercrystalline pores contribute more to production as they are much more permeable (Zhang et al., 2013). Other minor pore types that occur include dissolution-enlarged intercrystalline pores, interparticle pores, interclastic pores, and micro-pores (Choquette and Pray, 1970; Zhao et al., 2005; Ma et al., 2007; Qiang, 2007; Ma et al., 2008a, 2008b; Wei et al., 2011; Sun et al., 2015; Yu et al., 2015).

Tectonic setting

Sichuan Basin is a large intracratonic basin located in the western part of the Paleo-Yangtze Platform, Southwest China (Ma et al., 2007). It is a rhombohedral basin surrounded by a series of fold zones and is sub-divided into the Northwestern Sichuan depression, Central Sichuan transitional uplift and Southeastern high fold zone (Figure 1.1A). During Permian-Triassic, the Yangtze plate, one of the three major Precambrian continental blocks of China, was a displaced terrane within the Tethyan Ocean (McElhinny et al., 1981; Lin et al., 1985). The passive margin setting of the plate near the equator favored carbonate production in the Sichuan Basin. Puguang gas field is located on a NNE-trending fault-bounded anticline in the eastern fold zone of the Sichuan Basin (Figure 1.1 C). Folds and thrust faults were created during Cenozoic Yanshanian and Himalayan movements. The Feixianguan Formation was deposited in

the Early Triassic, during active Mesozoic Indosinian movements, which are characterized by repeated uplifts perturbed by a few local subsidence events. Two regional unconformities formed after uplifting movements were recognized by Yu et al. (2015), at the top of the first and second members of Feixianguan Formation (T1f1 and T1f2). Various pore types occur below these two unconformities, including isolated moldic pores, dissolution-enlarged fractures, cavities, and breccia pores (Fan et al., 2005; Yu et al., 2015). The penecontemporaneous karstification and massive dissolution during the uplift phase greatly enhanced reservoir quality. During the late Triassic to Jurassic, the Yangtze plate collided with the North China Plate, followed by terrestrial deposition.

Depositional environment and sedimentary facies

Pre-Permian tectonic compression resulted in basement flexure and differential plate movement between western and eastern parts of the studied region (Figure 1.1B) (Ma et al., 2007). Furthermore, the development of growth faults during the Permian led to more subsidence of the western part, which became a deep-water continental shelf with little sedimentation, whereas the East became a thick carbonate platform (Zhao et al., 2005; Chen et al., 2014). During the Late Permian, a rimmed carbonate platform was established above the gentle ramp following the development of carbonate reefs and shoals along the margins. During the Triassic, the basin gradually filled, and the water depth of the basin decreased as the entire basin was uplifted (Ma et al., 2007). As a result, a restricted evaporitic platform formed the interior of the marginal carbonate shoal. At the end of Early Triassic, a uniform carbonate platform had formed.

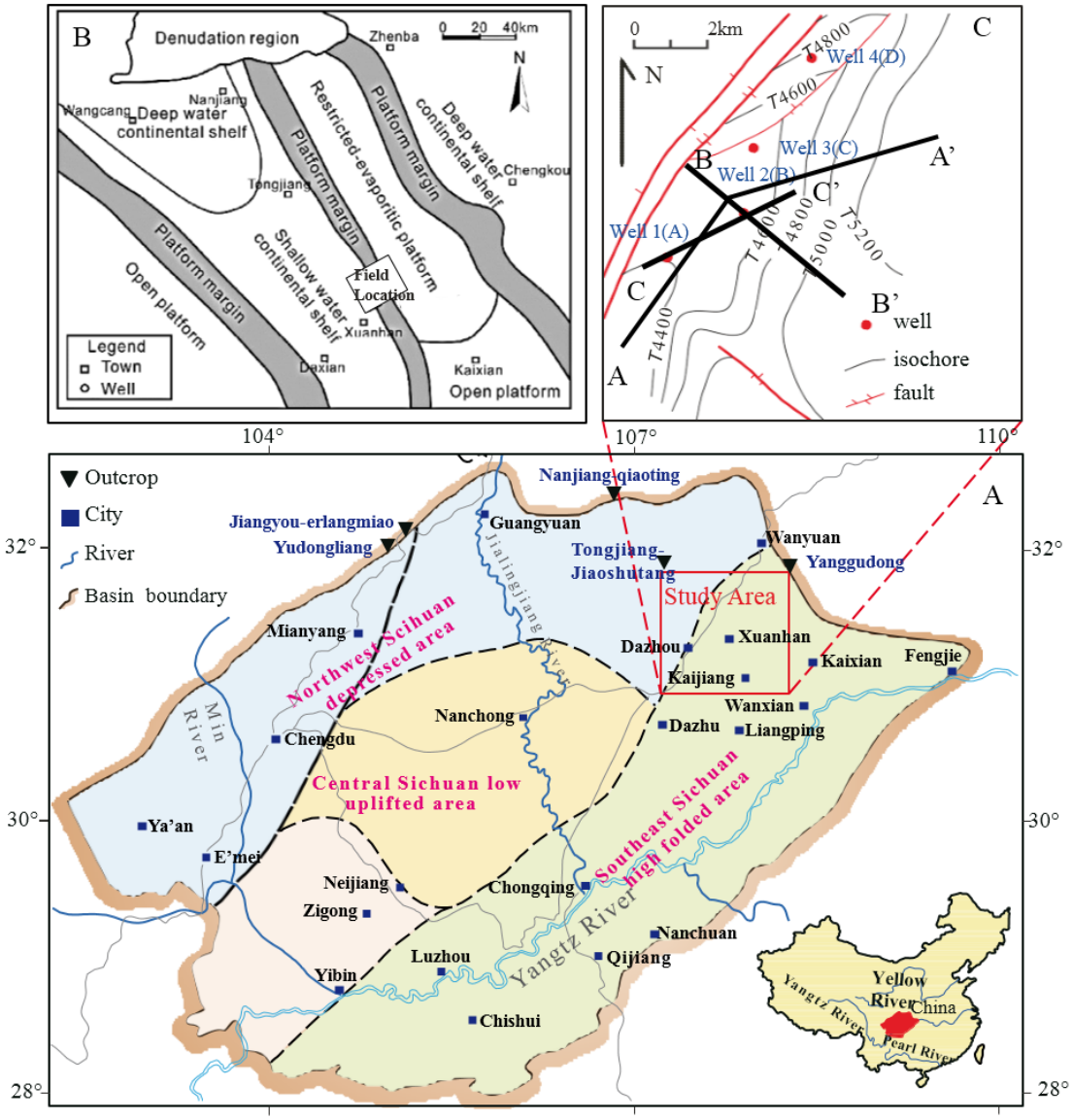

Figure 1. 1 A) Tectonic units map of Sichuan Basin, China. B) Paleo-facies map in the northeastern part of Sichuan Basin and the location of the field. C) Structure map of Puguang Gas Field. The locations of four production wells are shown. The well names will follow Well A, B, C, D in Chapter III and Well1, 2, 3, 4 in Chapter IV. The three lines on map "C" are selected to show the cross-sections of data in Chapter III and IV. Modified from Ma et al. (2007) and Yu et al. (2015).

Along the carbonate platform, facies changed landward from shallow marine open platform, marginal carbonate shoal, and restricted platform to an evaporitic platform (Ma et al., 2006; Feng et al., 2008; Wei et al., 2011; Sun et al., 2015). High-quality reservoirs occur in the carbonate shoal facies. Ooid grains were deposited at the platform margins, where storm waves impacted deposition (Wang et al. 2005). Compared to marginal shoals, open platform and restricted platform settings had relatively low hydrodynamic energy and thus lower reservoir quality.

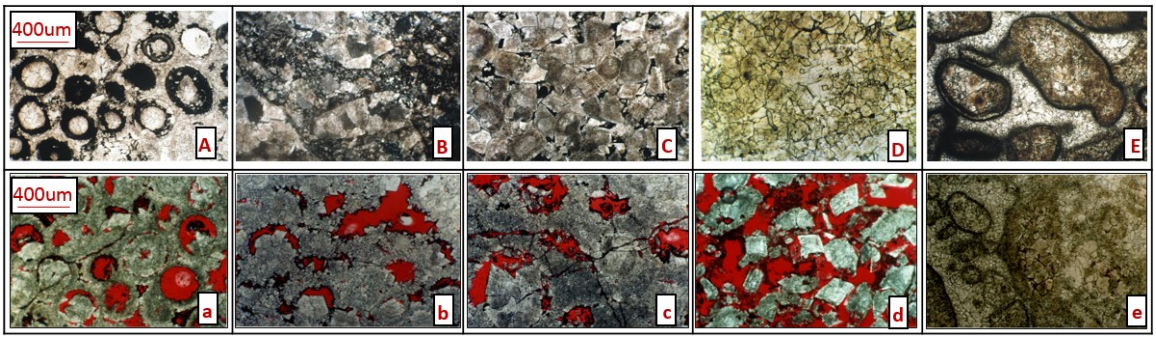

Figure 1. 2 Different rock types and pore types observed in thin sections with the same scale: A: oolitic dolostone with developed moldic pores; B: brecciated gravels; C: residual oolitic dolostone with developed meso-intercrystalline pores; D: dolomicrite with micro-intercrystalline pores; E: oolitic dolostone with developed micrite envelope around ooid grains; a): moldic and intragranular pores; b): intragranular and intercrystalline pores; c): intercrystalline pores dominated, scattered intragranular pores; d): intercrystalline pores; e): micro-intercrystalline pores.a, b, c, d, and e are cast sections with pore spaces shown in red.

Within the ooid shoal facies (Figure 1.2), rock types include dolomudstone, oolitic dolomite, and gravel bearing oolitic dolomite (Huang et al., 2009; Zhang et al., 2011). Within these rock types, oolitic dolomite is the dominant producing reservoir for Puguang field. The ooid grains commonly were selectively dissolved and filled with

geo-petal structures. Under tectonic stress, some of the oolitic dolomites were brecciated and further dissolved, creating recrystallized residual oolitic dolomite with enhanced reservoir quality (Ma et al., 2007). As dolomitization and dissolution advanced, sucrosic oolitic dolomite with excellent reservoir quality was generated.

Sequence stratigraphy

Feixianguan Formation (Figure 1.3) has a total thickness of 300 – 500 m and was sub-divided into four members from bottom to top: Fei1 (T1f1), Fei2 (T1f2), Fei3 (T1f3), and Fei4 (T1f4) based on core and wireline log correlation (Cai et al., 2004; Ma et al., 2008b, Jiang et al., 2013). T1f1 and T1f2 are dominated by high-energy, shelf margin ooid shoal deposits with good porosity (Ma et al., 2006). They are composed of fine-to-medium sand-size oolitic dolomite or residual oolitic dolomite, with dissolved porosity and intercrystalline porosity. T1f3 is characterized as a transition from fine sand sized dolomite at the base to lime mudstone at the top due to the change from evaporitic platform deposition to open platform deposition. T1f4 contains shale and gypsum within the evaporitic platform (Wang et al., 2002). The 2nd-order sequence is composed of three 3rd-order sequences separated by the two unconformities at the top of Fei1 and Fei2 (Qiao et al., 2010; Guo et al., 2011; Yu et al., 2015). Below the two unconformities, reservoirs with dissolved moldic pores are common. The occurrence of moldic pores thus may be indicative of sub-aerial exposure and hiatus (Yu et al., 2015). Further subdivision of Feixianguan Formation (Figure 1.3) is nine 4th-order sequences (Xiao et al., 2010; Zhang et al., 2010). Transgressive System Tract (TST) of each sequence was favorable for the development of lagoon, carbonate shoal, and inter-shoal and deposition

of limestone, and sparry oolitic dolomite. The dominant syn-depositional diagenetic alterations were marine cementation and micritization. In contrast, Highstand System Tract (HST) of each sequence is favorable for the development of evaporitic or restricted platforms and deposition of dolomitic limestone, dolomudstone, and gypsum. The major producing reservoirs are in the prograding carbonate shoals, with enhanced reservoir quality by dissolution and dolomitization (Ma et al., 2007, 2008a, 2008b).

Diagenesis and parasequence

Diagenesis plays a significant role in the generation and preservation of reservoir porosity in the subsurface (Wang et al., 2010). Moldic porosity at Feixianguan reservoir was formed after selective dissolution, following sea level drop and subaerial exposure of the ooid grains to the meteoric water. Intercrystalline porosity with high connectivity was developed after dolomitization (Zheng et al., 2011). Early dolomitization helped produce and preserve porosity, whereas the development of open fractures led to further dissolution and recrystallization. In the study field, dolomitization could have benefited from the high content of H_2S (>14%) generated from thermal sulfate reduction (TSR) (Ma et al., 2008b). TSR is good for the preservation of dolomite as it consumes sulfate and decreases the solubility of dolomite.

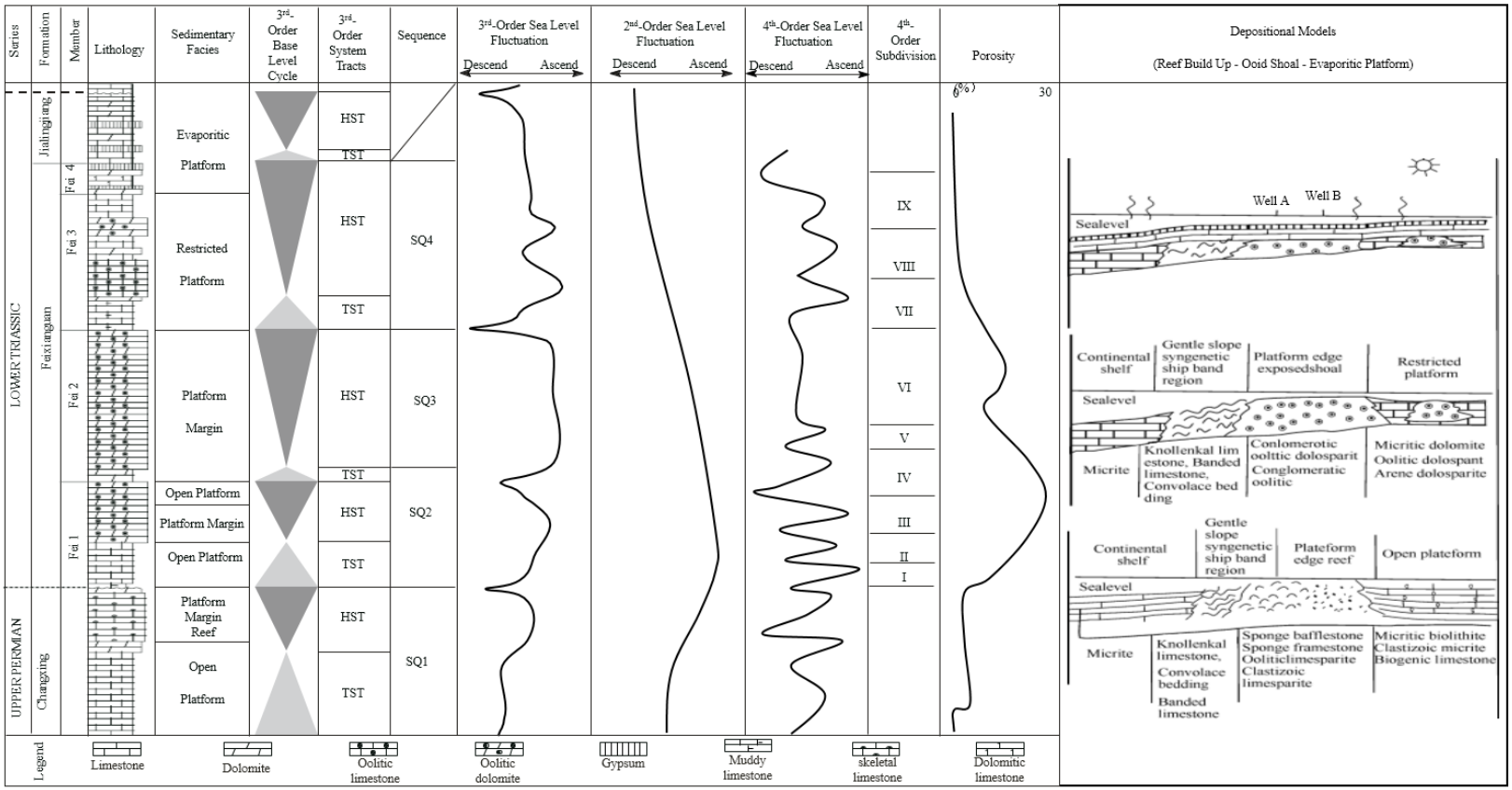

Figure 1. 3 Stratigraphic column from Permian to Triassic in Sichuan basin, China. Lithology and sedimentary facies variation, 3rd- and 2nd- order sea level variation, porosity distribution, and depositional models are shown. The region has experienced one large 2nd-order sea level cycle and three 3rd-order sea level cycles which can be sub-divided into nine 4th-order sea level cycles. Porosity is mostly developed in Fei1-2 members (Modified from Ma et al., 2008b and Yu et al., 2015).

The diagenetic evolution of Feixianguan reservoir (Figure1.4) followed five steps (Ma et al., 2008b): 1) Syn-depositional marine cementation and micritization occurred in the marine phreatic zone. Grains were surrounded by isopachous, fibrous, and rimming dolomite or micritic envelopes. Approximately 55% of the depositional intergranular pores were occupied. 2) Meteoric dissolution and cementation occurred in the vadose zone. Selective dissolution resulted in abundant intragranular and moldic pores with occasional geo-petal structures. 3) Cementation and dolomitization occurred in the mixing water phreatic zone. Most of the ooid limestone transformed to oolitic dolomite. 4) Shallow burial diagenesis produced compaction, early pressure-induced dissolution, and mosaic to blocky cementation occurred. 5) Deep burial diagenesis continued, producing fracturing, non-selective dissolution, and recrystallization. Most of the dolomite reservoirs are formed early and experienced significant modifications after deep burial.

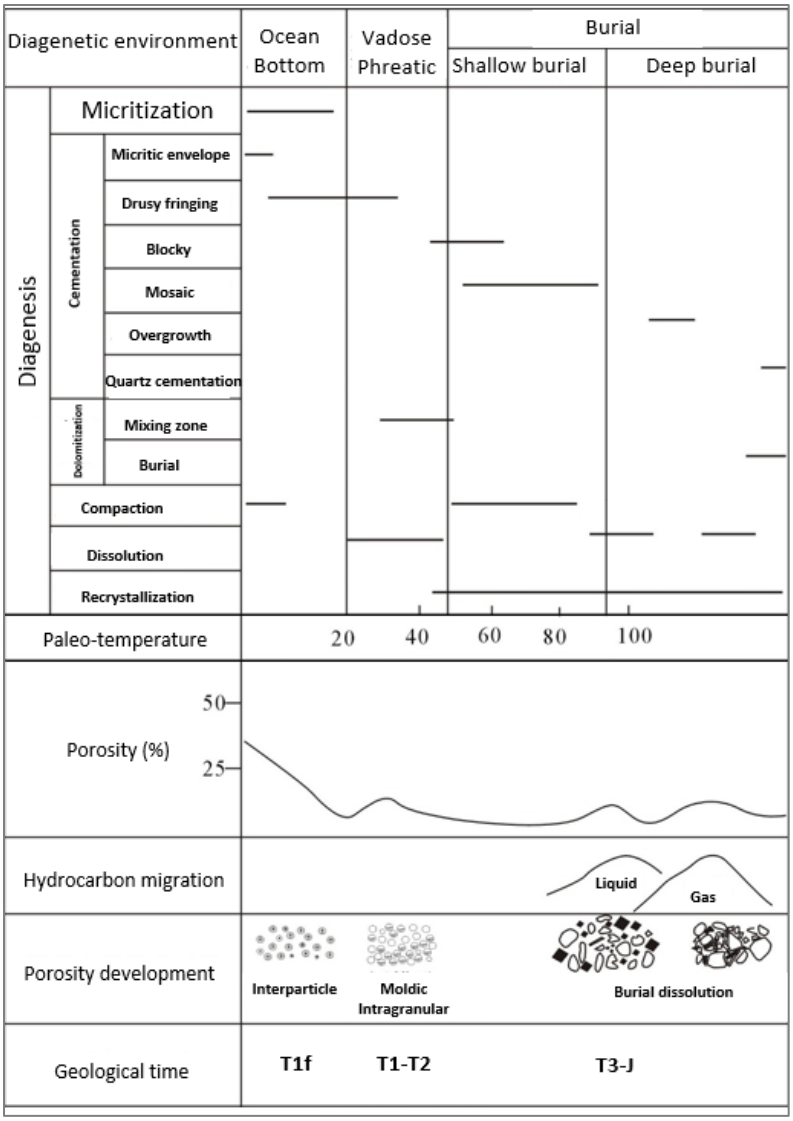

Figure 1. 4 Paragenetic sequence and evolution of porosity in the Feixianguan Formation with the temperature in C^{o} (modified from Ma et al., 2008b).

Reservoir performance overview

The Feixianguan Formation reservoirs are composed of oolitic dolomite, residual oolitic dolomite, crystalline dolomite, dissolved dolomite, etc. (Ma et al. 2008a). The depositional pores are barely preserved after compaction and diagenesis. Two distinct

secondary pore types occur in the reservoirs: dissolution pores and intercrystalline pores, which complicated the permeability and porosity relations. Figure 1.5 shows the histograms for the four dominant types of dolomite in the studied field. The residual oolitic dolomite with medium to macro- sand size crystals, higher percentages of large pore throats for the intercrystalline pores has high porosity and high permeability. Oolitic dolomite dominated by moldic and intragranular pores are associated with the bimodal distribution of pore throat size yet most of the pore throats are small. These rocks often have high porosity but low permeability. Crystallized dolomite composed of fine-medium sized crystals has low porosity but relatively high permeability, due to the higher percentage of large pore throats. Dolomudstone consisting of fine dolomite crystals are featured with very small pore throat size and low porosity, thus have relatively low permeability. In brief, reservoir quality differs significantly within the Feixianguan Formation among dolomitic units with different rock textures.

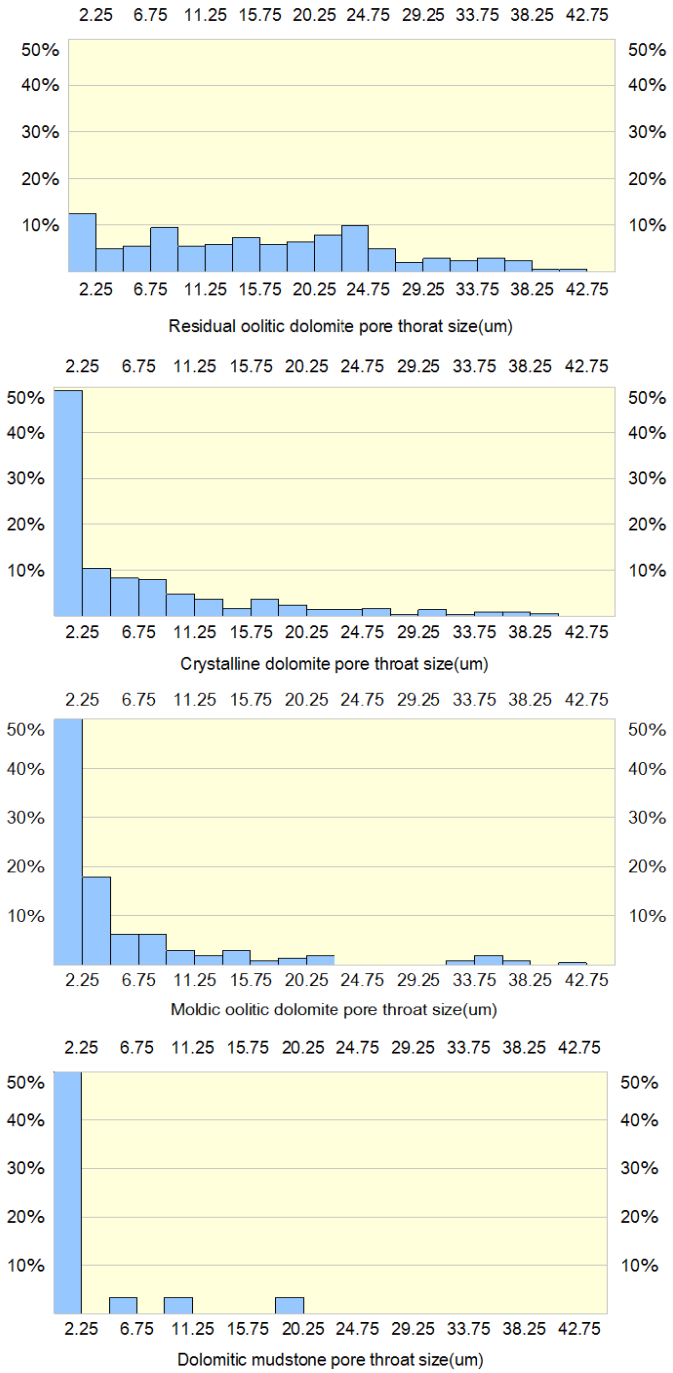

Figure 1. 5 Histograms showing pore throat size distribution for different types of dolomite. The maximum vertical frequency is set to be 50% for better comparison of data. The dominant pore throat size and the standard deviation are decreasing from residual oolitic dolomite to crystalline dolomite, moldic dolomite, and dolo-mudstone.

I.4 Summary of dissertation chapters

Depositional systems/sedimentary facies and later diagenetic modification in carbonate rocks result in a significantly different pore types, resulting in strong heterogeneity in elastic properties and complex permeability and porosity relationships (Eberli et al., 2003; Kumar and Han, 2005). Giant gas reservoirs with diverse pore types occur, in the Early Triassic dolomite in Puguang Field, Sichuan, China. The objective of this study is to understand geological controls on carbonate rock heterogeneity, with its application for both reading sea level fluctuations and being essential to reservoir management. We divide the study into three parts following the workflows are shown in Figure 1.6.

Chapter II demonstrates the quantitative characterization of carbonate pore structure and permeability based on the integrated study of core and log data. The methodology is highlighted by the orange arrows in Figure 1.6. Mercury Injection Capillary Pressure and Leverett J-function curves from core analysis show that five distinct pore systems occur in the Early Triassic, Puguang Gas Field, which evolved from moldic pore dominant to sucrosic macro-intercrystalline, mixed moldic and intercrystalline, meso-intercrystalline, and micro-intercrystalline. Integrated analysis of resistivity, velocity, and neutron-density logs agrees with the core analysis in discrimination of pore types. The methods applied are comparing the differences between shallow and deep resistivity, and between neutron and density; evaluating Archie's cementation factor (m), Sun's frame flexibility factor (γ_μ), and Castagna's S

factor, respectively. When comparing the effectiveness of each method for pore type estimation, m and γ_μ are the best in distinguishing all pore types for the studied formation. When $m > 2.4$, $\gamma_\mu < 4$, the reservoir zone is dominated by moldic pores; when $1.6 < m < 2.4$, $4 < \gamma_\mu < 8$, meso to macro intercrystalline pores are dominant; and when $m < 1.6$ and $\gamma_\mu > 8$, micro intercrystalline pores are prevalent. The established pore structure indicator γ_μ is further used in Chapter III and Chapter IV to understand the spatial variation of pore structure and permeability.

Chapter III focuses on the geological controls of sea level change and diagenesis, on the diverse pore types. The methodology is outlined by the blue arrows in Figure 1.6. The frame flexibility factor (γ_μ) introduced in Chapter II is applied as a pore structure indicator (PSI) to quantify the episodic variations of pore structure observable from cores, in the forms of crystalline, peloidal, moldic oolitic dolomite to dolomudstone in upward shallowing sequences. The results from petrography and PSI analysis illustrate that PSI < 4 is associated with moldic oolitic dolomite dominated by moldic porosity. Since moldic porosity is developed after dissolution, the lowest values of PSI may indicate potential unconformities and subaerial exposures. Above the moldic zones, PSI is larger than 4, indicating the dominant pore type is intercrystalline porosity. The increasing of PSI, indicate the decreasing of crystal size associated with the seepage reflux of fluid during sea level regression. The results from the integrated study of PSI, stable isotopes (δ^{18} O and δ^{13} C), and cathodoluminescence suggest that moldic oolitic dolomite at the marginal shoals was formed by early subaerial dissolution. Below the moldic oolitic dolomite, the peloidal dolomite may be developed from microbial

mediated protodolomite in the restricted platform. Crystalline dolomite was then developed from peloidal dolomite by reflux dolomitization. Continued dolomitization improved pore connectivity and permeability.

In Chapter IV, we investigated the spatial distribution of pore structure and permeability controlled by the geological variation, such as sea level fluctuation and dolomitization. The methodology is outlined by the green arrows in Figure 1.6. We continued using the frame flexibility factor (γ_μ) from Chapters II and III as an index to quantify the pore structure changes controlled by sea level change and dolomitization. We used this index to classify various permeability trends resulting from different pore types. For the studied reservoirs of the Puguang gas field, Sichuan Basin, China, when $\gamma_\mu > 4$, the pore type is dominated by intercrystalline pores with large pore throat sizes and high connectivity, which yield a higher permeability trend; when $\gamma_\mu < 4$, the pore type consists of isolated moldic pores, which have a lower permeability trend. The evaluation of spatial pore structure variation is then completed with seismic stratigraphic interpretation and inversion. The inversion results show agreement with sedimentology and stratigraphy in that the carbonate shoal reservoirs started to develop during transgression and were widely distributed during early regression; within the ooid shoals, moldic pores of oolitic dolomite are widely distributed below unconformities due to selective dissolution. Below the moldic zones, intercrystalline porosity is widely distributed, which changed micro-intercrystalline porosity of dolomudstone to macro-intercrystalline porosity of crystalline dolomite, as a consequence of reflux

dolomitization. Based on different permeability-porosity relations constrained by γ_μ, the seismic inversion results are used to understand the spatial variation of permeability.

In the Appendices, we listed the supplemental materials used to arrive at our major conclusions described in Chapter V. Appendix A shows cross plots of core measured permeability and porosity from wells with core data. Appendix B displays the statistical data for the J function analysis. Appendix C lists tables of statistic distribution of porosity and permeability considering sedimentary sequences and depositional facies. Appendix D shows the cross plots of elastic properties against porosities in the studied carbonate formation. Appendix E demonstrates the detailed pore type evaluation for different wells using the methods described in Chapter II. Appendix F shows the correlation of pore structure with sea level cyclicities from different wells. Appendix G displays the two examples of seismic well ties used for inversion. For comparison, we also studied the pore structure heterogeneity in a much shallower formation from onshore Alabama, USA. The comparative study is documented in details in Appendix H.

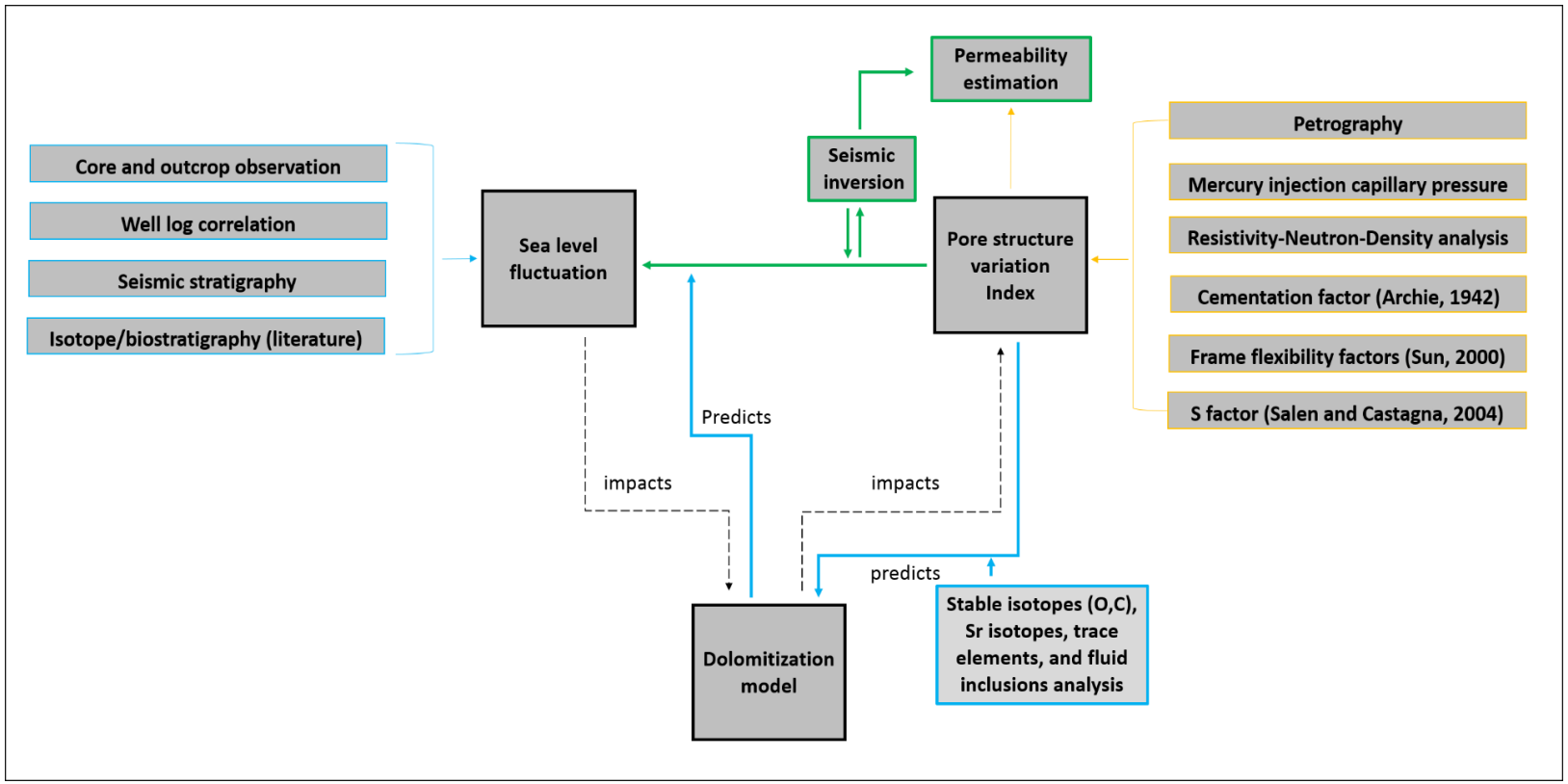

Figure 1. 6 Summary of methodology and workflow applied for this study.

CHAPTER II

PETROPHYSICAL AND ROCK PHYSICAL CHARACTERIZATION OF CARBONATE PORE STRUCTURES

II.1 Synopsis

Carbonate rocks have complex pore structures, which lead to strong heterogeneity in petrophysical and elastic properties. In this paper, rock physics based study of core and well log data is performed to estimate the pore structure variation in the Early Triassic reservoir, Puguang Gas Field. Core analysis on Mercury Injection Capillary Pressure and Leverett J-function curves show that five distinct pore types are distributed vertically in five zones, which evolves from moldic pore dominant to, sucrosic macro-intercrystalline, mixed moldic and intercrystalline, meso-intercrystalline, and micro-intercrystalline, from Zone 1 to Zone 5 in the upward shallowing sequence. Reservoir performance is the best in Zone 2 followed by Zone 1, 4, and 3. Multi-evaluation of resistivity, velocity, neutron-density logs agrees with the core analysis on discrimination of pore types, especially among Zone 1 and 2. The methods applied include calculating the differences between shallow and deep resistivity, and between neutron and density; evaluating Archie's cementation factor (m), Sun's frame flexibility factor ($\gamma\mu$), and Castagna's S factor. It is found that m and $\gamma\mu$ are most effective in distinguishing all five zones of the studied formation. When $m > 2.4$, $\gamma\mu < 4$, the reservoir zone is dominated by moldic pores; when $1.6 < m < 2.4$, $4 < \gamma\mu < 8$, meso to macro intercrystalline pores are dominant; and when $m < 1.6$ and $\gamma\mu > 8$, micro intercrystalline pores are prevalent. The results of pore structure evaluation can be

further applied to constrain the estimation of permeability for better reservoir management.

II.2 Introduction

Carbonate rocks often are composed of various pore structures due to variation in depositional rock fabrics or diagenetic modification (Dunham, 1962; Lucia, 1995; Anselmetti, 2001; Tonietto, 2014). The large variations of pore structures can lead to complex permeability-porosity relationships for both hydraulic and electrical flow, which makes the estimation of permeability and fluid saturation difficult (Nelson, 1994; Rezaee et al., 2007). Furthermore, carbonate pore structure can significantly affect exploitation by changing the efficiency of matrix acidizing (Etten et al., 2015). A better understanding of the pore geometries, their connectivity, and genesis, thus, can refine prediction of potential fluid flow zones, estimation of water saturation, reserves, and hydrocarbon recovery. Many carbonate rock pore classifications were developed over the decades to describe the origins and geometries of different pore types based on core data (Archie, 1952; Dunham, 1962; Choquette and Pray, 1970; Lucia, 1995; Ahr, 2008). These classifications are mostly from the petrographical or petrophysical description and are useful to illuminate the different carbonate pore configurations. However, more quantitative classification of carbonate pore types needs much improvement and is essential for the prediction of field-wide reservoir performance.

Mercury Injection Capillary Pressure (MICP) analysis is a standard petrophysical method for characterizing pore features (Purcell, 1949; Dullien and Dhawan, 1974;

Wardlaw, 1976; Van Brakel, 1981; Jennings, 1987; Melas and Friedman, 1992; Aliakbardoust and Rahimpour-Bonab, 2013; Anovitz and Cole, 2015). The shape of the MICP curves is determined by grain sorting, pore throat size distribution and connectivity of the rock samples, which control the permeability and reservoir quality (Wong et al., 1984; Katz and Thompson, 1986). Reservoir performance can be predicted by evaluating the irreducible water saturation, pore-throat size distributions, displacement pressure and other parameters extracted from MICP curves (Dullien, 1975a, 1976). In addition, the mercury-injection withdrawal is often used to reproduce reservoir conditions and can be indicative of recovery efficiency of hydrocarbon with lowered pressure (Wardlaw, 1976; Wardlaw and Taylor, 1976). Many other rock typing methods were developed recently by petrophysicists to understand the rock texture related fluid flow (Porras, 1998; Porras and Campos, 2001; Varavur et al., 2005; Skalinski et al., 2010; Mishra et al., 2012; Norbisrath et al., 2015; Shahalipour et al., 2015). Commonly used methods include flow zone index (FZI), J-function from capillary pressure measurement, nuclear magnetic resonance (NMR), and the neural network method (Shahalipour et al., 2015). However, the MICP method and the other rock typing methods often have a high reliance on core measurements, thin sections, and SEM data; and some of the methods focused on porosity instead of pore type heterogeneity (Phukan, 2011). More integration of well logging data is necessary to understand the field-wide variation of pore structure (e.g. Skalinski et al., 2006).

Wireline logging is widely used in the oil and gas industry to estimate subsurface rock and fluid properties for exploration, drilling, and production. Conventional logs

such as electric and sonic logs can be further evaluated to quantitatively interpret pore type, considering the significant impact of pore structure on sonic wave propagation, electric current transmission and other petrophysical behaviors (Archie, 1942; Brie et al., 1985; Anselmetti and Elberli, 1993; Weger et al., 2004; Calvert and Ballay, 2011). Laboratory experiments indicate that, at a given porosity, carbonate rock with moldic or intraparticle porosity has higher velocity and resistivity than rocks with interparticle, intercrystalline or microporosity (Anselmetti and Eberli, 1993) and Verwer et al., 2011). Many methods thus have been developed to integrate core and well log data for pore type prediction (e.g. Anselmetti and Eberli, 1999; Lucia, 1995). In the field, a comparison of sonic-porosity and neutron-porosity often is used as a secondary porosity index (SPI) that can indicate the presence of vugs and fractures (Schlumberger, 1991). The velocity deviation log is introduced to predict pore type and permeability (Anselmetti and Eberli, 1999). The velocity-deviation log is derived from a comparison of the measured sonic velocity and the velocity from Wyllie's time-average equation. To estimate pore structure variation more quantitatively, many rock physics models also were developed over the years (Brie et al., 1985; Xu and White, 1995; Salem and Chilingarian, 1999; Sun, 2000; Salen and Castagna, 2004; Verwer et al., 2011; Adesokan and Sun, 2014; Sun et al., 2015). For instance, one of the rock physics models developed recently by Sun (2000), was applied with success to evaluate pore structure variation in the producing fields (Gartner et al., 2005; El-Wazeer et al., 2010; Dou, 2011; Zhang, 2014). In this model, Sun introduced the frame flexibility factor (γ, γ_μ) as pore structure

proxies to explain the significant differences in velocity at a fixed porosity caused by pore structure variations.

The carbonate reservoirs for this study from Puguang Gas Field have various pore structures, resulting in significantly different production and recovery in the same formation. In this paper, integrated study of core and log data is applied to better understand the pore type variation and reservoir heterogeneity in the studied field. The MICP, J-function, core porosity and permeability were analyzed first to classify pore types. Integrated analysis of resistivity, velocity, and neutron-density logs was then applied to estimate pore types. We evaluated the following parameters: the differences between shallow and deep resistivity, between neutron porosity and density, Archie's cementation factor (m), Sun's frame flexibility factor (γ_μ), and Castagna's S factor. Afterward, the effectiveness and limitations of each method for pore type evaluation are discussed to assist the future application of these methods in other fields. The results of pore type analysis will be further applied to classify the permeability-porosity trends for better estimation of permeability.

II.3 Methods

In this section, an integrated approach using common core and log data to estimate carbonate pore types is outlined, including the analysis of MICP and Leverett J-function curves, and five rock physics methods.

II.3.1 Mercury injection capillary pressure (MICP)

Capillary pressure curves subject to mercury injection and withdrawal, contain useful information concerning pore size and shape, pore throat size and geometry, and grain sorting (Wardlaw and Taylor, 1976). In this study, we first analyzed the MICP curves and the related petrophysical parameters, such as pore throat tortuosity, irreducible water saturation ($S_{\min}$), capillary pressure at 10% and 50% Hg injection (P_{10}, P_{50}), and Leverett J-function values, as well as thin sections, to classify the different pore types observed in the studied Feixianguan carbonate gas reservoir.

Leverett J-function from the MICP is a dimensionless function of water saturation describing the capillary pressure (Leverett, 1941). All of the capillary pressure data from a specific formation usually can be reduced to a single J-function versus the saturation curve. J-function curve analysis often is indicative of pore geometry if wettability is the same because the ratio of permeability versus porosity is associated with the mean hydraulic radius of pore throats. Based on the MICP data, the J-function is calculated using the following equation:

$$J(Sw) = \frac{Pc(Sw)}{\sigma \cos\theta}\sqrt{\kappa/\phi} \qquad (2.1)$$

Where P_c is capillary pressure in pascal, κ is permeability in md, ϕ is porosity (0-1), σ is the interfacial tension in N/m, and θ is the contact angle.

II.3.2 Resistivity evaluation

In this paper, we use two different methods to analyze resistivity data to investigate the influence of pore structure variations in resistivity. The first method we propose is to correlate the difference between deep and shallow resistivity to permeability and the second approach is to study the influence of pore structure on the cementation factor *m* in Archie's law (Archie, 1942).

The difference between deep and shallow resistivity

For porous and permeable reservoirs, mud filtrate invasion may affect the accuracy of rock properties determined from logging tools. Invasion in the highly permeable zones often leads to a strong difference between the shallow and deep resistivity readings (R_s , R_d). Therefore, this resistivity contrast can be used to detect reservoirs with high permeability, as shown in Eq. 2.2. For instance, carbonate reservoirs dominated by fractures and dissolution-enlarged intercrystalline pores with higher permeability may have stronger resistivity contrast than carbonate rocks that have moldic pores or micro-intercrystalline pores and less mud filtrate invasion.

$$\mathrm{f}(\mathrm{logRd},\mathrm{logRs}) = \frac{\mathrm{logRd} - \mathrm{logRs}}{\mathrm{logRd} + \mathrm{logRs}} \tag{2.2}$$

Cementation factor m

Using Archie's law (Archie, 1952), cementation factor *m* is calculated using the deep resistivity log (R_t), apparent water resistivity log (R_{wa}) and density derived porosity logs (ϕ), based on the following Eqs. 2.3-2.4:

$$FF = \frac{Rt}{RWA} \tag{2.3}$$

$$m = \frac{\log \frac{a}{FF}}{\log \phi} \tag{2.4}$$

, where FF is the formation factor, *a* is assumed to be 1 and porosity is derived from density.

Similar to many other methods attempted to derive cementation factor, *m*, from Archie's equation, this approach also assumes *a* equals to 1 (e.g. Neustaedter, 1968; Sethi, 1979; Rasmus, 1983; Borai, 1987; Focke and Munn, 1987). In fact, the value of *a* also varies following the changes in pore structure. In this study, *a* is assumed to be constant, considering the larger influence of pore structure on *m* than on *a*.

II.3.3 Sonic velocity evaluation

We also used two rock physics methods to study the effect of pore structure on sonic wave propagation. The first method is an evaluation of the effectiveness of the S factor, introduced by Salen and Castagna (2004), for discrimination of pore shape; the second method is an investigation of the effect of pore type variation on sonic velocities using frame flexibility factors from a rock physics model (Sun, 2000).

Pore shape factor S

Saleh and Castagna (2004) introduced an exponent to the solid-phase term of Wyllie's equation, termed pore shape factor *S*, considering the effect of pore shape on sonic velocity. The Wyllie's time-average equation is shown in Eq. 2.5 (Wyllie et al., 1956):

$$\frac{1}{V} = \frac{1-\phi}{V_m} + \frac{1}{V_f} \tag{2.5}$$

The modified Wyllie's time average equation is shown in Eq. 2.6:

$$\frac{1}{V} = \frac{1-\phi_B}{Vm^s} + \frac{\phi_B}{Vf} \tag{2.6}$$

The velocity of the rock (V) is from sonic log measurements; the velocities of the matrix (V_m) and fluid (V_f) are taken to be 6530 m/s and 1500 m/s, respectively, which are close to the velocity values of dolomite and water. ϕ is the total porosity. ϕ_B is the porosity calculated using density-neutron logs. S is pore shape factor, which can be approximated by the following equations:

$$S = 1 + (\frac{\phi_s}{\phi_B}) \times \frac{\phi_B}{6.5/Vm - 3\phi_s + 2\phi_B\phi_s} \tag{2.7}$$

$$\phi_s = \frac{\phi_s - \phi_p}{1-\phi_p} \tag{2.8}$$

, where ϕ_p is the primary medium porosity calculated using Wyllie time average equation.

Frame flexibility factor γμ

A rock physics model introduced the frame flexibility factors (γ, γ_μ) are used as proxies for pore structure for a given mineralogy and fluid type (Sun, 2000, 2004). The introduced factors are related to the connectivity tensor and characterize the effects of pore structure, grain contacts, and grain coupling, cementation and pore connectivity on the flexibility and elasticity of porous rocks (Sun, 2004). In this study, the shear frame

flexibility factor (γ_μ) from Sun's model is used to estimate pore structure, such as pore shape and size.

$$V_p = \sqrt{\frac{K + \frac{4}{3}\mu}{\rho}} \tag{2.9}$$

$$V_s = \sqrt{\frac{\mu}{\rho}} \tag{2.10}$$

$$K_d = K_s(1-\phi)^{\gamma} \tag{2.11}$$

$$\mu_d = \mu_s(1-\phi)^{\gamma_\mu} \tag{2.12}$$

For the studied gas reservoir rock, we simply use

$$K = K_d$$

and

$$\mu = \mu_d \tag{2.13}$$

Vp and *Vs* are the *P-wave* and *S-wave* velocities, while ρ is density. *K* and μ are the bulk and shear moduli for the rock, respectively. K_d, μ_d, K_s, and μ_s are the dry frame and solid matrix bulk moduli and shear moduli, respectively; γ and γ_μ are the frame flexibility factors. In the equations, the porosity is derived from density logging (ϕ). K_s and μ_s are derived from laboratory measurements of dolomite.

II.3.4 Neutron-Density evaluation

We further evaluated the effect of pore structure on density and neutron (D-N) measurements by correlating D-N to permeability. Density and Neutron are active

source measurements and have different depths of investigation. In the case of mud filtrate invasion, for a permeable gas reservoir, density logs may read values from mud filtrate, which are much higher than gas (Wiley and Patchett, 1994). For instance, under similar gas saturation, permeable rocks dominated by intercrystalline porosity may have significant separation between neutron and density logs after mud filtrate invasion. The separation can be quantified by Eq. 2.14 in the studied formation, where NPHI is neutron porosity, Den is density.

$$f(D-N) = [(2-Den)-(NPHI-5)/30]*100 \quad (2.14)$$

II.4 Results

In this study, the effect of pore structure on rock properties and reservoir performance is evaluated from different perspectives using common core and well log measurements. As outlined in the Methods section, pore type classification was performed first using MICP and J-function analysis. Five rock physics parameters were then used to quantify the different pore types classified from core analysis. The effectiveness of each method for pore type evaluation will be compared and discussed.

II.4.1 Pore type classification from core analysis

MICP curve analysis

Mercury capillary pressure curves can be used to estimate rock properties, such as porosity, effective porosity, pore throat size and its distribution, and fluid saturation (Wardlaw and Taylor, 1976). In this study, we attempt to classify the pore types by

integrated study of pore throat size distribution, sorting or tortuosity of the pores, critical pore-throat size (*Rc*), irreducible water saturation (S_{min}), and displacement pressure (P_d).

Four distinct types of pore structures with significantly different permeability-porosity relationships occur in the studied Feixianguan gas reservoirs, including micro-intercrystalline, medium intercrystalline, large intercrystalline and moldic porosity. Four pore structures or a mixture of them provide six capillary injection and withdraw curves (Figure 2.1). Example "a" is dominated by micro-intercrystalline porosity and is considered as non-reservoir facies. The pore throat size is small and narrowly distributed. The MICP curve has a very high yet flat plateau, indicating good sorting. However, P_d and S_{min} are high, indicating poor reservoir quality (Figure 2.1.a). Examples b, c, and d show a mixture of moldic and intercrystalline porosity; they are dominated by large moldic, moldic and intercrystalline, and intercrystalline porosity respectively (Figure 2.1.b.c.d). From sample b to d, the crystal size and pore throat size increase with advanced dolomitization. All three samples display a broad and bimodal distribution of pore throat size, MICP curves with a steep slope and two possible plateaus, and relatively small P_d. Therefore, it is difficult to differentiate examples b and c, for further reservoir evaluation. Even though example b has a much higher porosity (16%) than example c (8%), their permeability are the same around 0.2 md. To better evaluate reservoir quality for the mixed pore system, J-function analysis is applied, and the results are discussed later. Examples e and f were from reservoirs with large intercrystalline porosity and great production rates (Figure 2.1.e.f). The MICP curves are characterized as having low, flat plateaus with very low P_d and S_{min}. As the dominant pore throat size

increases from a to f, the reservoir performance improves. Therefore, the capillary pressure curves and their extracted parameters of tortuosity, P_d and S_{min} can be used to evaluate pore type, even though ambiguities exist in the mixed pore types.

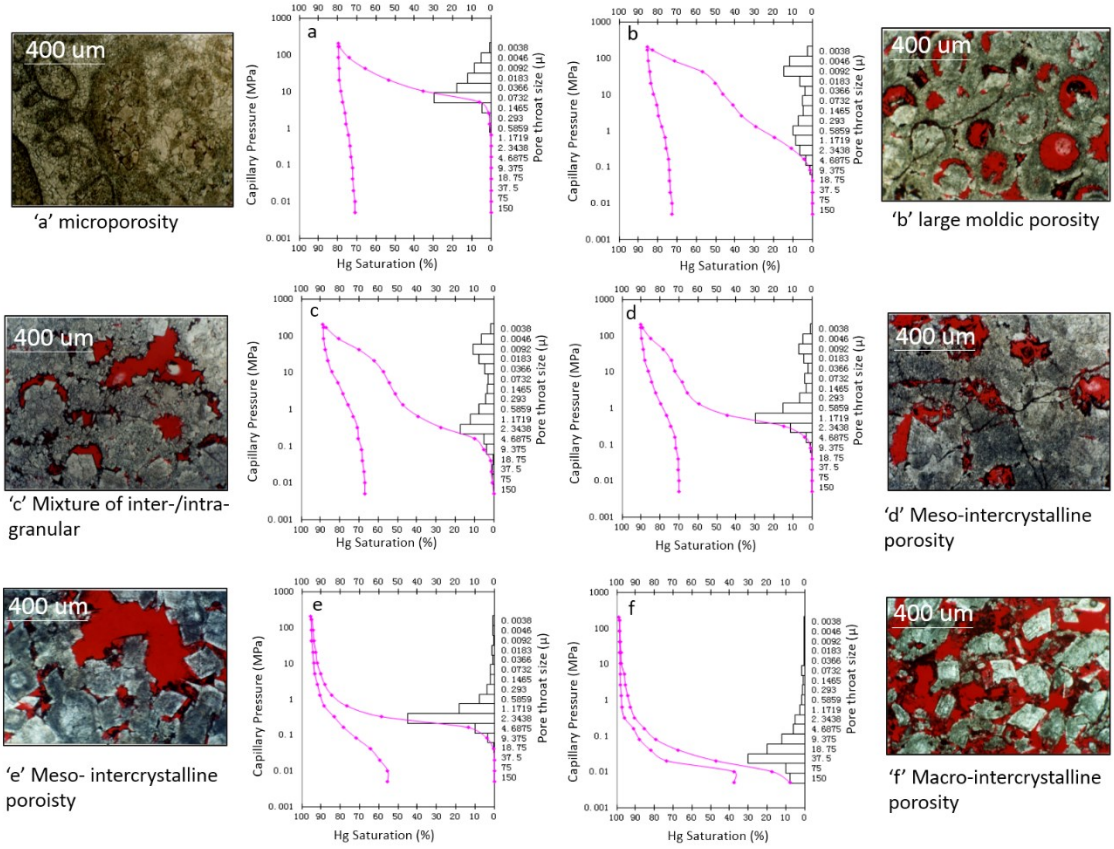

Figure 2. 1 Mercury injection and withdrawal curves and thin section photomicrographs for the six different pore systems; red color in the thin sections are pore space: a) micro-intercrystalline pores; b) moldic and intragranular pores; c) intragranular and intercrystalline pores; d) intercrystalline pores dominated, scattered intragranular pores; e) intercrystalline pores; f) large and sucrosic intercrystalline pores. The crystal sizes increase with enhanced reservoir quality.

Figure 2.2 shows three cross-plots of permeability, S_{min}, tortuosity and P_d, where tortuosity is defined as a property of curve being tortuous and might be expressed in terms of porosity and formation factor (Amyx et al., 1960; Dullien, 1975b; Dullien, 1976). The strong correlation of permeability, S_{min} with tortuosity and P_d confirms that these extracted parameters indicative of pore type can be used to understand reservoir performance. For instance, sample f, dominated by large intercrystalline porosity, has very low P_d, low tortuosity and S_{min}, and excellent production.

J-function curve analysis

To better distinguish the mixed pore types with two or more pore structures, such as examples b, c, d in Figure 2.1, statistical analysis of J function curves was performed. The results show very distinct features for the different pore types (Figure 2.3). The slope of the curve, the saturation at the inflection point and the largest measured J-function value are increasing in the order of moldic dominant (purple), meso-intercrystalline dominant (green), to large intercrystalline pore system (red), indicating decreasing irreducible water saturation and improving permeability and reservoir quality. Additional pore types identified from the J-function analysis are irregular dissolved porosity (yellow) and micro-intercrystalline porosity (black).

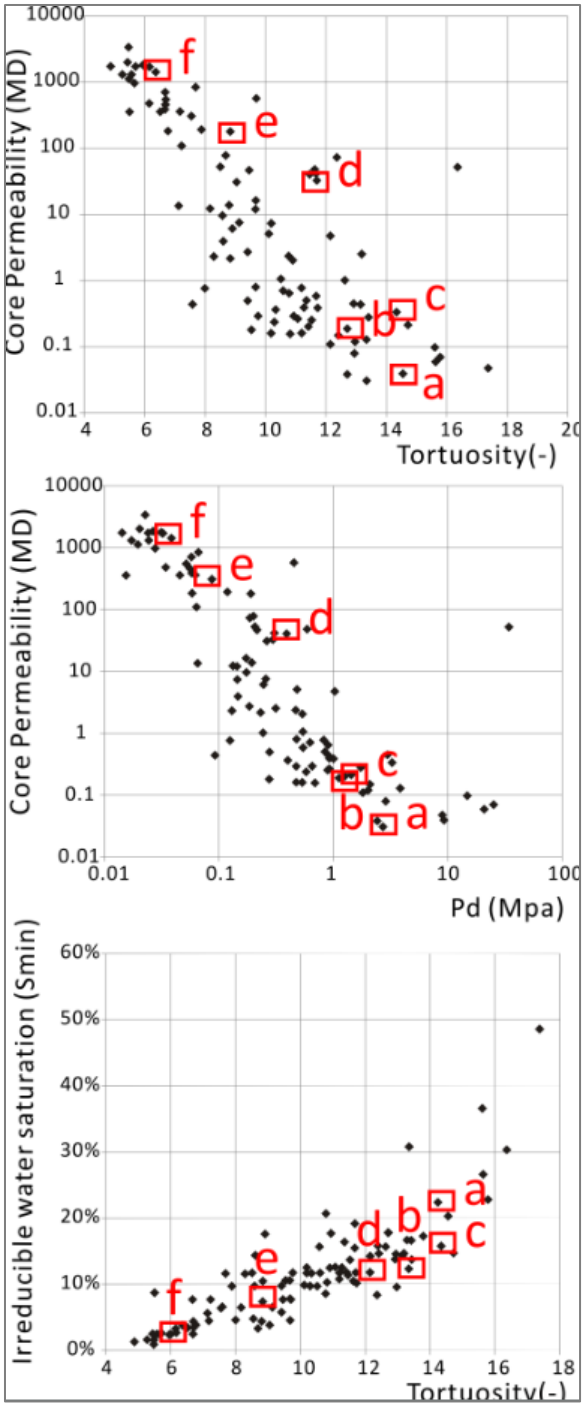

Figure 2. 2 Cross-plots of petrophysical parameters from permeability and capillary pressure analysis of core data. Tortuosity, displacement pressure P_d, and irreducible water saturation S_{min} values are extracted from capillary pressure curves. Tortuosity explains the complexity of fluid flow paths and sorting of pore throats in the rock (Amyx et al., 1960). The capillary pressure curves for the selected examples (a to f) are shown in Figure 2.6.

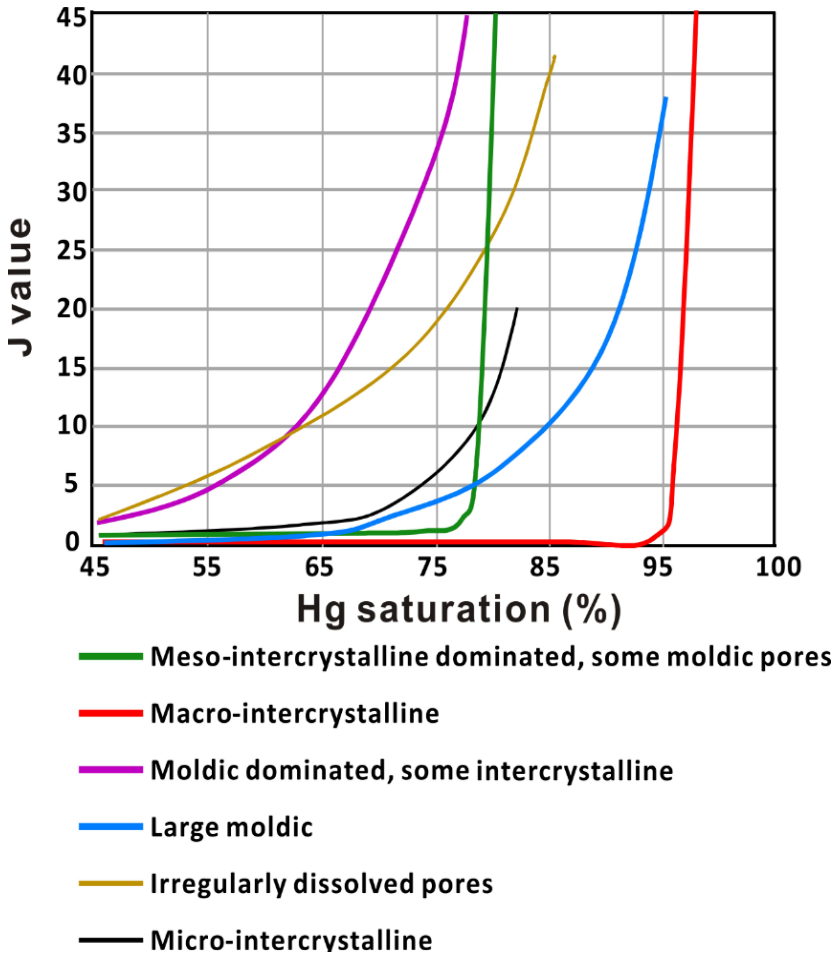

Figure 2. 3 Leverett J-function curves for all six pore systems observed from the core. The characteristics vary as the size and shape of pores changes.

Figure 2.4 displays the J-function and saturation data for the four major pore types. The color in Figure 2.4 is the same as Figure 2.3.

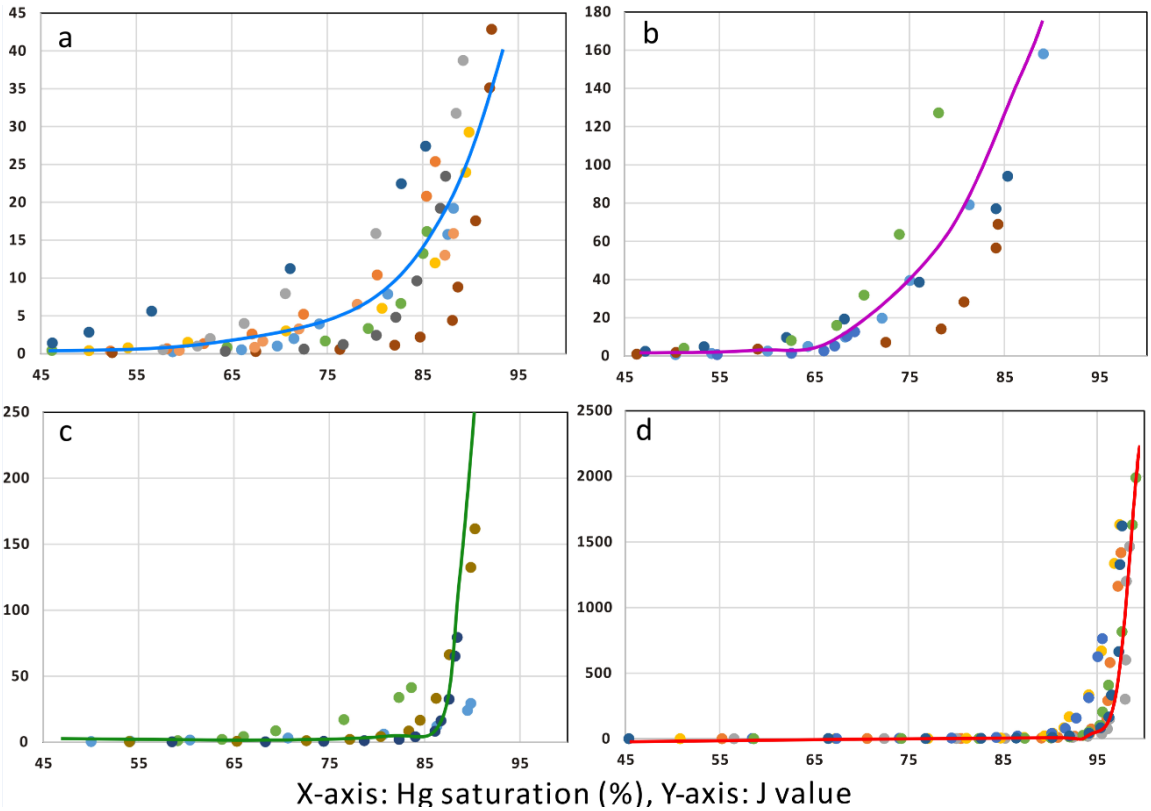

Figure 2. 4 Sample data for Leverett J-function analysis for four distinct pore types shown in Figure 2.3. The color code is consistent with Figure 2.3 and indicates different pore types. The highest J value of samples and the slope of curves increases in the plots from a to d.

Pore type guided reservoir zonation

Based on the results of MICP, J function, and thin section analysis, pore types are classified for the studied carbonate reservoir (Figure 2.5). From the base to top, pore types changed from moldic pore dominant to sucrosic macro-intercrystalline, mixed moldic and intercrystalline (moldic dominated), meso-intercrystalline, and micro-intercrystalline successively. Using the parameters from MICP analysis such as the pore throat sizes and capillary pressures at 10% and 50% of mercury injection (Rc_{10}, Rc_{50},

P_{10}, and P_{50}), tortuosity and S_{min}, five zones with distinct pore types are defined. Zone 1: reservoirs are dominated by large moldic porosity with large pore size, small pore throat sizes (Rc_{10} and Rc_{50}), high capillary pressures (P_{10} and P_{50}), high tortuosity, great S_{min}, and high core porosity but low core permeability. In this zone, a significant amount of residue gas is expected as the pores are isolated and difficult to flow. Zone 2: reservoirs are dominated by sucrosic intercrystalline porosity with excellent reservoir quality. They have large pore throats, very low P_{10} and P_{50}, very low tortuosity, low S_{min}, and high core porosity and permeability. Zone 3: reservoir has mixed pore types of moldic and intercrystalline. Reservoir quality is fair from field production. The pore throat size is smaller than Zone 2 and larger than Zone 1. They have relatively high P_{10} and P_{50}, slightly higher tortuosity than Zone 2, and low core porosity and permeability. Zone 4 reservoirs are dominated by meso-intercrystalline porosity with some scattered moldic porosity. These reservoirs contain smaller pores with larger pore throats, and slightly higher core porosity and permeability, thus better reservoir quality than Zone 3. Tortuosity can be high or low depending on the crystal size. Zone 5 is non-reservoir unless fractured. The dominant pore type in Zone 5 is micro-intercrystalline, containing very narrow pore throats with very high displacement pressure. Fluid often is not movable in Zone 5. The average, maximum, and minimum values of core measured porosity and permeability for the five zones are compared in Figure 2.6. Production agrees with this plot that reservoir performance is best in Zone 2 followed by Zone 1, Zone 4, and Zone 3.

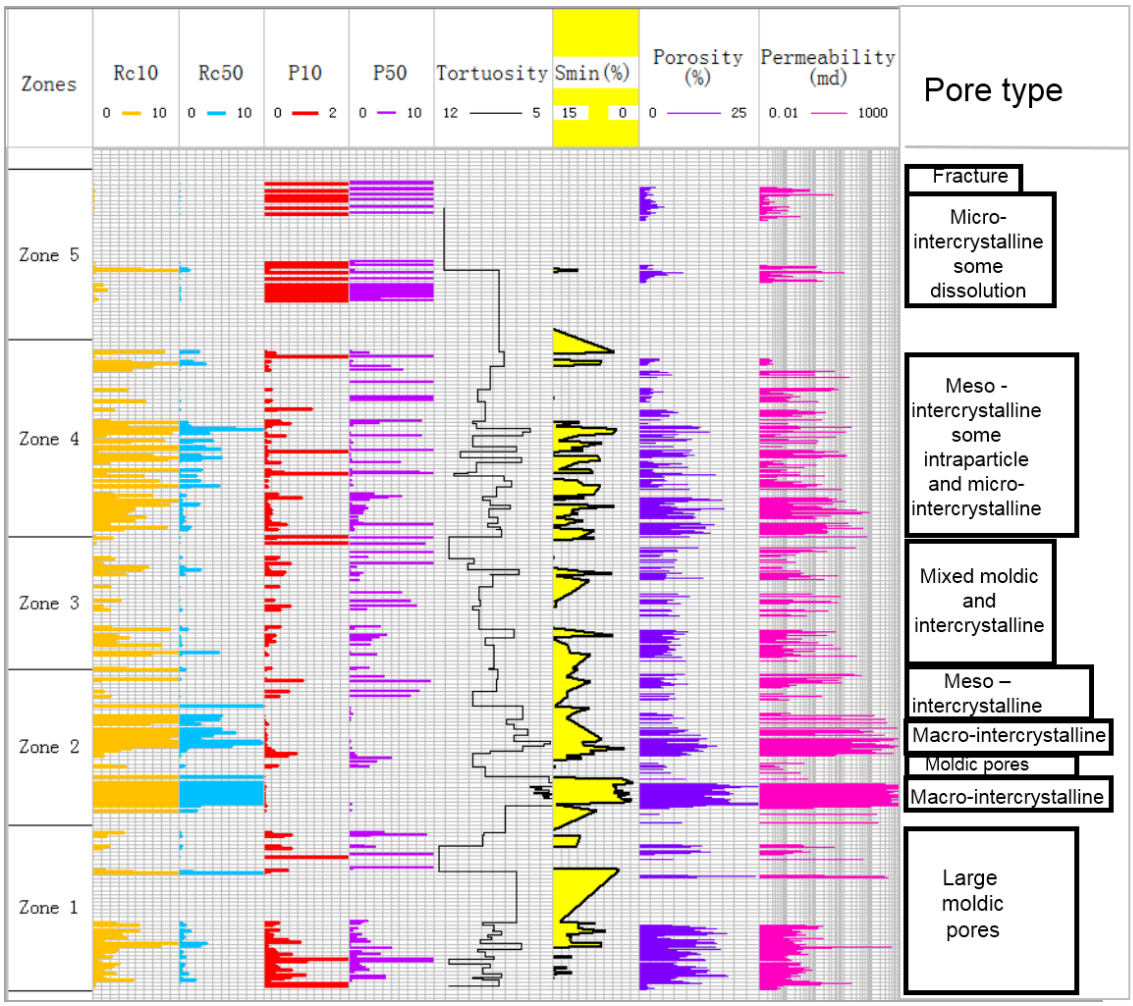

Figure 2. 5 Pore structure interpretation and formation zonation based on core measurements. Tracks from left to right show dominant pore throat sizes and capillary pressures at 10% and 50% injection of Hg (Rc_{10}, Rc_{50}, P_{10}, and P_{50}), pore space tortuosity, irreducible water saturation S_{min}, core porosity, core permeability, thin sections, and interpretation of pore types.

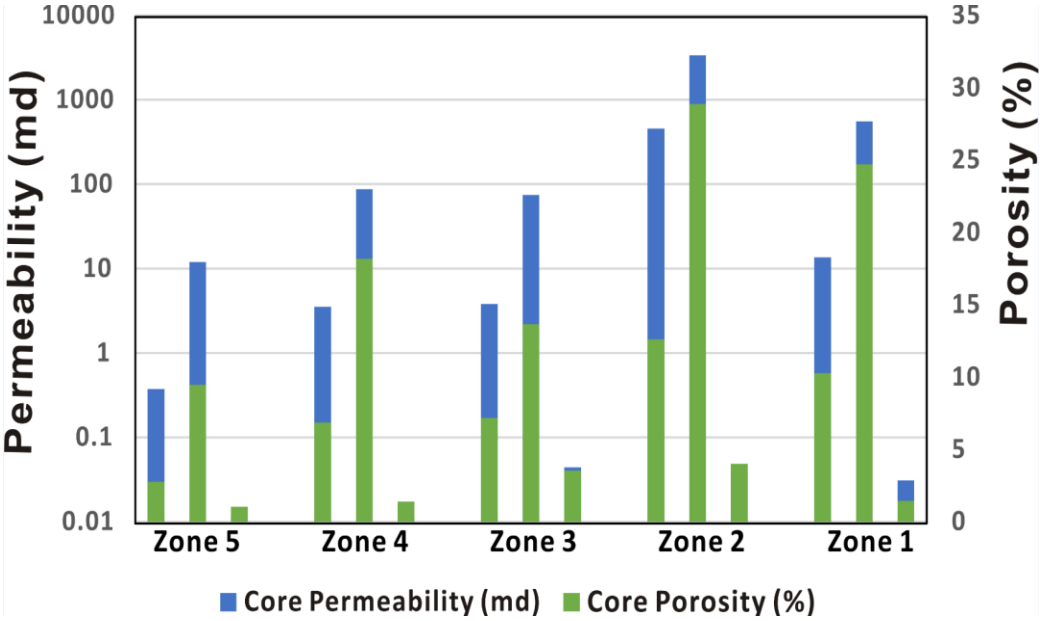

Figure 2. 6 Histograms comparing core porosity and permeability among the five interpreted zones. The three bars for each zone show average, maximum, and minimum values respectively from left to right.

II.4.2 Pore type estimation by well log analysis

Pore type variation can significantly affect the reservoir properties such as velocity and resistivity. Figure 2.7 shows the cross plot of sonic velocity (V_p) versus porosity. Pore structure variation in the thin sections causes large differences in velocity at a given porosity. For example, when $\gamma_\mu < 4$, the dominant pore type is moldic; when $4 < \gamma_\mu < 12$, the dominant pore type is intercrystalline; when $\gamma_\mu > 12$, most of the pores are micro-intercrystalline pores. Under the same pore type such as shown by the yellow dots, the velocity varies following the changes in the porosity and grain size.

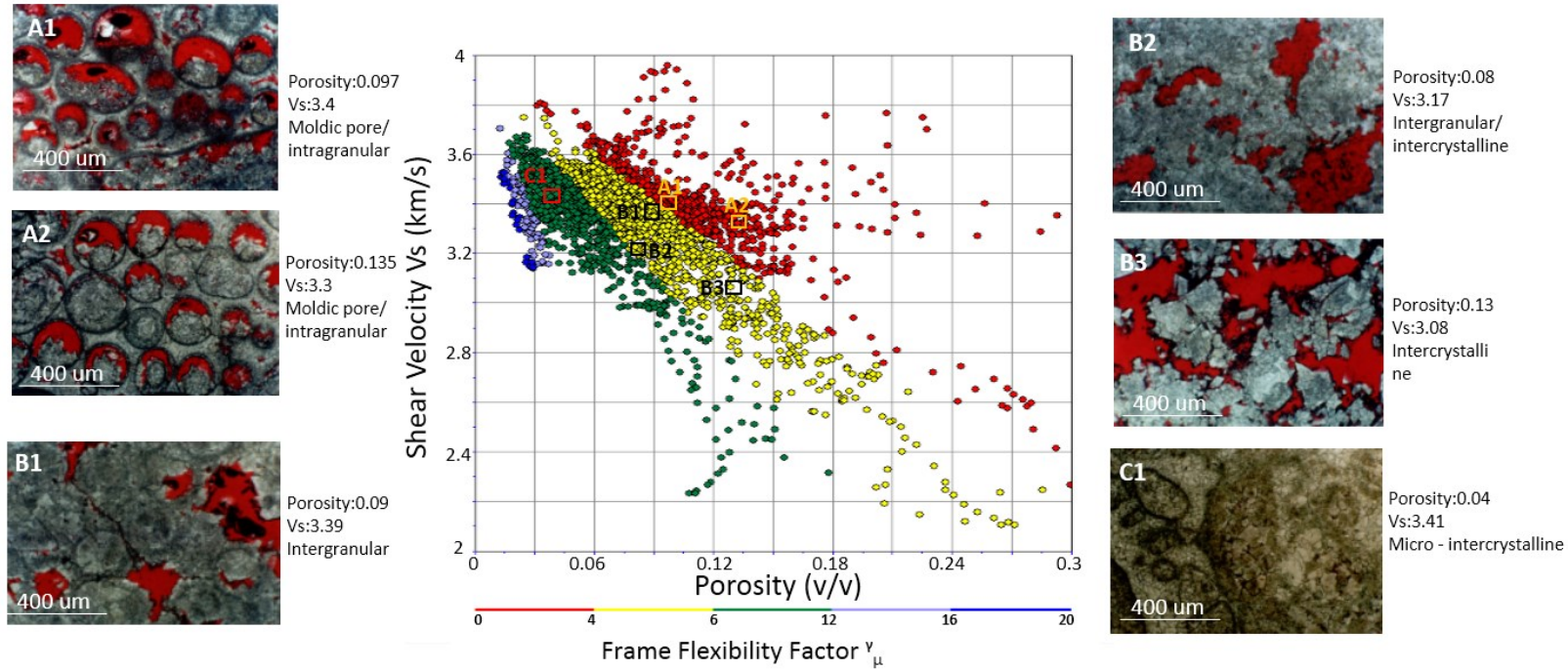

Figure 2. 7 Cross-plot of shear velocity V_p with density porosity. Frame flexibility factor γ_μ is shown in color. Different pore types are shown in the cast sections on the right. At a given porosity, moldic pore is showing higher velocity and lower γ_μ. Velocity also decreases as dolomitization developed (shown from B1 to B2 and B3).

Next, the pore type estimation is conducted using resistivity, sonic, density and neutron log data. For example, the results of well log analysis for the same interval of the same well are shown in Figure 2.8. The displayed log curves are velocities for shear (V_s), compressional (V_p) and Stoneley wave (V_{st}), neutron porosity, density, deep and shallow resistivity, and pore structure indicators calculated by the five different methods. Compared to the pore type evaluation results from core analysis, all indicators can separate moldic pores in Zone 1 from sucrosic intercrystalline pores in Zone 2. The black lines in the displayed tracks act as the boundaries between moldic pores and intercrystalline pores. However, discriminating between mixed moldic and intercrystalline pores (Zone 3) and meso-intercrystalline pores (Zone 4), and between meso-intercrystalline (Zone 4) and micro-intercrystalline (Zone 5) is more difficult. The cementation factor (m) and frame flexibility factor (γ_μ) are the best parameters to separate all five zones with distinct pore types. Moldic pores have $m > 2.4$, $\gamma_\mu < 4$ whereas meso and macro intercrystalline pores have $1.6 < m < 2.4$, $4 < \gamma_\mu < 8$. Micro intercrystalline pores have $m < 1.6$ and $\gamma_\mu > 8$. Therefore, an integrated approach using conventional well log data are proposed and shown in Figure 2.9, which may be applied to assist the evaluation of complex pore types in carbonate rocks. Reservoirs dominated by the macro- to meso-intercrystalline pores, shown by the purple color, are the best candidates for production.

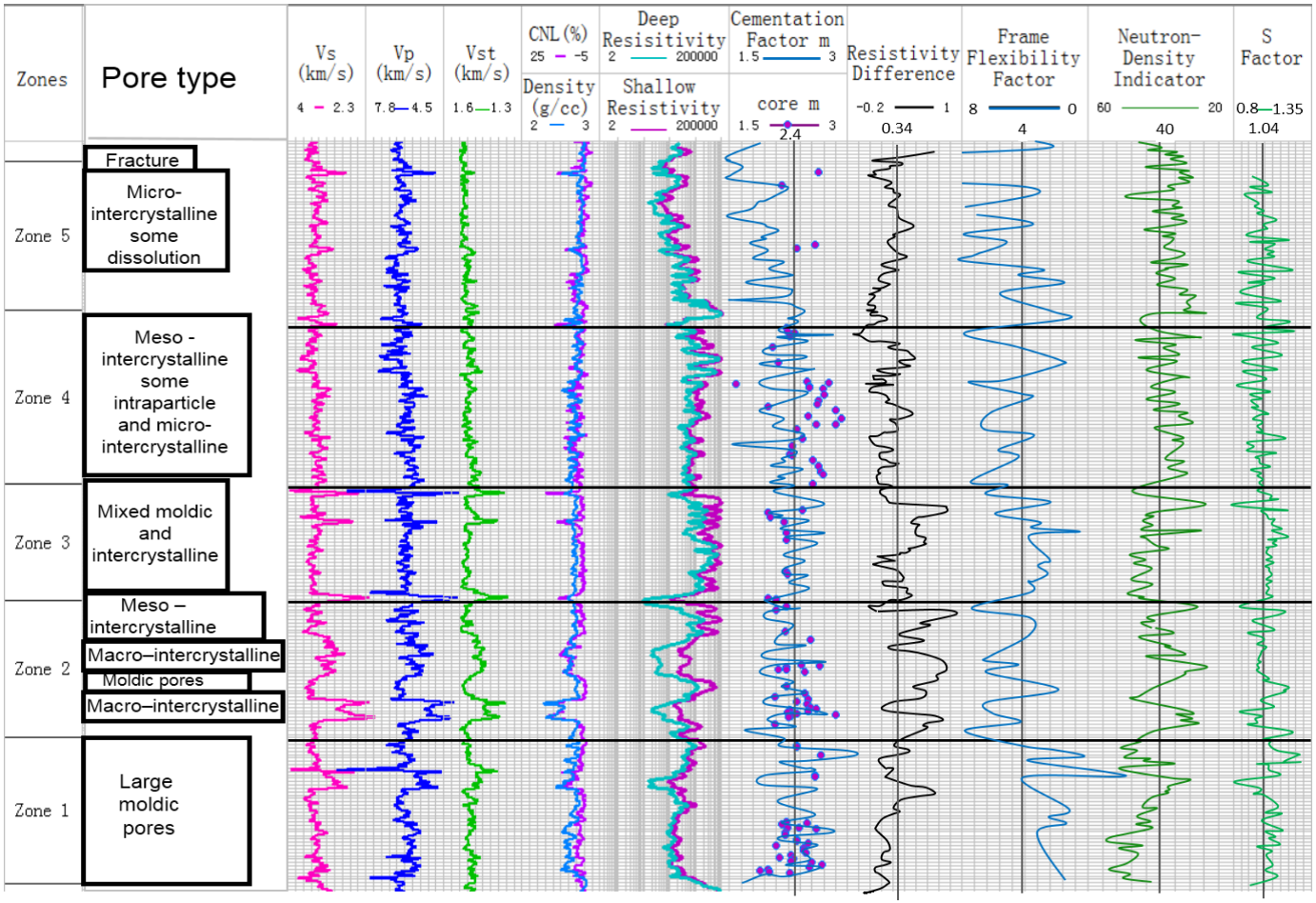

Figure 2. 8 Well log characterization of the different pore types observed from the core; input logs are V_s, V_p, neutron porosity (CNL), density, and deep/shallow resistivity; the created pore structure indicators are cementation factor, resistivity difference, frame flexibility factor, neutron-density difference, and S factor. All five methods are effective in distinguishing Zone 2 and Zone 1.

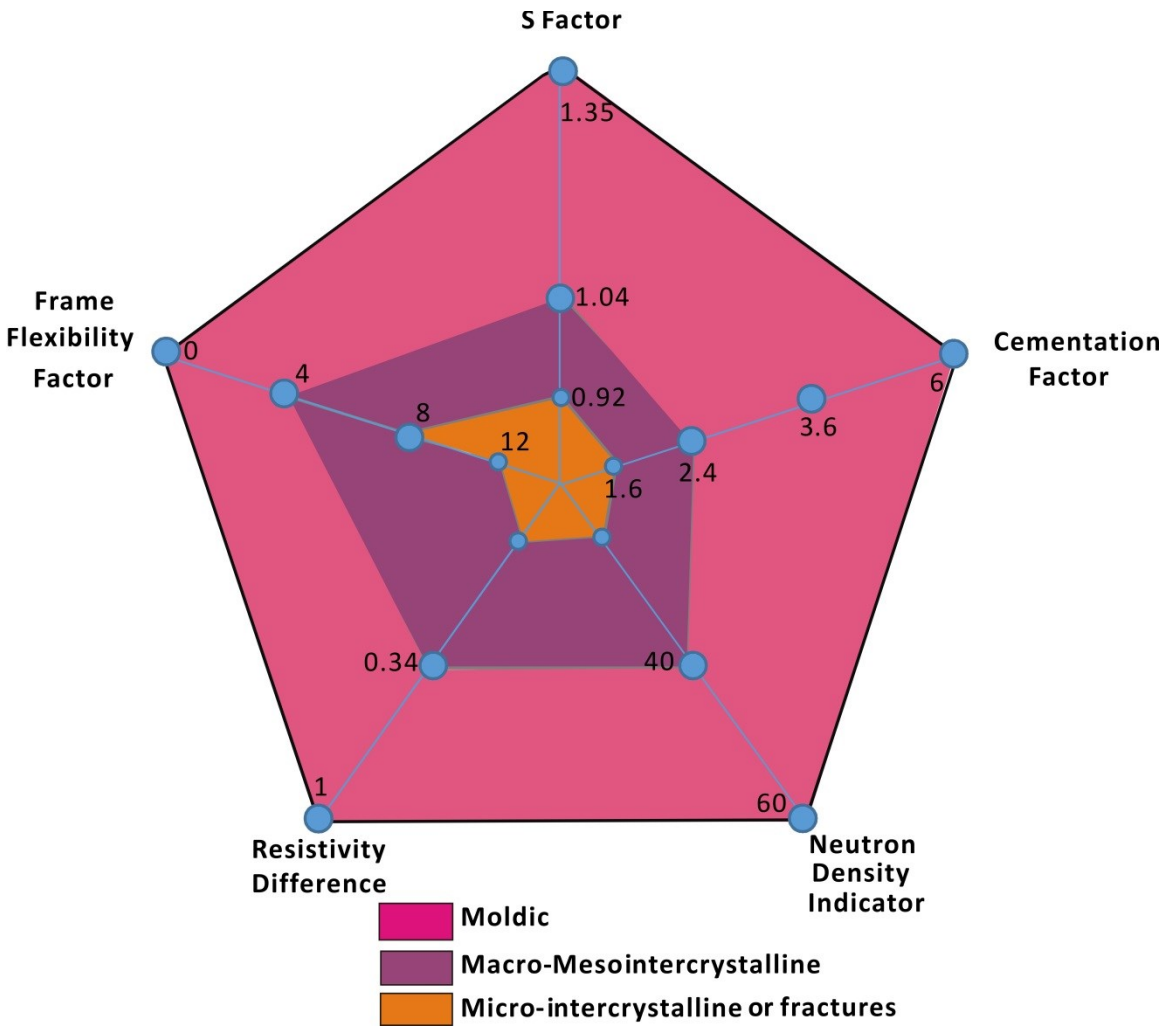

Figure 2. 9 Integrated predictions of dominant pore types for the studied formation with five criteria. Better reservoir quality is expected in the Macro- intercrystalline pores showing by the purple color.

II.4.3 Discussion

Comparison of different rock physics methods

In this study, we attempted to quantify the effect of pore structure variation on standard log measurements such as resistivity, sonic velocity, neutron, and density, using several well-established methods. Each method applied has its limitation and advantages. A better understanding of the differences among the methods can benefit their future applications for pore structure prediction in other fields.

The resistivity difference method is an indirect and relatively qualitative method to separate macro- intercrystalline pores and fractures from micro-intercrystalline pores and moldic pores because this method is essentially based on the degree of mud filtrate invasion controlled by permeability. This method is effective in separating permeable zones from dense zones and thus shows good correlation with Stoneley wave velocity (Figure 2.8). However, resistivity differences cannot distinguish large moldic pores and meso-intercrystalline from micro-intercrystalline pores and fractures. The S factor introduced by Saleh and Castagna (2004) is a laboratory parameter introduced to correct the velocity calculated from Wyllie's time average equation, considering the effect of pore shapes on velocity. It is effective in separating rounded moldic pores from planar intercrystalline pores (e.g. Zone 1 and 2). However, it does not take into account the size of pores as much as the shape. Therefore, it is difficult to separate large intercrystalline pores from small intercrystalline pores (e.g. Zone 4 and 5). Sun's frame flexibility factor and Archie's cementation factor are physical parameters that are affected by pore size, pore shape, pore connectivity, and many other parameters (Sun, 2000). They can be

applied to more efficiently describe reservoir performance and explain complex permeability behaviors. Even though the derivation of frame flexibility factor acquires the prior knowledge of shear wave velocity, the application of this parameter shows potential to extend evaluation of pore structure on a larger scale using seismic data, and to guide reservoir simulation (Gartner et al., 2005; El-Wazeer et al., 2010; Dou, 2011).

To better understand the relationships between different pore shape indicators, various cross-plots are analyzed. Cementation factor m and frame flexibility factor γ_μ show good correlation while there is no obvious correlation between either of the two and resistivity difference factor (Figure 2.10). Figure 2.11a shows the cross-plot of S factor with γ_μ, colored by m. Blue and green color with $m > 2.4$ indicates moldic or vuggy pores. A value of 1.04 for S can be used to separate these pores from intercrystalline pores with $m < 2.4$. However, within yellow dots where mostly intercrystalline pores are, there is a small variation in S as γ_μ increases. It is thus difficult to separate intercrystalline pores associated with different crystal sizes. When S factor is larger than 1.04, it does not correlate with the frame flexibility factor, indicating that S factor is not effective to describe these frame related pores, such as dissolved vugs. Figure 2.11b is the cross-plot of S with m, colored by γ_μ. Similarly, the S factor does not correlate with m for S larger than 1.04, whereas m and γ_μ are effective in distinguishing the different pore types. When $\gamma_\mu < 4$, $m > 4$, moldic pores and vugs are dominated. Vugs have larger m and smaller γ_μ than moldic pores. When $4 < \gamma_\mu < 8$, $1.6 < m < 2.4$, macro-intercrystalline pores dominated. When γ_μ is large, and m is small, micro-intercrystalline pores are prevalent.

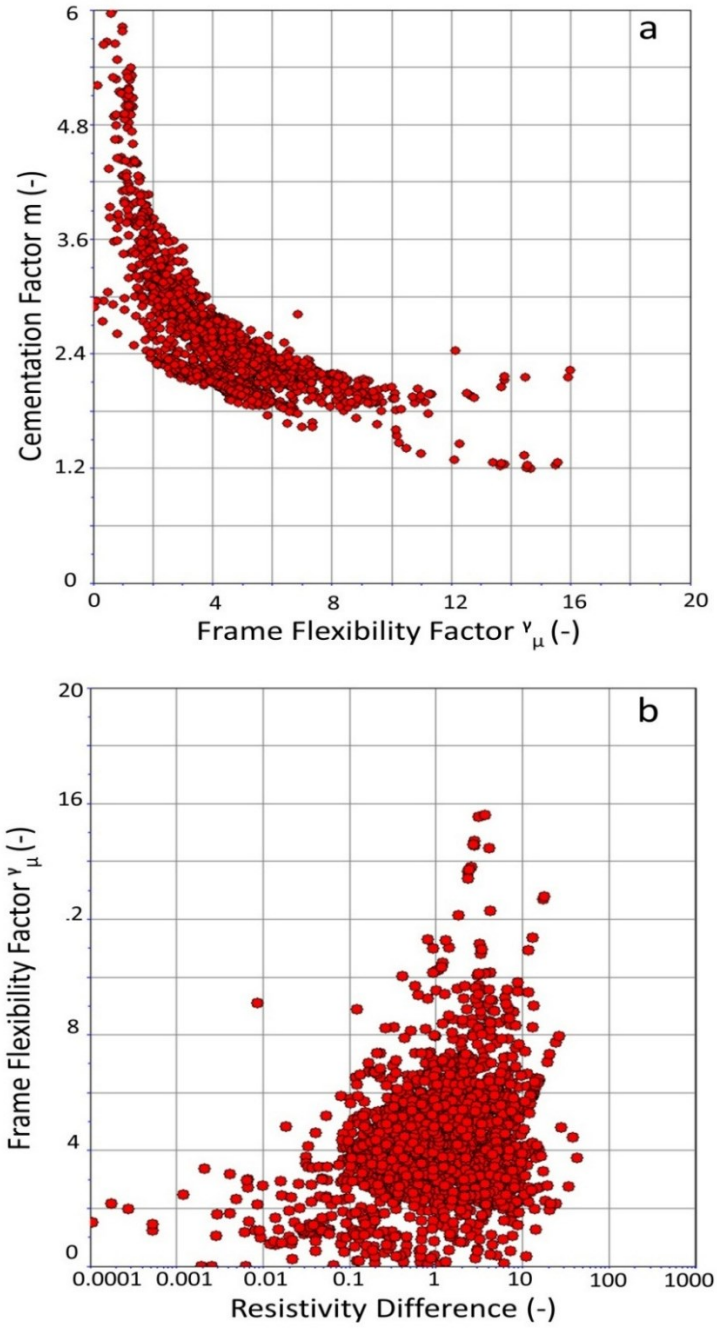

Figure 2. 10 a): Cross-plot of cementation factor, m and frame flexibility factor, γ_μ; b): Cross-plot of frame flexibility factor, γ_μ and the pore structure indicator from resistivity difference method. The m vs. γ_μ correlation (a) is better, as these factors are physically related to pore geometry.

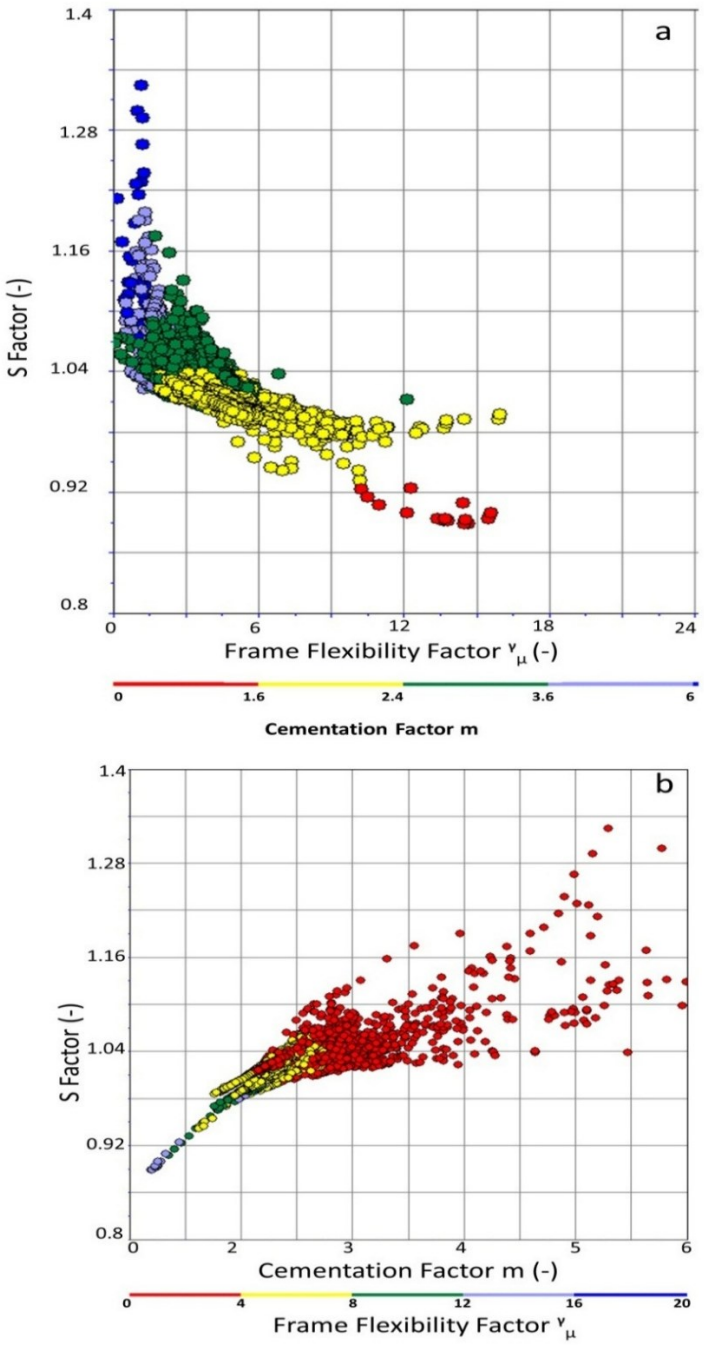

Figure 2. 11 a) Cross-plot of S factor against frame flexibility factor, γ_μ, colored by cementation factor m; b) cross-plot of S factor against cementation factor m, colored by frame flexibility factor γ_μ. Intercrystalline pores and moldic pores can be distinguished by a cutoff value of 1.04 for S factor as indicated by m and γ_μ. The m and γ_μ better characterize other pore types.

Permeability estimation

In the studied Puguang gas field, one of the challenges for production is the poor recovery from porous grainstone reservoirs, due to complex permeability-porosity behaviors caused by the pore structure variation. As discussed, reservoir performances differ significantly following the pore structure variations in the five zones classified from core analysis. Production from zones dominated by large isolated moldic pores is much more challenging than from zones with connected intercrystalline pores. Accurate estimation of pore type and permeability is thus crucial for better reservoir management. The pore structure indicators introduced in this study may be used to assist the estimation of permeability from porosity by classifying different permeability-porosity trends. Figure 2.12 shows examples of using cementation factor m and frame flexibility factor γ_μ to constrain permeability estimation. The plots are from two zones with distinct pore types (Zone 1 and 2). The upper interval is entirely dolomitized with high permeability whereas the lower interval is mostly moldic oolitic grainstone with low permeability. Both m and γ_μ are effective to classify the two permeability trends for the two reservoir intervals with distinctive pore types. When $\gamma_\mu < 4$, $m > 4$, the low permeability trend persists, and the dominant pore type is isolated moldic pores; porosity ranges between 0.16-0.30, and permeability ranges between 0.02-8 md. When $\gamma_\mu > 4$, $m < 4$, the high permeability trend is observed, and the dominant pore type is secondary intercrystalline pore; porosity ranges between 0.01-0.16, and permeability ranges between 0.08-900 md. Compared to crystalline dolomite with connected intercrystalline pores, the ooid grains with isolated large moldic pores have low γ_μ and high m values.

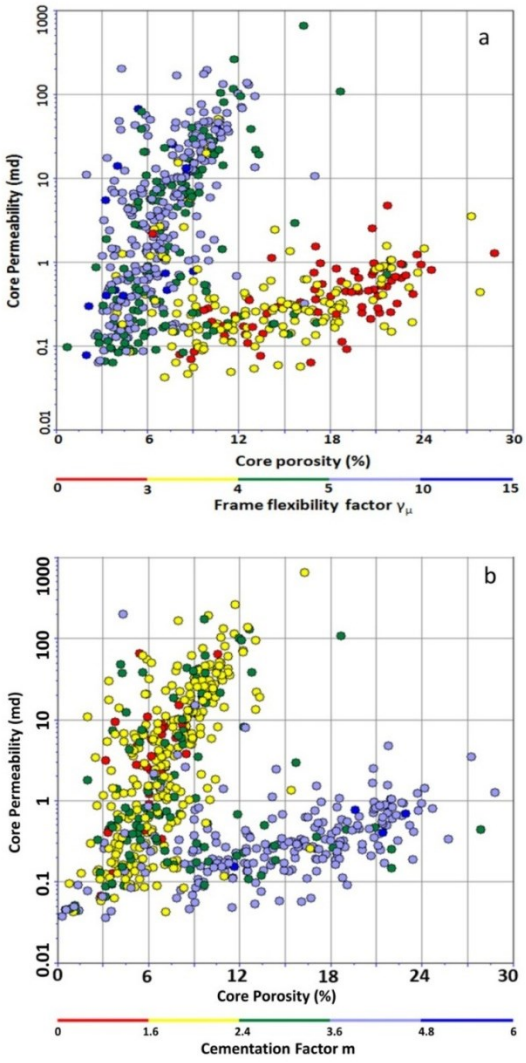

Figure 2. 12 Cross-plots of core permeability vs. core porosity colored by (a) frame flexibility factor, γ_μ and (b) cementation factor, m. Two trends are observed for two different pore systems. The higher permeability trend is for rocks dominated by intercrystalline pores, whereas the lower permeability trend is for rocks dominated by moldic pores.

The new permeability estimation using different permeability-porosity relationships for different pore types constrained by the pore structure indicators, such as

γ_μ and m, shows much better correlation with the core permeability than the previous results from linear transform (Figure 2.13). The results can be further applied to reservoir modeling and simulation to improve the hydrocarbon recovery.

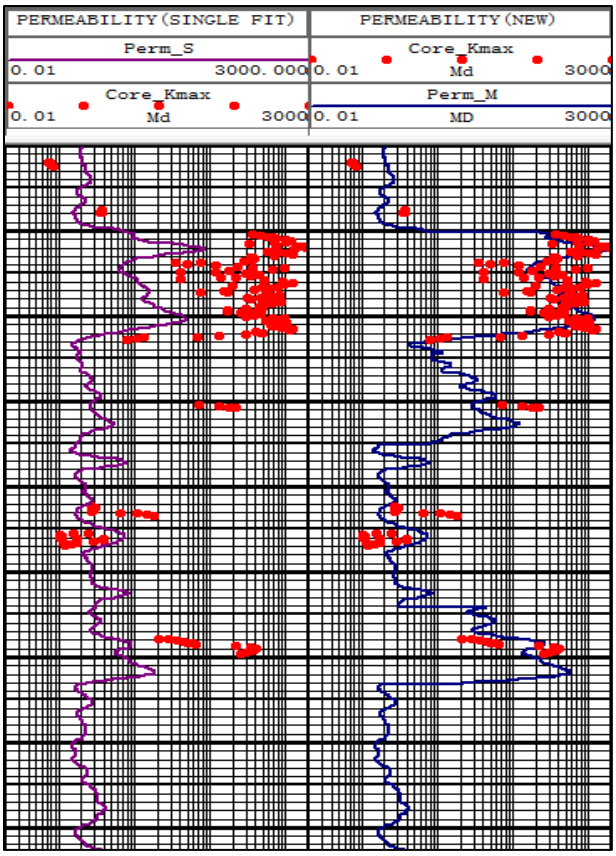

Figure 2. 13 Comparison of permeability curves computed from the linear regression (left) and the new multi-regressions of porosity (right). Core measured permeability is shown by the red dots. The multi-regressions are applied to different pore types distinguished by pore structure indicators. The permeability from multi-regression, demonstrated by the black line on the right track, has a much better correlation with core measurements than the correlation on the left track.

Shear velocity estimation

To apply seismic data for pore type evaluation, a rock physics method of pore type prediction is essential. However, this requires the input of shear-wave data. As shown in Figure 2.8, shear wave velocity and compressional wave velocity act differently as the pore type changes. The V_p/V_s ratio shows correlation with different pore types. As a result, upon applying the pore structure indicators, shear wave velocity can be predicted. Figure 2.14 shows two unique V_p/V_s relationships for the two different pore types. The predicted shear wave velocity agrees with measured velocity.

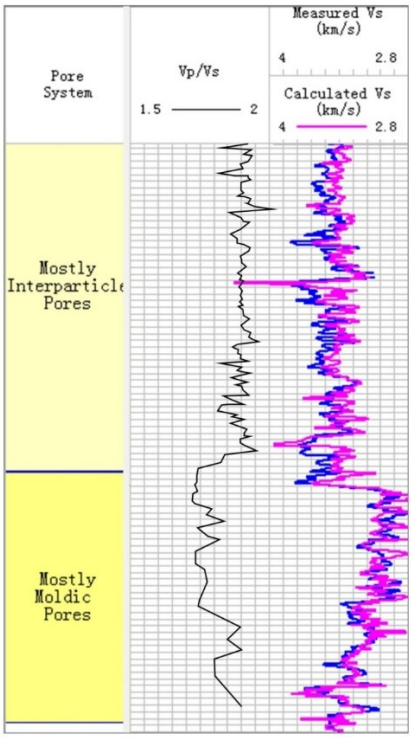

Figure 2. 14 Comparison of measured shear velocity and calculated shear velocity for two reservoir zones with distinct *Vp/Vs* ratios. Synthetic shear velocity is calculated based on the different values for *Vp/Vs* ratio for different pore systems interpreted by *m* or γ_{μ}.

II.5 Conclusions

Conventional core and log measurements can be integrated to evaluate carbonate pore structures and better predict reservoir performance. Based on mercury injection capillary pressure measurements (MICP) and other core data, five zones with distinct pore types and reservoir performances are distinguished and classified for the Early Triassic reservoirs in Puguang Gas Field. The five zones are characterized as moldic pore dominant (Zone 1), sucrosic macro-intercrystalline (Zone 2), mixed moldic and intercrystalline (moldic dominated) (Zone 3), meso-intercrystalline (Zone 4), and micro-intercrystalline (Zone 5), from bottom to top. All zones show distinct features for pore throat sizes (e.g. Rc_{10} and Rc_{50}), pore throat tortuosity, displacement pressure P_d, capillary pressures (e.g. P_{10} and P_{50}), irreducible water saturation S_{min} and Leverett J-function. Integrated analysis of resistivity, velocity, neutron-density logs improves estimation of pore types and can be applied when core data are not available. We investigated using the following parameters: the differences between shallow and deep resistivity, and between neutron and density porosity; cementation factor (m) from Archie's law; frame flexibility factor (γ_μ) from Sun's rock physics model; S factor from Castagna's modified Wyllie's equation. All of the parameters are useful to separate moldic-pores-dominated zones from intercrystalline-pore-dominated zones. The m and γ_μ factors are the most effective to separate all four reservoir zones with distinct pore types. When $m > 2.4$, $\gamma_\mu < 4$, the zone is dominated by moldic pores; when $1.6 < m < 2.4$, $4 < \gamma_\mu < 8$, meso- to macro- intercrystalline pores are most abundant; when $m < 1.6$ and

$\gamma_\mu > 8$, intercrystalline pores dominate. Based on pore type evaluation from cores and well logs, better estimations of permeability for reservoir production can be achieved.

CHAPTER III

INTEGRATED STUDY OF THE INFLUENCE OF SEA LEVEL CHANGE ON DOLOMITIZATION AND PORE STRUCTURE EVOLUTION

III.1 Synopsis

Sea level fluctuations can significantly affect carbonate deposition and diagenesis. Giant gas reservoirs are present after these processes, in the early Triassic dolomites in Puguang Field, Sichuan, China. The goal of this study is to understand the sea level control on rock textures and reservoir performances in the studied dolomite formation. A pore structure indicator (PSI) from a rock physics model was used to quantify the episodic variations of pore structure observable from cores, in the form of crystalline, peloidal, moldic oolitic dolomite to dolomicrite in the upward shallowing sequences. The results from petrography and PSI analysis illustrate that, PSI < 4 is associated with moldic oolitic dolomite dominated by moldic porosity, which may indicate subaerial exposure and unconformities. The increasing of PSI (PSI > 4), correlates with the development of intercrystalline porosity following sea level regression. Within the ooid shoal facies, PSI curves also show two prominent changes, which correlate with the two uplifting events. However, PSI curves show a steady regression pattern outside of the shoal complex. The results from the integrated study of PSI, δ^{18}O and δ^{13}C isotopes, and cathodoluminescence images suggest that triggered by the microbial dolomitization, the continued development of peloidal dolomite and crystalline dolomite from moldic oolitic dolomite might be resulted from reflux dolomitization. The evolution of dolomite textures improved pore connectivity and

permeability. The results suggest that PSI is potential to assist better understanding of geological controls on reservoir development.

III.2 Introduction

Sichuan Basin gas cumulative production and proven gas reserves were approximately 0.64 and 70.63 TCF (Trillion cubic feet), respectively, in 2009. Proven gas reserves in Puguang Gas Field, discovered in 2003, are 12.36 TCF (Hao et al., 2009). The Permian and Triassic dolomite reservoirs contribute to 37% of the total production. Buried 5,000 m below the surface, the reservoir porosity ranges between 1-29%, and permeability ranges between 0.01-9,664 md (Ma et al., 2007). The high-quality dolomite reservoirs formed under a series of favorable geological conditions, including their location within an aragonite sea with dry heat/arid climate (Zhang et al., 2014). The aragonite and high-magnesium calcite deposited in the aragonite sea were easily dissolved to generate porosity and provide sources of Mg^{2+} with exposure to meteoric freshwater. The dry climate during Triassic helped preserve the primary and secondary porosity because of the scarcity of diagenetic fluids and cement (Sibley, 1980). Dolomitization was favored after the flow of Mg^{2+} fluid in these porous rocks after the initialization of dolomitization by microbial sulfate reduction in the tidal flats or restricted lagoon. The Early Triassic oolitic shoals in Puguang Gas Field were massively dolomitized from the microbial-mediated protodolomite under the circulation of Mg^{2+} rich fluid in the porous shoals driven by the sea level regression. Dolomitization helped preserve porosity and permeability after burial, owing to its reduced potential for

pressure dissolution (e.g. Amthor et al., 1994). Excellent reservoir quality occurs in these dolomites (Ma et al., 2005, 2007; Wang et al., 2009). Other factors contributed to the great reservoir quality besides diagenesis including early gas charge, deep and rapid burial, overpressure, highly matured organic matter, and long-term interaction between hydrocarbon-water-rock (Ma et al., 2008a). These factors are important not only for the preservation of porosity and hydrocarbon but also for the advanced dolomitization. Many studies have shown that organic sediments as a result of sulfate reduction and methanogenesis may solve the kinetic problems for early dolomitization by changing the chemistry of pore water, such as limiting the hydration of Mg and Ca ions, increase alkalinity and PH, and etc. (e.g., Vasconcelos and McKenzie, 1997; Mazzullo, 2000; Gingras et al., 2004).

Although dolomitization is favored in the studied carbonate formation, its mechanisms behind are widely debated (Wei et al., 2005; Zhao et al., 2005; Chen et al., 2008; Ma et al., 2008b; Wang et al., 2009; Huang et al., 2009; Pan et al., 2010, 2012; Hang et al., 2011; Jiang et al., 2013; Chen et al., 2014; Jiang et al., 2014; Yu et al., 2015). Most previous studies rely on standard geochemical and petrographic methods. However, there are often many uncertainties from such analyses, especially for massively recrystallized dolomite (Machel, 2004). Instead, the textural relationships have shown particular importance in deducing the dolomitization processes (Moss and Tucker, 1996; Machel, 2004). For instance, oolitic shoals are susceptible to have matrix selective dolomitization from lower temperature dolomitizing fluid with a good preservation of moldic porosity, whereas complete replacement of the rock by dolomite

is expected with higher temperature dolomitizing fluid (Machel, 2004). For reflux dolomitization, the dolomite crystals changed from tight and small crystals to large crystals in loose contact following the flow of Mg^{2+} from the surface (Machel, 2004). In the studied Feixianguan dolomite reservoir, these different textures are observed, which indicate that different dolomitization processes may occur. During these processes, sea level fluctuation may affect dolomitization, by two ways: first, by influencing the deposition of carbonate facies and the primary rock fabrics that affect the later dolomitization patterns; secondly, by influencing the circulation of Mg^{2+} sea water (Beales, 1953; Morrow, 1978; Sun, 1994; Ehrenberg, 2004; Lasemi, 2010). Therefore, a better understanding of pore structure variations may indicate sea level changes and infer dolomitization processes.

However, pore structure prediction without core data is difficult. Studies have shown that under similar mineral composition, fluid content, temperature, pressure, and porosity, pore structure variation can greatly change petrophysical properties and result in different sonic, density and neutron log responses (e.g. Brie et al., 1985; Weger et al., 2009). Thus, wireline logs can be used to diagnose pore structures types. Variable rock physics methods have been applied to predict pore structure (Brie et al., 1985; Xu and White, 1995; Salem and Chilingarian, 1999; Sun, 2000; Salen and Castagna, 2004; Dou et al., 2011; Verwer et al., 2011; Adesokan and Sun, 2014; Sun et al., 2015). Simple, large vuggy, moldic pores, have higher cementation factor than intricate, small micropores from their distinctive resistivity responses (Verwer et al., 2011). Based on the Kuster and Toksoz model, effective medium and Gassmann theories, a velocity

model was built, considering a mixture of grains with different aspect-ratio (Xu and White, 1995). Moreover, a rock physical parameter, γ, independent from porosity was introduced to describe pore structure effect on elastic wave velocity (Sun, 2000, 2004).

The relation between pore structure variation and sea level changes is not well understood. In this study, the shear frame flexibility factor from Sun's (2000) model was used as a pore structure indicator (PSI) to estimate carbonate pore structures and their stratigraphic relations in the subsurface. The results were used to clarify sea level variations, understand dolomitization and reservoir performance in the Early Triassic Feixianguan dolomite reservoirs, Puguang Gas Field, China. Although the microbial dolomitization is believed to the basis for the advanced dolomitization, we focused on discussing the possibilities of the large-scale dolomitization processes controlled by regional fluid flow, such as seepage reflux, mixing zone, burial dolomitization.

III.3 Methods

This study integrates petrographic description with rock physics modeling to understand the spatial variation of pore structure in the studied carbonate formation. The quantitative analysis of pore structure variation will then be correlated with sea level curves. Afterward, the stratigraphic relationships of rock textures associated with the sea level changes were integrated with geochemical data to understand the dolomitization mechanisms.

III.3.1 Rock physics model

A rock physics model based on an extended Biot theory of poroelasticity and introduced frame flexibility factors (γ, γ_μ) to characterize the effect of pore structure on the flexibility of the rock frame under deformation (Sun, 2000, 2004). They are used as proxies for pore structure in carbonate rocks and are independent of porosity (Sun, 2000). The derivation of frame flexibility factors is illustrated in details in the Methods section of Chapter II. We choose frame flexibility factor γ_μ for this part of the study because it proved to be the most efficient parameter to describe the pore structure variation (Chapter II) and can be applied later to the seismic characterization of pore structure. In this Chapter, the shear flexibility factor will be referred to as pore structure indicator (PSI) for simplification.

III.3.2 Dolomitization evaluation

Many studies have suggested that the geometry of a dolomite body and its lithological/petrographic associations can be used to deduce the origin of dolomite (e.g. Hardie 1987; Warren, 1989). Penecontemporaneous dolomicrite after evaporative pumping is often associated with fine-grained crystal size (<10 to 20 μm) and stratiform presence on the platform. Reflux dolomite often is associated with overlying evaporites and dissolution breccias. Reflux dolomite located proximal to the refluxing brine sources are more fine-grained, mimetic, and have a higher proportion of dolomite crystals, while those located distally are more replacive, coarsely crystallized, have a decreased proportion of the dolomite crystals (Warren, 2000). Mixing zone dolomite occurs near

the edges of the former lenses of meteoric water and often are located below regional unconformities at intrabasin paleo-highs or shoreline/strandline trends. Evaporitic reflux and mixing zone dolomite are coarser than penecontemporaneous dolomites as they are away from Mg^{2+} rich brine source (Machel, 2004). However, they are finer than dolomite after deep burial modification. Therefore, dolomite from different origins may have variable textures, distributions, and stratigraphic relations.

In this study, we apply the frame flexibility factors as pore structure indicators (PSI) to understand the distributions of different dolomite rocks and their stratigraphic relations. The results will be then integrated with $\delta^{18}O$ and $\delta^{13}C$ isotopes and cathodoluminescence analysis from three wells to evaluate the previous conclusions on dolomitization mechanisms (Ma et al., 2008b; Pan et al., 2010; Jiang et al., 2013, 2014).

III.4 Results

III.4.1 Petrographic analysis

We identified four significantly different types of dolomite (Figure 3.1) occurring periodically in upward shallowing sequences in the Feixianguan Formation at the platform margin, which is consistent with the petrographic observations from previous studies (e.g. Huang et al., 2009; Pan et al., 2010). They are crystalline, peloidal, dolomudstone, moldic oolitic dolomite, respectively. Based on the vertical distribution of different dolomite textures (Warren, 2000), the initial hypothesis for dolomitization is that: upper moldic oolitic dolomite was generated by early dolomitization, along with fabric selective dissolution; middle peloidal dolomite were developed from microbial

mediated dolomudstone by early reflux dolomitization; crystalline dolomite were developed afterward by advanced reflux dolomitization or burial dolomitization. Crystalline dolomite was then transformed to a relatively coarser, sucrosic dolomite, due to relatively low Mg/Ca ratio from the refluxed fluid and limited volumes of burial-derived dolomitizing fluids (Warren, 2000). However, due to the intensive evaporation and limited influence from meteoric water (Wang et al., 2005; Ma et al., 2008), the hypothesis for dolomitization within the restricted platform is slightly different that reflux dolomitization possibly dominated below the microbial-mediated dolomudstone.

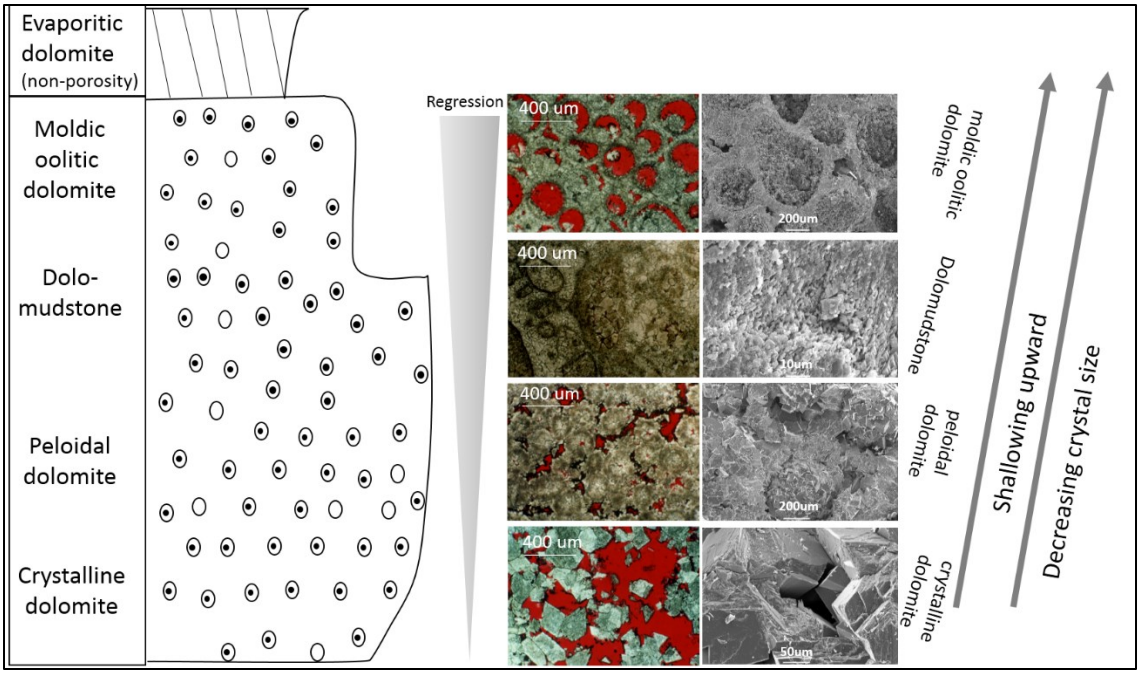

Figure 3. 1 Pore evolution following one shallowing-upward cycle in the Feixianguan Formation. Thin sections and SEM photomicrographs are shown for each type of dolomite to illustrate the pore geometry. Following the burial, pores transformed from moldic, micro-intercrystalline, meso-intercrystalline to macro- intercrystalline.

III.4.2 Rock physical characterization

To test the hypotheses of dolomitization processes proposed during the initial petrographic investigation, we studied the spatial variation of dolomite texture, and its stratigraphic relation and correlation with sea level change, using the pore structure indicator (PSI) from a rock physics model. The hypotheses can be acceptable if the geographical distribution of different dolomite agrees with the regional understanding of carbonate deposition and flow of diagenetic fluids (e.g. Feng et al., 2008; Chen et al., 2008; Wang et al., 2008; Wang et al., 2009; Chen et al., 2014, 2015).

Pore structure variation within the massive dolomite

Pore structure variation in carbonate rocks often leads to significantly different permeability and porosity relations. Therefore, a valid pore structure indicator should be able to explain these different relations. In this study, frame flexibility factor, γ_μ, from a rock physics model is used as an indicator (PSI) to quantitatively estimate pore structure and effectively classify the different permeability-porosity trends associated with diversified pore structures. Figure 3.2 shows the cross plot of core permeability and core porosity for the studied dolomite formation. When PSI < 4, oolitic dolomite dominated, as shown by the thin section of sample C. It has a higher porosity (0.16-0.3) but relatively lower permeability (0.02-8 md). When 8 < PSI < 20, the crystalline dolomite is prevalent, as shown by the thin section of sample A. It has a medium porosity (0.01-0.16) but higher permeability (0.08-900 md); the value of PSI increases as the size of dolomite crystal and the permeability of the rock decreases. When 4 < PSI < 8, it is mostly peloidal dolomite, as shown by B2, with a medium ranged permeability. On this

cross plot, two upward shallowing sequences were indicated by the varying PSI, which could be related to different diagenetic paths at the shelf margin and within the restricted platform. Consistent with the petrographic observations, the deposition sequence shown by arrows from marked points a to c and c to b is expected to occur at the marginal carbonate shoal (Figure 3.1). In contrast, the deposition sequence from a to b might occur within the internally restricted platform. The crystal size of dolomite and porosity decreases upward as it gets closer to the source of diagenetic fluid and has experienced a longer period of dolomite cementation (Michael, 2004, pg.17).

It is noted that even though the studied Feixianguan Formation has been mostly dolomitized, the rock texture (e.g. pore structure) can be significantly different. In addition to climate, compaction, and other factors, sea level change may have a strong control on such differences.

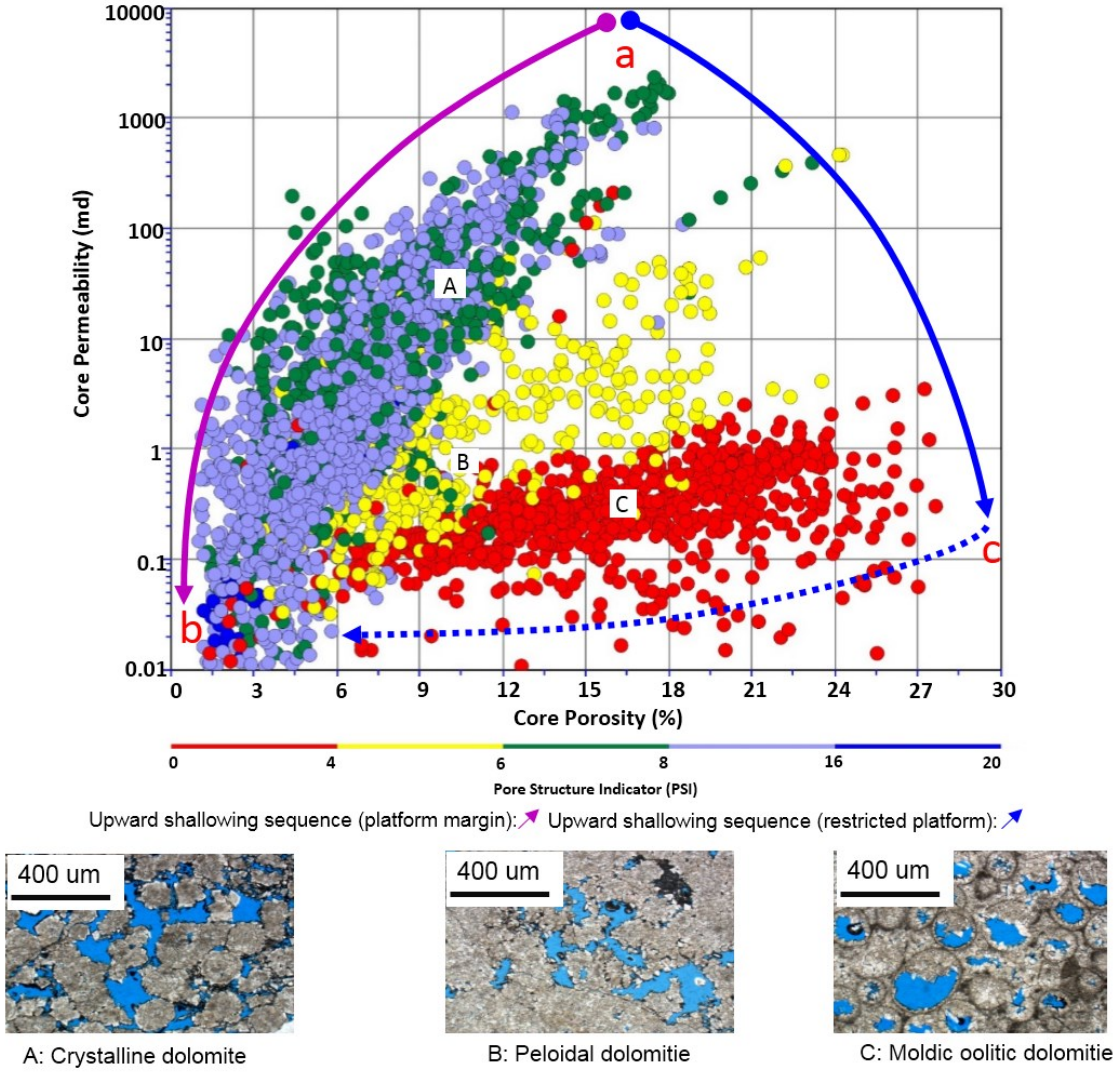

Figure 3. 2 Cross-plot of core permeability vs. porosity colored by pore structure indicator (PSI) based on data from four cored wells (Well A, B, C, and D). Thin sections of samples from the observed three permeability trends are shown. Sample A is from the highest permeability trend, dominated by intercrystalline pores as shown in the thin section, while sample C is from the lowest trend dominated by moldic pores as shown in the corresponding thin section. Sample B in the middle is from a mixture of intragranular and intercrystalline pores.

Sea level control on dolomite texture

Sea level change may significantly affect the depositional facies, diagenesis, and the corresponding pore structures (Ginsburg, 2001; Coe, 2003). In the studied field, ooids are often deposited at the shelf margin, near the mean sea level, with agitated wave energy. In the studied Feixianguan Formation, ooid grains are prograding basinward following sea level regression. Moldic pores are developed in oolitic grains after sea level regression by selectively dissolution during subaerial exposure. In the early Triassic strata, episodic developments of moldic pores correlate with the occurrences of local unconformities. The unconformities were generated by relative sea level falls after Indosinian uplifting movements (Yu et al., 2015). Other than moldic pores, intercrystalline pores after dolomitization were intensely developed within the carbonate platform during regression. Dolomite crystals evolved from mimetic and fine-grained to euhedral and sucrosic following the sea level driven flow of Mg^{2+}-rich fluid.

In this paper, pore structure indicator (PSI) calculated from well logs was adopted to quantitatively correlate the variation of pore structure with sea level change. The results from petrography and rock physics analysis demonstrated that moldic porosity dominates when PSI is less than 4, whereas intercrystalline porosity is prevalent when PSI is higher than 4. PSI also increases as the size of the intercrystalline pores and dolomite crystals decreases. Figure 3.3 displays the pore structure indicator (PSI), gamma ray (GR), core porosity and permeability, third order sea level fluctuation curve, and pore type interpretation from petrography. Consistently with the previous analysis, moldic pores with relatively high porosity and low permeability occurred where PSI is

low, less than 4. Moldic porosity within the oolitic grainstone occur after subaerial dissolution and is widely distributed below the unconformities. Hence, the two strong inflections of PSI curve above the moldic pores (PSI <4), correlate with the occurrences of two regional unconformities. Above the moldic zones, the transition from lower to higher PSI and the sea level regression are in agreement. The reason is that following the sea level drop and intensive dolomitization, dolomite crystals grows with larger intercrystalline porosity. We also observe that PSI shows a better correlation with the sea level curve than GR, which only shows a general trend of regression. GR log is widely applied in siliciclastic rocks for the interpretation of sedimentary facies and depositional cycles. It is more sensitive to the volumetric of shale, which does not change much in the studied massive dolomite. Instead, PSI log may be more applicable in carbonate rocks. The simple Fast Fourier Transform (FFT) analyses were performed for the PSI curve and 3rd-order sea level curve. The result show very similar amplitude versus frequency response and cyclicity in the lower frequency range.

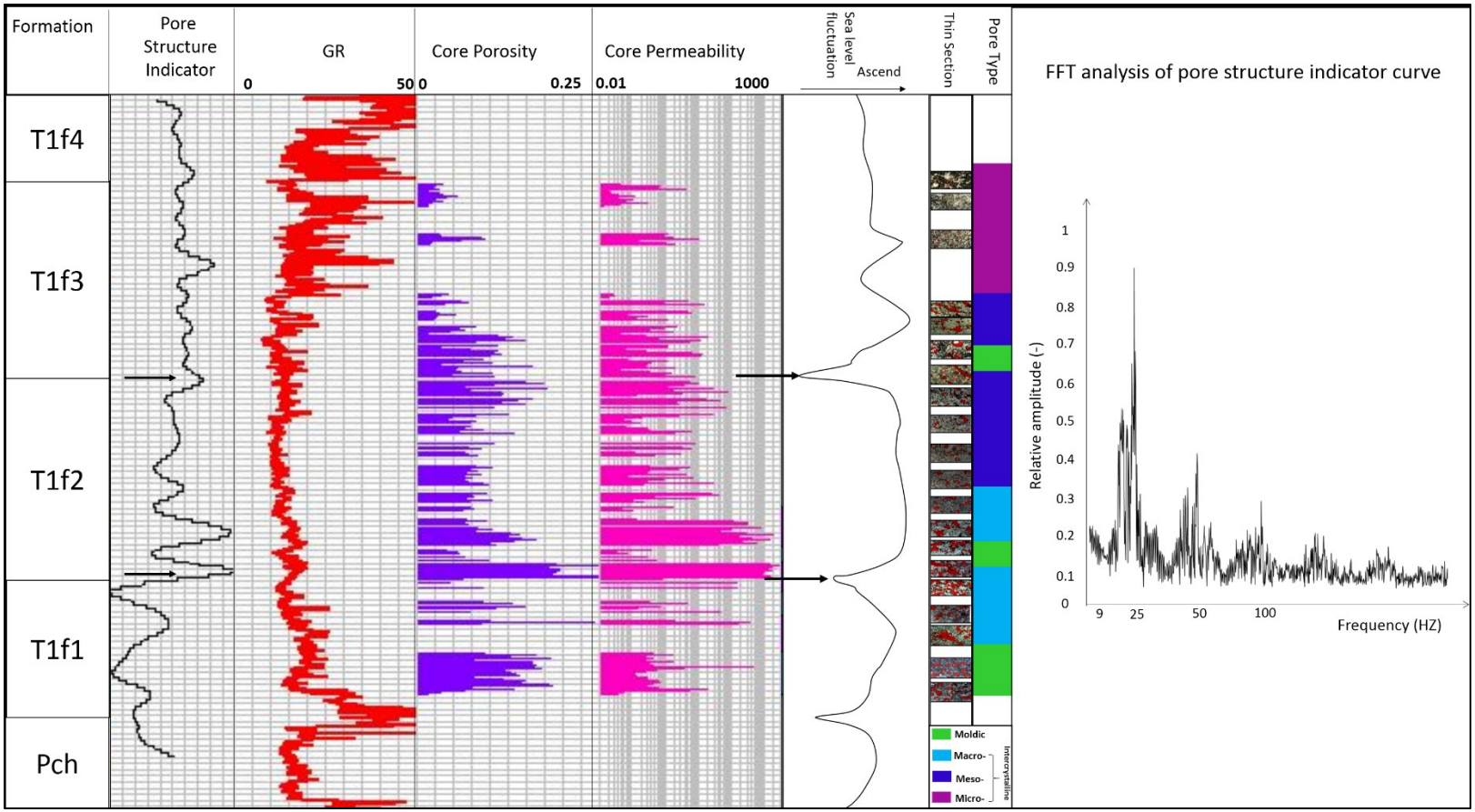

Figure 3. 3 Comparison of pore structure indicator (PSI) and GR log with sea level curve for Well B. Pore type interpretation from the core is shown as well. The formation is subdivided into four members. Arrows indicate the two unconformities. FFT is applied for comparison of PSI curve.

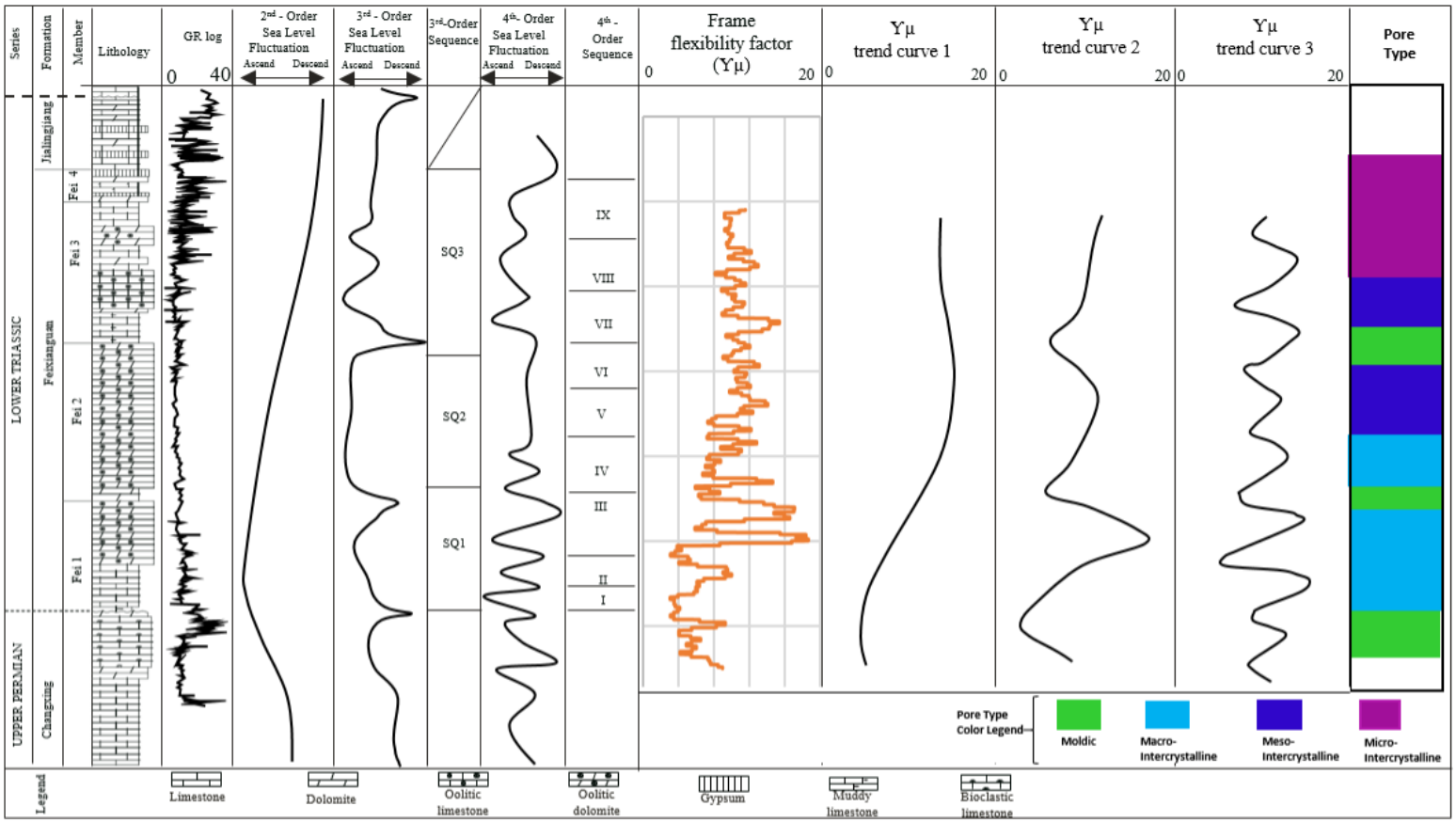

Figure 3. 4 Log correlation for Well B with the tracks showing different ordered sea level curves and there trend curves analyzed from frame flexibility factor curve, and pore structure interpretation from core analysis. The γ_μ curve shows good correlation with core analysis on pore type prediction. The three γ_μ trend curves correlate with the three sea level curves of different orders.

The results from FFT analysis illustrate that the different-frequency-cyclicity of sea level fluctuation can be related to the pore structure evolution in the studied carbonate formation. Hence, we analyzed the trends for the pore structure indicator curve based on frequency. Figure 3.4 shows the low frequency, medium frequency, and high-frequency trend curves extracted from the original γ_μ curve. When compared to the three sea level cycles with different frequencies, the three processed trend curves show correlation with the 2nd-order, 3rd-order, and 4th-order sea level curves respectively. GR log is also plotted here for comparison. It only gives a general regression trend, which could correlate with the long-term 2nd-order sea level change. Therefore, the pore structure variation is more informative of higher frequency sea level fluctuations controlled by other geological factors other than eustasy. For example, the three sequences illustrated by the middle γ_μ trend curve correlate with the three tectonic events. The interpretation is that moldic porosity with much lower value for γ_μ is generated only after the exposure that followed the uplifting. Above the moldic porous zones, the transition from macro-intercrystalline to meso-intercrystalline porosity with decreasing crystal size, indicated by the increasing γ_μ value, follows the sea level regression.

Considering the significant influence of 3rd-order sea level cycle on the development of reservoirs, we further applied the correlation analysis of pore structure with 3rd-order sea level curves to other available wells (Figure 3.5). Overall, all of the wells display a long term regression pattern, following regional 2nd-order sea level

change. However, the internal shape and cyclicity of the curves differ between wells inside and outside of the ooid shoal facies belt. Within the shoals, on PSI curves, two strong inflection points above the zones with very low PSI values, correlate well with the occurrence of two regional unconformities. Three 3rd-order sequences are easily identified on these curves. The reason is that at these locations, shoals have experienced intensive exposure and pervasive development of moldic pores. Outside of the shoal complex, PSI curves show a steady regression pattern with much smaller scale fluctuations, because intercrystalline pores were widely developed with no obvious development of moldic pores. The size of the intercrystalline pores decreases in the upward sequence. The petrography results further confirmed that two diagenetic evolution sequences exist in the studied carbonate platform, with one of the sequences illustrated in Figure 3.1.

III.4.3 Spatial distribution of dolomite

The results from petrography and rock physics analysis indicate that PSI log can be useful to distinguish different dolomite types by revealing pore structure. PSI model, thus, is predictive of the spatial distribution of different dolomite bodies by illustrating the distribution of their characteristic pore structures. Figure 3.6 shows one cross section along four cored wells, displaying only the cored intervals. The subdivision of the formation follows the 4th-order sea level fluctuations. The displayed curves are core porosity, core permeability, and PSI respectively. Moldic pores are characterized as having relatively high porosity yet low permeability and PSI. Integrated with thin section

analysis, four moldic oolitic dolomite beds, prograding from the interior of the carbonate platform (East) towards the basin (West) are interpreted.

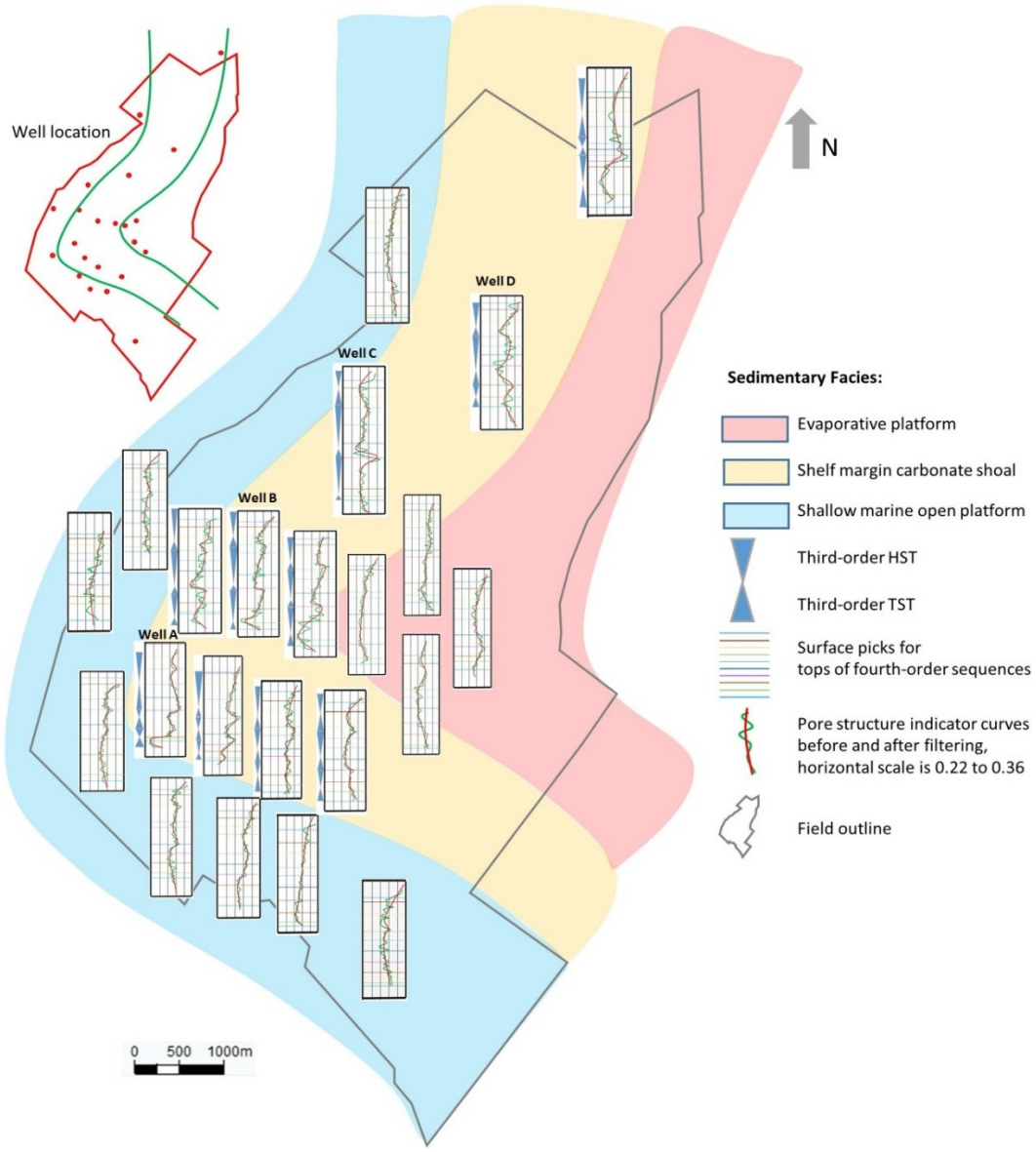

Figure 3. 5 Field map overlaid by pore structure curves from wells available. Different pore structure evolutions are observed when comparing those within ooid shoals with those outside.

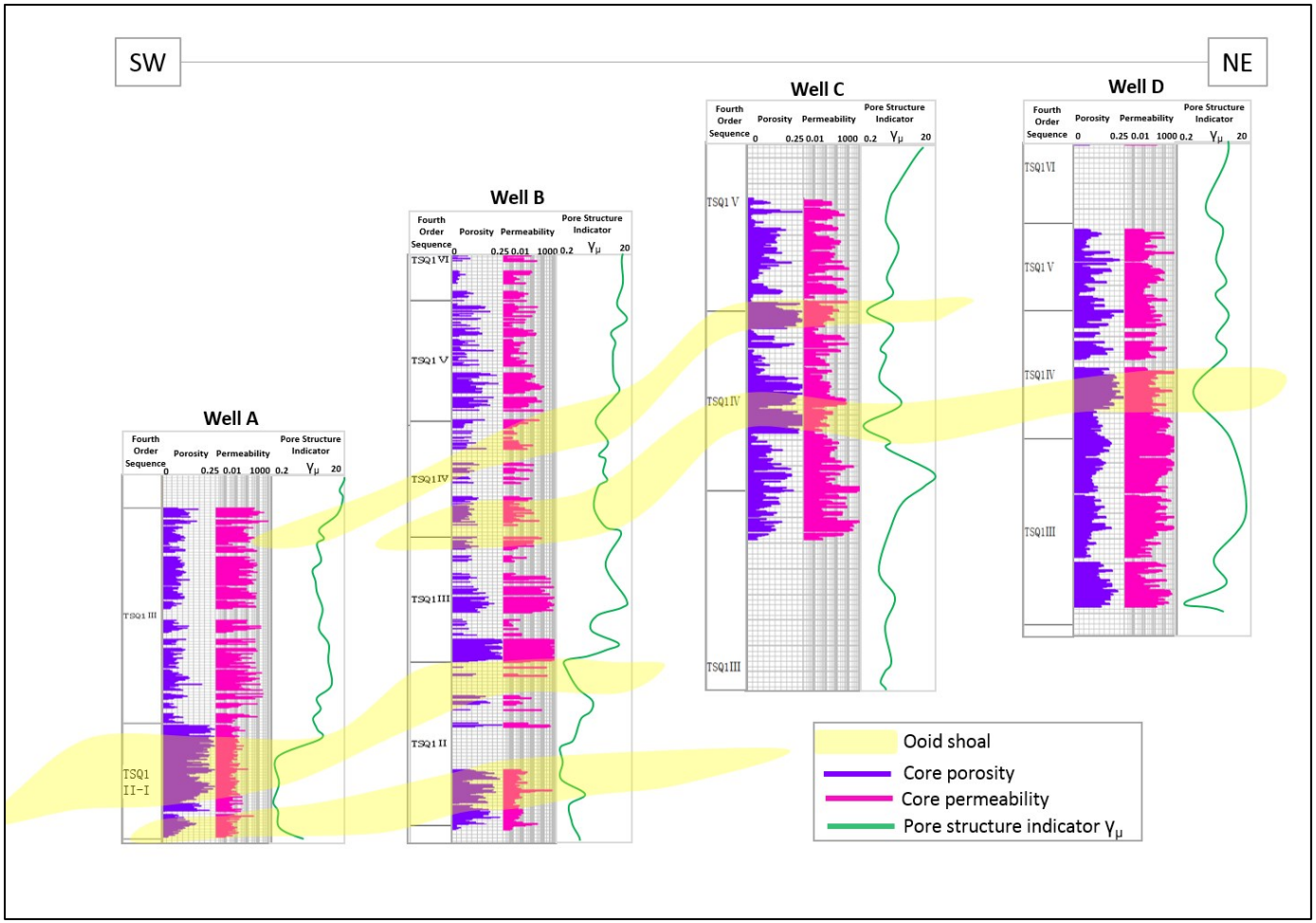

Figure 3. 6 Equal spaced well cross-section of four cored wells, showing porosity-permeability variation, ooid shoal distribution, refer to the map in Figure 1.1 for well locations. Moldic pores have high porosity, low permeability, and low PSI.

Figure 3.7 shows the same well cross section of a model built from PSI logs. Oolitic dolomite with developed moldic porosity (low PSI), shown in warm yellow color, is found at the shelf margin. The distribution of the dolomite bodies is clearly imaged on the cross section. The oolitic dolomite at the edge is laterally distributed with a lenticular shape whereas the crystalline dolomite in the restricted platform is vertically distributed. The distributions of different dolomite bodies show similar patterns to reflux dolomite at the shelf margin and within restricted platform respectively (Machel, 2004; Badiozamani, 1973).

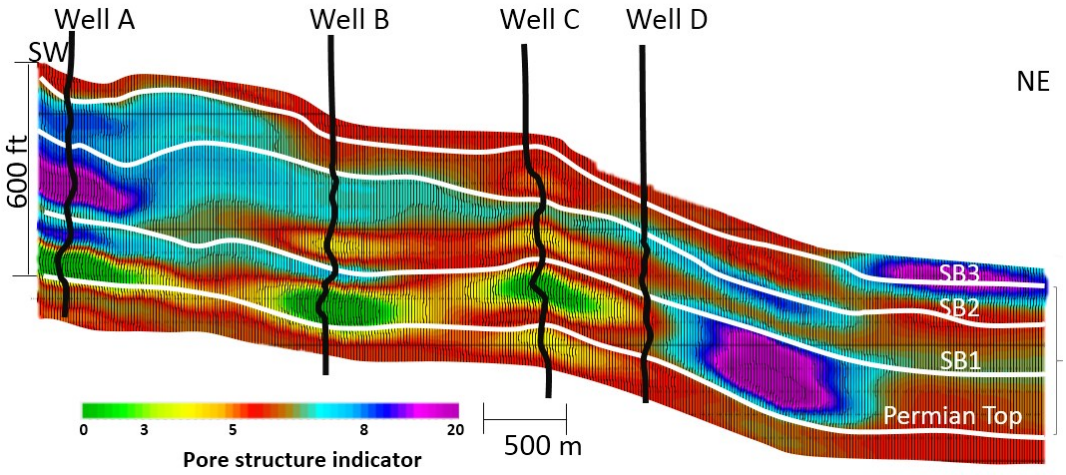

Figure 3. 7 Pore structure model built from pore structure indicator (PSI) curves, refer to the map in Figure 1.1 for the location of the cross-section. Different colors indicate different pore types. Four surfaces are shown in the PSI model. They are the sequence boundaries (SB) above Permian reef, Fei1, and Fei2 reservoirs, and Fei3 non-reservoir respectively.

III.5 Discussion

III.5.1 Dolomitization mechanisms

The studied gas reservoir was intensely dolomitized with improved pore connectivity, and enhanced reservoir quality. However, the dolomitization mechanisms are still under discussion. Previous studies show that meteoric mixing-zone dolomitization, burial dolomitization, and seepage-reflux dolomitization (Zengler et al., 1980) are the three most popular mechanisms for the reservoirs while penenecontemponeous dolomitization is supported for overlying dolomudstone (e.g. Ma et al., 2008b; Pan et al., 2010, 2012; Jiang et al., 2013). Ma et al. (2008b) suggested mixing-zone dolomitization and burial dolomitization, based on the observations of fabric selective dissolution of ooid grains as well as well-ordered crystal form and saddle dolomite. Jiang et al. (2013) and Chen et al. (2014, 2015) suggested reflux dolomitization because the measured δ^{18} O and δ^{13} C, Sr/Ca, and $^{87}Sr/^{86}Sr$ values agree with the ones from Triassic seawater. Pan et al. (2010) suggested Fexianguan dolomite reservoirs were mostly early formed and modified after burial. Dolomite are early formed as they are fabric-selective, rich in Ca-, Na-rich, and poor in Sr; dolomite was modified during deep burial, indicated by replacement of dolomite along stylolite, occurrence of saddle dolomite, and the change of dolomite texture with depleted δ^{18} O. Even though the interpretations of dolomitization are quite different in these studies, the data that have been used to support their arguments are in agreement. For instance, many studies observed fabric selective dolomitization, similar $^{87}Sr/^{67}Sr$ and δ^{13} C isotopes values of the dolomitizing fluid and coeval Triassic sea water; evaporate facies,

dolomitization along stylolites after burial, changing crystal sizes with burial. This evidence suggested that all the proposed dolomitization processes may occur in the studied field, however, with a different intensity or at different locations. However, the potential microbial dolomitization has a limited investigation in the Feixianguan Formation. Studies from modern dolomite in offshore Brazil have shown that evaporitic or restricted platform was favorable places for the early microbial dolomitization associated with sulfate reduction (Vasconcelos et al., 1995; Vasconcelos and Mckenzie, 1997). With the wide distribution of tidal flats and evaporates in the studied Feixianguan Formation, the microbial dolomitization is most likely to occur during early deposition. In addition, thermal sulfate reduction and high contents of organic matters occurred in the studied formation (Cai et al., 2004; Hao et al., 2009), are favorable for the burial microbial dolomitization (Mazzullo, 2000).

The studied carbonate platform has been massively dolomitized, which is extremely difficult by only reflux or mixing zone dolomitization (Machel, 2004), without the assistance from microbial bacteria. In this study, we first want to propose that the advanced dolomitization in the studied Feixianguan Formation could be microbial mediated at a very early stage following the deposition. However, with limited geochemical data, we focused on studying the recrystallization of microbial generated dolomite from the perspective of regional fluid flow driven by sea level regression. Based on the pore structure variation observed from petrographic analysis and PSI study and Machel's (2004) review, our hypothesis is that starting from the microbial protodolomite, refluxing dolomitization dominate following the seepage reflux

of Mg^{2+} rich diagenetic fluids. At the platform margin, selective dissolution of ooid grains and replacement of matrix by dolomite also occurred at the top of ooid shoals. In addition, burial dolomitization significantly modified the early formed dolomite and occasionally generate sucrosic dolomite with excellent reservoir quality. Other mechanisms such as transgressive dolomitization as a result of sea water flooding are possible but need more validation (Moss and Tucker, 1996).

To test the hypothesis, we studied the stable isotope and cathodoluminescence image from three wells with two wells at the center and one well at the edge of the shoal complex. Well A and Well B at the center show light and positive δ^{13} C, indicating the dolomite were early formed and dolomitization may be dominated by the reflux of sea water (Figure 3.8.). The positive δ^{13} C value may also indicate that the initial microbial dolomitization that triggered the reflux dolomitization could be of sulfate reduction origin (Mazzullo, 2000). However, arguments on mixing zone dolomitization exist, because the values of δ^{18} O and δ^{13} C (-6 ‰ to -2 ‰ and 1 ‰ to 4 ‰ SMOW respectively) fall into the mixing zone category of diagenetic environments (Choquette and James, 1987). However, with no further geochemical data to valid the theory of mixing zone dolomitization, it will not be our focus of discussion. Overall, the δ^{18} O value is in the negative range, which indicates the dolomitizing fluid may be warm due to the activity of living microbial. Burial dolomitization should not be ignored as the dull color is illustrated on the cathodoluminescence image, which indicates the increase in the ratio of Fe^{2+}/ Mn^{2+} following the burial.

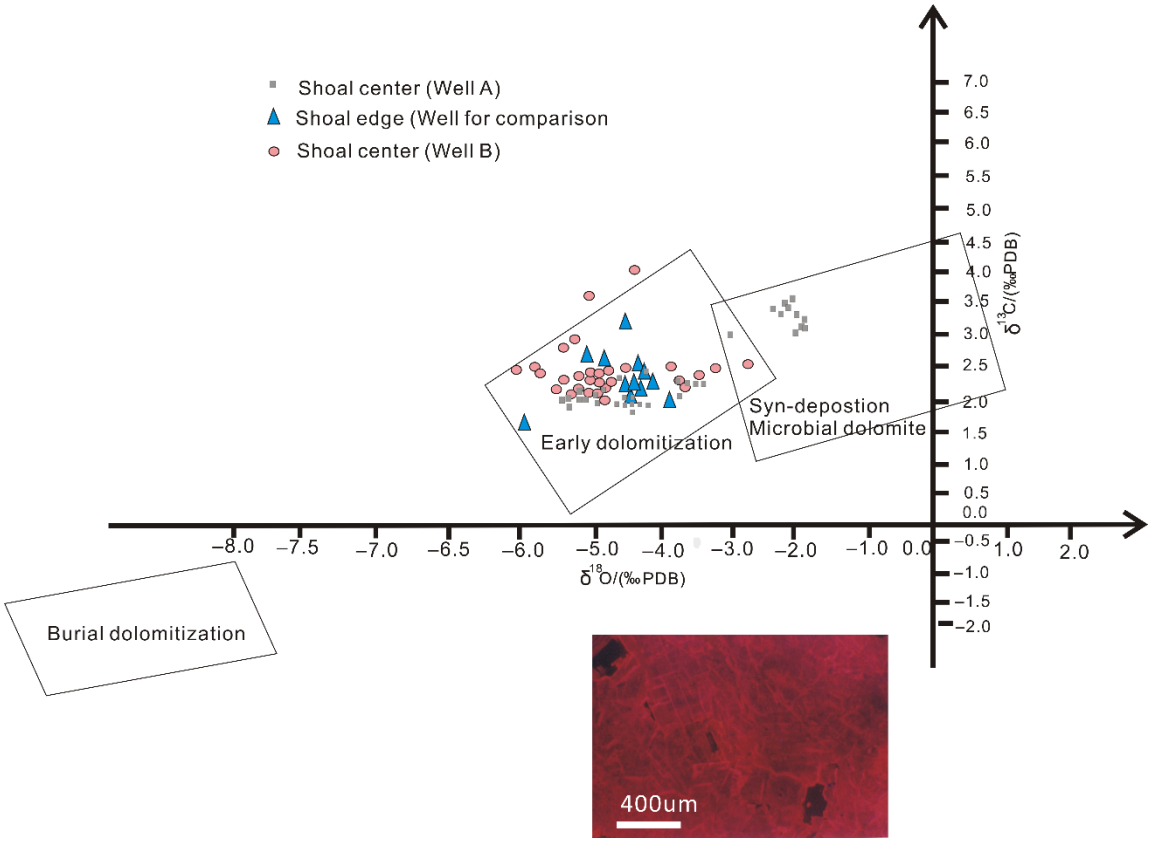

Figure 3. 8 Isotope analysis of samples from three wells with one cathodoluminescence (CL) image selected to show the existence of burial dolomitization. Isotope values indicate the dolomitization was formed at an early stage (part of the data came from Chen et al., 2015).

III.5.2 Sea level control on deposition, dolomitization, and pore structure

In the Early Triassic, the underlying Permian carbonate rimmed platform built up by sponges and reefs was transformed into carbonate ramp after a significant sea level rise (Figure 3.9. a). The isolated carbonate platform has a sedimentary setting that is favorable for the generation and accumulation of oolites. During sea level highstand, increased storminess, due to the prevalence of ramps, led to agitating water conditions

and development of oolites (Mei et al., 2012). It was after later sea level drop that the whole platform was dolomitized (Figure 3.9.b).

Controlled by the sea level change, the diagenetic modification of depositional rock fabrics follow two distinctive paths at the platform margin and within the platform, resulting in significantly different rock textures (Figure 3.9.c.d). At the platform margin, four different pore structures of dolomite formed in the upward shallowing sequence. From base to top, crystalline dolomite was gradually replaced by peloidal dolomite, dolomudstone, and moldic oolitic dolomite with decreasing crystal size (Figure 3.1). In contrast, within the restricted platform, the interior of the shoal complex, dolomudstone transformed to crystalline dolomite directly with no presence of moldic porosity. The size of the crystal also increases with burial. The overlay of the depositional sequence developed in the restricted platform on the sequence at the platform margin could be indicative of significant sea level drop.

The significant pore structure variation (Figure 3.9.c.d) contributes to the dolomitization processes (e.g. Tan et al., 2012). The results from this study show that the center part of the shoal complex at the topographic higher position is susceptible to selective dissolution and matrix selective dolomitization after exposure, while the fringes of the shoal complex are susceptible to reflux dolomitization. At the center, affected by meteoric water, moldic porosity was formed within the ooid grains whereas the matrix was replaced by dolomite cements. The dissolution of aragonite and high-Mg calcite provided the source to form the dolomite cement. At the fringes, following the reflux of

Mg^{2+}-rich sea water, dolomitization transforms the ooid limestone to crystalline dolomite, whereas ooid grains and matrix were homogeneously dolomitized. At the early stage, dolomite was often peloidal shaped with visible depositional fabrics of ooid grains. With burial, advanced reflux dolomitization obliterated the depositional texture and formed massive crystalline dolomite. The crystal sizes increased with burial as they have more spaces to grow from the reduced volumes of Mg^{2+} fluid. Similarly, the internally restricted platform could be dominated by the reflux dolomitization, with no development of moldic porosity related dolomite cement. After the early dolomitization, the studied carbonate platform has been deeply buried. Burial modification of early dolomites (Figure 3.9.d), further enhanced the reservoir quality.

Therefore, pore structure can be indicative of geographic location; its variation may be used to predict sea level fluctuation and understand dolomitization. Rock-physics-based analysis of pore structure as shown in this study demonstrates potential to understand better the dolomitization processes associated with sea level change.

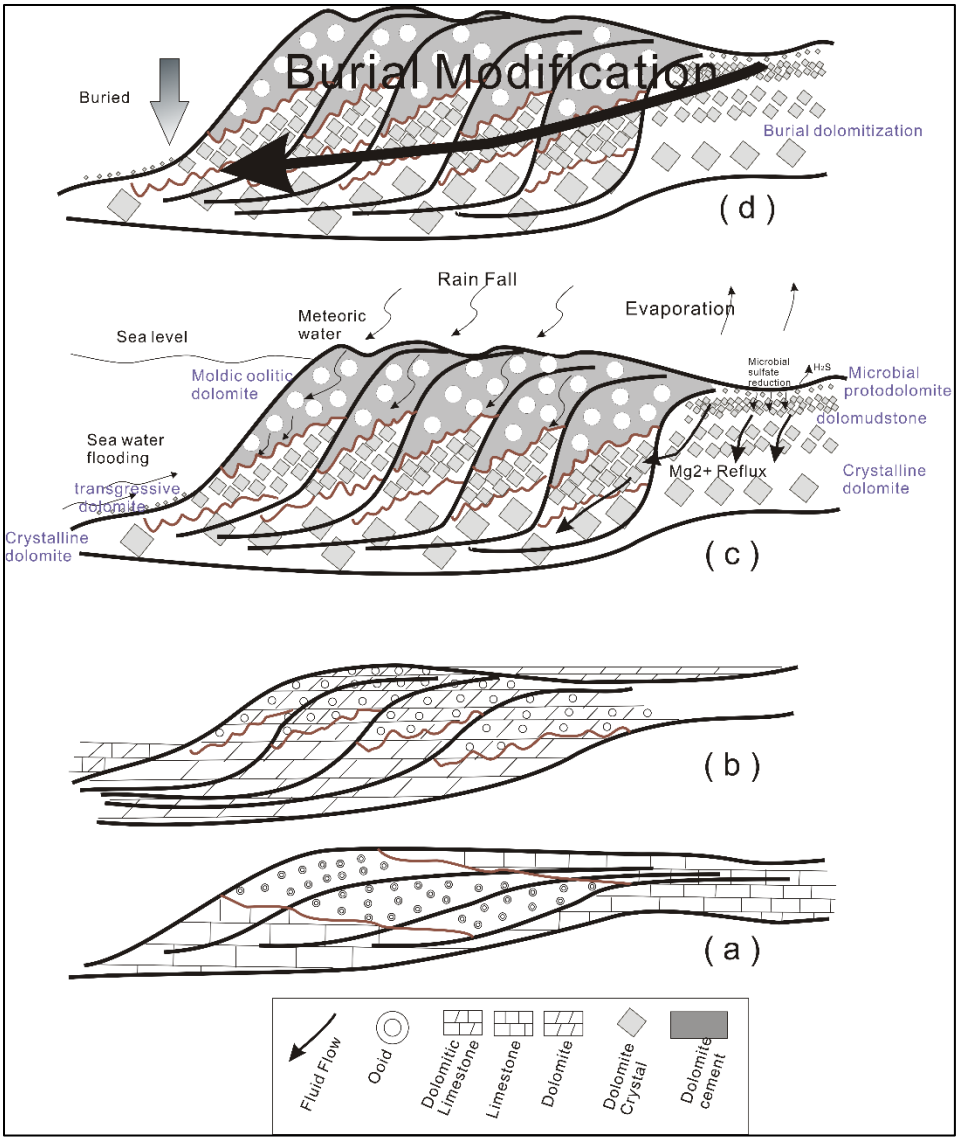

Figure 3. 9 Deposition and dolomitization models for the studied carbonate platform. Ooid shoals are deposited and prograding toward the basin. Different dolomitization mechanisms exist following varied fluid flow directions and topographic change. Moldic pores found below the sequence boundary (SB) are created by selective dissolution after exposure. Mixing-zone dolomite, reflux dolomite, and burial dolomite exist below SB. (a) Ooid shoals are developed following sea level regression in the Early Triassic. (b) Afterward, the platform is dolomitized. (c) Different dolomitization mechanisms transformed the platform following varied fluid flow directions and topographic change. (d) Under burial, burial dolomitization occurs.

III.5.3 Application to reservoir characterization

In the studied Feixianguan Formation reservoirs, reservoir quality differs significantly, resulting in difficulty for production. Tables 1-5 in Appendix C list the comparison of core measured porosity and permeability between different stratigraphic units and sedimentary facies. Ooid shoal facies show the best reservoir quality when compared to the other facies. Within the ooid shoals, high-quality reservoirs were preferentially developed in the 4^{th}-order-sequences II-V, which belongs to the early HST on the 2^{nd}-order sea level cycle, because dissolution and dolomitization occurred after sea level regression. In addition, complex permeability-porosity relations occur due to the strong variation of pore structure after dolomitization. For example, the crystalline dolomite with developed intercrystalline porosity has a higher permeability at a given porosity than oolitic dolomite dominated by moldic and intragranular porosity (Figure 3.2). The investigation of the geological controls on permeability and porosity heterogeneity from this study can be applied to better manage the reservoirs in Puguang field or other similar fields. For instance, the prediction of the spatial distribution of permeability will be discussed in Chapter IV.

III.5.4 Advantages and limitations of the application

In this study, we attempted for the first time to use a rock physics model to correlate the pore structure variation with sea level change and explain the dolomitization mechanisms from the perspective of pore structure evolution. This study shows the potential to apply the results of pore structure prediction to sequence

stratigraphy study in carbonate shoal reservoirs. Compared to GR, pore structure indicator (PSI) may lead to better understanding of sea level fluctuation.

However, it should be noted that the proposed methodology has its limitations in the application. At this stage, this method can only be applicable for qualitative interpretation of sea level variation and is more effective to explain relative sea level changes than absolute changes. Other rock physical or petrophysical methods for pore structure indication may be more applicable in a different field. We also suggest having more data to validate the dolomitization hypotheses proposed in this study.

III.6 Conclusions

Sichuan basin was located at the passive margin of an arid paleo-aragonite sea near the equator, a place favorable for dolomitization during Early Triassic. Accompanied by dissolution, dolomitization greatly improved reservoir quality by improving porosity and pore connectivity. However, the reservoir performance varied within the massive dolomite due to internal pore structure difference. Four different types of dolomite with distinctive rock textures were observed in the upward shallowing sequences and explained by the dolomitization process associated with sea level fluctuations. They are described as crystalline dolomite, peloidal dolomite, dolomudstone, and moldic oolitic dolomite respectively. Crystalline dolomite has fair porosity and good permeability while the moldic oolitic dolomite has good porosity with low permeability. Moldic oolitic dolomite was formed after early selective dissolution and cementation. Peloidal and Crystalline dolomite were developed from the microbially

mediated protodolomite after the reflux of Mg^{2+}-rich fluid. Pore structure indicator (PSI) established from a rock physics model was used to correlate textural difference of dolomite with sea level variation. It is observed that the PSI increases as sea level drops. In the upward shallowing cycle, PSI increases as the pores evolved from macro- and meso-intercrystalline in crystalline dolomite to micro-intercrystalline in dolomudstone. The evolution follows the reflux of dolomitizing fluid due to sea level regression. At the top of the sequence, periodic occurrences of moldic pores with very low PSI correlate well with the unconformities. Sea level fluctuations controlled dolomitization and managed reservoir quality. The pore structure prediction forms a good reference for sea level study.

CHAPTER IV

QUANTIFICATION OF THE GEOLOGICAL CONTROL OF CARBONATE PORE TYPES ON PERMEABILITY BY ROCK PHYSICS GUIDED SEISMIC INVERSION

IV.1 Synopsis

Geological deposition and later diagenetic modification in carbonate rocks can lead to a significant variation of the pore type, resulting in complex permeability and porosity relationships. In this paper, we use a frame flexibility factor (γ_μ) from a rock physics model as an index to quantify the pore structure changes caused by the geological variation of different pore types. The pore structure index is established at well locations where core and log data are available and is then used to classify various permeability trends resulting from different pore types. For the studied reservoirs of the Puguang gas field, Sichuan Basin, China, it is found that when $\gamma_\mu > 4$, the pore type is dominated by intercrystalline pores with large pore throat sizes and high connectivity, which yield a higher permeability trend; when $\gamma_\mu < 4$, the pore type consists of isolated moldic pores, which have a lower permeability trend. The evaluation of spatial pore structure variation is then completed with seismic stratigraphic interpretation and inversion. The inversion results show agreement with sedimentology and stratigraphy in that the carbonate shoal reservoirs started to develop at transgression and were widely distributed during early regression; within the ooid shoals, moldic pores of oolitic dolomite are widely distributed below the unconformities and on the top set of prograding clinoforms as a result of selective dissolution. Below the moldic zones, the development of intercrystalline porosity follows the reflux of dolomitizing fluid. Based

on different permeability-porosity relations constrained by γ_μ, the seismic inversion results are used to understand the spatial variation of permeability.

IV.2 Introduction

Carbonate rocks are much more sensitive to chemical reaction than siliciclastic rocks. The diagenetic alteration of carbonate rocks can create diverse pore types and complex permeability and porosity relationships (Choquette and Pray, 1970; Bathurst, 1972, Lucia 1983). The diagenetic alteration of pore types can also influence the mechanical properties of the rock, which can further affect seismic properties (Grude, 2013). Large scatter of sonic wave velocities are caused by the variation of pore structure in both laboratory acoustic experiments and field log data (Anselmetti and Eberli, 1993). Acoustic and seismic velocity information may thus be used to analyze pore type variation. Many methods were developed over the years to analyze experimental data under laboratory conditions and to attempt to estimate pore structure at well locations (Kuster and Toksoz, 1974; O'Connell and Budiansky, 1974; Toksoz et al., 1976; Tosaya and Nur, 1982; Xu and White, 1995; Adesokan and Sun, 2014). For instance, the Differential Effective Medium (DEM) theory aims to understand the influence of pore aspect ratios on velocity-porosity (Cleary, 1978; Norris, 1985; Xu and White, 1995). As aspect ratio increases, the pore shape changes from linear and flat to round, which may correspond to the evolution from fractures and intercrystalline porosity to the moldic pore type in carbonate rocks. Interpretation of the spatial changes

in pore structure at a larger scale using 2D- or 3D- seismic data needs much improvement.

One of the methods developed recently to use seismic data to evaluate the spatial variation of pore structure is to combine a two-parameter velocity model with core and log analysis and seismic inversion (Sun, 2000; Dou et al., 2011). In this model, frame flexibility factors (γ, γ_μ) are introduced phenomenologically as proxies for pore structure. They are theoretically independent of porosity and are effective in explaining the large velocity difference at a constant porosity (Sun, 2004). The method was successfully applied for pore type evaluation in carbonate rocks in the San Andreas Formation in the Permian Basin, USA (Dou, 2011) and the deeply buried carbonate hills of Baohai Bay Basin, China (Zhang, 2014).

Many models have been developed to estimate permeability from porosity (Nelson, 1994; Lucia, 1995; Lonoy, 2006). Most of the predictive models for permeability fall into three categories: grain size, surface area, and pore dimensions (Nelson, 1994). He also reported that, given similar pore types, permeability might be expected to correlate with porosity. However, even for a single pore type, such as interparticle porosity, permeability could change by four orders of magnitude for a specific porosity (Lucia, 1995). Lucia tried to use grain size to constrain the permeability-porosity trends. Studies of permeability-porosity relations in carbonate rocks agree that in addition to porosity, other parameters including pore type, grain size, and pore structure play important roles in controlling permeability (Nelson, 1994; Lucia,

1995; Lonoy, 2006; Dou, 2011). The bulk frame flexibility factor in the Sun model was used for seismic inversion of spatial variation of pore type and permeability (Gartner et al., 2005 and El-Wazeer et al., 2010). Furthermore, the permeability estimates based on rock physics was used to build a static model for reservoir simulation with the accurate lateral variability of the rock properties while preserving vertical resolution (El-Wazeer et al., 2010).

The Puguang gas field in this study has a significant variation of different pore types resulting in strong heterogeneity in permeability (Ma et al., 2007). We integrate core and log analysis with seismic interpretation and inversion for quantifying the effect of geological variation of pore types on elastic properties and permeability of the field. Model-based post-stack inversion and angle stack inversion guided by rock physics are performed to further evaluate geological controls such as sea level changes on pore type and permeability variation. Different permeability-porosity relations classified by the pore structure index are applied to seismic inversion results to understand the spatial variation of permeability of the studied field.

IV.3 Methods

We applied shear frame flexibility factor $\gamma\mu$ from Sun (2000) model to assist pore structure and permeability estimation. We applied model-based inversion in Hampson-Russell Software to predict Acoustic Impedance (*AI*), Shear Impedance (*SI*), Poisson Impedance (*PI*), and Elastic Impedance (*EI*). *PI* derivation, which is shown

later, is one of the feasibility studies to test the effectiveness of pore type prediction using seismic data.

IV.3.1 Rock physics model

Many rock physics models were developed to estimate the elastic properties of subsurface porous rocks (Mavko et al., 2009). Models originally developed for cracked rocks such as those by O'Connell and Budiansky (1974), Toksoz et al., (1976), Hudson (1980) and others, are valid for the low-porosity crack concentration of only a few percent, assuming that the pore spaces are isolated and non-interacting. Differential Effective Medium (DEM) models were further developed to overcome some of the assumptions such as low porosity and a single aspect ratio to describe complex pore structures in real rocks (e.g., Xu and White, 1995). In this study, we adopt the Sun model for rock physics analysis, which is an extension of the Biot theory of poroelasticity by introducing the frame flexibility factors (γ, γ_μ) to consider the effect of pore structure on mechanical properties, while porosities can vary from 0 to 100% (e.g., Biot, 1962a, 1962b; Sun, 2000; El-Wazeer et al., 2010). The extended Biot model is rather phenomenological, and the frame flexibility factors are effectively functions of the aspect ratio and other parameters. When the porosity is very small and the rock is dry, the moduli-porosity relationships are also linear, as in other crack models noted above, but with a gradient dependent on the pore structure index or γ_μ or the geologic pore type.

The frame flexibility factors (γ, γ_μ) are used as proxies or indices for pore structure in gas-saturated carbonate rocks in this study. The derivation of these factors is

shown in Eqs.2.9-2.13 in Chapter II. Compared with previous work where the frame flexibility factor (γ) from the bulk modulus was used to extract pore structure information from seismic (e.g., Dou et al., 2011, El-Wazeer et al., 2010), this work investigates the potential of using γ_μ from the shear modulus as the pore structure index to differentiate pore types and classify various permeability trends resulting from different pore types. Consistent with Chapter III, the pore structure index (γ_μ) is first established at well locations from the core and log analysis. It is then used in seismic inversion to quantify 3-dimensional pore structure changes associated with the geological variation. Afterward, the pore structure index is applied to assist classifying permeability-porosity relationships.

IV.3.2 Seismic inversion

A method for the simultaneous inversion of porosity and the frame flexibility factor from seismic angle gathers involves an integration of core and log analysis (Dou, 2011). We applied Dou's (2011) method to predict the frame flexibility factor from 3D seismic data and to understand the spatial changes of the pore structure in the studied field. Dou's (2011) method (Eqs.9-10), acquires a prior knowledge of elastic impedance (*EI*) (Connolly, 1999). *EI* is a generalization of the acoustic impedance at non-normal angles of incidence and can be estimated from seismic angle stack inversion, which is given by Connolly (1999) as

$$EI = V_p^{\,a} V_s^{\,b} \rho^c \tag{4.1}$$

where *a, b*, and *c* are coefficients that depend on the incident angle θ: $a=1+\tan^2\theta$, $b=-8\beta\sin^2\theta$, and $c=1-4\beta\sin^2\theta$, where $\beta=(V_s/V_p)^2$. *Vp, Vs,* and ρ are defined in Eqs.1-2.

When the incident angle θ is zero, the *EI* is equal to the *P*-wave acoustic impedance (*AI*) as from Eq. 4.2:

$$AI = V_p \times \rho \tag{4.2}$$

Based on the rock physics model and elastic impedance in Eqs. 1-8, Dou's method for porosity and frame flexibility factor inversion is summarized in Eqs. 4.3-4.4:

$$\frac{EI}{AI^{(2c-a-b)}} = (K + \frac{4}{3}\mu)^{(a+0.5b-c)}\mu^{0.5b} \tag{4.3}$$

$$\frac{\lambda}{AI^2} = \frac{3K-2\mu}{3K+4\mu} \tag{4.4}$$

where *EI* is the elastic impedance; *AI* is acoustic impedance; a, b, and c are the same angle-dependent parameters defined below Eq. 4.1; *K* and μ are the bulk and shear moduli; and λ is a Lame constant that is a function of acoustic impedance (*AI*), shear impedance (*SI*), and density (ρ):

$$SI = V_s \times \rho \tag{4.5}$$

$$\lambda = \frac{AI^2 - SI^2}{\rho} \tag{4.6}$$

By solving the above equation 2.9 to 2.13 and 4.1 to 4.6, the frame flexibility factor (γ) and the porosity (ϕ) can be determined after seismic inversion of *AI*, *SI*, and *EI* (Russell and Toksoz, 1991; Hampson et al., 2005; Dou, 2011). *AI*, *SI*, and *EI* can be

calculated from model-based inversion, simultaneous inversion, and angle stack inversion, respectively, in the Hampson-Russell software package (HRS). K and μ can be calculated from AI, SI, and EI (Eqs. 4.3-4.6). Using Eqs.2.9-2.13 in Chapter II, the spatial variations of γ and ϕ can be estimated. In this study, the ratio of γ and γ_μ is set to be a constant, which is valid when the lithology does not change much and the porosity is not too low, such as 5% (Sun, 2004).

IV.3.3 Poisson impedance (PI)

Before the seismic inversion of frame flexibility factor γ_μ., we did the feasibility study on the predictability of pore structure from seismic data using Poisson Impedance. Poisson Impedance (PI) is defined in Eq. 4.7, where c is the inverse of the slope of the litho-fluid trends. On the AI versus SI cross plot, it is hard to differentiate the litho-fluid distributions by the horizontal or vertical axes. By rotating the axis parallel with the litho-fluid trends would ensure a distinct discrimination of the lithology and fluid (Quakenbush et al., 2006). For this study, lithology and fluid does not change much. PI is applied to distinguish the two distinct pore systems. The value of "c" is determined by the slope of a pore-structure trend, which is determined by frame flexibility factor γ_μ (Figure 4.1).

$$PI = AI - cSI \tag{4.7}$$

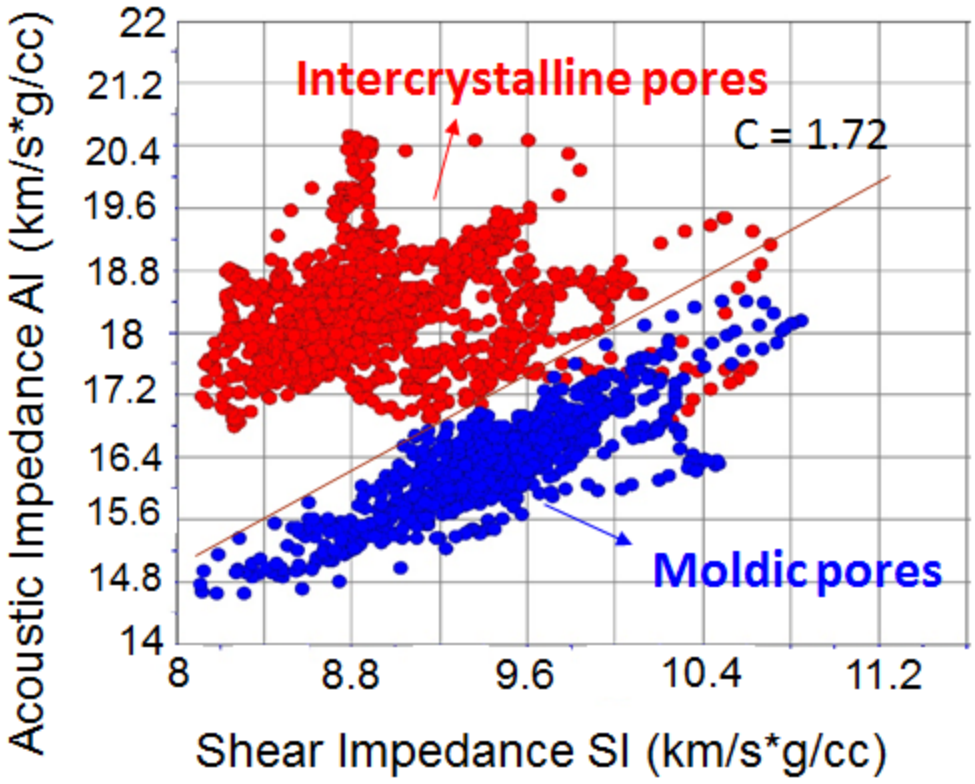

Figure 4. 1 Cross-plot of *AI* versus *SI*, red and blue points are indicative of intercrystalline pores and moldic pores respectively from core observation.

IV.3.4 Permeability-porosity model

Many studies attempted to estimate permeability from rock properties over the decades as briefly reviewed in the Introduction, and most of them tried to incorporate parameters such as grain size, surface area, or pore dimensions, in addition to porosity (e.g., Nelson, 1994). In this study, we focus on evaluating the effect of secondary pore types on permeability using core, well log and seismic data with the assistance of pore structure index. Based on the integrated core and log analysis, we find that various

permeability-porosity relations exist for different pore types, and can be distinguished by the pore structure index γ_μ. Two main permeability-porosity trends are described by the following two equations,

$$\text{When } \gamma_\mu < 4,\ \kappa = A\phi^3 + B\phi^2 + C\phi + D \tag{4.8}$$

$$\text{When } \gamma_\mu > 4,\ \kappa = E\phi^F \tag{4.9}$$

where κ is permeability in md, ϕ is porosity in fraction, and A, B, C, D, E, and F are constants, which are 80, 18, 3, 0.004, 5.5, 1.6, respectively (see sub-subsection *Classification of permeability-porosity trends* in the RESULTS AND DISCUSSIONS section of Chapter IV).

It should be noted that the frame flexibility factor (γ, γ_μ) or aspect ratio in other crack models has no exact mathematical relation to permeability, just as porosity has no exact mathematically-derivable relation to permeability without reducing to simple conceptualized models. However statistically and for reservoir rocks, laboratory experiments over the last half a century demonstrate that approximate relations between permeability and porosity do exist particularly for sandstone reservoirs. Like many previous investigations on the permeability-porosity relations (e.g. Lucia, 1983; Nelson, 1994), this study attempts to use the γ_μ from the shear modulus as a pore structure index to classify the porosity-permeability trends in carbonate rocks, because the shear motion is much more sensitive to pore connectivity variation than the pore volumetric change.

We also mention that for a rock with a given porosity, the pressure dependence of both acoustic velocity and permeability can be an important diagnostic tool for pore shape discrimination (e.g., Nur and Simmons, 1969; Gavrilenko and Gueguen, 1989; Anselmetti and Eberli, 1993; Sun and Goldberg, 1997). Sun and Goldberg (1997) developed an empirical relationship of aspect ratio change with pressure for a given rock type using the extended Biot theory and the experimental data from Nur and Simmons (1969). Anselmetti and Eberli (1993) reported that the gradient of velocity change with pressure for low-velocity samples is higher than the increase of velocities in samples with high velocities, more or less dependent on pore type. However, in this study, no pressure-dependent permeability or sonic velocity data are available. We will thus use permeability measured at constant pressure to investigate the control of pore type and its link to the pore structure index.

IV.4 Results

IV.4.1 Core and log analysis

Using thin sections available, pore type variations and their geological control are thoroughly investigated. Pore structure indices calculated from sonic, density and porosity logs are compared with core-observed pore type variation for quantitative classification of both pore type and permeability-porosity trends. Inversion of pore structure index is then tested on the log-scale for later seismic application, using the acoustic impedance (*AI*) and offset-dependent elastic impedance (*EI*) calculated from log data.

Pore structure analysis

Pore structure variations can strongly affect the acoustic velocities and elastic properties of carbonate rocks, especially when the mineralogy, fluid content, and porosity of the rocks are similar. In this study, large scatters of elastic properties such as acoustic impedance (*AI*) are observed (Figure 4.2). Integrating other data with petrographic analysis, we find that the variations of *AI* at a given porosity are controlled by the pore structure variation and that the shear frame flexibility factor γ_μ can be effective for classifying the different pore types. The thin sections of the selected samples, impregnated with epoxy (Figure 4.2), with the red color indicating porosity. By examining core data including thin sections for the selected samples shown in Figure 4.2, we find that when $\gamma_\mu < 4$, the dominant pore type is moldic; when $4 < \gamma_\mu < 12$, the dominant pore type is intercrystalline; and when $\gamma_\mu > 12$, micro-intercrystalline porosity is prevalent. Given the same pore type, with similar γ_μ values, impedance varies as a result of changes in porosity, cementation, or degree of dolomitization. For example, within the intercrystalline pores shown by the yellow dots (Figure 4.2), *AI* decreases as dolomitization advances and porosity increases after burial. The steep *AI*-porosity trends in different pore systems are similar to the diagenetic trends recognized in the silici-clastic reservoirs (Dvorkin and Nur, 1996). From points A to D, the arrows concisely outline a diagenetic sequence similar to previous studies of diagenesis (Ma et al., 2008).

To better understand the effect of pore structure on *AI*, we plot the *AI* against the product of γ_μ (Figure 4.2.b) and porosity (Zhang, 2015). The relationship becomes much more linear as we consider the effect of pore structure on *AI*. More moldic porosity is

expected to be present in the upper half of the data and more intercrystalline porosity in the lower half because moldic pores have much lower γ_μ value than intercrystalline pores at a similar porosity. However, higher porosity moldic pores and lower porosity intercrystalline pores, illustrated by A3 and C3, can have very similar *AI* values. Therefore, acoustic impedance inversion alone may not be sufficient, and pre-stack inversion is necessary to understand pore structure variation.

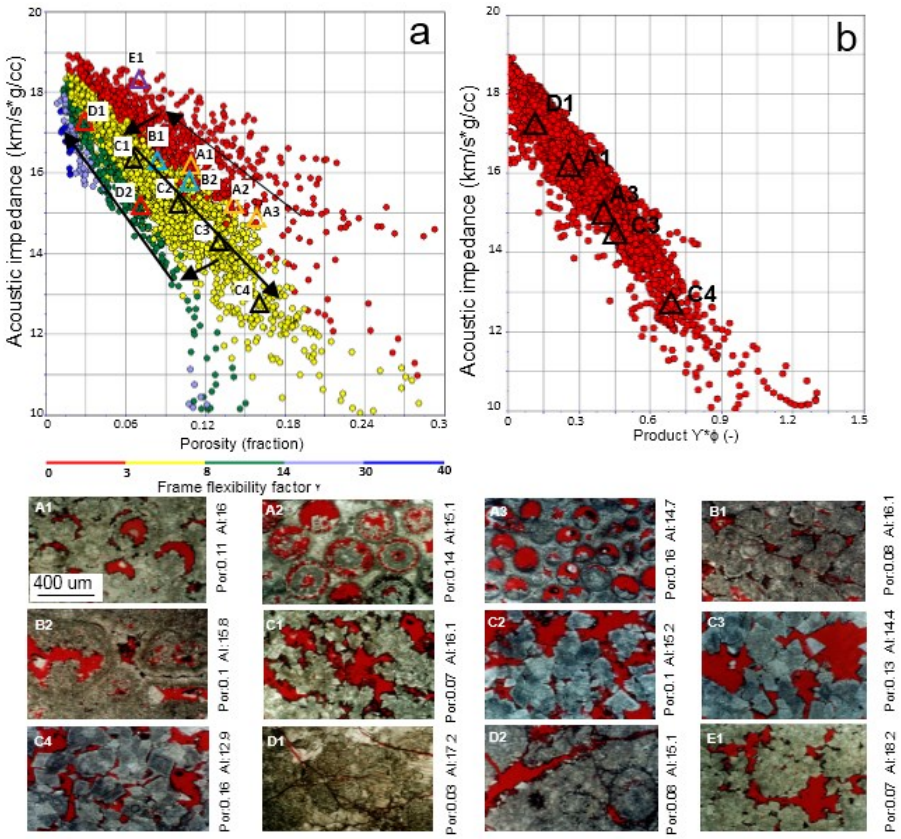

Figure 4. 2 a） crossplot of *AI* versus porosity colored by frame flexibility factor γ; b) cross plot of *AI* versus the product of γ and porosity. Thin sections of selected samples show the different pore types. A points and E point are showing moldic porosity, B points are showing a mixture of moldic and intergranular porosity. C points are showing intercrystalline porosity. D points are showing microporosity. The scales for all thin sections are the same as shown in the first one.

Classification of permeability-porosity trends

Permeability in carbonate rocks can change by orders of magnitude as a result of pore structure variations. In this study, we investigate different empirical permeability-porosity relationships for various pore types using measured permeability at a constant pressure. The results from Chapter II and III have demonstrated that the pore structure index γ_μ is effective for discrimination of pore types and classification of different permeability-porosity trends (e.g. Figure 2.12, Figure 3.2). As shown in Figure 2.12, two distinct permeability-porosity trends occur in the studied reservoir, which are determined by two different pore types, namely, intercrystalline and moldic pores, and which can be distinguished by using an approximate γ_μ cut-off value of 4. On the cross-plot, the lower permeability trend is on the rocks with isolated moldic porosity, where $\gamma_\mu < 4$. The porosity ranges from 0.16-0.3, and permeability ranges from 0.02-8 md. A possible explanation for the lower values of γ_μ is that the strong cementation between the isolated moldic porosity leads to a rigid rock frame with lower shear strength. The higher permeability trend is on the rocks with partially dissolved intercrystalline porosity, where $\gamma_\mu > 4$. The porosity ranges from 0.01-0.16 and permeability ranges from 0.08-900 md. It is noted that the γ_μ value in this field example is used to determine the gradients of different permeability-porosity trends, not the permeability values. The pore size or grain size and pore connectivity for a given porosity are very different for these two pore types, and so are their changes with porosity, especially when porosity is not small. In turn, the two trends of variation of pore connectivity or permeability with porosity are drastically different. By applying different empirical fittings to the two permeability-

porosity trends with distinctive pore types, distinguished by γ_μ (Figure 2.12), we built a new permeability model (see Eqs.4.8-4.9). Based on this model, the spatial distribution of permeability can be calculated from seismically inverted porosity and γ_μ.

Feasibility study for log scale inversion of pore structure index

A feasibility study of inversion of pore structure index from well logging data is necessary before the method can be applied for extracting the reservoir properties from seismic data. The *AI* values at zero offset and *EI* values at 30^o offset are estimated from the well log data. Figure 4.3.A shows that the intercrystalline pore system in the upper interval has significantly higher *EI* than the moldic pore systems in the lower interval. Figure 4.3.B indicates that the frame flexibility factor γ_μ can be used to clarify different *AI-Vp/Vs* relationships introduced by pore type variation. Both results illustrate that pore structure has an effect on the shear properties of the rock; thus, it is feasible to extract the pore structure information from angle stack inversion.

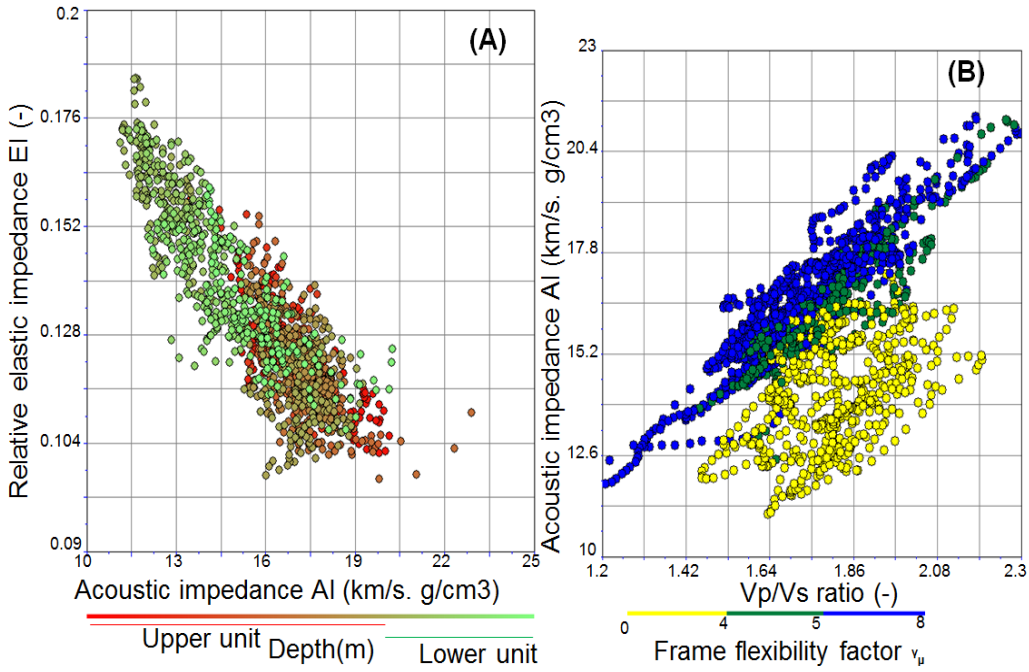

Figure 4. 3 Feasibility analysis of seismic inversion: (A) Cross-plot of the calculated elastic impedance at 30° offset with the acoustic impedance at zero offsets. Depth is shown in color. The upper unit is mostly intercrystalline pores while the lower one is mostly moldic pores (B) Cross plot of acoustic impedance with *Vp/Vs* ratio. Frame flexibility factor (γ_μ) is shown in color.

Another direct feasibility study applied is the study of poisson impedance for pore structure characterization. In the studied gas field, variations of pore structure exceed those of lithology and fluid content. It is observed that unlike common application of poisson's ratio to identify hydrocarbon, poisson's ratio is a good parameter to indicate pore structure. Similarly, poisson impedance can be a useful attribute for the purpose of qualitative pore structure interpretation and can be used to separate the two distinct pore systems. Figure 4.4 shows that zone A and C has similar porosity but significant permeability and pore throat size. Zone A is dominated by

intercrystalline pores while zone C is dominated by moldic pores. It is observed that *AI* and *SI* show low values for both zones while frame flexibility factor, poisson's ratio, and poisson impedance can effectively distinguish the two systems.

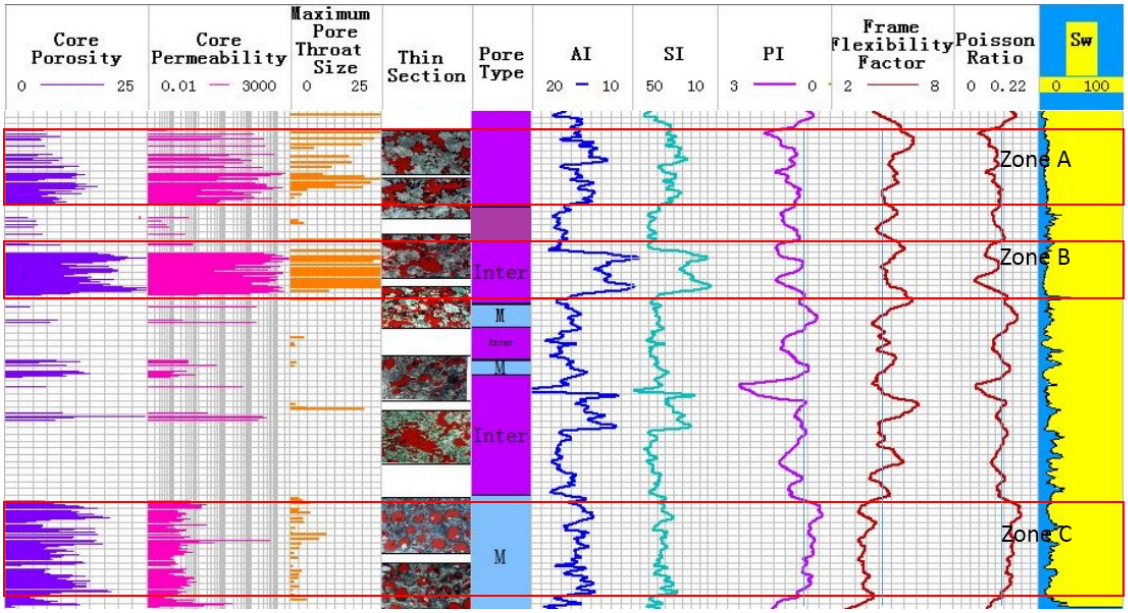

Figure 4. 4 Formation evaluation, tracks shown are core porosity, core permeability, maximum pore throat size, thin sections, interpreted pore types, *AI, SI, PI*, frame flexibility factor γ, poission's ratio (*PR*), poission impedance, water saturation. Zone A and B are dominated by intercrystalline pores while zone C is dominated by moldic pores. *PI* agrees with γ and *PR* in explaining pore structure difference between zone A and C.

From four cored wells, a value of 1.7 is chosen for "c" to compute *PI* from *AI* and *SI*. Figure 4.5 is a cross plot of calculated *PI* and porosity from wells with shear data colored by γ. It demonstrates that by applying a cutoff to *PI*, reservoirs dominated by moldic pores ($\gamma < 3$) may be separated from the ones dominated by intercrystalline pores ($\gamma > 3$). *PI* > 1000 (m/s*g/cc) can be used to locate crystalline dolomite layer, which has

proved to have a better permeability (Figure 3.2). The result may be applied to guide directional drilling in these layers for hydrocarbon exploration. However, it is rather qualitative than quantitative and is not efficient to characterize the heterogeneity within the crystalline dolomite. The results of PI inversion are used to confirm the feasibility of applying pre-stack seismic inversion for pore structure prediction in a sensible geological manner.

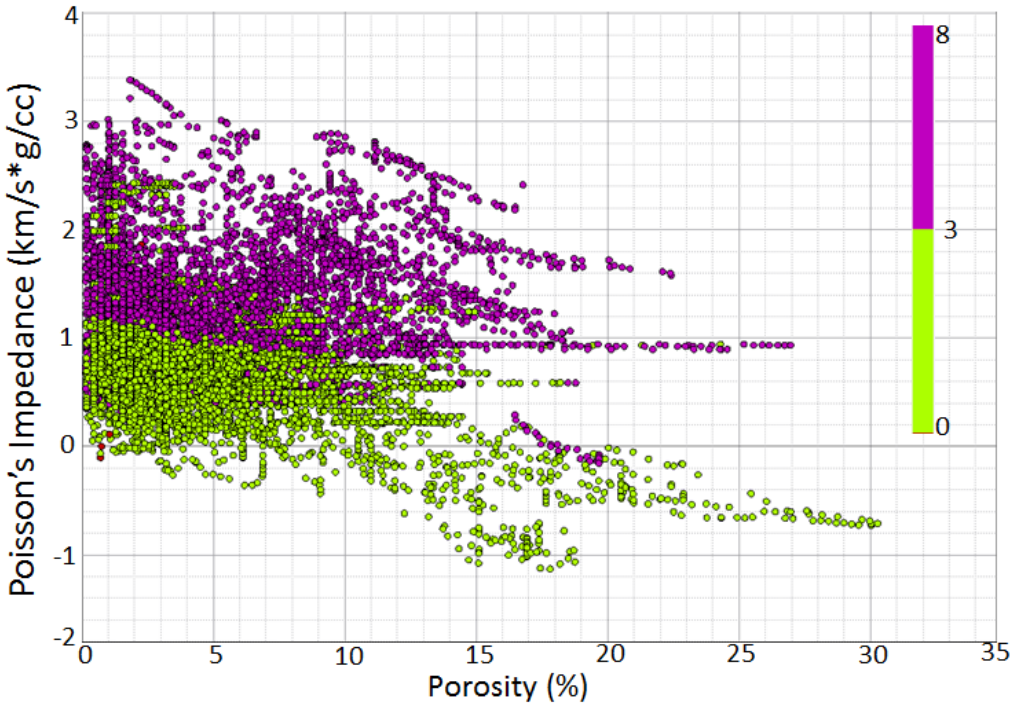

Figure 4. 5 Crossplot of *PI* versus porosity colored by frame flexibility factor γ.

IV.4.2 Seismic Inversion

Impedance volume obtained after seismic inversion has the advantage of eliminating wavelet side-lobes and false stratigraphy-like effects which can greatly improve sequence-stratigraphic analysis (Karimi, 2015). In this study, model-based inversions are performed to assist seismic interpretation of depositional facies and reservoir properties and their variations associated with sea level changes. The input model for inversion is built using well logs, and the stratigraphic surfaces are interpreted from seismic data. The variations of impedances should correspond with the major changes observed on well logs and in seismic data; thus, they are expected to follow the stratigraphic variations.

Post-stack acoustic impedance inversion

Acoustic impedance *(AI)*, as a function of velocity and density, may give useful information on rock properties and stratigraphy (Lindseth, 1979). Figure 4.6 shows a cross-section of acoustic impedance flattened on the top of the Permian strata to better illustrate the stratigraphy at the time of deposition. The shape and sequence architecture of low- and high-*AI* beds are clearly delineated on the section. Within the studied interval, the top of the section has very high *AI*, shown by the purple color, whereas the lower part is dominated by low *AI*.

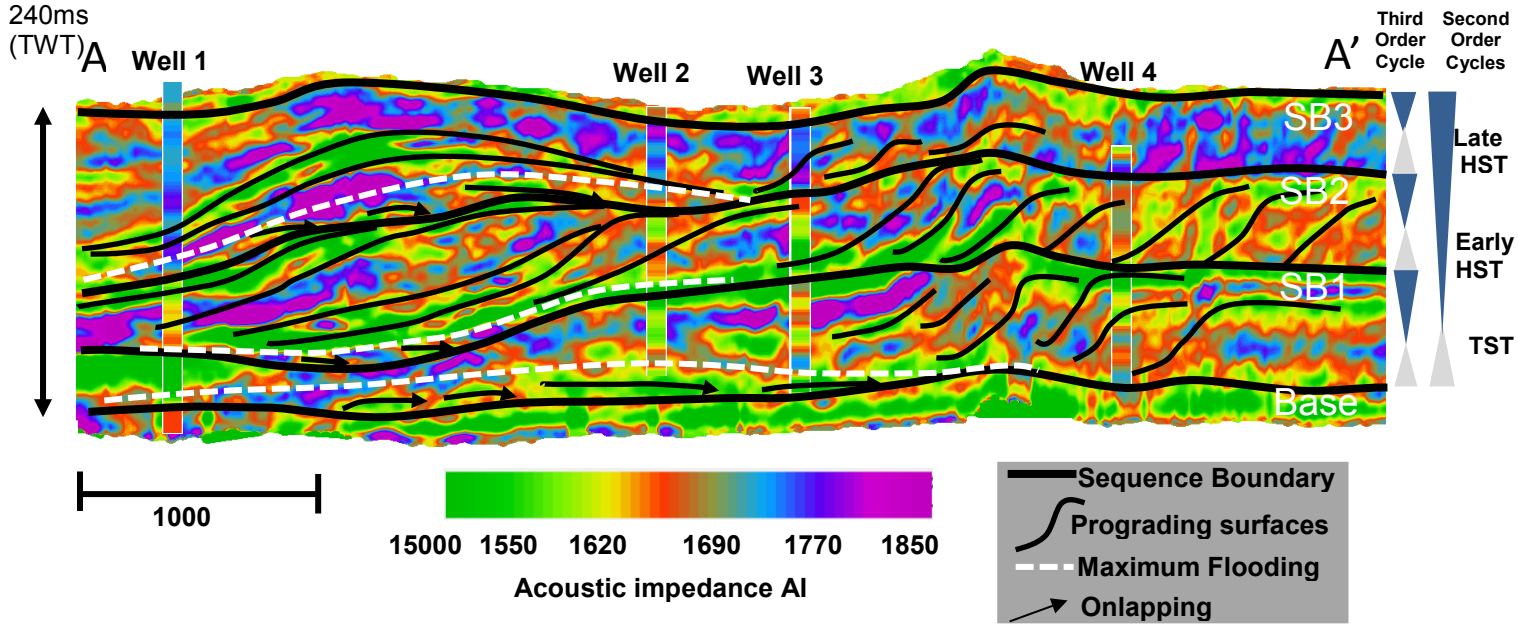

Figure 4. 6 Post-stack acoustic impedance inversion result across five production wells with sequence stratigraphy interpretation illustrated. Sequence boundaries are shown in solid lines while internal progradating surfaces are shown in dash lines. The inserted tracks show calculated values of *AI* from well logs. The line location is shown in Figure1.1 as A-A'.

Figure 4.7 shows five slices of *AI* at different times following the second-order sea level change. Slice 1 shows a limited distribution of low *AI*; slice 2 and slice 3 display wide distributions of low *AI*; slice 4 and slice 5 illustrate the development of high *AI*. In addition, the area with low *AI* gradually moves to the south from slices 2 to 5. Both Figures 4.6 and 4.7 show that *AI* varies greatly within the studied interval, indicating changes in rock properties, and thus, in depositional facies.

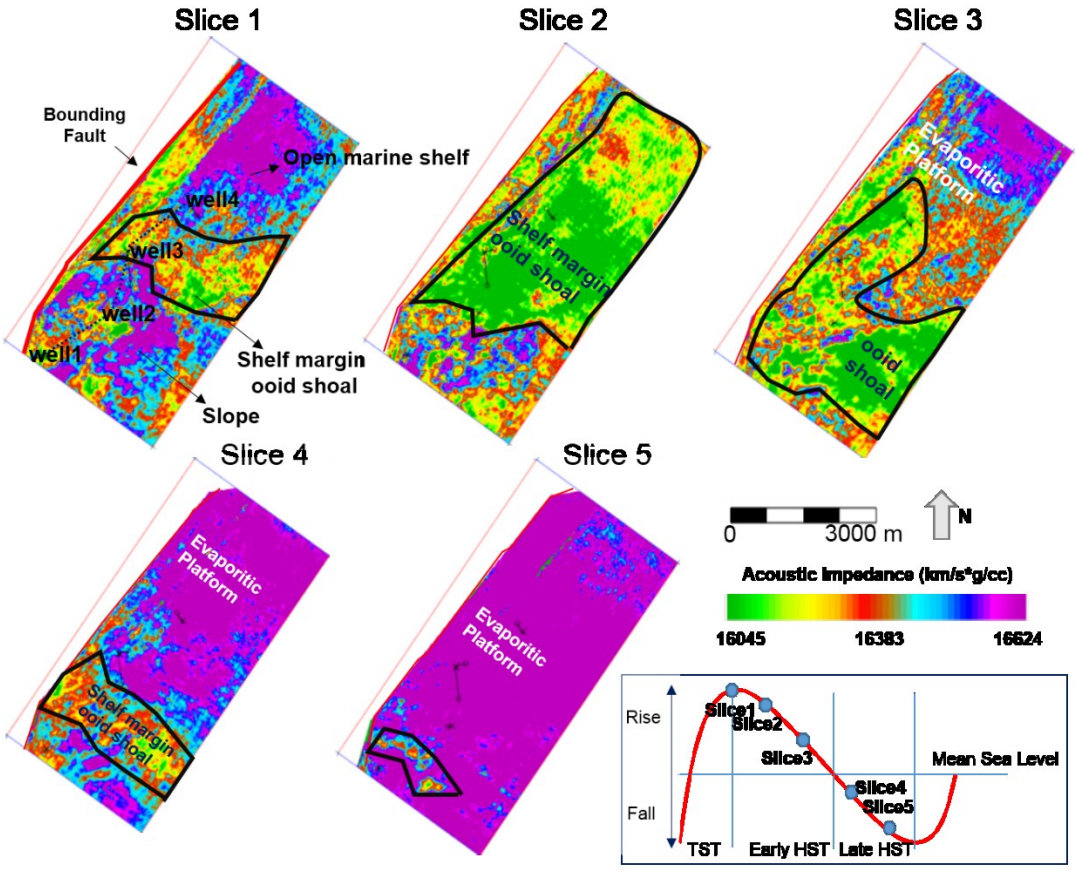

Figure 4. 7 Five horizon slices of acoustic impedance volumes, parallel to the base of Feixianguan Formation, at a different time following sea level regression. The relative location of the slices on the 2nd-order sea level cycle is shown. The black lines outlined the distribution of ooid shoals on the maps.

The variation of depositional facies during sea level cycles follows a repeatable pattern and is often associated with specific sequence architecture (Eberli and Ginsburg, 1989). Sequence stratigraphy was developed to understand sea-level changes by analyzing these genetically related sequences; it is illustrated in seismic inversion by the spatial variation of acoustic impedance. The studied Feixianguan Formation was deposited following the Early Triassic eustatic sea level fall. The related diagenetic alteration of rock fabrics follows the regional tectonics and relative sea level fall. Figure 4.8 shows one cross-section along four cored wells. The well correlations based on GR and resistivity logs and cores agree with the previous studies from the core, log, outcrop and seismic data in the following ways. During the Early Triassic, this region experienced one 2nd-order and three 3rd-order sea level fluctuations (Ma et al., 2007; Yu et al., 2015) (Figure 1.2). The well correlation shows that, following the second-order sea level change, ooid shoals were widely distributed during the early regression and gradually replaced by evaporitic facies that developed at late regression. Following the 3rd-order sea level changes, three flooding events associated with high-GR lime mud were identified above the sequence boundaries, after the episodic tectonic events. Consistent with the well correlation, seismic data display a similar stratigraphy (Figure 4.9). Three different sets of prograding beds from the Early Triassic are observed on seismic profiles. The sequence boundaries separating the prograding sets are identified by downlapping or onlapping patterns above and truncation or toplapping below; most of the boundaries display strong continuity, reflecting a significant variation in depositional facies or lithology following the sea level change.

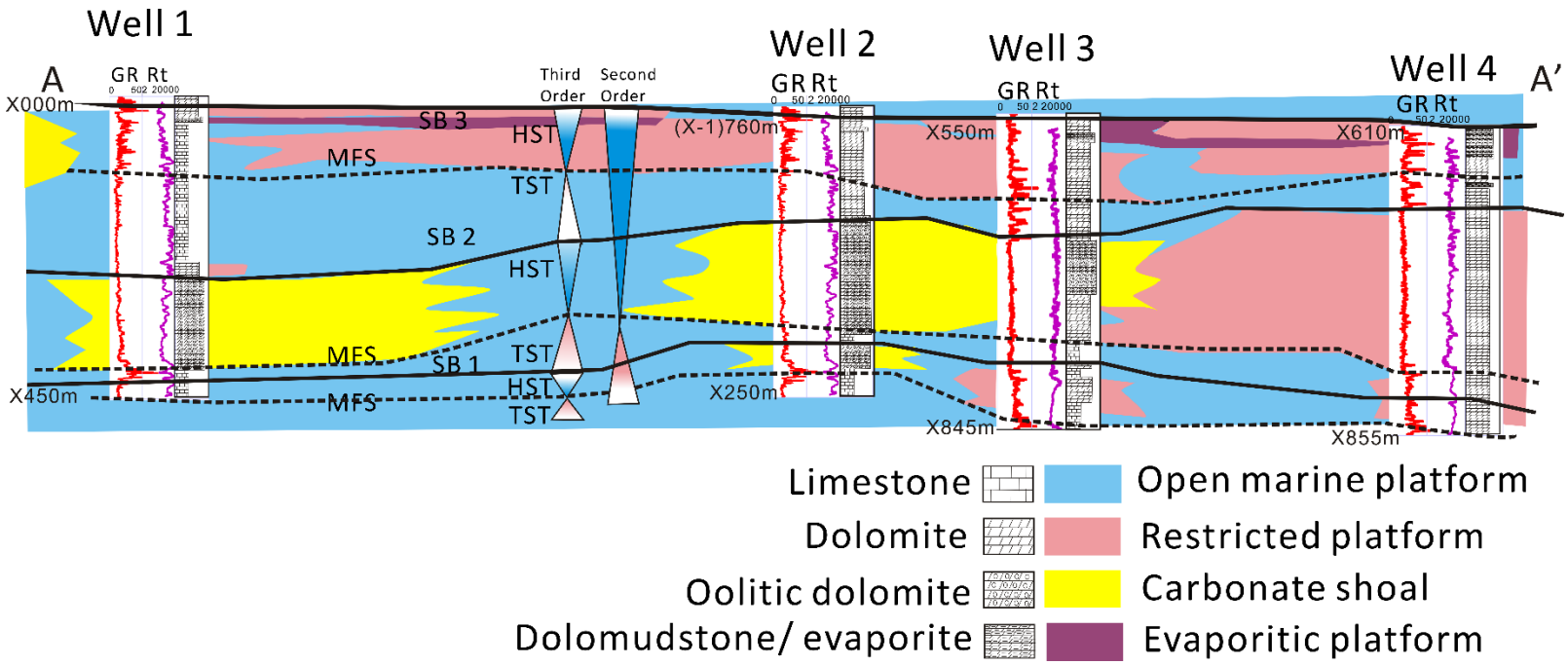

Figure 4. 8 The well cross section along the same four wells as shown in Figure 4.6 and Figure 4.9, with interpreted stratigraphic surfaces and depositional facies from the core and log analysis. The displayed logs are GR and Resistivity. The line location is shown as A-A' in Figure 1.1.

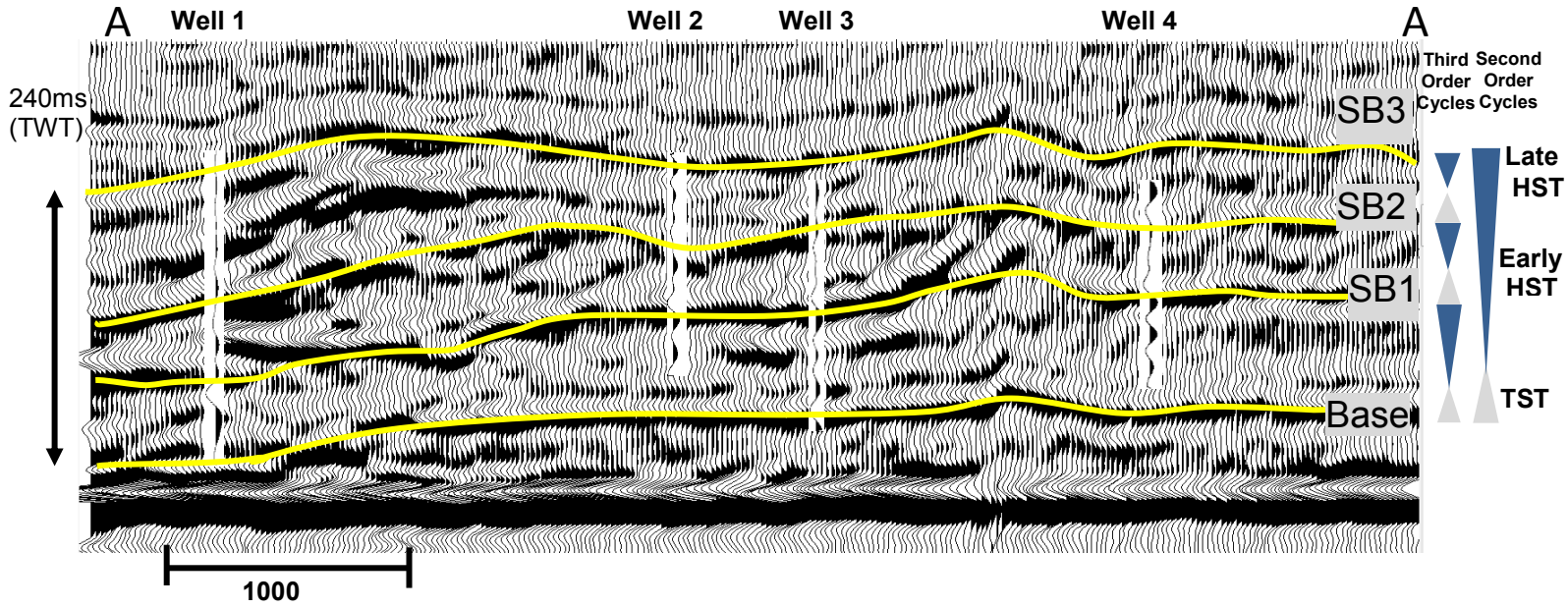

Figure 4. 9 A seismic line showing the interpretation of key stratigraphic surfaces and synthetic seismic traces. The line location is consistent with the line shown in Figure 4.6.

In Figure 4.6, the prograding patterns after inversion agree with the seismic data, and the sequence boundaries and internal sequence characteristics are clearly shown on acoustic impedance. Both of them show three separated prograding sets between the interpreted 3rd-order sequence boundaries. These boundaries are associated with low impedance, possibly caused by high porosity after subaerial exposure and dissolution. Within each sequence, the periodic variation of low *AI* and high *AI* records the prograding of ooid shoals through time. From shelf to margin (A' to A), the shape of low-*AI* beds changes from strongly progradational to aggradational following the increasing of accommodation space. In addition, the onlapping patterns above the sequence boundaries are shown by the low-*AI* beds at the margin.

The results from core and log analysis have shown that low *AI* indicates porous carbonate ooid shoals; high *AI* indicates either open marine lime mudstone or evaporitic dolomudstone (Figure 4.2). Therefore, the variation of *AI* after inversion agrees with the regional stratigraphy that open marine lime mudstone (low *AI)* dominated the deposition during the initial rapid sea level rise (Figure 4.7). High-porosity ooid shoals (low *AI)*, were prevalent after the initial sea level drop and gradually shifted seaward and were replaced by the evaporitic dolomicrite following the sea level drop.

Poisson impedance inversion (feasibility study)

Figure 4.10 displays a *PI* cross section across the first three wells shown in the *AI* cross section. The low values indicate reservoirs dominated by moldic pores whose reservoirs are more developed and connected during Early HST. The interpretation of *PI*

agrees with the interpretation of frame flexibility factor curves. Figure 4.11 displays three slices from TST, Early HST, and Late HST respectively on the 2nd-order sea level cycle. Slice 1 illustrates that during transgression, ooid grains started to develop but were restricted. From Slice 1 to Slice 2, it indicates that as sea level falls, moldic pores are widely developed after meteoric dissolution. Slice 3 reveals that during Late HST, it is mostly micro-intercrystalline pores from dolomudstone deposited on the evaporatic platform.

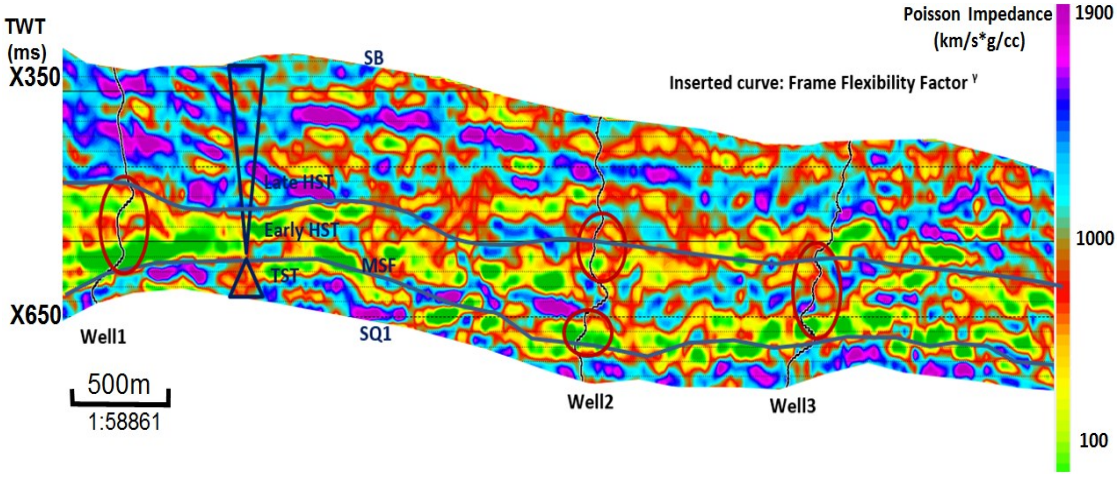

Figure 4. 10 Cross-section of Poisson Impedance across three wells. The boundaries between TST and early HST, and between early and late HST, on the 2nd order sea level cycle are shown. Inserted cure is frame flexibility factor. Circled zones are dominated by moldic pores.

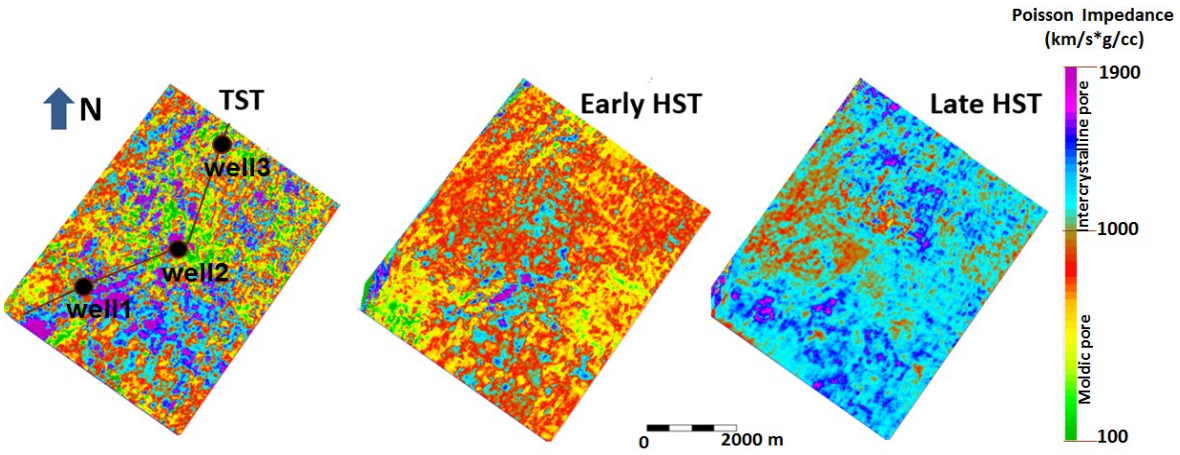

Figure 4. 11 Three slices of *PI* during TST, Early HST and Late HST on the 2nd order sea level cycle respectively. The change of color indicates pore structure changes.

Prestack inversion of pore structure

The variation of *AI* may be controlled by porosity or pore type changes (Figure 4.2). Therefore, it is difficult to use only *AI* for evaluation of pore type variation. The feasibility studies demonstrated that it is possible to extract pore type from prestack seismic inversion. As outlined in the Methods section, the porosity and the frame flexibility factor (γ_μ) are simultaneously inverted from prestack seismic data. The results from core and log analysis have shown that a cut-off value of 4 for γ_μ is effective for distinguishing moldic porosity from intercrystalline porosity (Figure 2.12). Figure 4.12 shows one W-E cross-section of inverted frame flexibility factor γ_μ. It is observed that moldic pores ($\gamma_\mu < 4$) are more widely distributed in the middle of the cross-section, which belongs to the early HST on the 2nd-order sea level cycle interpreted from seismic data. In addition, there are three vertical sets of prograding beds delineated by the variation of γ_μ, which correlates well with the three regional 3rd-order sea level cycles

identified from well correlation and seismic data. In each prograding set, it is observed that moldic pores with a warm color ($\gamma_\mu < 4$) are pervasively developed and connected on the top set of each group of prograding clinoforms, below the sequence boundaries. Within the clinoforms, the prograding of moldic layers (orange color), are followed by the prograding of intercrystalline layers, shown by the blue color ($\gamma_\mu > 4$). Figure 4.13 displays three RMS maps of the frame flexibility factor γ_μ for TST, Early HST, and Late HST on the second-order sea level cycle, which changed from mostly micro-intercrystalline pores ($\gamma_\mu > 4$) to pervasive development of moldic porosity ($\gamma_\mu < 4$), and then mostly micro-intercrystalline porosity ($\gamma_\mu > 4$). The variation of the pore structure index γ_μ as a result of changes in deposition or diagenesis agrees with the stratigraphy. Affected by the eustatic 2nd-order sea level change, the deposition changed from lime mud or transgressive dolomite with tiny intercrystalline porosity ($\gamma_\mu > 8$) during transgression to ooid shoals with developed moldic porosity ($\gamma_\mu < 4$) and large intercrystalline porosity ($4 < \gamma_\mu < 8$) during early regression, and finally dolomudstone with micro-intercrystalline porosity ($\gamma_\mu > 8$) at late regression. Controlled by the third-order relative sea level changes, the episodic variation of pore types illustrated by the prograding sets is shown in Figure 4.12. On each set, moldic porosity located below the sequence boundary is created by selective dissolution of ooid grains after exposure (Yu et al., 2015). Within the clinoforms, the moldic pores are transformed to intercrystalline pores after refluxing or burial dolomitization. Above the sequence boundaries, extremely small intercrystalline pores may occur in the transgressive dolomite (Moss and Tucker, 1996).

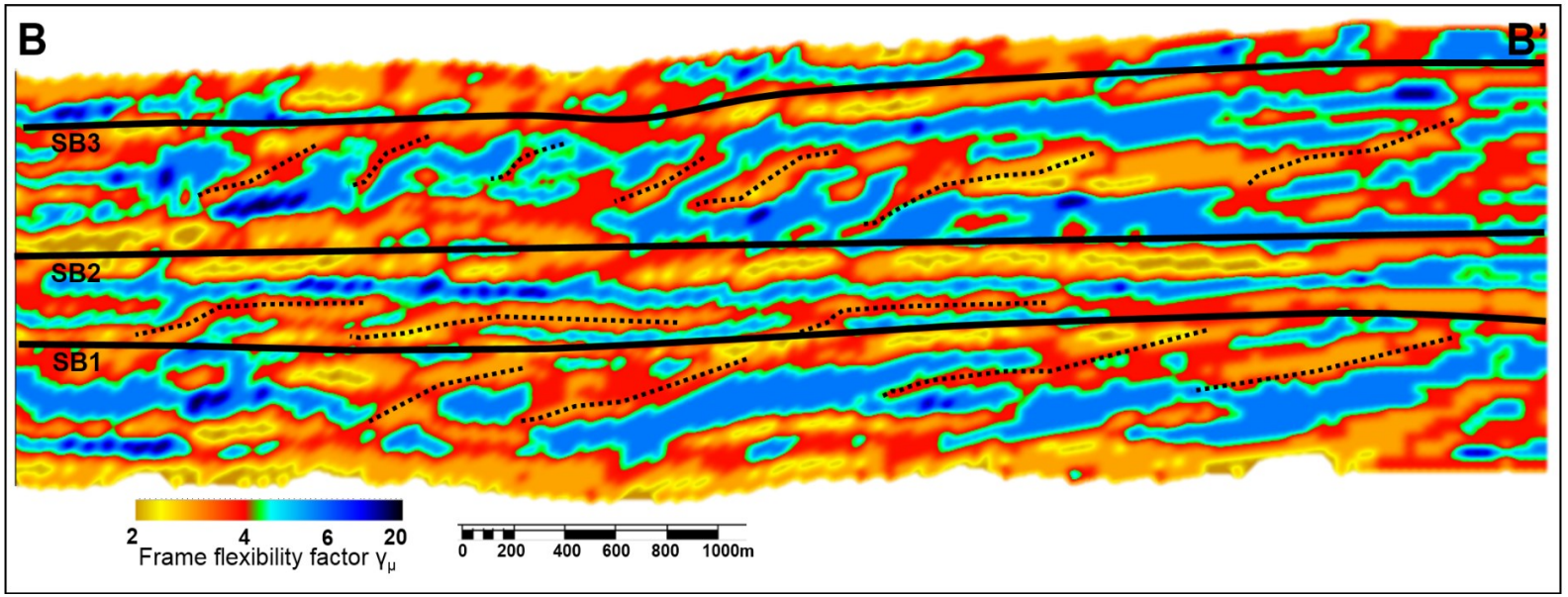

Figure 4. 12 One random West-East cross-section of inverted frame flexibility factor (γ_μ) with interpreted 3rd-order sequence boundaries (SB), which shows three sets of prograding clinoforms. The section is flattened on the second sequence boundary (SB2). Warm color indicates potential areas of moldic pores. They are widely distributed below the sequence boundaries. The line location is shown as B-B' in Figure 1.1.

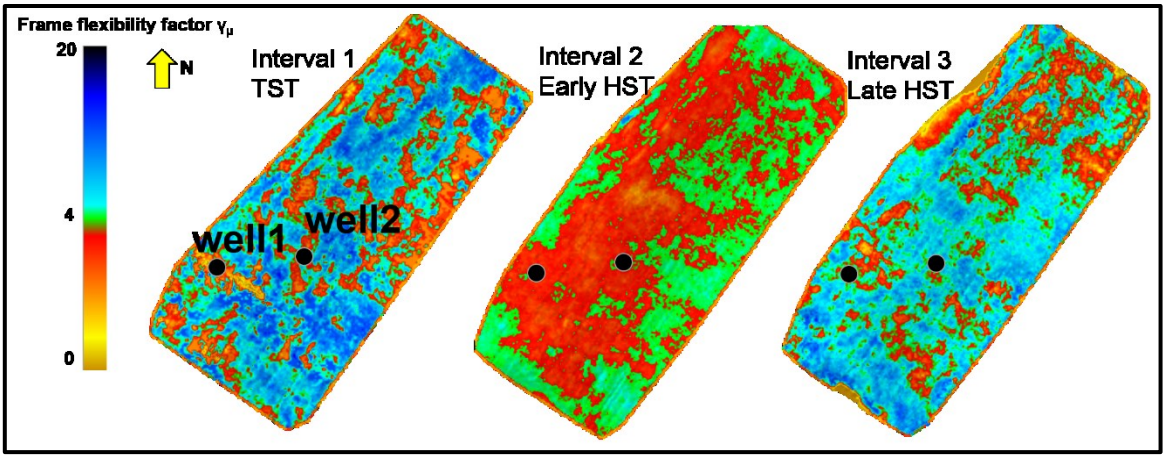

Figure 4. 13 Three RMS maps of frame flexibility factor (γ_μ) for TST, early HST, and late HST intervals during the regional 2nd-order sea level cycle. RMS attribute is calculated based on windows set by the interpreted flooding surface and sequence boundaries.

Figure 4.14 shows the RMS maps of the frame flexibility factor using a10 ms window above and below the three sequence boundaries. It again illustrates that moldic pores indicated by low γ_μ values are widely distributed below the three regional third-order sequence boundaries, while intercrystalline pores indicated by high γ_μ values are located above the moldic pores.

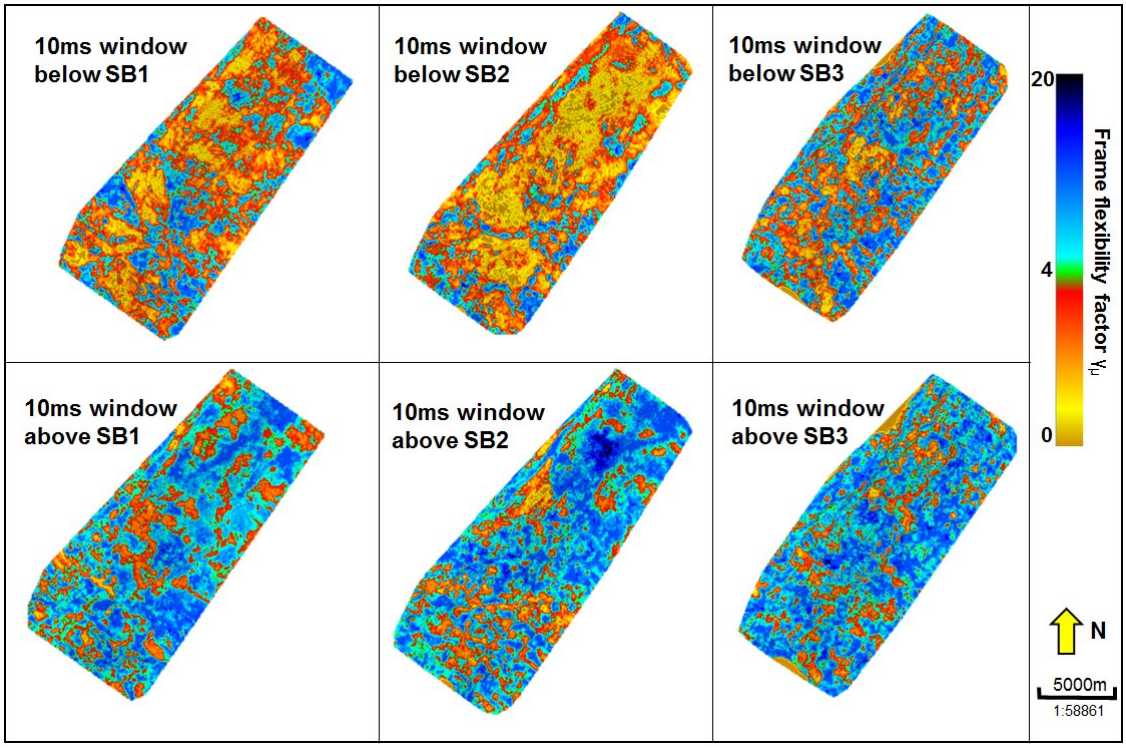

Figure 4. 14 Six RMS maps of frame flexibility factor (γ_μ) using 10 ms above and below the three sequence boundaries respectively, which shows more development of moldic porosity (lower γ_μ) below the sequence boundaries.

Geological controls on reservoir heterogeneity

The inversion results further confirmed the deposition and diagenetic model described in Chapter III (Figure 3.9). The ooid shoals are prograding basinward following the sea level regression. Controlled by the different fluid flow paths, diagenesis and the resulting pore types vary across the platform (Machel, 2004). Moldic pores were previously developed at the topographic highs, below the sequence boundaries, from meteoric leaching following early sea level fall (Yu et al., 2015). Below the connected oolitic dolomite bed, crystalline dolomites are developed following

the refluxing of Mg^{2+}-rich sea water (Ma et al., 2008; Jiang et al., 2013). Farther away from the surface and the source of Mg^{2+}, the size of dolomite crystals increases. Above the sequence boundary, transgressive dolomite may develop along with lime mud deposition at the slope of the platform (Moss and Tucker, 1996). It is deposited as a result of sea water flooding.

In Chapter III, the trend analysis of pore structure indicator logs reveals the potential correlation between sea level cyclicity and pore structure variation. In this Chapter, we will continue the correlative study using the pore structure information obtained from seismic inversion. Figure 4.15 shows four seismic sections: the original inverted γ_μ volume, and its filtered volumes. Consistent with the log analysis, the three filtered volumes correlate with the sea level cycles at different frequencies. The results may assist future study on geological controls of the relative sea level change.

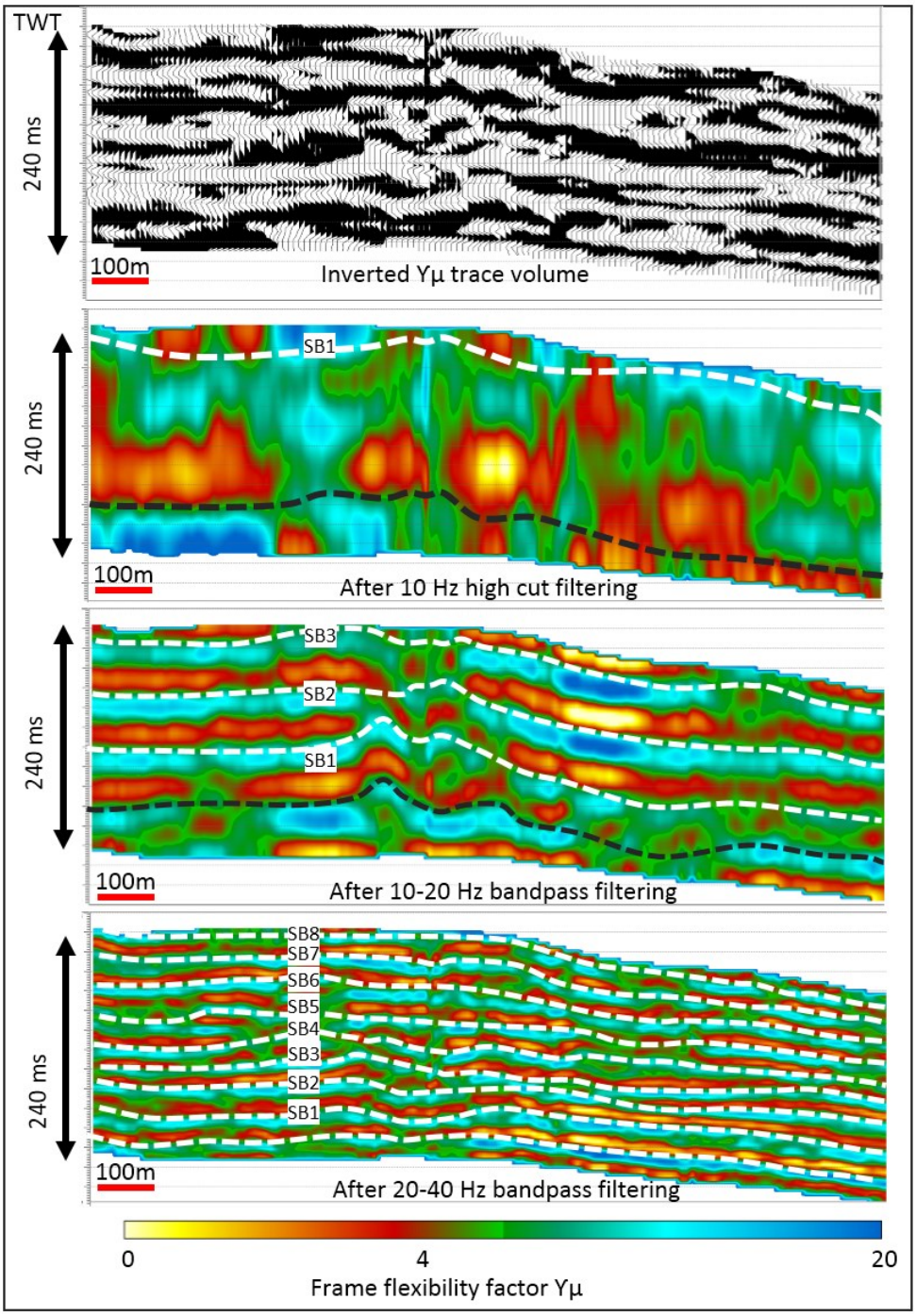

Figure 4. 15 Comparision of several frame flexibility factor volumes after seismic inversion and filtering. From top to bottom, they panels are displaying the original inverted section, the one after 10 Hz high-cut filtering, 10-20 Hz bandpass filtering, and 20-40 Hz bandpass filtering. The white lines are interpreted sequence boundaries. The γ_μ volumes of different frequencies correlate with sea level fluctuations at 2nd-order, 3rd-order, and 4th-order respectively (Figure 3.4). The line location is shown in Figure 1.1 as C-C'.

Permeability estimation

The spatial distribution of permeability is calculated based on the inversion results of the porosity and the frame flexibility factor (γ_μ) and the core-established permeability-porosity relations (see Eqs. 4.8-4.9). The result reinforces the fact that the spatial distribution of permeability in the field is controlled by both the porosity and the pore structure. Figure 4.16 shows the inversion results of reservoir properties using the same line from Well 1 to Well 2. From top to bottom, the original seismic amplitude, inverted porosity, pore structure parameter, and permeability are displayed. The results show that for the prograding ooid shoals, reservoirs highlighted by the green polygons have high porosity but relatively low permeability, as they are dominated by moldic porosity ($\gamma_\mu < 4$). Meanwhile, reservoirs highlighted by the purple polygons have fair porosity but very good permeability, as most of them are dominated by connected intercrystalline porosity ($\gamma_\mu > 4$).

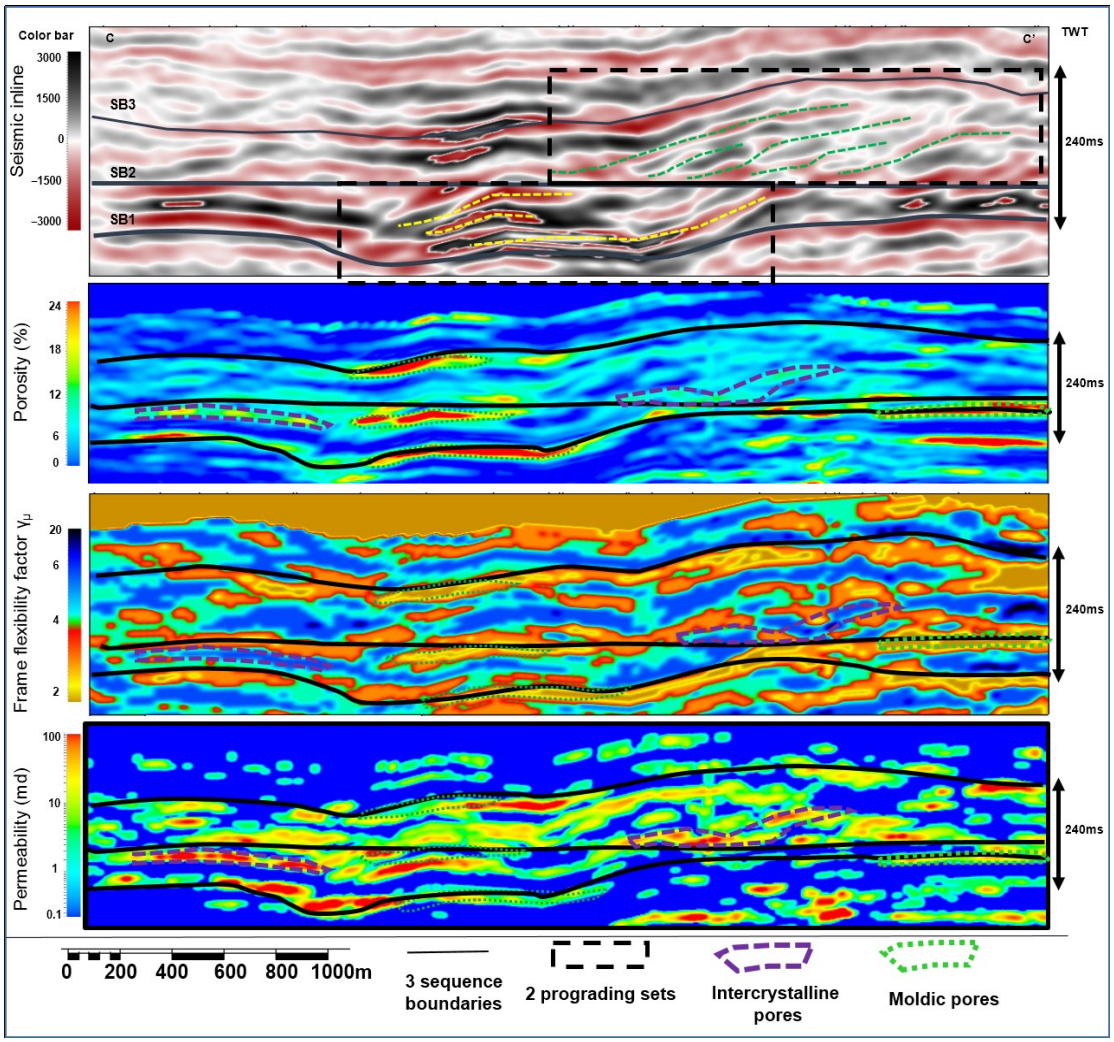

Figure 4. 16 Rock physics based angle stack inversion results on a seismic line from Well 1 to Well 2. From top to bottom, it shows original seismic, inverted porosity, frame flexibility factor (γ_μ), and permeability respectively. The section is flattened on the second sequence boundary (SB2). Intercrystalline pores are showing medium porosity but very high permeability while moldic pores are showing high porosity but lower permeability. The line location is shown in Figure 1.1 as 'C-C'.

IV.5 Conclusions

The geological alteration of pore structure can significantly change the elastic properties and permeability of carbonate rocks. The permeability and porosity relation is thus difficult to describe. The shear frame flexibility factor (γ_μ) is used as a pore structure index to classify carbonate pore types and quantify their influence on elastic properties and permeability. Two distinct permeability trends are identified and distinguished by γ_μ with a value of 4 based on core and log analysis. The low-permeability trend is mainly in ooid grainstone beds with isolated moldic pores, and the high-permeability trend is primarily located in diagenetic dolomite with intercrystalline pores.

Seismic inversion of the *AI*, porosity, and the frame flexibility factor (γ_μ) is applied to understand the geological controls on the spatial variation of the pore type and to evaluate the heterogeneity of the permeability determined by the pore structure. The results indicate that carbonate shoals (low *AI*) are developed and prograde seaward following the 2nd-order sea level regression. Moldic pores ($\gamma_\mu < 4$) are more developed during early regression, whereas micro-intercrystalline pores ($\gamma_\mu > 12$) dominate during late regression. Moldic pores are also widely developed below the 3rd-order sequence boundaries. In addition,-regional fluid flow and diagenetic paths, as well as their stratigraphic relationships with the sequence boundaries, are interpreted. The results confirmed the proposed dolomitization models in Chapter III that reflux dolomitization and burial dolomitization are dominant following the microbial dolomitization. The

inversion results are then applied to evaluate the spatial variation of permeability based on the permeability-porosity relations established from the core. A better understanding of the geological controls on permeability variation will improve reservoir prediction for future exploration and production.

CHAPTER V

SUMMARY

Located on the passive margin of an arid paleo-aragonite sea near the equator, Sichuan basin was a place favorable for dolomitization during Early Triassic. Dolomitization along with dissolution greatly improved reservoir quality by enhancing porosity and pore connectivity. However, permeability varied significantly at a given porosity within the massive dolomite due to the strong variation in pore structure. Four different types of dolomite with distinctive rock textures and are described as crystalline, peloid, moldic oolitic dolomite, and dolomudstone. In this study, pore structure indicators were first established at wells using core and log data to understand the vertical variation of pore structure. The selected pore structure indicator was then integrated with the geochemistry and petrographic data to explain the geological control on pore structure such as different dolomitization processes controlled by sea level changes. Afterward, the spatial variation of pore structure and permeability was estimated by seismic inversion.

Based on mercury injection capillary pressure measurements (MICP) and other core data, five zones with distinct pore types and reservoir performances are distinguished and classified for the Early Triassic Feixianguan reservoirs in Puguang Gas Field. The five zones are characterized as moldic pore dominant (Zone 1), sucrosic macro-intercrystalline (Zone 2), mixed moldic and intercrystalline (moldic dominated) (Zone 3), meso-intercrystalline (Zone 4), and micro-intercrystalline (Zone 5), from

bottom to top. All zones show distinct features for pore throat sizes (e.g. Rc_{10} and Rc_{50}), pore throat tortuosity, displacement pressure P_d, capillary pressures (e.g. P_{10} and P_{50}), irreducible water saturation S_{min} and Leverett J-function. Integrated evaluation of resistivity, velocity, neutron-density logs helps estimate pore types classified from core analysis. The parameters evaluated for pore type estimation include the differences between shallow and deep resistivity, and between neutron and density, cementation factor (m) from Archie's law, frame flexibility factor (γ_μ) from Sun's rock physics model, S factor from Castagna's modified Wyllie's equation. All of the parameters are useful to separate moldic pores dominated zone from intercrystalline pore dominated zones. The m and γ_μ factors are the most efficient to separate all four reservoir zones with distinct pore types. It is observed that when $m > 2.4$, $\gamma_\mu < 4$, the zone is dominated by moldic pores; when $1.6 < m < 2.4$, $4 < \gamma_\mu < 8$, it is meso to macro intercrystalline pores; when $m < 1.6$ and $\gamma_\mu > 8$, it is dominated by intercrystalline pores. Based on the pore type evaluation from core and logs, better estimation of permeability for reservoir production can be expected. Two distinct permeability trends are identified and distinguished by γ_μ with a value of 4 based on core and log analysis. The low-permeability trend is mainly found in ooid grainstones with isolated moldic pores, and the high-permeability trend is primarily located in diagenetic dolomite with intercrystalline pores.

The variation of pore structure indicator γ_μ correlates with the sea level fluctuations in the studied field due to the diagenetic evolution associated with sea level change. The indicator γ_μ increases as sea level decreases. In the upward shallowing

cycle, γ_μ increases as the pores evolved from macro- and meso- intercrystalline in crystalline dolomite to micro-intercrystalline in dolomudstone. Occurrences of moldic pores with very low γ_μ correlate well with the unconformities after uplifting events. Along with other geochemistry and petrography analysis, different dolomitization mechanisms are discussed. Dolomitization was possibly triggered by microbial sulfate reduction in the tidal flat or lagoons. Afterward, the reflux dolomitization and burial dolomitization result in the distinct evolution of crystal textures from micro-intercrystalline to macro-intercrystalline pores down dip. Moldic oolitic dolomite at the top was formed after early fabric selective dolomitization.

Seismic inversion of the *AI*, porosity, and the frame flexibility factor (γ_μ) has shown similar patterns observed from the core and log analysis. The results demonstrate that carbonate shoals (low *AI*) may be developed at early transgression and prograde seaward following the 2nd-order sea level regression. Moldic pores (γ_μ <4) are more developed during early regression, whereas micro-intercrystalline pores (γ_μ > 12) dominate during late regression. Moldic pores are also widely developed and better connected below the 3rd-order sequence boundaries. In addition, the inversion results further confirmed the dolomitization hypotheses suggested from the core and log analysis. Lastly, the inversion results were applied to evaluate the spatial variation of permeability based on the permeability-porosity relations established from the core. A better understanding of the geological controls on permeability variation will improve reservoir prediction for future exploration and production.

REFERENCES

Adams, J. E., and M. L. Rhodes. 1960, Dolomitization by seepage refluxion: AAPG Bulletin, **44**, no. 12, 1912-1920.

Adesokan, H., and Y. F. Sun. 2014, Rock-physics-based estimation of critical-clay-volume fraction and its effect on seismic velocity and petrophysical properties: Geophysics, **79**, no. 3, 175-185.

Ahr, W. M. 1973, The carbonate ramp: an alternative to the shelf model: Gulf Coast Association of Geological Societies Transactions, **23**, 221-225.

Ahr, W. M. 2008, Geology of carbonate reservoirs: John Wiley & Sons, New Jersey.

Aliakbardoust, E., and H. Rahimpour-Bonab. 2013, Effects of pore geometry and rock properties on water saturation of a carbonate reservoir: Journal of Petroleum Science and Engineering, **112**, 296-309.

Amthor, J. E., E. W. Mountjoy, and H. G. Machel. 1994, Regional-scale porosity and permeability variations in Upper Devonian Leduc buildups: implications for reservoir development and prediction in carbonates: AAPG Bulletin, **78**, no. 10, 1541-1558.

Amyx, J. W., D. M. Bass, and R. L. Whiting. 1960, Petroleum reservoir engineering: physical properties. Vol. 1: McGraw-Hill College.

Anovitz, L. M., and D. R. Cole. 2015, Characterization and analysis of porosity and pore structures: Reviews in Mineralogy & Geochemistry, **80**, 61-164. doi: 10.2138/rmg.2015.80.04.

Anselmetti, F. S. 2001, Sonic velocity in carbonates—A combined product of depositional lithology and diagenetic alterations: SEPM Special Publication No. 70, 193-216.

Anselmetti, F. S., and G. P. Eberli. 1993, Controls on sonic velocity in carbonates: Pure and Applied Geophysics, **141**, no. 2-4, 287-323. doi: 10.1007/Bf00998333.

Anselmetti, F. S., and G. P. Eberli. 1999, The velocity-deviation log: a tool to predict pore type and permeability trends in carbonate drill holes from sonic and porosity or density logs: AAPG Bulletin, **83**, no. 3, 450-466.

Archie, G. E. 1942, The electrical resistivity log as an aid in determining some reservoir characteristics: Transactions of the American Institute of Mining and Metallurgical Engineers, **146**, 54-61.

Archie, G. E. 1952, Classification of carbonate reservoir rocks and petrophysical considerations: AAPG Bulletin, **36**, no. 2, 278-298.

Badiozamani, K. 1973, The Dorag dolomitization model--application to the Middle Ordovician of Wisconsin: Journal of Sedimentary Research, **43**, no. 4, 965-984.

Bathurst, R. G. C. 1972, Carbonate sediments and their diagenesis. Vol. 12: Elsevier.

Beales, F. W. 1953, Dolomitic mottling in Palliser (Devonian) limestone, Banff and Jasper National Parks, Alberta: AAPG Bulletin, 37, no. 10, 2281-2293.

Biot, M. A. 1962a, Generalized theory of acoustic propagation in porous dissipative media: The Journal of the Acoustical Society of America, **34**, no. 9A, 1254-1264.

Biot, M. A. 1962b, Mechanics of deformation and acoustic propagation in porous media: Journal of Applied Physics, **33**, no. 4, 1482-1498.

Borai, A. M. 1987, A new correlation for the cementation factor in low-porosity carbonates: SPE Formation Evaluation, **2**, no. 04, 495-499.

Brie, A., D. L. Johnson, and R. D. Nurmi. 1985, Effect of spherical pores on sonic and resistivity measurements, Paper read at SPWLA 26th Annual Logging Symposium.

Cai, C. F., Z. Y. Xie, R. H. Worden, G. Y. Hu, L. S. Wang, and H. He. 2004, Methane-dominated thermochemical sulphate reduction in the Triassic Feixianguan Formation East Sichuan Basin, China: towards prediction of fatal H 2 S concentrations: Marine and Petroleum Geology, **21**, no. 10, 1265-1279.

Calvert, S., and G. Ballay. 2011, Basic logs unlock complex carbonate pore properties, Paper read at SPWLA 52nd Annual Logging Symposium.

Chen, H., J. C. Tian, X. Zhang, Y. Yang, and G. Fu. 2008, Dolomization genetic of the Lower Triassic Feixianguan Group oolitic beach in Northeast Sichuan Basin [J]: Natural Gas Industry, **1**, 010.

Chen, P. Y., X. C. Tan, H. Liu, T. Ma, B. Luo, X. F. Jiang, Y. Yu, and X. J. Jin. 2014, Formation mechanism of reservoir oolitic dolomite in Lower Triassic Feixianguan Formation, northeastern Sichuan Basin, southwest China: Journal of Central South University, **21**, 3263-3274.

Chen, P. Y., X. C. Tan, H. T. Yang, M. Tang, Y. W. Jiang, X. J. Jin, and Y. Yu. 2015, Characteristics and genesis of the Feixianguan Formation oolitic shoal reservoir, Puguang gas field, Sichuan Basin, China: Frontiers of earth science, **9**, no. 1, 26-39.

Choquette, P. W., and N. P. James. 1987, Diagenesis# 12. Diagenesis in Limestones-3. The deep burial environment: Geoscience Canada, **14**, no. 1.

Choquette, P. W., and L. C. Pray. 1970, Geologic nomenclature and classification of porosity in sedimentary carbonates: AAPG Bulletin, **54**, no. 2, 207-250.

Churcher, P. L., and A. H. Majid. 1989, Similarities between the Tangent-Wabamun type play of the Alberta Basin and the Albion-Scipio type play of the Michigan Basin: Bulletin of Canadian Petroleum Geology, **37**, no. 2, 241-245.

Cleary, M. P. 1978, Elastic and dynamic response regimes of fluid-impregnated solids with diverse microstructures: International Journal of Solids and Structures, **14**, no. 10, 795-819.

Coe, A. L. 2003, The sedimentary record of sea-level change: Cambridge University Press.

Connolly, P. 1999, Elastic impedance: The Leading Edge, **18**, no. 4, 438-452.

Dou, Q. F. 2011, Rock physics-based carbonate reservoir pore type evaluation by combining geological, petrophysical and seismic data: Dissertation, Texas A&M University.

Dou, Q. F., Y. F. Sun, and C. Sullivan. 2011, Rock-physics-based carbonate pore type characterization and reservoir permeability heterogeneity evaluation, Upper San Andres reservoir, Permian Basin, west Texas: Journal of Applied Geophysics, **74**, no. 1, 8-18. doi: 10.1016/j.jappgeo.2011.02.010.

Doveton, J. H. 1999, Basics of oil & gas log analysis: Kansas Geological Survey, **510**.

Dullien, F. A. L. 1975a, Effects of pore structure on capillary and flow Phenomena in sandstones: Journal of Canadian Petroleum Technology, **14**, no. 3, 48-55.

Dullien, F. A. L. 1975b, Prediction of tortuosity-factors from pore structure data: Aiche Journal, **21**, no. 4, 820-822. doi: DOI 10.1002/aic.690210431.

Dullien, F. A. L. 1976, Single-phase and 2-phase flow in capillary networks: Abstracts of Papers of the American Chemical Society, 19-19.

Dullien, F. A. L. 1992, Porous media-fluid transport and pore structure: Access Online via Elsevier.

Dullien, F. A. L., and G. K. Dhawan. 1974, Characterization of pore structure by a combination of quantitative photomicrography and mercury porosimetry: Journal of

Colloid and Interface Science, **47**, no. 2, 337-349.

Dunham, R. J. 1962, Classification of carbonate rocks according to depositional textures: AAPG Memoir, 108-121.

Dvorkin, J., and A. Nur. 1996, Elasticity of high-porosity sandstones: theory for two North Sea data sets: Geophysics, **61**, no. 5, 1363-1370.

Eberli, G. P., G. T. Baechle, F. S. Anselmetti, and M. L. Incze. 2003, Factors controlling elastic properties in carbonate sediments and rocks: The Leading Edge, 22, no. 7, 654-660.

Eberli, G. P., and R. N. Ginsburg. 1989, Cenozoic progradation of northwestern Great Bahama Bank, a record of lateral platform growth and sea-level fluctuations: SEPM Special Publication No. 44, 339-351.

Ehrenberg, S. N. 2004, Porosity and permeability in Miocene carbonate platforms on the Marion Plateau, offshore NE Australia: relationships to stratigraphy, facies and dolomitization: The geometry and petrogenesis of dolomite hydrocarbon reservoirs: Geological Society (London) Special Publication, 235, 233-253.

El-Wazeer, F., A. Vizamora, A. Al Hamedi, H. Al-Housani, P. Abram, and S. Busman. 2010, Integrating rock physics, seismic reservoir characterization and static modeling of carbonates: A case study from the United Arab Emirates. 9th Middle East Geosciences Conference, GEO 2010: GeoArabia, Journal of the Middle East Petroleum Geosciences, **16**, no. 2, 187.

Etten, J., D. Zhu, and A. D. Hill. 2015, The combined effect of permeability and pore structure on carbonate matrix acidizing, Paper read at EUROPEC 2015.
Fan, J. S. 2005, Characteristics of carbonate reservoirs for oil and gas fields in the world and essential controlling factors for their formation: Dixue Qianyuan(Earth Science Frontiers), **12**, no. 3, 23-30.

Feng, C. W., X. Z. Wang, F. Zhang, Y. J. Fang, G. S. Chen, Y. Yang, and T. Q. Yang. 2008, The sedimentary facies of Lower Triassic Fei1-Fei3 formation on an isolated carbonate platform, Northeastern China, Sichuan (in Chinese): China Geology, **35**, no. 1, 54-66.

Fischer, A. G., T. D. Herbert, G. Napoleone, I. P. Silva, and M. Ripepe. 1991, Albian pelagic rhythms (Piobbico core): Journal of Sedimentary Research, **61**, no. 7.

Focke, J. W., and D. Munn. 1987, Cementation exponents in Middle Eastern carbonate reservoirs: SPE formation evaluation, **2**, no. 02, 155-167.

Gartner, G. L., P. D. Wagner, G. T. Baechle, Y. F. Sun, R. Weger, G. P. Eberli, W. Asyee, H. Hillgartner, K. Van der Kolk, and J. Leguijt. 2005, Obtaining permeability from seismic data-a new breakthrough in carbonate reservoir modelling, Paper read at International Petroleum Technology Conference.

Gavrilenko, P., and Y. Gueguen. 1989, Pressure dependence of permeability: a model for cracked rocks: Geophysical Journal International, **98**, no. 1, 159-172.

Gingras, M. K., S. G. Pemberton, K. Muelenbachs, and H. Machel. 2004, Conceptual models for burrow‐related, selective dolomitization with textural and isotopic evidence from the Tyndall Stone, Canada: Geobiology, 2, no. 1, 21-30.

Ginsburg, R. N. 2001, Subsurface geology of a prograding carbonate platform margin, Great Bahama Bank: results of the Bahamas Drilling Project.

Green D.W., and G.P. Willhite, 1999, Title: improved oil recovery in Mississippian carbonate reservoirs of Kansas -- near term -- class 2, Report, The University of Kansas Center for Research Inc.

Grotzinger, J. P. 1986, Upward shallowing platform cycles: a response to 2.2 billion years of low-amplitude, high-frequency (Milankovitch band) sea level oscillations: Paleoceanography, **1**, no. 4, 403-416.

Grude, S., J. Dvorkin, and M. Landrø. 2013, Rock physics estimation of cement type and impact on the permeability for the Snohvit Field, the Barents Sea, Paper read at 2013 SEG Annual Meeting.

Guo, T. L. 2011, Sequence strata of the platform edge in the Changxing and Feixianguan formations in the Yuanba area, northeastern Sichuan Basin and their control on reservoirs [J]: Acta Petrolei Sinica, **3**, 002.

Hampson, D. P., B. H. Russell, and B. Bankhead. 2005, Simultaneous inversion of pre-stack seismic data, Paper read at 2005 SEG Annual Meeting.

Handford, C. R., and L. R. Baria. 2007, Geometry and seismic geomorphology of carbonate shoreface clinoforms, Jurassic Smackover Formation, north Louisiana: Geological Society, London, Special Publications, 277, no. 1, 171-185.

Hang, S. J., Y. Huang, Y. F. Lan, and K. K. Huang. 2011, A comparative study on strontium isotope composition of dolomites and their coeval seawater in the Late Permian-Early Triassic, NE Sichuan basin: Acta Petrologica Sinica, **27**, no. 12, 3831-3842.

Hao, F., T. L. Guo, C. G. Du, H. Y. Zou, X. Y. Cai, Y. M. Zhu, K. P. Li, C. W. Wang,

and Y. C. Zhang. 2009, Accumulation mechanisms and evolution history of the giant Puguang gas field, Sichuan Basin, China: Acta Geologica Sinica (English edition), **83**, no. 1, 136-145.

Hardie, L. A. 1987, Dolomitization: A critical view of some current views: Journal of Sedimentary Research, **57**, no. 1, 166-183.

Heydari, E., and L. R. Baria. 2006, Reservoir characteristics of the Smackover formation at the Little Cedar Creek Field, Conecuh County, Alabama: Gulf Coast Association of Geological Societies Transactions, **56**, 283-289.

Huang, S. J., H. P. Tong, L. H. Liu, Z. W. Hu, X. H. Zhang, J. L. Huan, and K. K. Huang. 2009, Petrography, geochemistry and dolomilization mechanisms of Feixianguan dolomites in Triassic, NE Sichuan, China: Acta Petrologica Sinica, **25**, no. 10, 2363-2372.

Hudson, J. A. 1980, Overall properties of a cracked solid: Mathematical Proceedings of the Cambridg e Philosophical Society, **88**, no. 2, 371-384.

Jennings, J. B. 1987, Capillary pressure techniques: application to exploration and development geology: AAPG Bulletin, **71**, no. 10, 1196-1209.

Jiang, L., C. F. Cai, R. H. Worden, K. K. Li, and L. Xiang. 2013, Reflux dolomitization of the upper Permian Changxing Formation and the Lower Triassic Feixianguan Formation, NE Sichuan Basin, China: Geofluids, **13**, no. 2, 232-245.

Jiang, L., R. H. Worden, C. F. Cai, K. K. Li, L. Xiang, L. L. Cai, and X. Y. He. 2014, Dolomitization of gas reservoirs: the upper Permian Changxing and lower Triassic Feixianguan Formations, Northeast Sichuan Basin, China: Journal of Sedimentary Research, **84**, no. 10, 792-815.

Karimi, P. 2015, Structure-constrained relative acoustic impedance using stratigraphic coordinates: Geophysics, **80**, no. 3, A63-A67.

Katz, A. J., and A. H. Thompson. 1986, Quantitative prediction of permeability in porous rock: Physical Review B, **34**, no. 11, 8179.

Kumar, M., and D. H. Han. 2005, Pore shape effect on elastic properties of carbonate rocks: SEG Technical Program Expanded Abstracts.

Kuster, G. T., and M. N. Toksöz. 1974, Velocity and attenuation of seismic waves in two-phase media: Part I. Theoretical formulations: Geophysics, **39**, no. 5, 587-606.

Lasemi, Y. 2010, Sea level and diagenetic controls on dolomite reservoir

compartmentalization: evidence from the Niagaran Racine Formation of the Sangamon Arch, West-Central Illinois, Paper read at AAPG Eastern Section Meeting Program and Abstracts.

Leverett, M. C. 1941, Capillary behavior in porous solids: Transactions of the American Institute of Mining and Metallurgical Engineers, **142**, 152-169.

Lin, J. L., M. Fuller, and W. Y. Zhang. 1985, Preliminary Phanerozoic polar wander paths for the North and South China blocks, Nature, **313**, 444-449.

Lindseth, R. O. 1979, Synthetic sonic logs-a process for stratigraphic interpretation: Geophysics, **44**, no. 1, 3-26.

Lønøy, A. 2006, Making sense of carbonate pore systems: AAPG Bulletin, **90**, no. 9, 1381-1405.

Lucia, F. J. 1983, Petrophysical parameters estimated from visual descriptions of carbonate rocks: a field classification of carbonate pore space: Journal of Petroleum Technology, **35**, no. 03, 629-637.

Lucia, F. J. 1995, Rock-fabric petrophysical classification of carbonate pore-space for reservoir characterization: AAPG Bulletin, **79**, no. 9, 1275-1300.

Lucia, F. J., C. Kerans, and J. W. Jennings Jr. 2003, Carbonate reservoir characterization: Journal of Petroleum Technology, **55**, no. 06, 70-72.

Ma, Y. S., T. L. Guo, X. F. Zhao, and X. Y. Cai. 2008b, The formation mechanism of high-quality dolomite reservoir in the deep of Puguang Gas Field: Science in China Series D-Earth Sciences, **51**, 53-64.

Ma, Y. S., X. S. Guo, and R. Fan. 2005, Reservoir prediction of Feixianguan Formation in Puguang gas field, northeast Sichuan Province: Petroleum Exploration and Development, **32**, no. 4, 60.

Ma, Y. S., X. S. Guo, T. L. Guo, R. Huan, X. Y. Cai, and G. X. Li. 2007, The Puguang gas field: new giant discovery in the mature Sichuan Basin, southwest China: AAPG Bulletin, **91**, no. 5, 627-643.

Ma, Y. S., C. L. Mou, X. S. Guo, Q. Yu, and Q. Y. Tan. 2006, Sedimentary facies and distribution of reservoir rocks from the Feixianguan Formation in the Daxian-Xuanhan region, NE Sichuan: Acta Geologica Sinica (English Edition), **80**, no. 1, 137-151.

Ma, Y. S., S. C. Zhang, T. L. Guo, G. Y. Zhu, X. Y. Cai, and M. W. Li. 2008a, Petroleum geology of the Puguang sour gas field in the Sichuan Basin, SW China:

Marine and Petroleum Geology, **25**, no. 4, 357-370.

Machel, H. G. 2004, Concepts and models of dolomitization: a critical reappraisal: Geological Society, London, Special Publications, **235**, no. 1, 7-63.

Mancini, E. A., and D. J. Benson. 1980, Regional stratigraphy of Upper Jurassic Smackover carbonates of southwest Alabama: Gulf Coast Association of Geological Societies Transactions, **30**, 151-165.

Mancini, E. A., W. C. Parcell, and W. M. Ahr. 2006, Upper Jurassic Smackover thrombolite buildups and associated nearshore facies, southwest Alabama: Gulf Coast Association of Geological Societies Transactions, **56**, 551-563.

Mancini, E. A., W. C. Parcell, W. M. Ahr, V. O. Ramirez, J. C. Llinas, and M. Cameron. 2008, Upper Jurassic updip stratigraphic trap and associated Smackover microbial and nearshore carbonate facies, eastern Gulf coastal plain: AAPG Bulletin, **92**, no. 4, 417-442.

Mancini, E. A., B. H. Tew, and R. M. Mink. 1990, Jurassic sequence stratigraphy in the Mississippi interior salt basin of Alabama: Gulf Coast Association of Geological Societies Transactions, **40**, 521-529.

Mavko, G., T. P. Mukerji, and J. Dvorkin. 2009, The rock physics handbook: Tools for seismic analysis of porous media: Cambridge university press.

Mazzullo, S. J. 2000, Organogenic dolomitization in peritidal to deep-sea sediments: Journal of Sedimentary Research, 70, no. 1, 10-23.

McElhinny, M. W., B. J. J. Embleton, X. H. Ma, and Z. K. Zhang. 1981, Fragmentation of Asia in the Permian, Nature, 212-216.

Mei, M. X., and J. H. Gao. 2012, Giant Induan oolite: A case study from the Lower Triassic Daye Formation in the western Hubei Province, South China: Geoscience Frontiers, **3**, no. 6, 843-851.

Melas, F. F., and G. M. Friedman. 1992, Petrophysical characteristics of the Jurassic Smackover Formation, Jay Field, Conecuh embayment, Alabama and Florida (1): AAPG Bulletin, **76**, no. 1, 81-100.

Mishra, P. K., A. Al-Harthy, J. M. Al-Kanderi, M. Al-Raisi, G. Al-Alawi, S. Alhashmi, and S. Turkey. 2012, Rock typing and characterization of carbonate reservoirs, Paper read at SPE Kuwait International Petroleum Conference and Exhibition.

Mollajan, A., and H. Memarian. 2016, Rock physics-based carbonate pore type

identification using Parzen classifier: Journal of Petroleum Science and Engineering, **145**, 205-212. doi: 10.1016/j.petrol.2016.03.021.

Morrow, D. W. 1978, Dolomitization of Lower Paleozoic burrow-fillings: Journal of Sedimentary Research, **48**, no. 1.

Moss, S. J., and M. E. Tucker. 1996, Dolomitization associated with transgressive surfaces—a mid-Cretaceous example: Sedimentary Geology, **107**, no. 1, 11-20.

Nelson, P. H. 1994, Permeability-porosity relationships in sedimentary rocks: The Log Analyst, **35**, no. 03.

Neustaedter, R. H. 1968, Log evaluation of deep Ellenburger gas zones, Paper read at SPE Deep Drilling and Development Symposium.

Norbisrath, J. H., G. P. Eberli, B. Laurich, G. Desbois, R. J. Weger, and J. L. Urai. 2015, Electrical and fluid flow properties of carbonate microporosity types from multiscale digital image analysis and mercury injection: AAPG Bulletin, **99**, no. 11, 2077-2098.

Norris, A. N. 1985, A differential scheme for the effective moduli of composites: Mechanics of Materials, **4**, no. 1, 1-16.

Nur, A., and G. Simmons. 1969, The effect of saturation on velocity in low porosity rocks: Earth and Planetary Science Letters, **7**, no. 2, 183-193.

O'Connell, R. J., and B. Budiansky. 1974, Seismic velocities in dry and saturated cracked solids: Journal of Geophysical Research, **79**, no. 35, 5412-5426.

Pan, L. Y., Z. G. Liu, C. Li, J. F. Shou, J. Y. Zhang, J. Zhang, A. J. Shen, J. G. Zhou, and X. P. Zheng. 2012, Dolomitization and its relationship with reservoir development of the Lower Triassic Feixianguan Formation in eastern Sichuan Basin: Journal of Palaeogeography, **14**, no. 2, 176-186.

Pan, L. Y., J. F. Shou, and J. G. Zhou. 2010, Dolomitization and reservoirs characteristics of Chx-Fxg Formation in Sichuan Basin (SW China), Paper read at AAPG International Conference and Exhibition, Sep 12-15, at Calgary, Alberta, Canada.

Phukan, M. 2011, XX-210 Petrographic analyses (TSD, XRD, SEM & LPSA) in Marrat Formation: Reservoir Geology Group, Core Laboratories, March 2011.

Porras, J. C. 1998, Determination of rock fabrics and pore types from pore throat radius and bulk volume water, and their relations to lithofacies, Carito North field, eastern Venezuela basin, Paper read at SPWLA 39th Annual Logging Symposium.

Porras, J. C., and O. Campos. 2001, Rock typing: a key approach for petrophysical characterization and definition of flow units, Santa Barbara field, Eastern Venezuela Basin, Paper read at SPE Latin American and Caribbean Petroleum Engineering Conference.

Purcell, W. R. 1949, Capillary pressures-their measurement using mercury and the calculation of permeability therefrom: Journal of Petroleum Technology, **1**, no. 02, 39-48.

Qiang, Z. T. 2007, Geology of carbonate reservoir: Beijing, China: University of Petroleum Press (in Chinese).

Qiao, Z. F., G. R. Li, S. X. Long, Z. Z. Jiang, W. Y. Hu, and W. M. Li. 2010, Characteristics and evolution model of sequence stratigraphy of Feixianguan Formation in the Northeast of Sichuan Basin: Acta Sedimentol Sin, **28**, 462-470.

Quakenbush, M., B. Shang, and C. Tuttle. 2006, Poisson impedance: The Leading Edge, **25**, no. 2, 128-138.

Rasmus, J. C. 1983, A variable cementation exponent, m, for fractured carbonates: The Log Analyst, **24**, no. 06.

Rezaee, M. R., H. Motiei, and E. Kazemadeh. 2007, A new method to acquire m exponent and tortuosity factor for microscopically heterogeneous carbonates: Journal of Petroleum Science and Engineering, **56**, no. 4, 241-251.

Ridgway, J. G. 2010, Upper Jurassic (Oxfordian) Smackover facies characterization at Little Cedar Creek Field, Conecuh County, Alabama. Thesis, The University of Alabama.

Russell, B., and M. N. Toksöz. 1991, Comparison of poststack seismic inversion methods, Paper read at 1991 SEG Annual Meeting.

Saleh, A. A., and J. R. Castagna. 2004, Revisiting the Wyllie time average equation in the case of near-spherical pores: Geophysics, **69**, no. 1, 45-55.

Salem, H. S., and G. V. Chilingarian. 1999, The cementation factor of Archie's equation for shaly sandstone reservoirs: Journal of Petroleum Science and Engineering, **23**, no. 2, 83-93.

Saller, A. H., and J. A. D. Dickson. 2011, Partial dolomitization of a Pennsylvanian limestone buildup by hydrothermal fluids and its effect on reservoir quality and performance: AAPG Bulletin, **95**, no. 10, 1745-1762.

Sarg, J. F. 1988, Carbonate sequence stratigraphy: SEPM Special Publication No. 42, 155-181.

Schlumberger. 1991, Log Interpretation Principles/Applications: Schlumberger Educational Services.

Sethi, D. K. 1979, Some considerations about the formation resistivity factor-porosity relations, Paper read at SPWLA 20th Annual Logging Symposium.

Shahalipour, G. R., S. Joneidi, and H. Hasani. 2015, Feature rock typing, the new approach in heterogeneous carbonate reservoirs. In Geoindia 2015, AAPG and APG. Greater Noida-india.

Sibley, D. F. 1980, Climatic control of dolomitization, Seroe Domi Formation (Pliocene), Bonaire, NA: SEPM Special Publication No. 28, 247-258.

Skalinski, M., S. Gottlib-Zeh, and B. Moss. 2006, Defining and predicting rock types in carbonates-preliminary results from an integrated approach using core and log data from the Tengiz field: Petrophysics, **47**, no. 01.

Skalinski, M., J. A. Kenter, S. Jenkins, and T. Tankersley. 2010, Updated rock type definition and pore type classification of a carbonate buildup, Tengiz Field, Republic of Kazakhstan (Russian), Paper read at SPE Caspian Carbonates Technology Conference.

Stanley, S. M. 2005, Earth system history: Macmillan.

Strasser, A. 1988, Shallowing-upward sequences in Purbeckian peritidal carbonates (lowermost Cretaceous, Swiss and French Jura Mountains): Sedimentology, **35**, no. 3, 369-383.

Sun, C. Y., M. Y. Hu, Z. G. Hu, D. Xue, and Z. H. Wang. 2015, Sequence-based lithofacies and Paleogeography of lower Triassic Feixianguan Formation in Sichuan Basin: Marine Origin Petroleum Geology, **3**, 005.

Sun, P. K., H. M. Xu, Q. F. Dou, H. Adesokan, Y. F. Sun, Q. F. Huang, and N. Jiang. 2015, Investigation of pore-type heterogeneity and its inherent genetic mechanisms in deeply buried carbonate reservoirs based on some analytical methods of rock physics: Journal of Natural Gas Science and Engineering, **27**, 385-398.

Sun, S. Q. 1994, A reappraisal of dolomite abundance and occurrence in the Phanerozoic: PERSPECTIVE: Journal of Sedimentary Research, **64,** no. 2.

Sun, Y. F. 2000, Core-log-seismic integration in hemipelagic marine sediments on the eastern flank of the Juan de Fuca Ridge, Paper read at Proceedings of the Ocean Drilling

Program. Scientific results.

Sun, Y. F. 2004, Pore structure effects on elastic wave propagation in rocks: AVO modelling: Journal of Geophysics and Engineering, **1**, no. 4, 268-276. doi: 10.1088/1742-2132/1/4/005.

Sun, Y. F., and D. Goldberg. 1997, Effects of aspect ratio on wave velocities in fractured rocks, Paper read at SEG, Expanded Abstracts.

Tan, X. C., L. Li, H. Liu, B. Luo, Y. Zhou, J. J. Wu, and X. Ding. 2011, General depositional features of the carbonate platform gas reservoir of the Lower Triassic Jialingjiang Formation in the Sichuan Basin of southwest China: Moxi gas field of the central basin: Carbonates and Evaporites, **26**, no. 4, 339-350.

Tan, X. C., L. Z. Zhao, B. Luo, X. F. Jiang, J. Cao, H. Liu, L. Li, X. B. Wu, and Y. Nie. 2012, Comparison of basic features and origins of oolitic shoal reservoirs between carbonate platform interior and platform margin locations in the Lower Triassic Feixianguan Formation of the Sichuan Basin, southwest China: Petroleum Science, **9**, no. 4, 417-428.

Toksöz, M. N., C. H. Cheng, and A. Timur. 1976, Velocities of seismic waves in porous rocks: Geophysics, **41**, no. 4, 621-645.

Tonietto, S. 2014, Pore characterization and classification in carbonate reservoirs and the influence of diagenesis on the pore system. Case study: Thrombolite and Grainstone units of the upper Jurassic Smackover Formation, Gulf of Mexico: Dissertation, Texas A&M University.

Tosaya, C., and A. Nur. 1982, Effects of diagenesis and clays on compressional velocities in rocks: Geophysical Research Letters, **9**, no. 1, 5-8.

Vail P.R., and R.M., Mitchum.1979, Global cycles of relative changes of sea level from seismic stratigraphy: resources, comparative structure, and eustatic changes in sea level: AAPG Memoir, 29, 469-472.

Van Brakel, J., S. Modrý, and M. Svata. 1981, Mercury porosimetry: state of the art: Powder Technology, **29**, no. 1, 1-12.

Varavur, S., H. Shebl, S. M. Salman, T. Shibasaki, and C. Dabbouk. 2005, Reservoir rock typing in a giant carbonate: paper SPE, **93477**, 12-15.

Vasconcelos, C., and J. A. McKenzie. 1997, Microbial mediation of modern dolomite precipitation and diagenesis under anoxic conditions (Lagoa Vermelha, Rio de Janeiro, Brazil): Journal of sedimentary Research, 67, no. 3.

Vasconcelos, C., J. A. McKenzie, S. Bernasconi, D. Grujic, and A. J. Tien. 1995, Microbial mediation as a possible mechanism for natural dolomite formation at low temperatures: Nature, 377, no. 6546, 220.

Verwer, K., G. P. Eberli, and R. J. Weger. 2011, Effect of pore structure on electrical resistivity in carbonates: AAPG Bulletin, **95**, no. 2, 175-190.

Wang, S. Y., X. Q. Jiang, H. L. Guan, and Y. J. Bao. 2009, Pore evolution of reservoirs of Feixianguan Formation in Puguang gas field in Northeastern Sichuan: Petroleum Geology & Experiment, **31**, no. 1, 26-30.

Wang, S. Y., X. Q. Jiang, H. L. Guan, and Y. J. Bao. 2010, Diagenesis effects of lower Triassic Feixianguan Formation reservoir in Puguang gas field, Northeast Sichuan: Petroleum Geology & Experiment, **32**, no. 4, 366-372.

Wang, X., F. Zhang, Z. Jiang, J. Zhang, and D. Zeng. 2008, A study of Feixianguan reservoir in northeast Sichuan Basin: Earth Sci Front, **15**, 117-122.

Wang, X. Z., F. Zhang, Q. Ma, M. P. Yang, Y. G. Wang, Y. C. Wen, Y. Yang, and J. Zhang. 2002, The characteristics of reef and bank and the fluctuation of sea-level in Feixianguan period of Late Permian-Early Triassic, East Sichuan Basin: Acta Sedimentologica Sinica, **20**, no. 2, 249-254.

Wang, Y., X. Z. Wang, Y. G. Wang, Y. C. Wen, Z. T. Qiang, B. Q. Wang, and J. Deng. 2009, Geochemical features of Lower Triassic Feixianguan dolomites to the Northeast of Sichuan (in Chinese): Acta Sedimentol Sin, **27**, no. 6.

Wang, Y. G., J. Zhang, X. G. Liu, D. D. Xu, X. R. Shi, S. J. Song, and Y. C. Wen. 2005, Sedimentary facies of evaporative carbonate platform of the Feixianguan Formation of Lower Triassic in northeastern Sichuan Basin: Journal of Palaeogeography, **7**, no. 3, 357-367.

Wardlaw, N. C. 1976, Pore geometry of carbonate rocks as revealed by pore casts and capillary-pressure: AAPG Bulletin, **60**, no. 2, 245-257.

Wardlaw, N. C., and R. P. Taylor. 1976, Mercury capillary pressure curves and the intepretation of pore structure and capillary behaviour in reservoir rocks: Bulletin of Canadian Petroleum Geology, **24**, no. 2, 225-262.

Warren, J. 2000, Dolomite: occurrence, evolution and economically important associations: Earth-Science Reviews, **52**, no. 1, 1-81.

Warren, J. K. 1989, Evaporite Sedimentology: USA.

Weger, R. J., G. T. Baechle, J. L. Masaferro, and G. P. Eberli. 2004, Effects of pore structure on sonic velocity in carbonates, Paper read at Society of Exploration Geophysicists, Expanded Abstracts.

Weger, R. J., G. P. Eberli, G. T. Baechle, J. L. Massaferro, and Y. F. Sun. 2009, Quantification of pore structure and its effect on sonic velocity and permeability in carbonates: AAPG Bulletin, **93**, no. 10, 1297-1317.

Wei, G. Q., W. Yang, Y. P. Wan, and H. Jin. 2011, Stratigraphic sequence and sedimentary facies distribution of the Permian-Middle Triassic in the northwestern margin of the Yangtze block: Acta Petrologica Sinica, **27**, no. 3, 741-748.

Wei, G. Q., W. Yang, L. Zhang, H. Jin, S. X. Wu, and J. H. Shen. 2005, Dolomitizatioin genetic model of Feixianguan group oolitic beach reservoir in Northeast Sichuan Basin: Natural Gas Geoscience, **2**, 005.

Wiley, R., and J. G. Patchett. 1994, The effects of invasion on density/thermal neutron porosity interpretation, Paper read at SPWLA 35th Annual Logging Symposium.

Wong, P. Z., J. Koplik, and J. P. Tomanic. 1984, Conductivity and permeability of rocks: Physical Review B, **30**, no. 11, 6606.

Wyllie, M. R. J., A. R. Gregory, and L. W. Gardner. 1956, Elastic wave velocities in heterogeneous and porous media: Geophysics, **21**, no. 1, 41-70.

Xiao, M. H., J. W. Jiang, H. Wang, Q. Wang, and F. Wang. 2010, The sequence characteristics and favorable reservoir of Feixianguan Formation in Puguang Gasfield: Offshore Oil, **4**, 012.

Xu, S. Y., and R. E. White. 1995, A new velocity model for clay-sand mixtures: Geophysical Prospecting, **43**, no. 1, 91-118.

Yu, Y., X. C. Tan, P. Y. Chen, H. T. Yang, T. Ma, J. Cao, and X. J. Jin. 2015, Discovery of hiatus in Feixianguan Formation and its geological implications, Sichuan Basin, SW China: Turkish Journal of Earth Sciences, **24**, no. 1, 39-55.

Zengler, D. H., J. D. Dunham, and R. L. Ethington. 1980, Concepts and models of dolomitization: SEPM Special Publication **28**.

Zhang, J., B. M. Zhang, and S. Xiuqin. 2014, Controlling effects of paleo-climate and paleo-ocean on formation of carbonate reservoirs: Petroleum Exploration and Development, **41**, no. 1, 135-143.

Zhang, T. T. 2014, Integration of rock physics and seismic inversion for carbonate reservoir characterization: Dissertation, Texas A&M University.

Zhang, T. T., Y. F. Sun, Q. F. Dou, H. R. Zhang, T. L. Guo, and X. Y. Cai. 2015, Improving porosity–velocity relationships using carbonate pore types: Journal of Computational Acoustics, **23**, no. 04, 1540006.

Zhang, X. F., T. L. Guo, B. Liu, X. Y. Fu, and S. L. Wu. 2013, Porosity formation and evolution of the deeply buried lower Triassic Feixianguan Formation, Puguang Gas Field, NE Sichuan Basin, China: Open Journal of Geology, **2013**.

Zhang, X. F., Y. l. He, Y. S. Ma, B. Liu, P. R. Zhao, J. X. Gao, and Y. K. Yang. 2011, Controls of sedimentation on reservoir formation in lower Triassic Feixianguan Formation, northeastern Sichuan Basin: Earth Science Frontiers, **18**, no. 4, 224-235.

Zhang, Y. C., C. Peng, Y. Yang, Y. Mei, and S. J. Wang. 2010, Identification of seismic sequences of high-energy oolitic beach reservoirs in the Feixianguan Formation in the Sichuan Basin [J]: Natural Gas Industry, **3**, 005.

Zhao, W. Z., P. Luo, G. S. Chen, H. Cao, and B. M. Zhang. 2005, Origin and reservoir rock characteristics of dolostones in the Early Triassic Feixianguan Formation, NE Sichuan Basin, China: Significance for future gas exploration: Journal of Petroleum Geology, **28**, no. 1, 83-100.

Zheng, R. C., L. R. Dang, H. G. Wen, Z. W. Chen, F. M. Chen, and H. J. Zhang. 2011, Diagenesis characteristics and system for dolostone in Feixianguan Formation of Northeast Sichuan: Earth Science—Journal of China University of Geosciences, **36**, no. 4, 659-669.

Zoeppritz, K. 1919, On the reflection and propagation of seismic waves at discontinuities: Erdbebenwellen VII B, 66-84.

APPENDIX A

PERMEABILITY-POROSITY REALTIONS

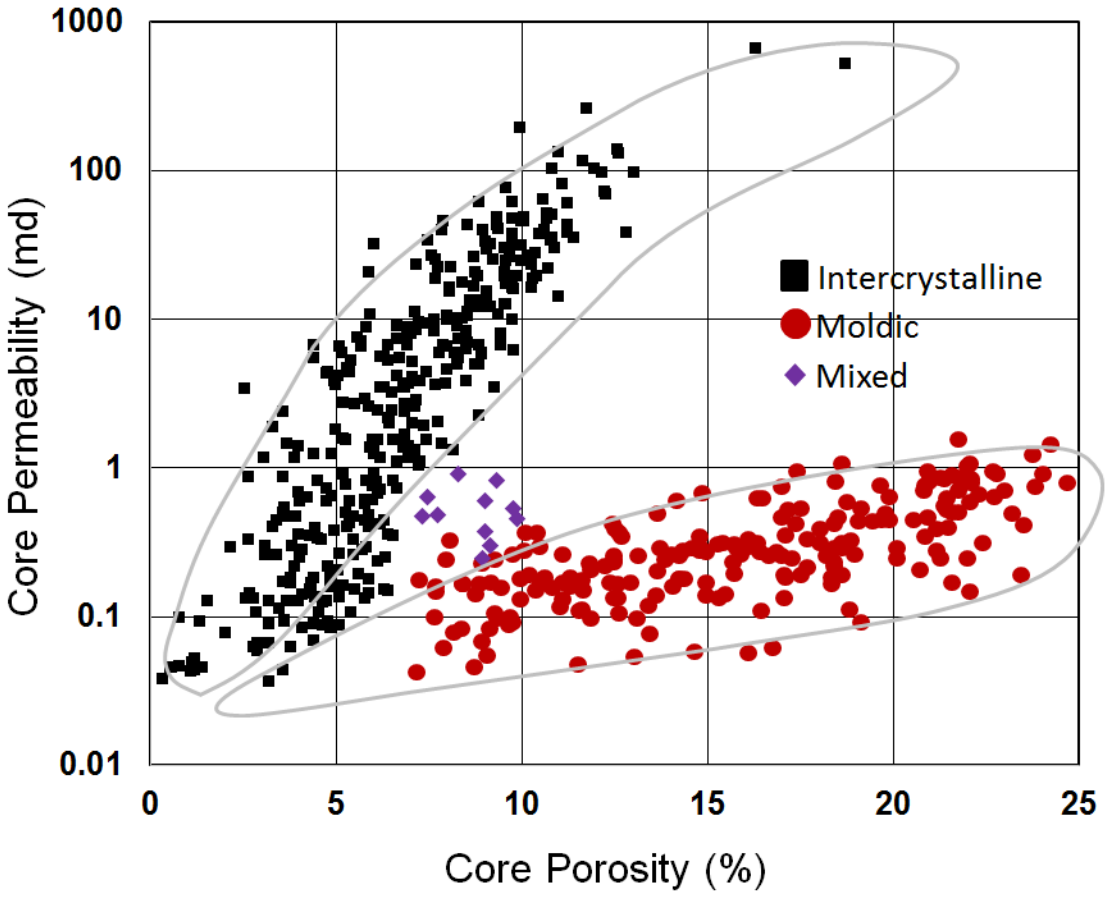

Figure A-1 Crossplot of air permeability and porosity from core measurements of Well 1. Two distinctive permeability trends are highlighted by the circles and will be used to compare this plot with the plots from other wells.

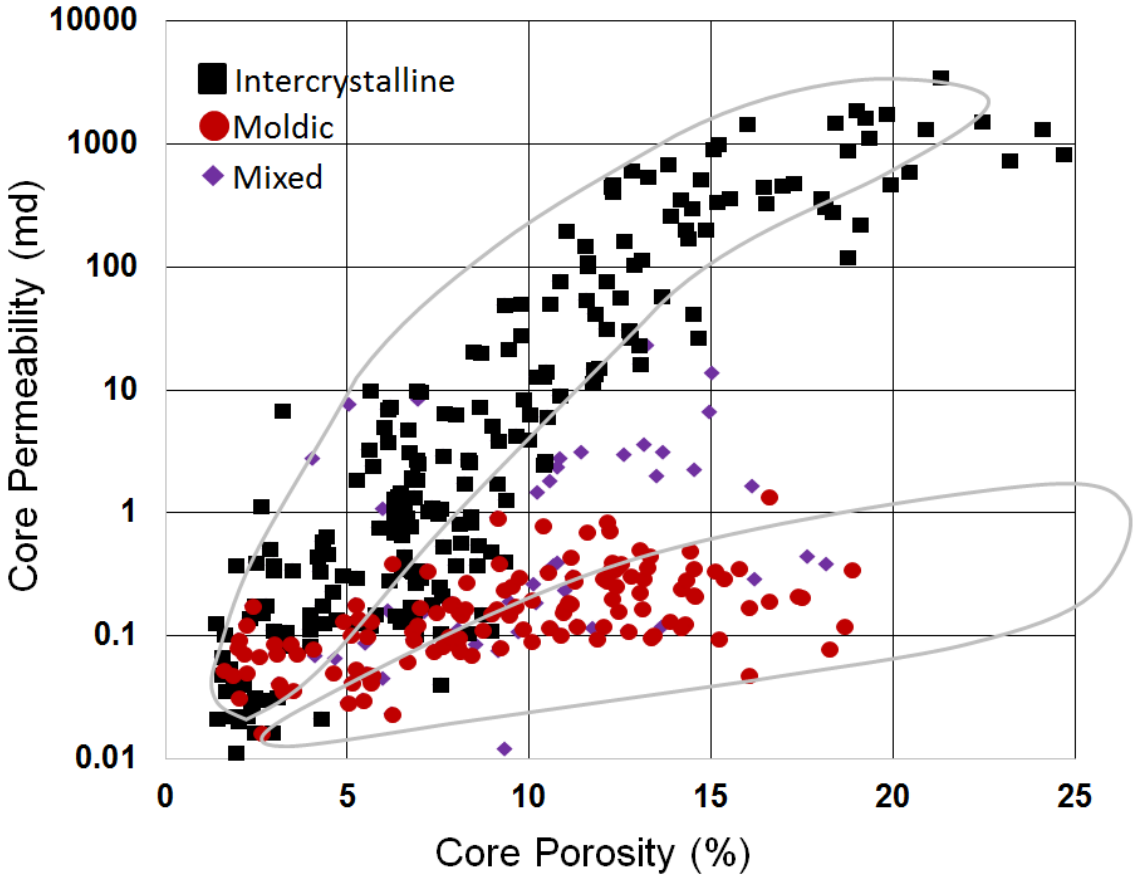

Figure A-2 Crossplot of air permeability and porosity from core measurements of Well 2. The two oval shaped circles are highlighting the permeability trends observed from Well 1.

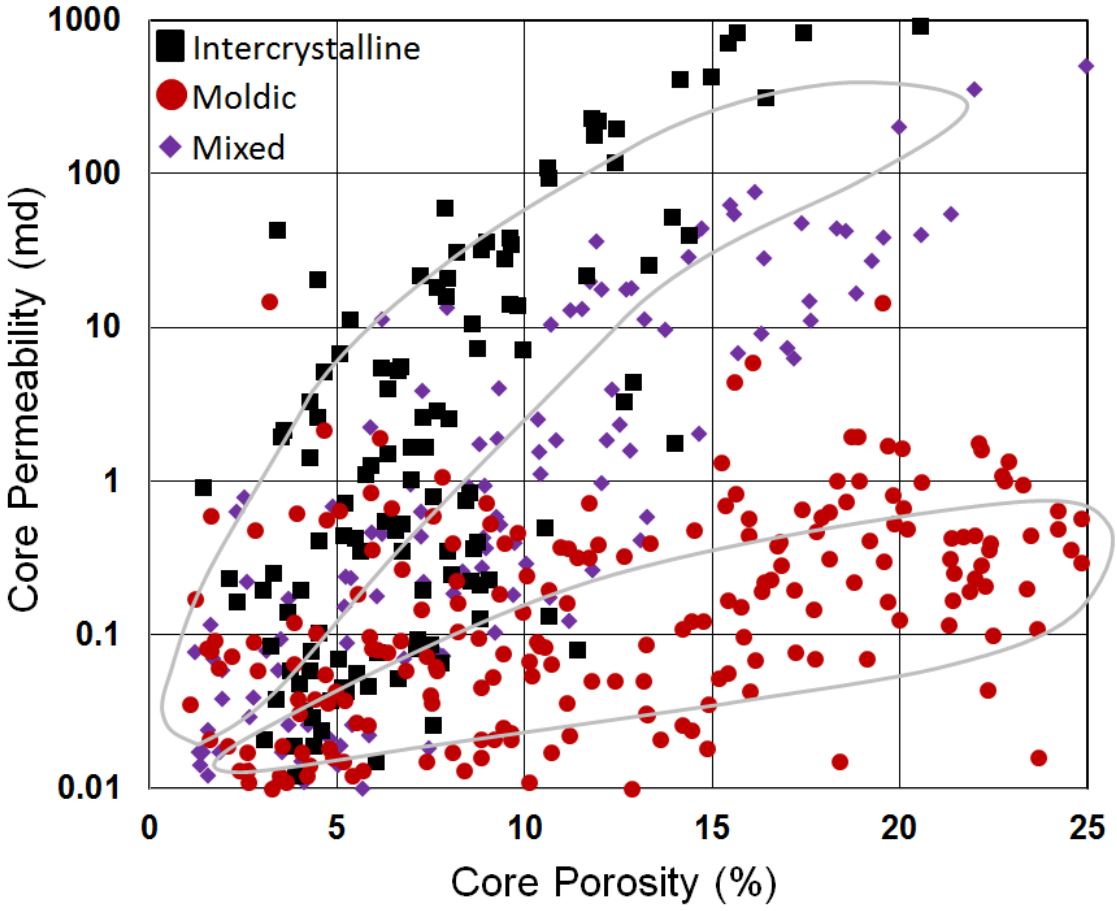

Figure A-3 Crossplot of air permeability and porosity from core measurements of Well3. The two oval shaped circles are highlighting the permeability trends observed from Well 1.

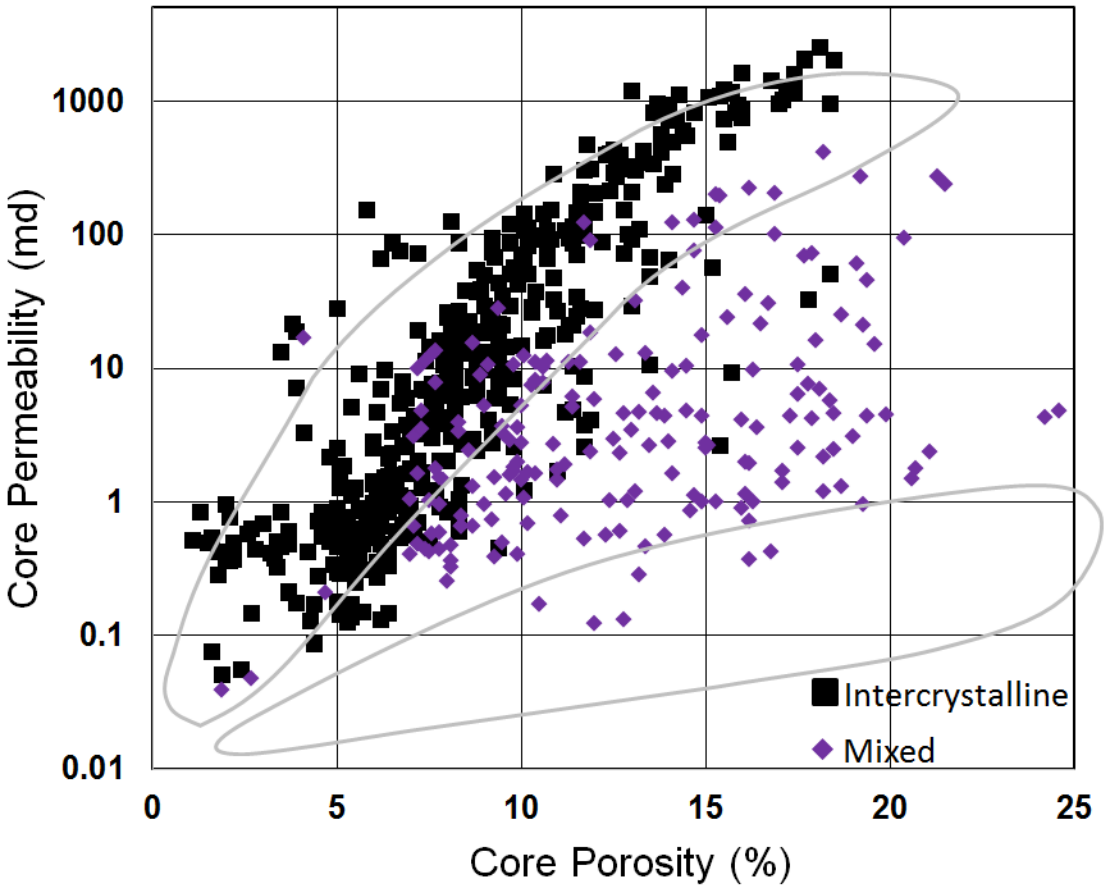

Figure A-3 Crossplot of air permeability and porosity from core measurements of Well4. The two oval shaped circles are highlighting the permeability trends observed from Well 1.

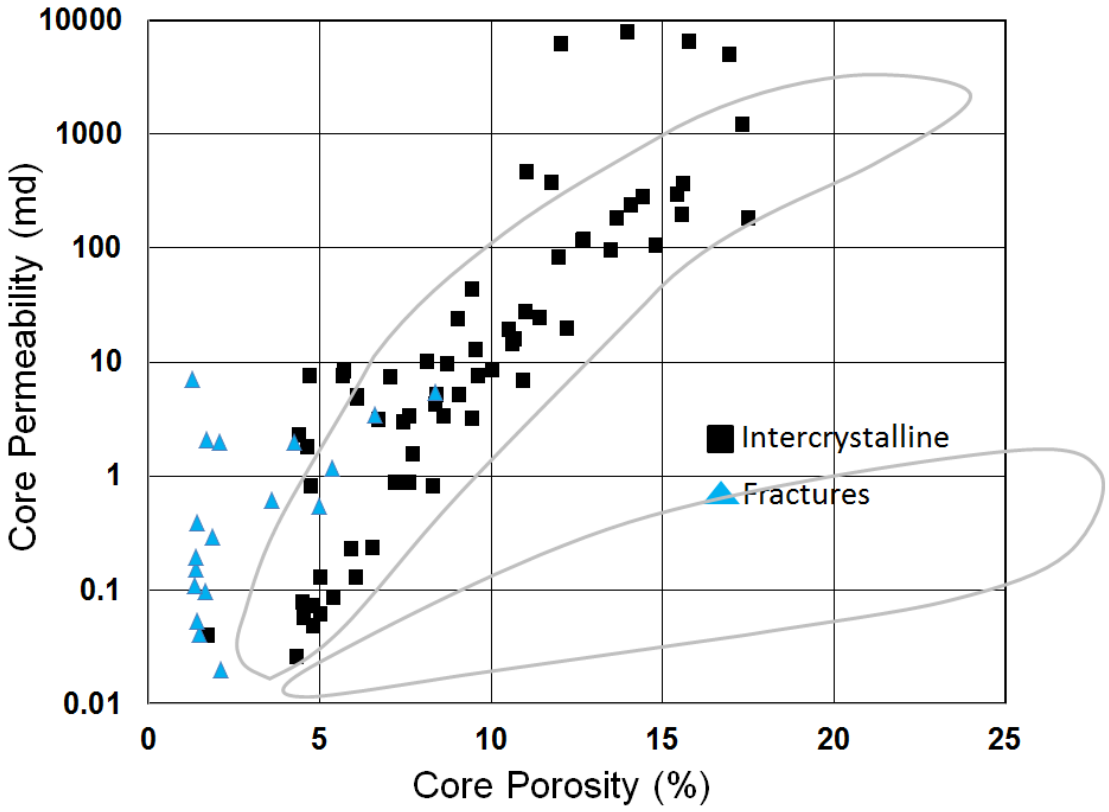

Figure A-4 Crossplot of air permeability and porosity from core measurements for one of the other wells with core data.

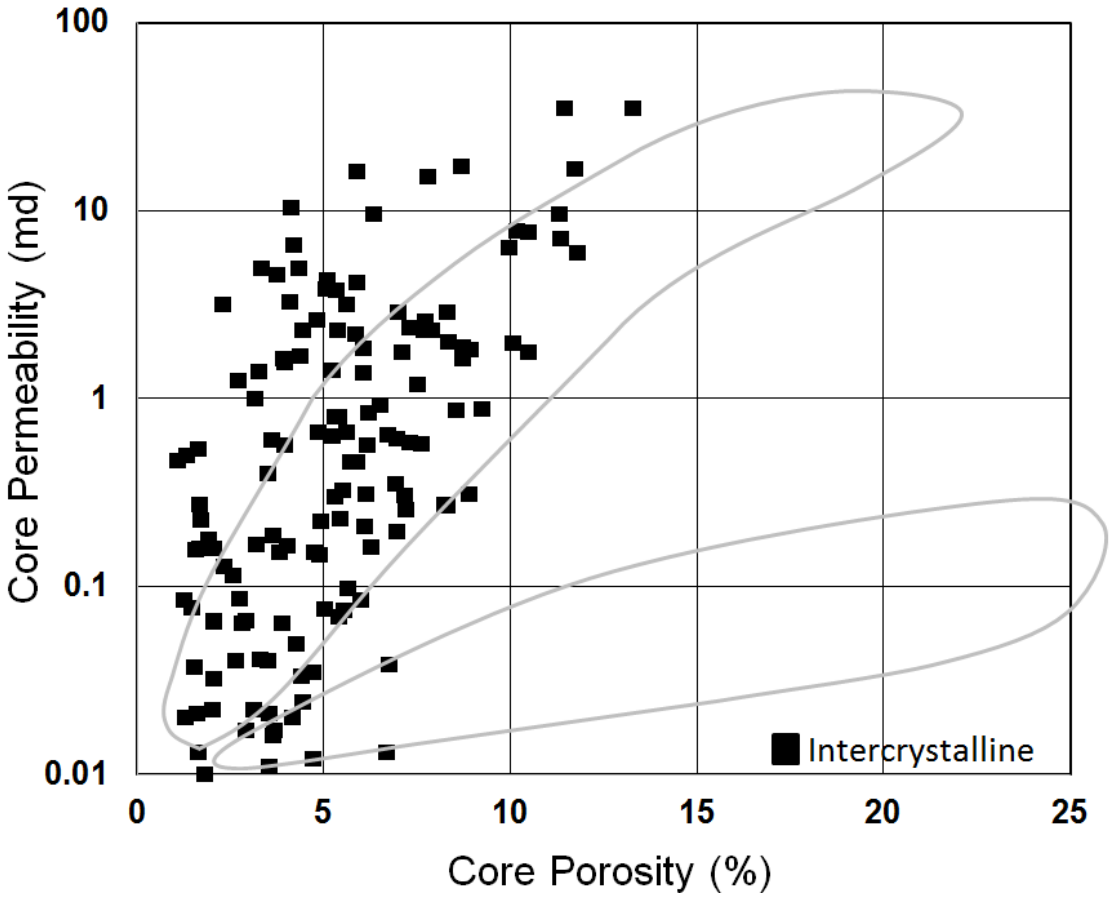

Figure A-5 Crossplot of air permeability and porosity from core measurements for one of the other wells with core data.

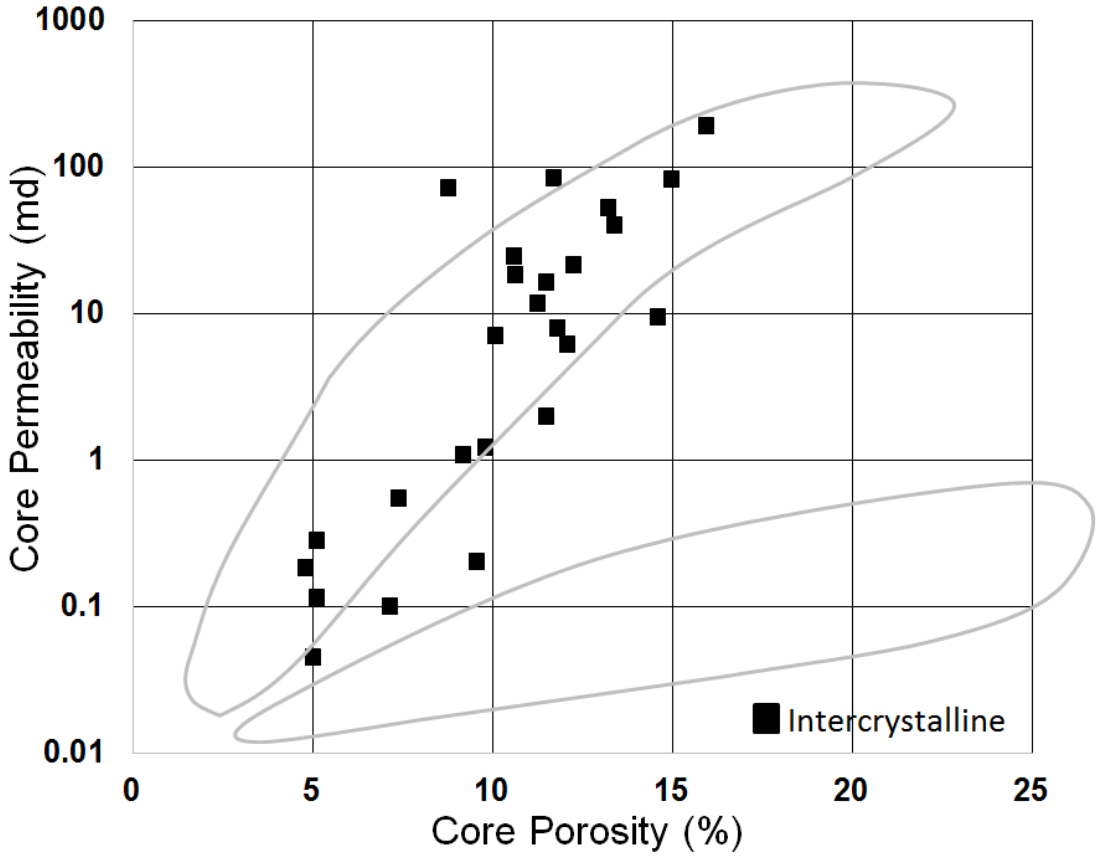

Figure A-6 Crossplot of air permeability and porosity from core measurements for one of the other wells with core data.

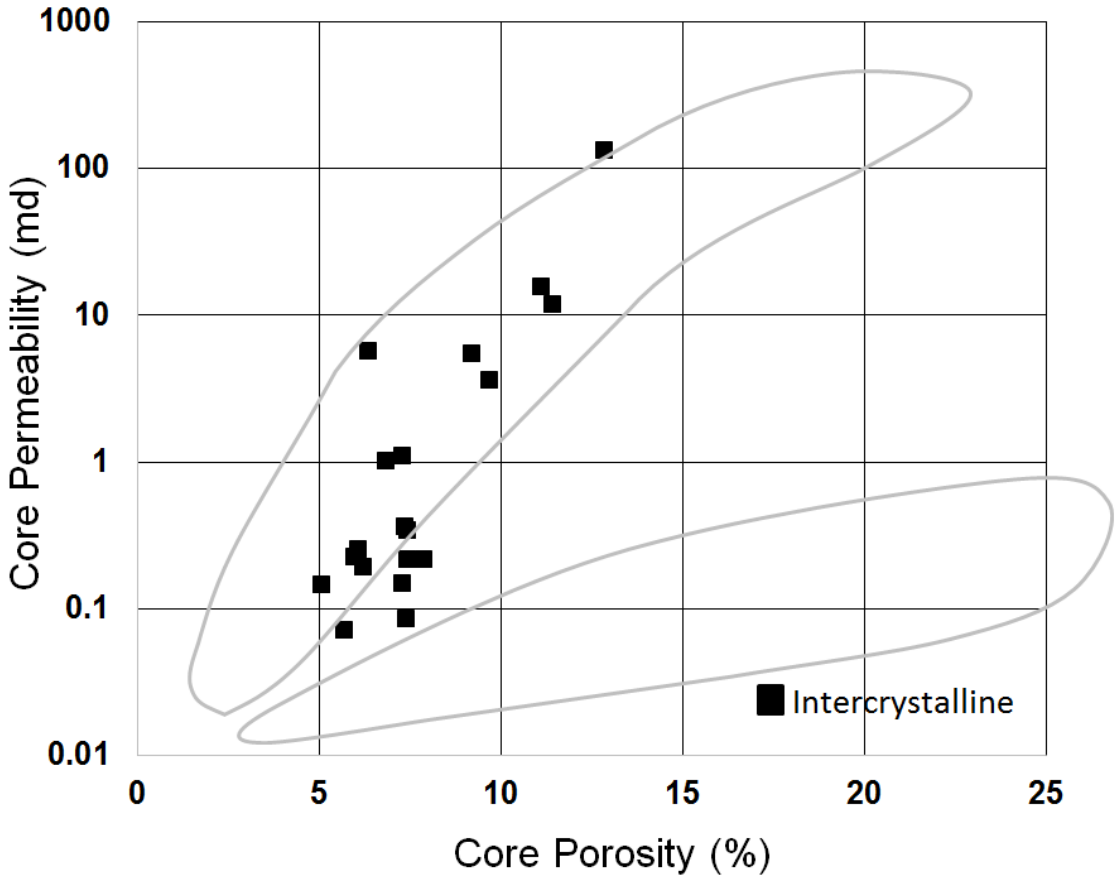

Figure A-7 Crossplot of air permeability and porosity from core measurements for one of the other wells with core data.

APPENDIX B

J-FUNCTION DATA FOR PORE TYPE CLASSIFICATION

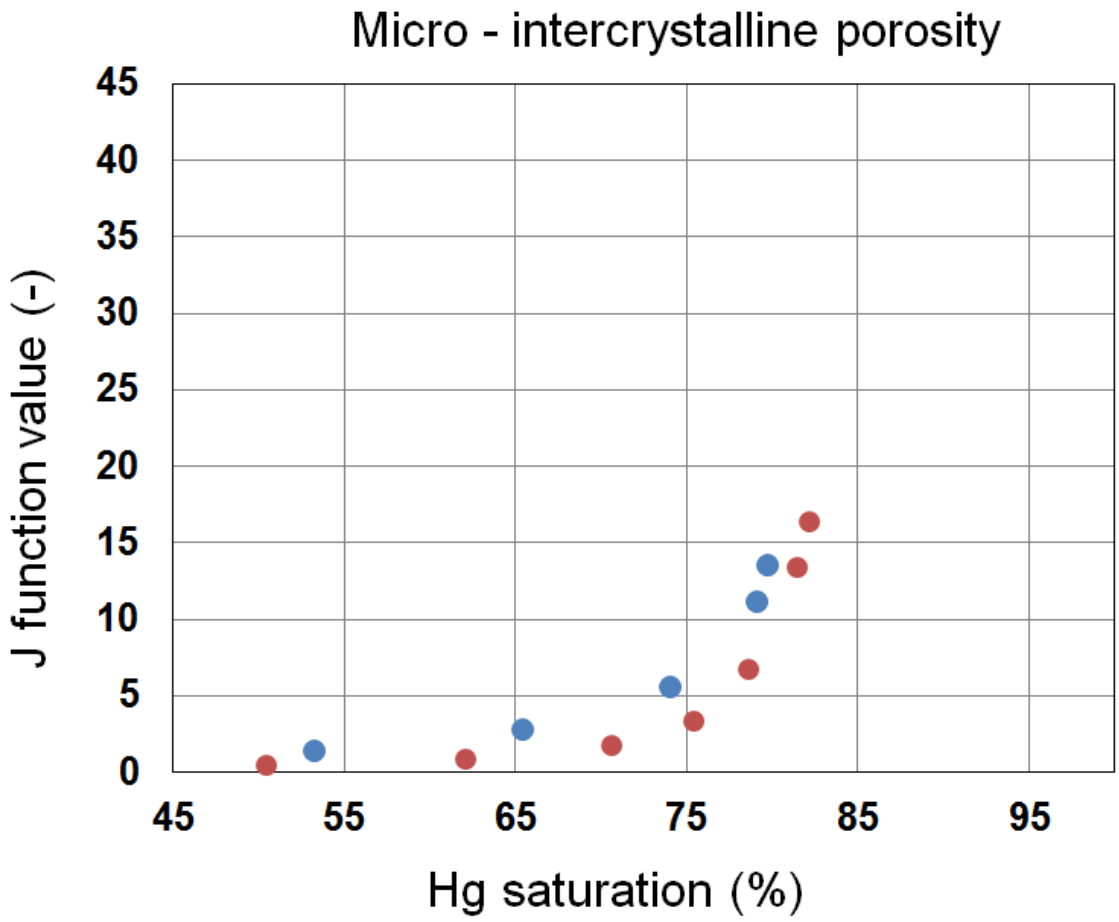

Figure A-8 Statistical data of J Function values for rock dominated by micro-intercrystalline porosity. This plot is related to Figure 2. 3.

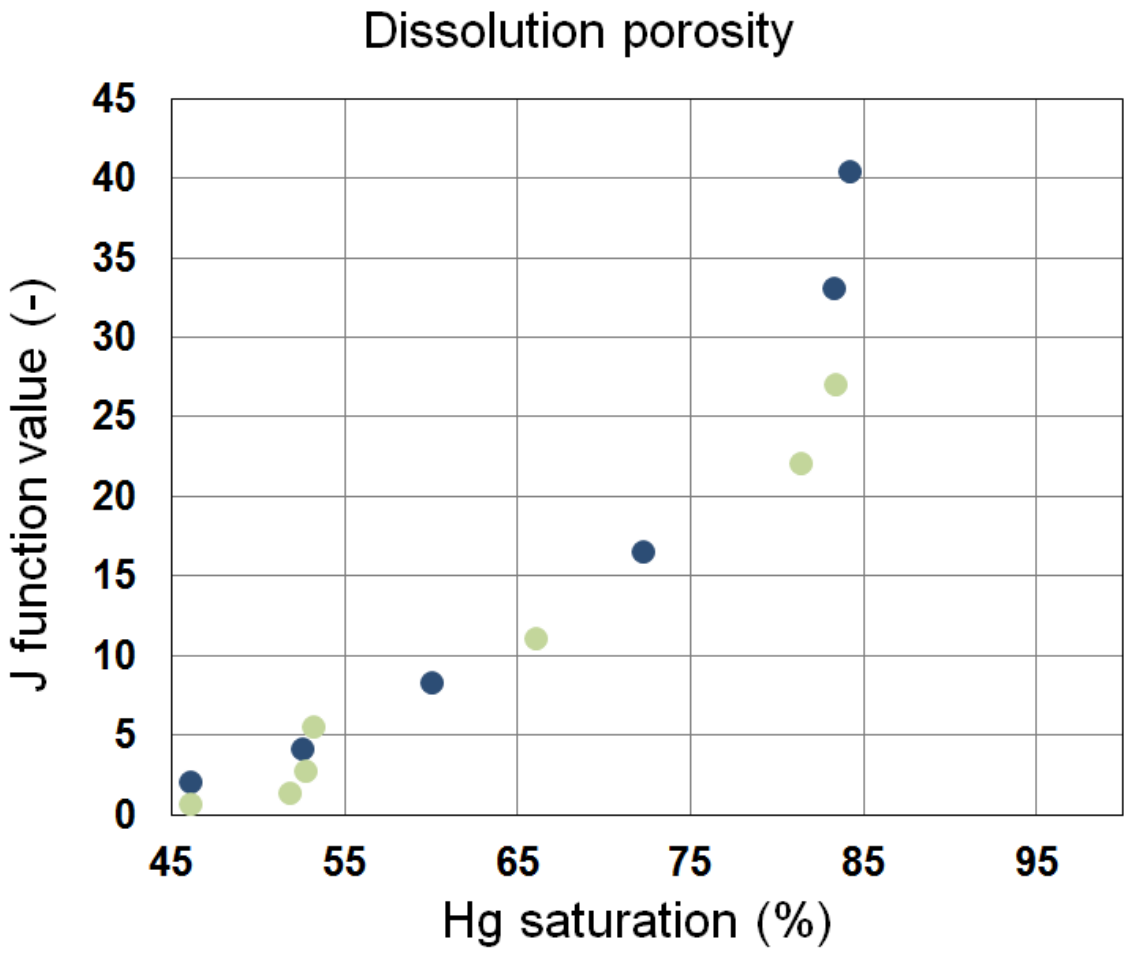

Figure A-9 Statistical data of J Function values for rock dominated by dissolution vugs. This plot is related to Figure 2. 3.

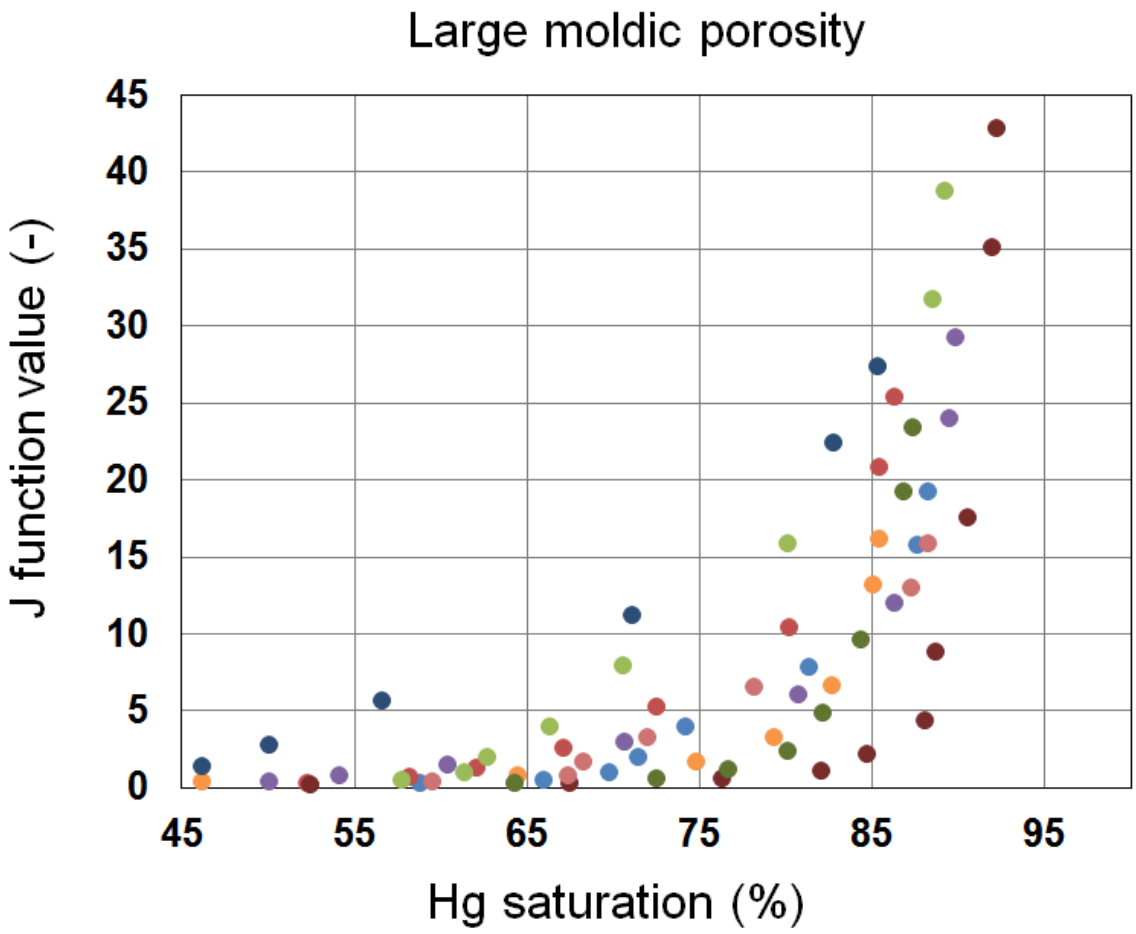

Figure A-10 Statistical data of J Function values for rock dominated by large moldic porosity. This plot is related to Figure 2. 3 and Figure 2. 4.

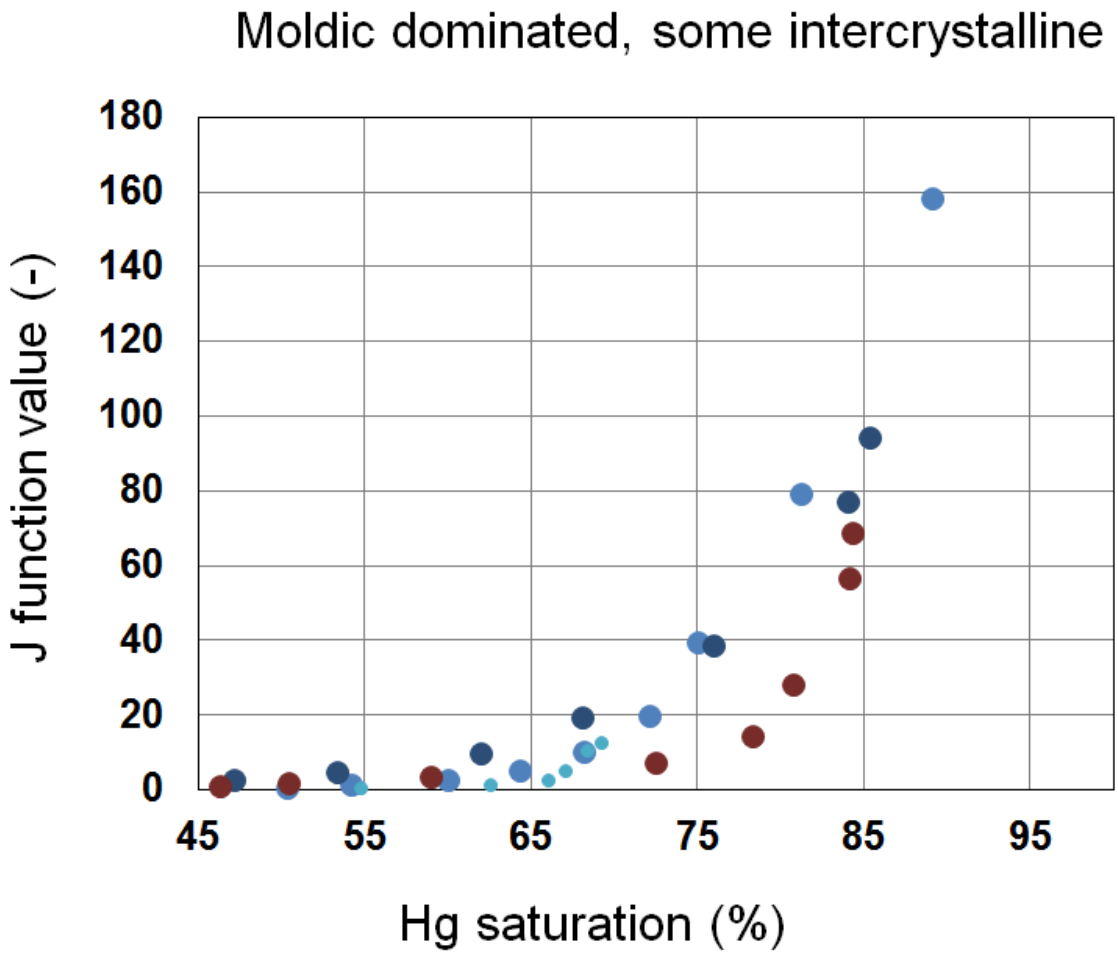

Figure A-11 Statistical data of J Function values for rock dominated by moldic porosity, with a mixture of some intercrystalline porosity. This plot is related to Figure 2. 3 and Figure 2. 4.

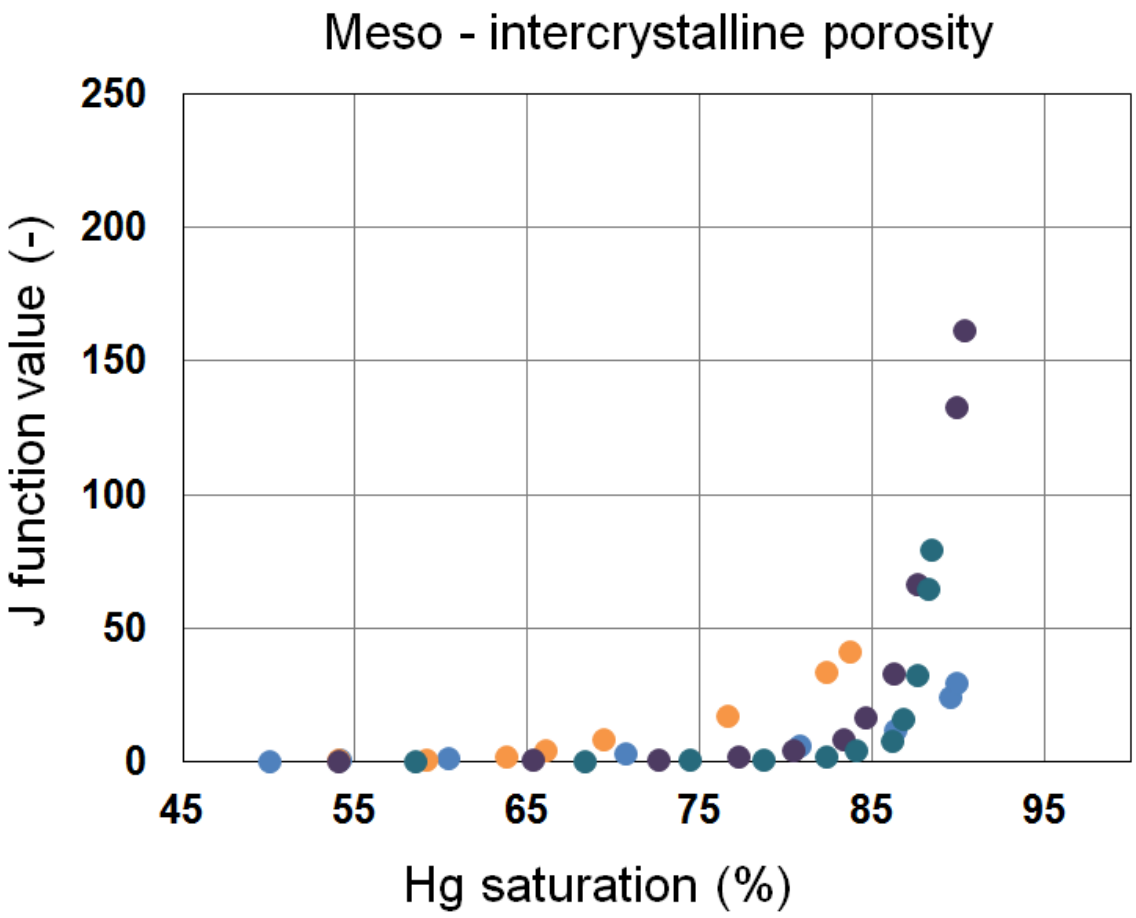

Figure A-12 Statistical data of J Function values for rock dominated by meso-intercrystalline porosity. This plot is related to Figure 2. 3 and Figure 2. 4.

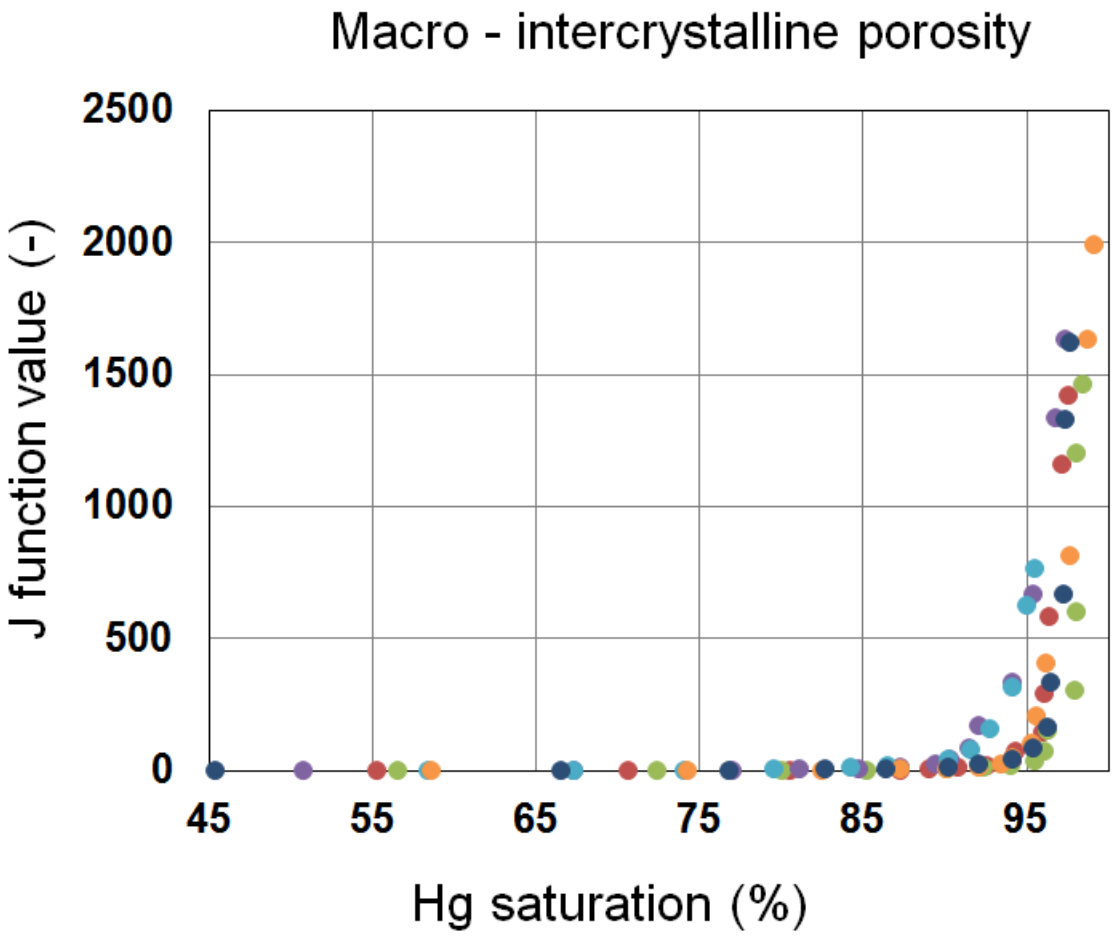

Figure A-13 Statistical data of J Function values for rock dominated by macro-intercrystalline porosity. This plot is related to Figure 2. 3 and Figure 2. 4.

APPENDIX C

COMPARSION OF RESERVOIR PROPERTIES

Table 1 Statistic information on core measured porosity and permeability for Well 1, to compare the permeability heterogeneity controlled by sea level fluctuations and sedimentary facies.

Well 1		**Core Porosity（%）**			**Horizontal Permeability（$\times10^{-3}\mu m^2$）**		
		Mean	**Maximum**	**Minimum**	**Mean**	**Maximum**	**Minimum**
Fourth-order subdivision	Ⅳ	0.99	1.56	0.32	0.05	0.13	0.037
	Ⅲ	7.07	18.71	0.78	16.99	647.71	0.062
	Ⅱ	15.35	28.84	1.98	0.64	29.8	0.046
	Ⅰ	6.38	11.02	1.36	0.27	1.09	0.036
Second-order Sequence	TST	0.96	1.56	0.32	0.072	0.13	0.037
	HST	10.06	28.84	0.78	10.51	647.71	0.036
Sedimentary Facies	Restricted Platform	8.35	17.04	3.4	20.44	259.62	0.148
	Marginal Ooid Shoal	10.32	28.84	0.78	8.95	647.71	0.036
	Open Marine Shelf	0.99	1.56	0.32	0.05	0.13	0.037

Table 2 Statistic information on core measured porosity and permeability for Well 2, to compare the permeability heterogeneity controlled by sea level fluctuations and sedimentary facies.

Well 2		**Core Porosity（%）**			**Horizontal Permeability（$\times10^{-3}\mu m^2$）**		
		Mean	**Maximum**	**Minimum**	**Mean**	**Maximum**	**Minimum**
Fourth-order subdivision	Ⅶ	2.71	9.46	1.04	0.39	11.89	0.012
	Ⅵ	3.68	8.38	1.38	1.06	16.72	0.011
	Ⅴ	7.88	18.2	1.56	4.91	86.35	0.012
	Ⅳ	7.02	13.65	3.53	1.514	32.34	0.044
	Ⅲ	12.02	28.86	4	406.66	3354.7	0.038
	Ⅱ	10.58	24.7	1.43	15.22	551.94	0.047
	Ⅰ	2.36	3.51	1.85	0.052	0.079	0.031
Second-order Sequence	TST	2.717	9.46	1.04	4.09	11.89	0.012
	HST	9.09	28.86	1.38	113.27	3354.69	0.011
Sedimentary Facies	Restricted Platform	3.47	15.02	1.04	0.85	22.58	0.011
	Marginal Ooid Shoal	8.59	28.86	1.38	248.43	3354.69	0.011

Table 3 Statistic information on core measured porosity and permeability for Well 3, to compare the permeability heterogeneity controlled by sea level fluctuations and sedimentary facies.

Well 3		**Core Porosity（%）**			**Horizontal Permeability（$\times 10^{-3}\mu m^2$）**		
		Mean	**Maximum**	**Minimum**	**Mean**	**Maximum**	**Minimum**
Fourth-order subdivision	Ⅴ	6.69	24.78	0.56	2.94	89	0.001
	Ⅳ	11.79	28.66	0.84	11.46	913	0.001
	Ⅲ	7.48	15.43	2.33	32.69	707	0.005
Second-order Sequence	TST	6.59	20.68	0.84	14.67	327	0.001
	HST	9.41	28.66	0.56	11.19	913	0.001
Sedimentary Facies	Restricted Platform	7.34	20.68	0.56	15.69	327	0.001
	Marginal Ooid Shoal	9.37	20.68	0.84	113.89	327	0.001
	Open Marine Shelf	1.77	11.65	0.84	1.16	6.95	0.001

Table 4 Statistic information on core measured porosity and permeability for Well 4, to compare the permeability heterogeneity controlled by sea level fluctuations and sedimentary facies.

Well 4		**Core Porosity（%）**			**Horizontal Permeability（$\times 10^{-3}\mu m^2$）**		
		Mean	**Maximum**	**Minimum**	**Mean**	**Maximum**	**Minimum**
Fourth-order subdivision	Ⅴ	7.16	22.2	1.1	12.75	904	0.203
	Ⅳ	11.17	25.8	1.8	40.11	1389	0.129
	Ⅲ	10.09	21.5	1.6	146.97	2526	0.039
Second-order Sequence	HST	9.81	25.8	1.1	85.43	2526	0.039
Sedimentary Facies	Marginal Ooid Shoal	9.81	25.8	1.1	85.43	2526	0.039

Table 5 Statistic information on core measured porosity and permeability for all four wells, to compare the permeability heterogeneity controlled by sea level fluctuations and sedimentary facies.

All four wells		**Core Porosity（%）**			**Horizontal Permeability（$\times10^{-3}\mu m^2$）**		
		Mean	**Maximum**	**Minimum**	**Mean**	**Maximum**	**Minimum**
Fourth-order subdivision	Ⅶ	2.85	10.83	1.04	0.76	31.01	0.012
	Ⅵ	3.68	8.38	1.38	1.06	16.72	0.011
	Ⅴ	7.01	24.78	0.32	6.15	904	0.001
	Ⅳ	11.08	28.66	0.84	20.61	1389	0.001
	Ⅲ	9.01	28.86	0.78	128.71	3354.7	0.005
	Ⅱ	13.66	28.84	1.43	5.82	551.94	0.047
	Ⅰ	5.48	11.02	1.36	0.225	1.09	0.031
Second-order Sequence	TST	2.52	9.46	0.32	0.35	11.89	0.012
	HST	9.62	28.86	0.56	52.94	3354.69	0.001
Sedimentary Facies	Restricted Platform	5.33	20.68	0.56	7.98	327	0.001
	Marginal Ooid Shoal	9.81	28.86	0.78	55.6	3354.69	0001
	Open Marine Shelf	1.53	11.65	0.32	0.82	6.95	0.001

APPENDIX D

ELASTIC PROPERTIES

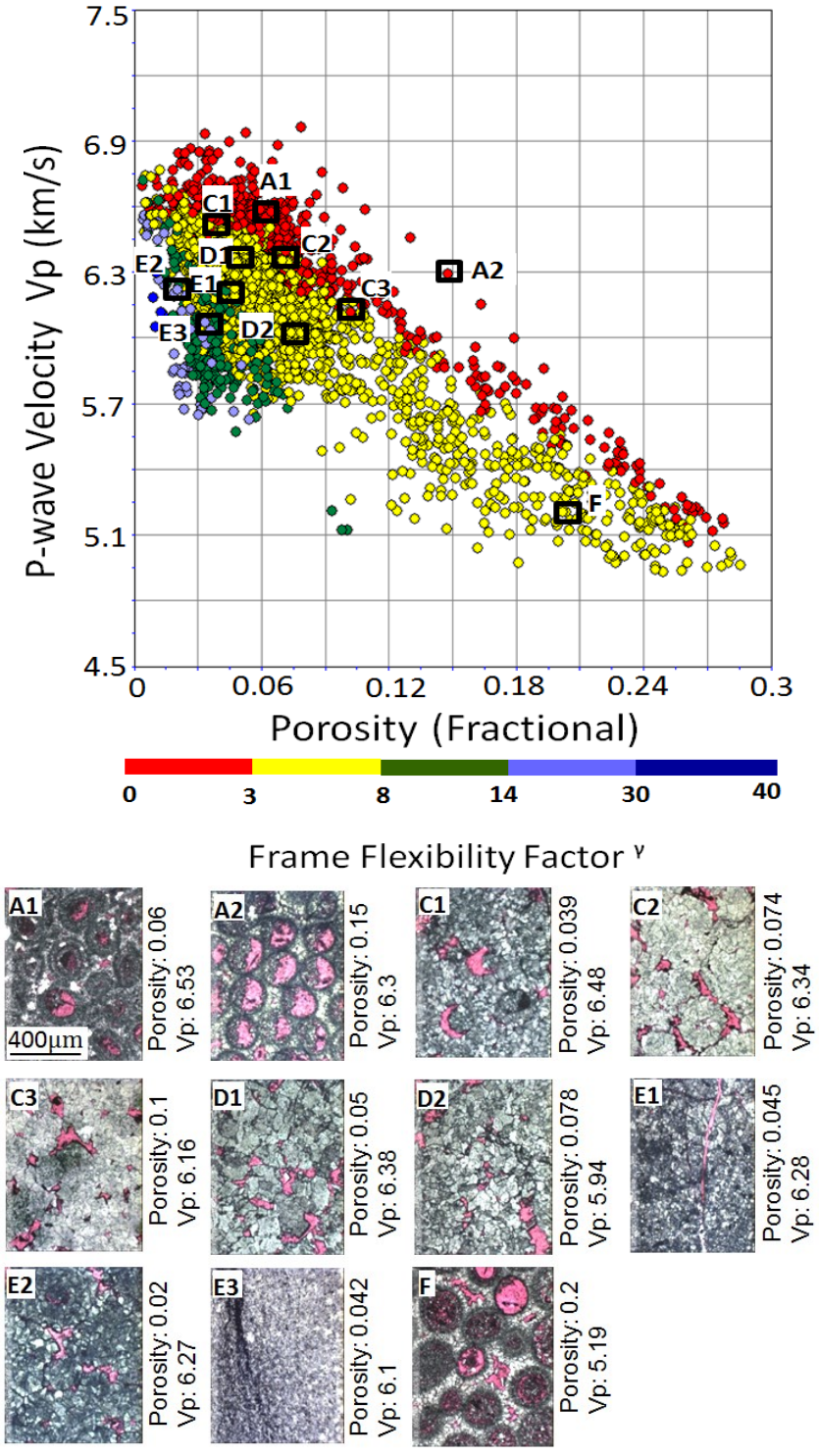

Figure A-14 Crossplot of P-wave velocity against porosity for Well 1, colored by Frame Flexibility Factor ϒ. The cast sections of the selected samples are also shown, with the red color indicating porosity. The scales for the thin sections are the same.

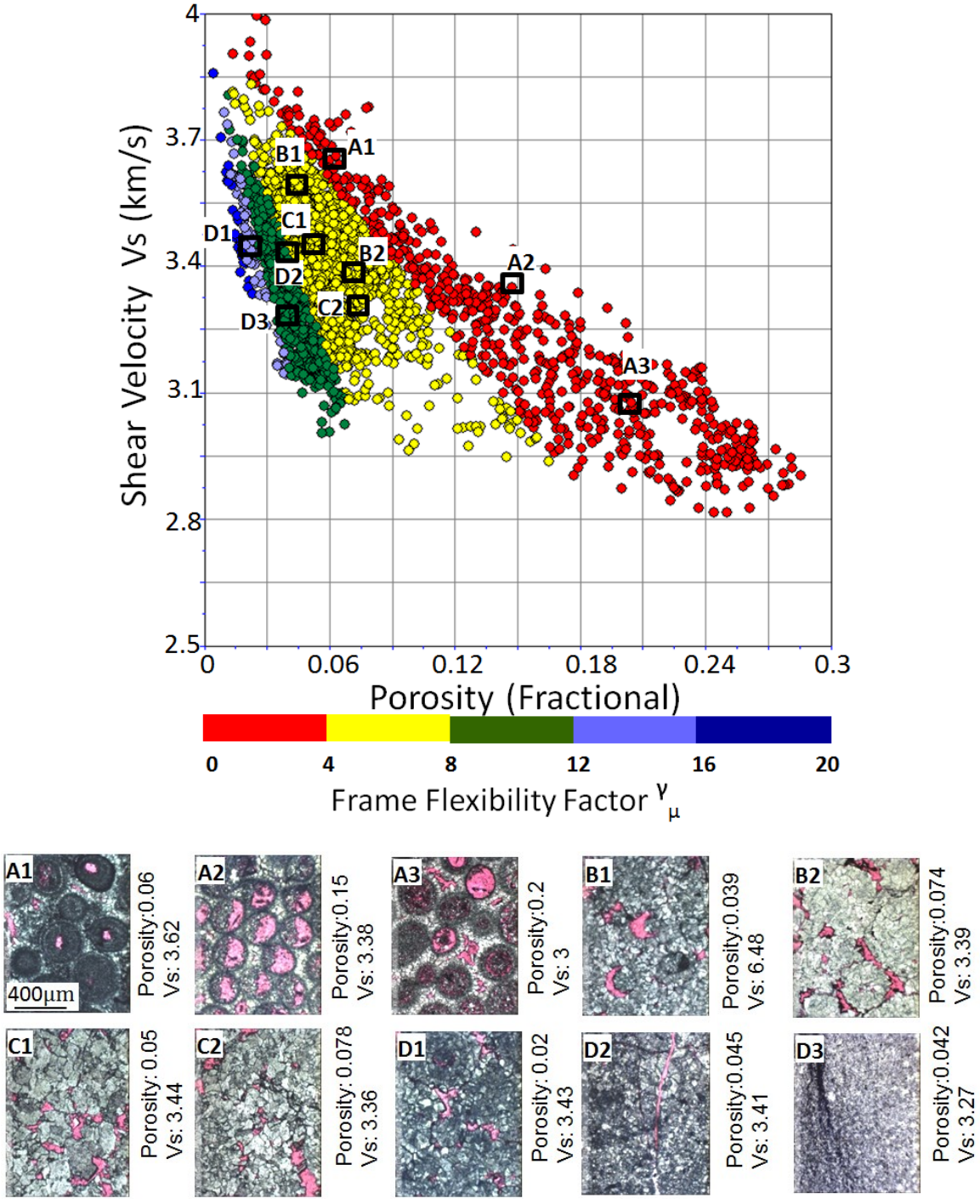

Figure A-15 Crossplot of shear wave velocity against porosity for Well 1, colored by Frame Flexibility Factor Υμ. The cast sections of the selected samples are also shown, with the red color indicating porosity. The scales for the thin sections are the same.

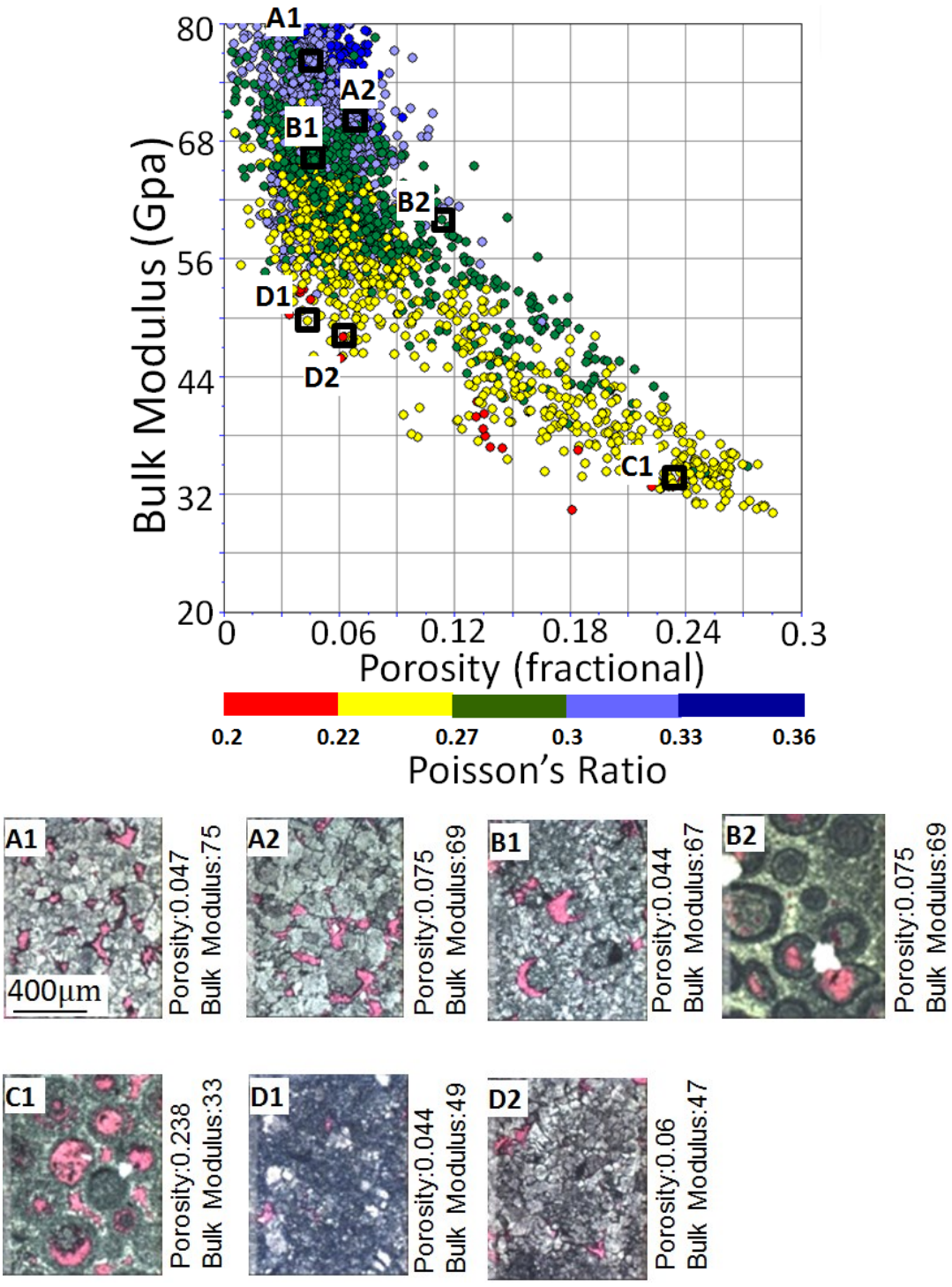

Figure A-16 Crossplot of bulk modulus against porosity for Well 1, colored by Poisson's Ratio. The cast sections of the selected samples are also shown, with the red color indicating porosity. The scales for the thin sections are the same.

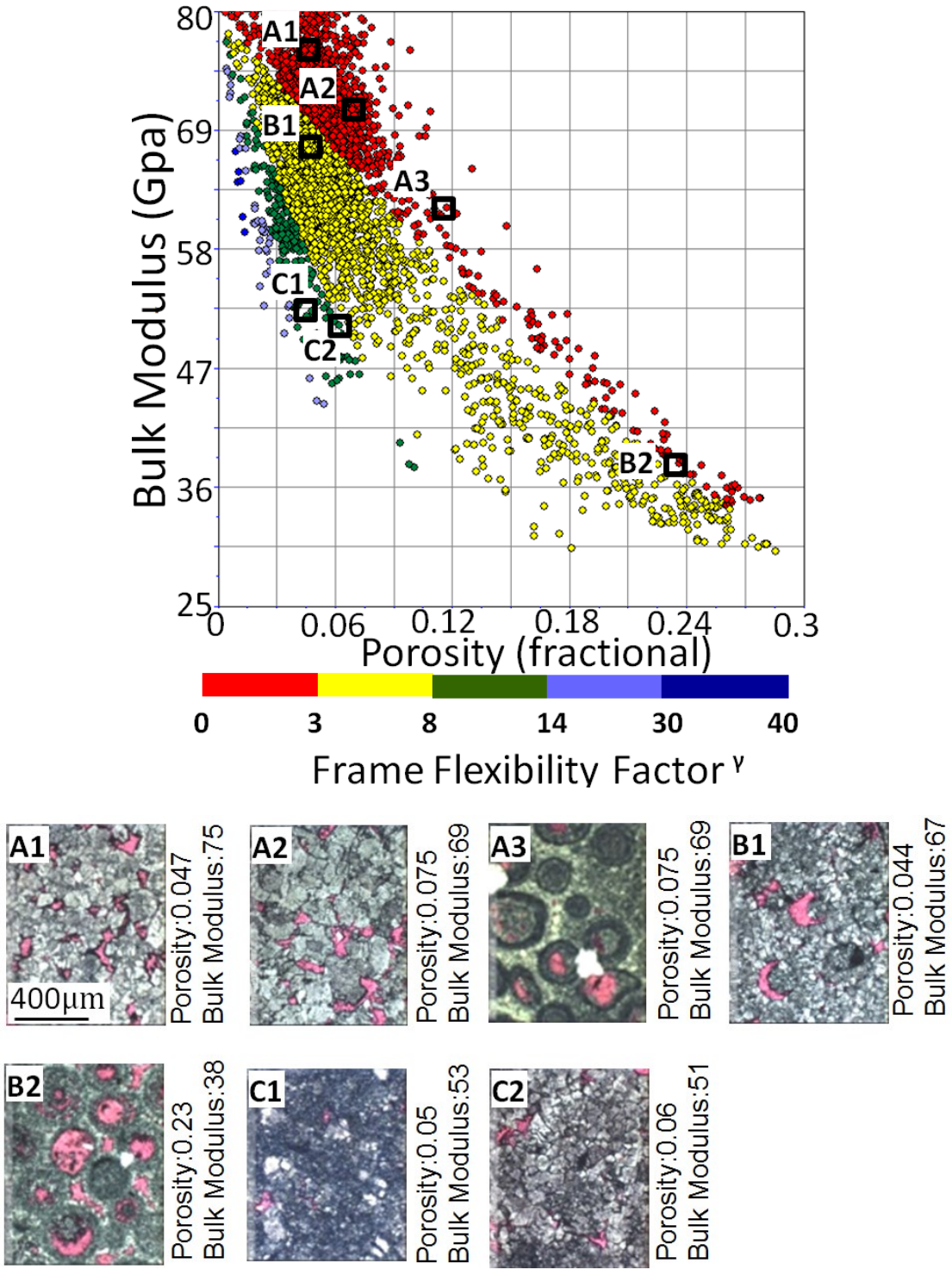

Figure A-17 Crossplot of bulk modulus against porosity for Well 1, colored by Frame Flexibility Factor ϒ. The cast sections of the selected samples are also shown, with the red color indicating porosity. The scales for the thin sections are the same.

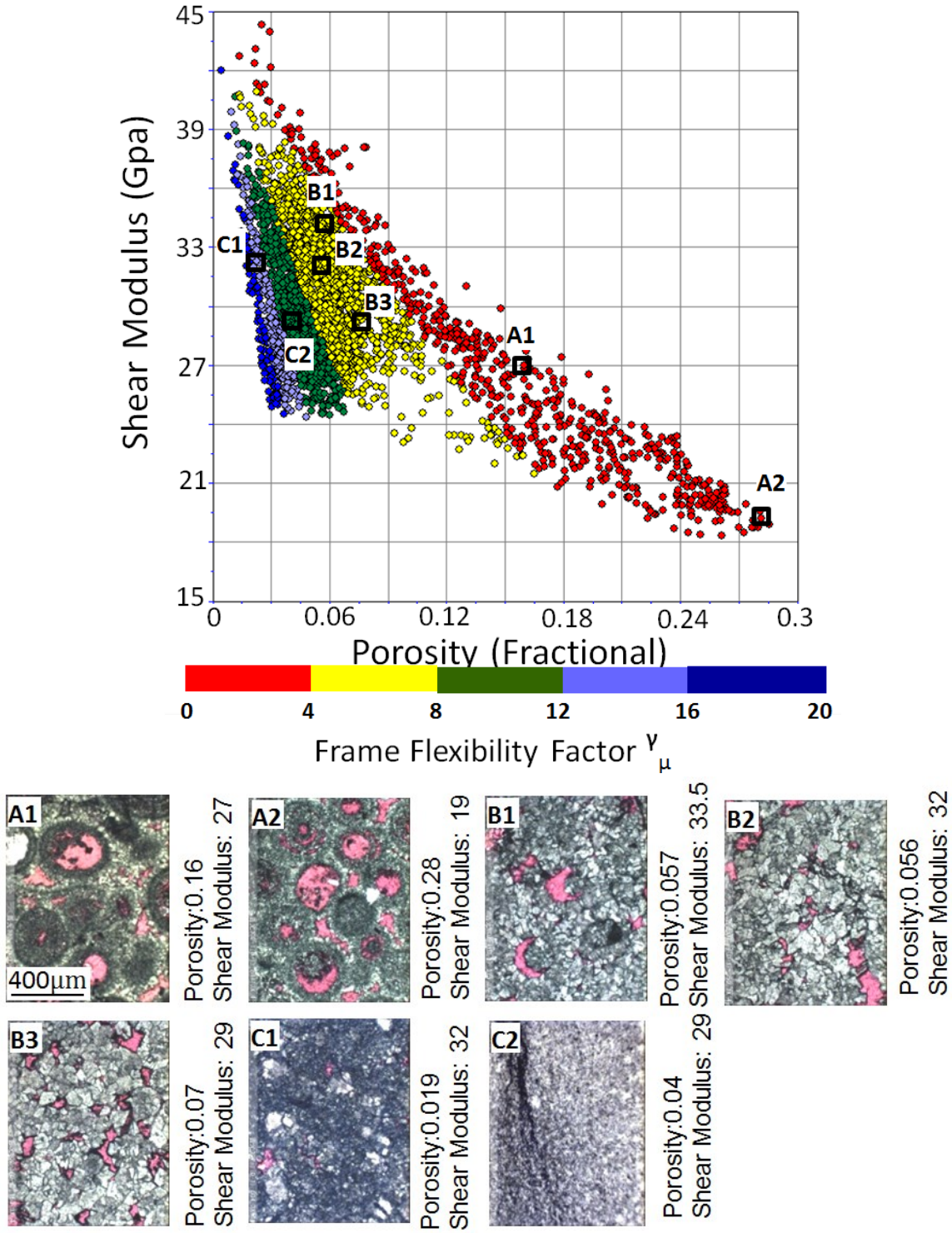

Figure A-18 Crossplot of shear modulus against porosity for Well 1, colored by Frame Flexibility Factor Ɣμ. The cast sections of the selected samples are also shown, with the red color indicating porosity. The scales for the thin sections are the same.

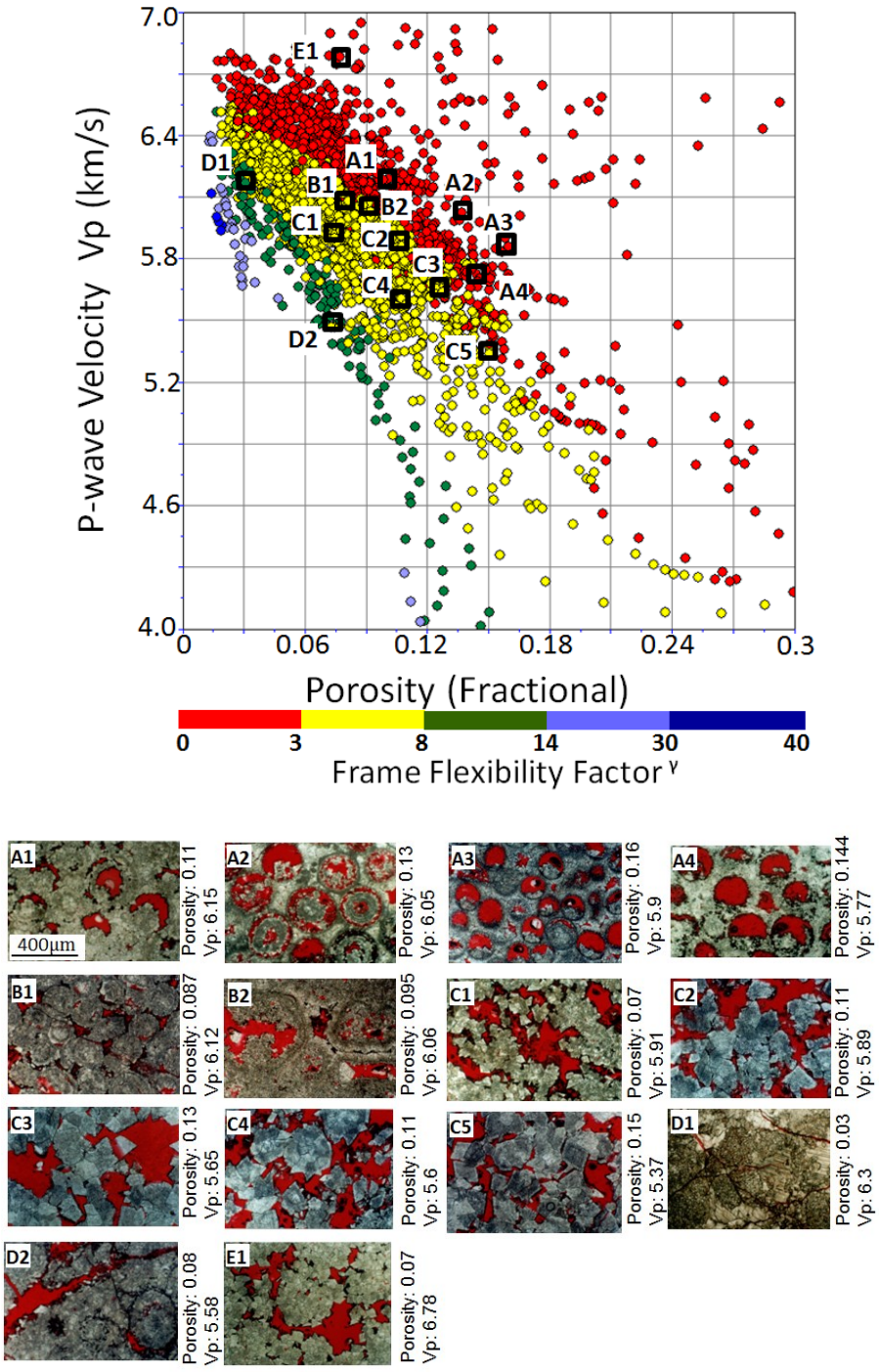

Figure A-19 Crossplot of P-wave velocity against porosity for Well 2, colored by Frame Flexibility Factor ϒ. The cast sections of the selected samples are also shown, with the red color indicating porosity. The scales for the thin sections are the same.

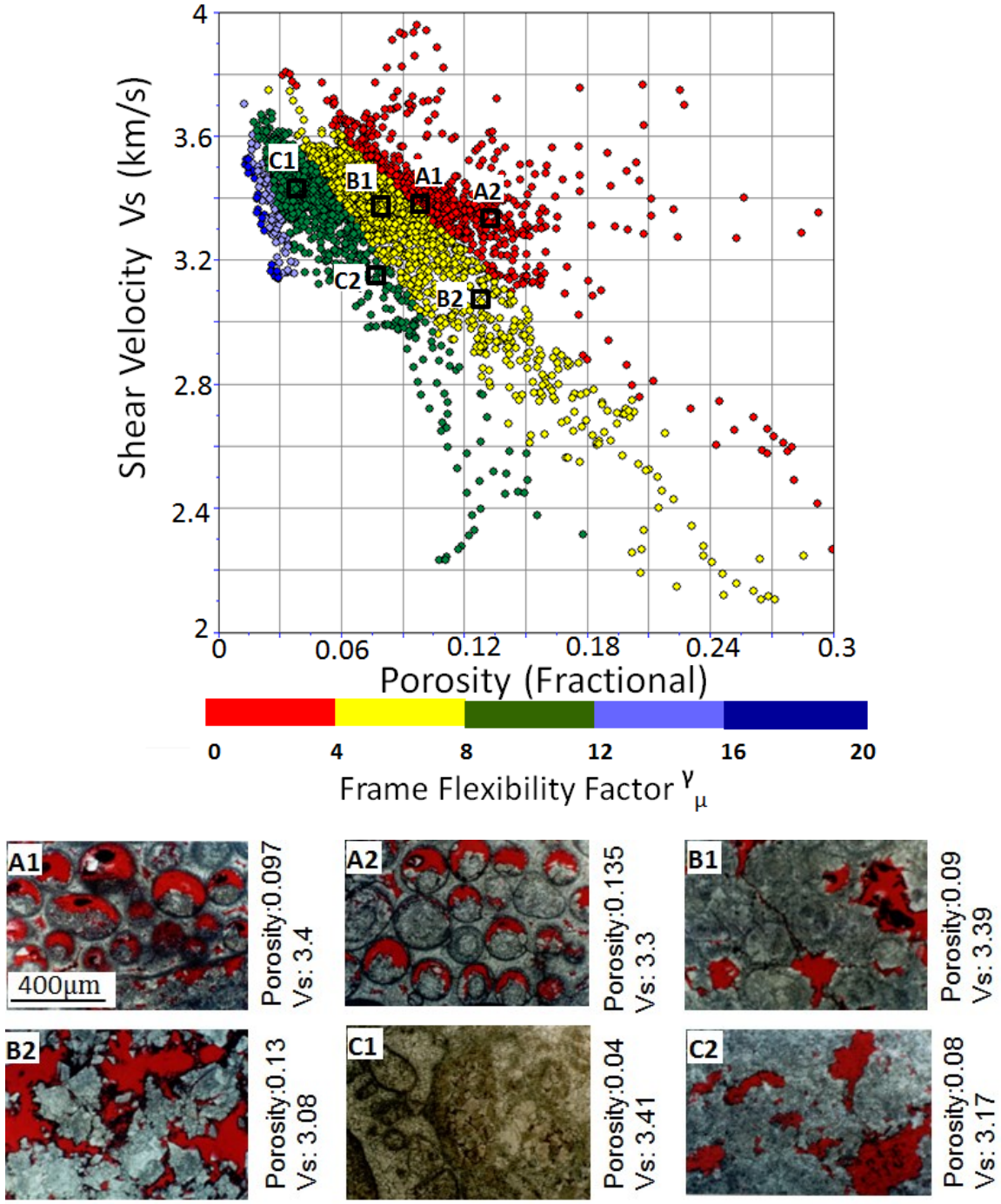

Figure A-20 Crossplot of shear wave velocity against porosity for Well 2, colored by Frame Flexibility Factor Υμ. The cast sections of the selected samples are also shown, with the red color indicating porosity. The scales for the thin sections are the same.

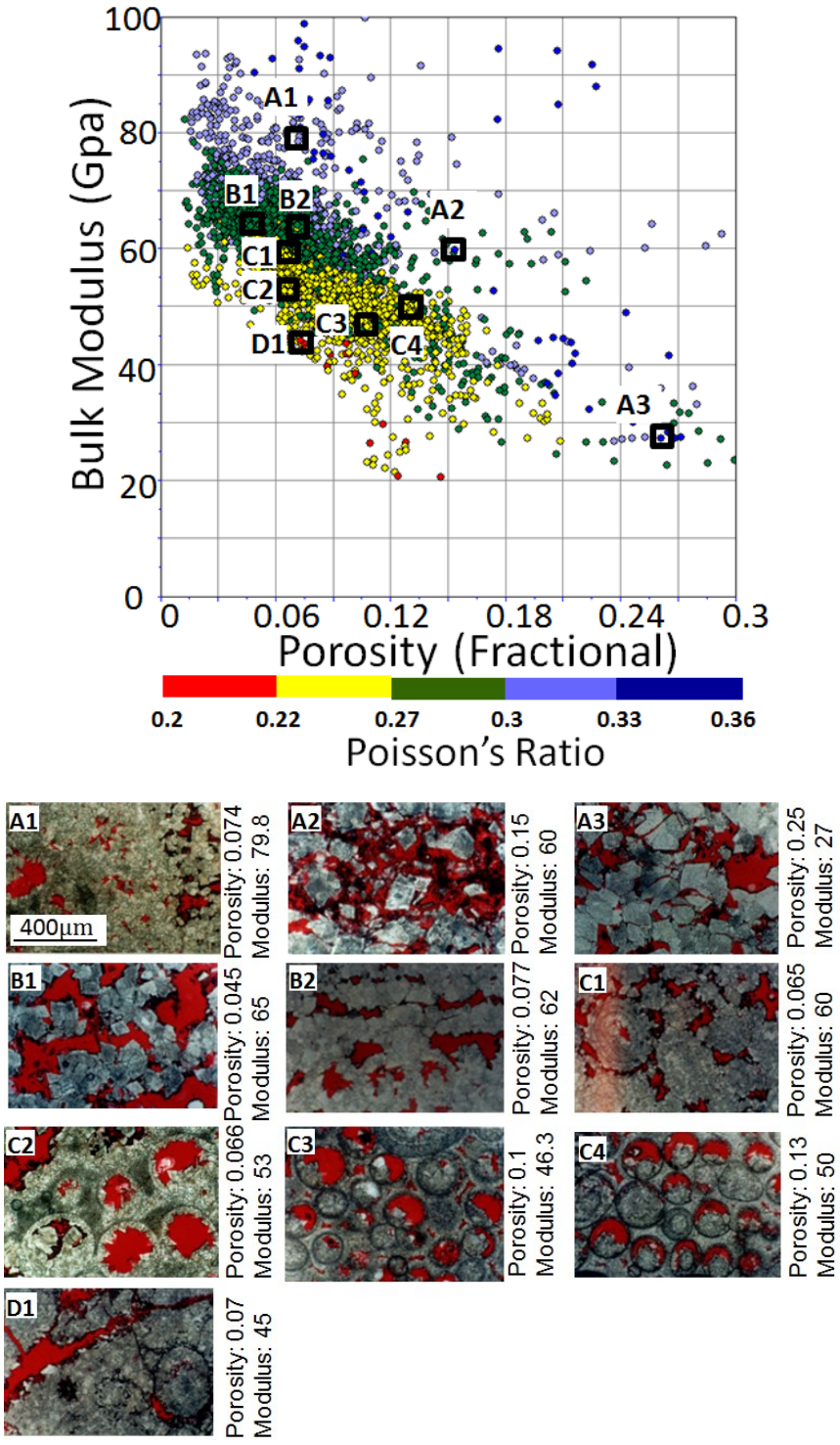

Figure A-21 Crossplot of bulk modulus against porosity for Well 2, colored by Poisson's Ratio. The cast sections of the selected samples are also shown, with the red color indicating porosity. The scales for the thin sections are the same.

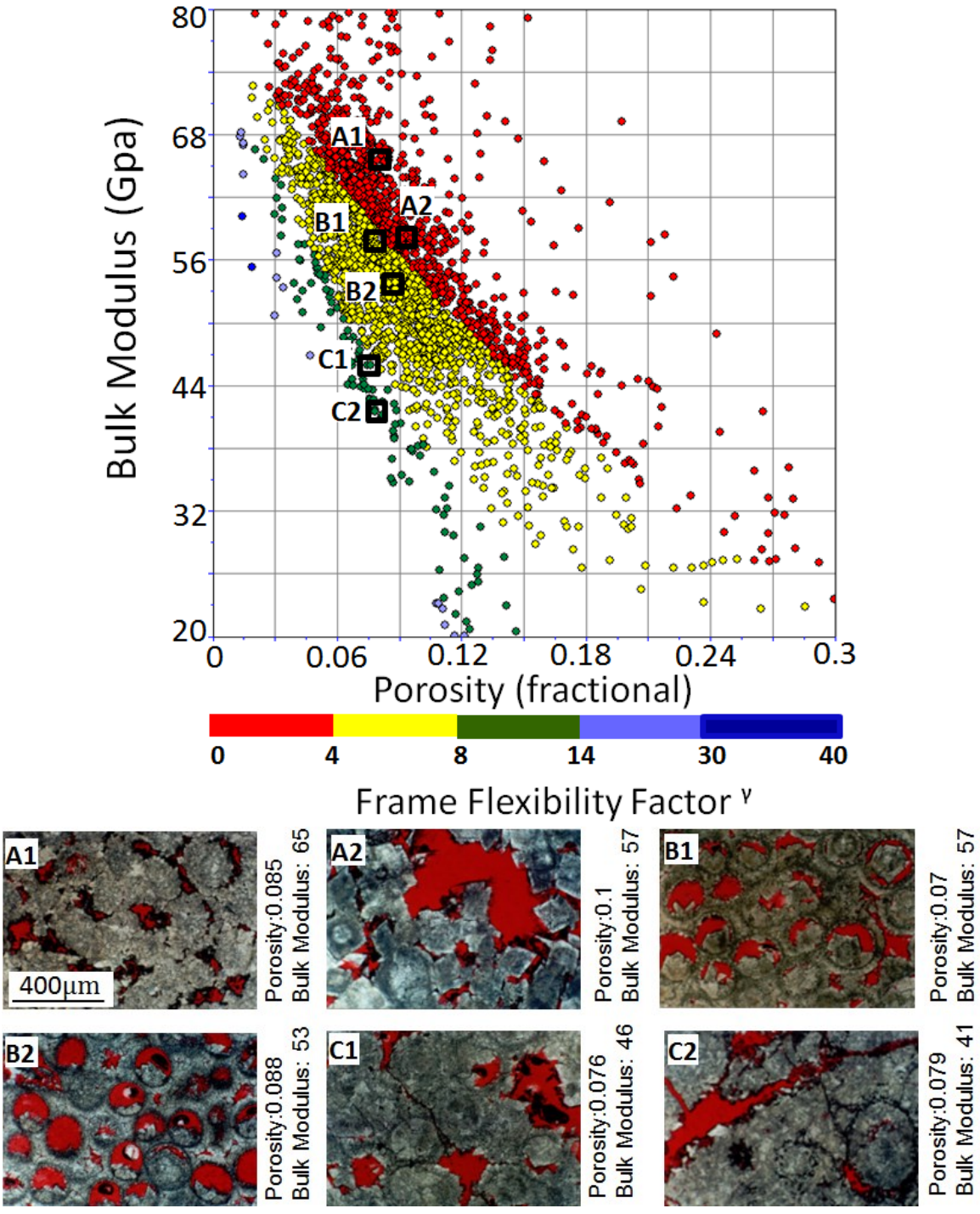

Figure A-22 Crossplot of bulk modulus against porosity for Well 2, colored by Frame Flexibility Factor ϒ. The cast sections of the selected samples are also shown, with the red color indicating porosity. The scales for the thin sections are the same.

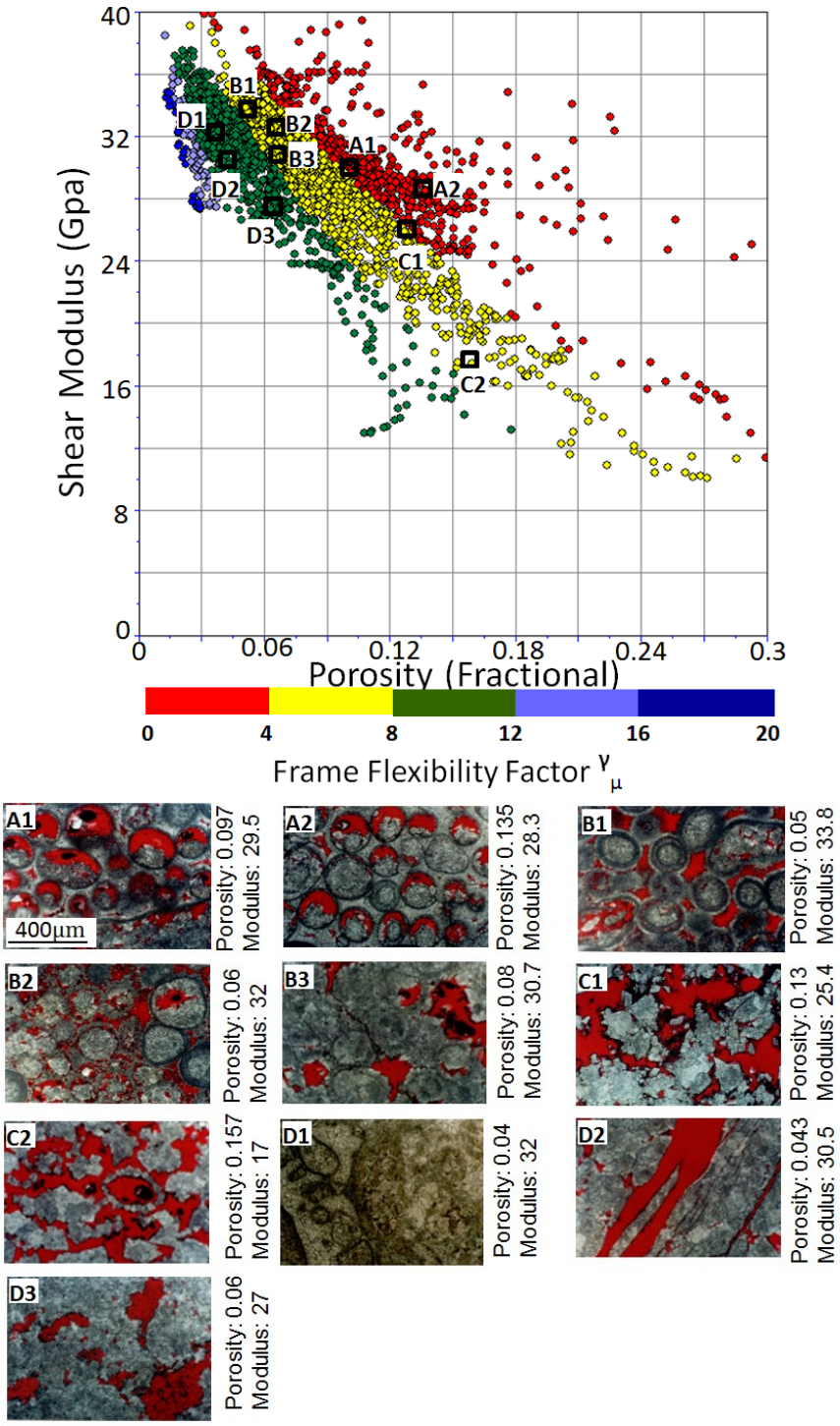

Figure A-23 Crossplot of shear modulus against porosity for Well 2, colored by Frame Flexibility Factor Υμ. The cast sections of the selected samples are also shown, with the red color indicating porosity. The scales for the thin sections are the same.

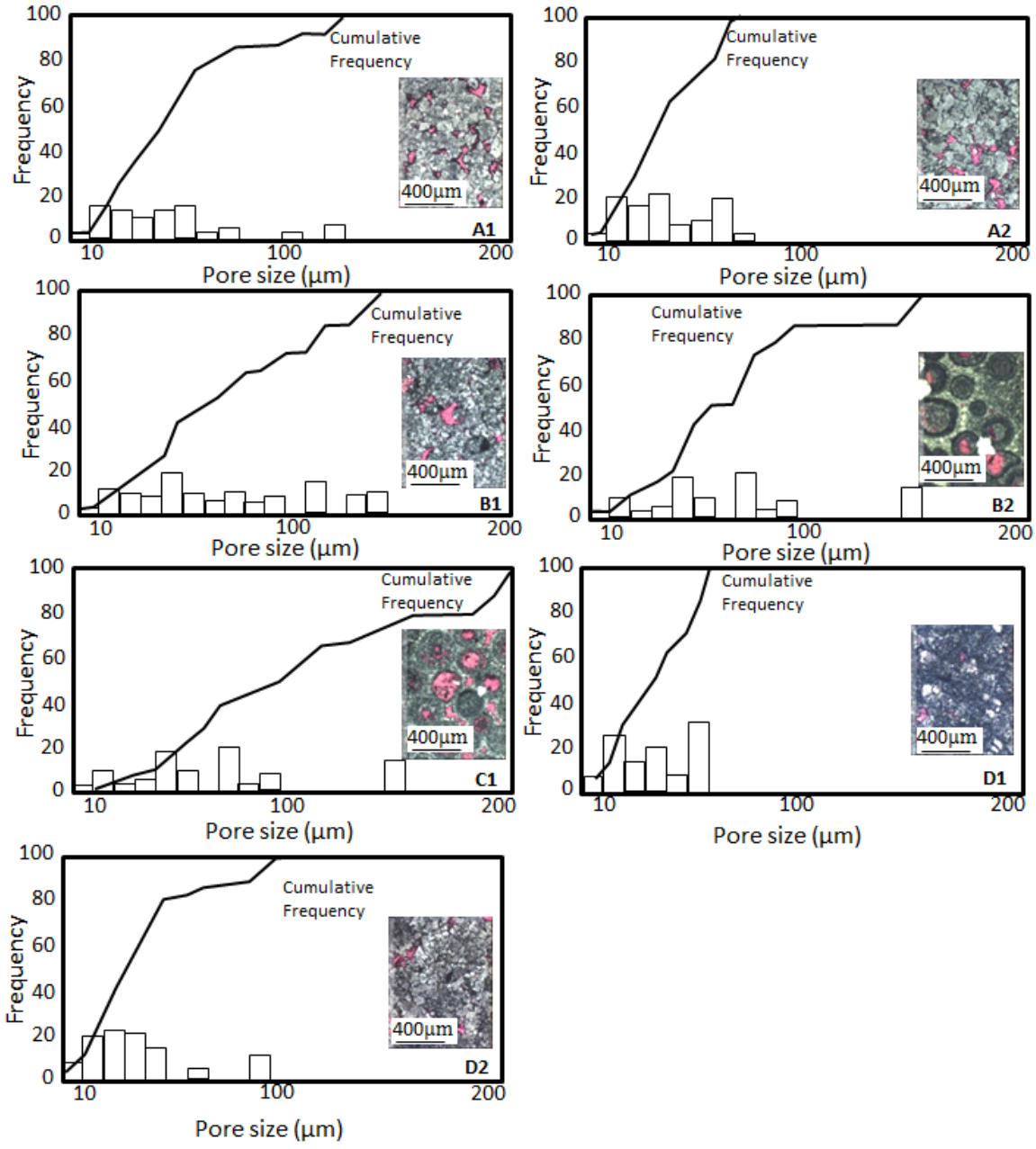

Figure A-24 Pore size distributions for the selected samples shown in Figure A-16.

APPENDIX E

PETROPHYSICAL EVALUATION OF PORE TYPE

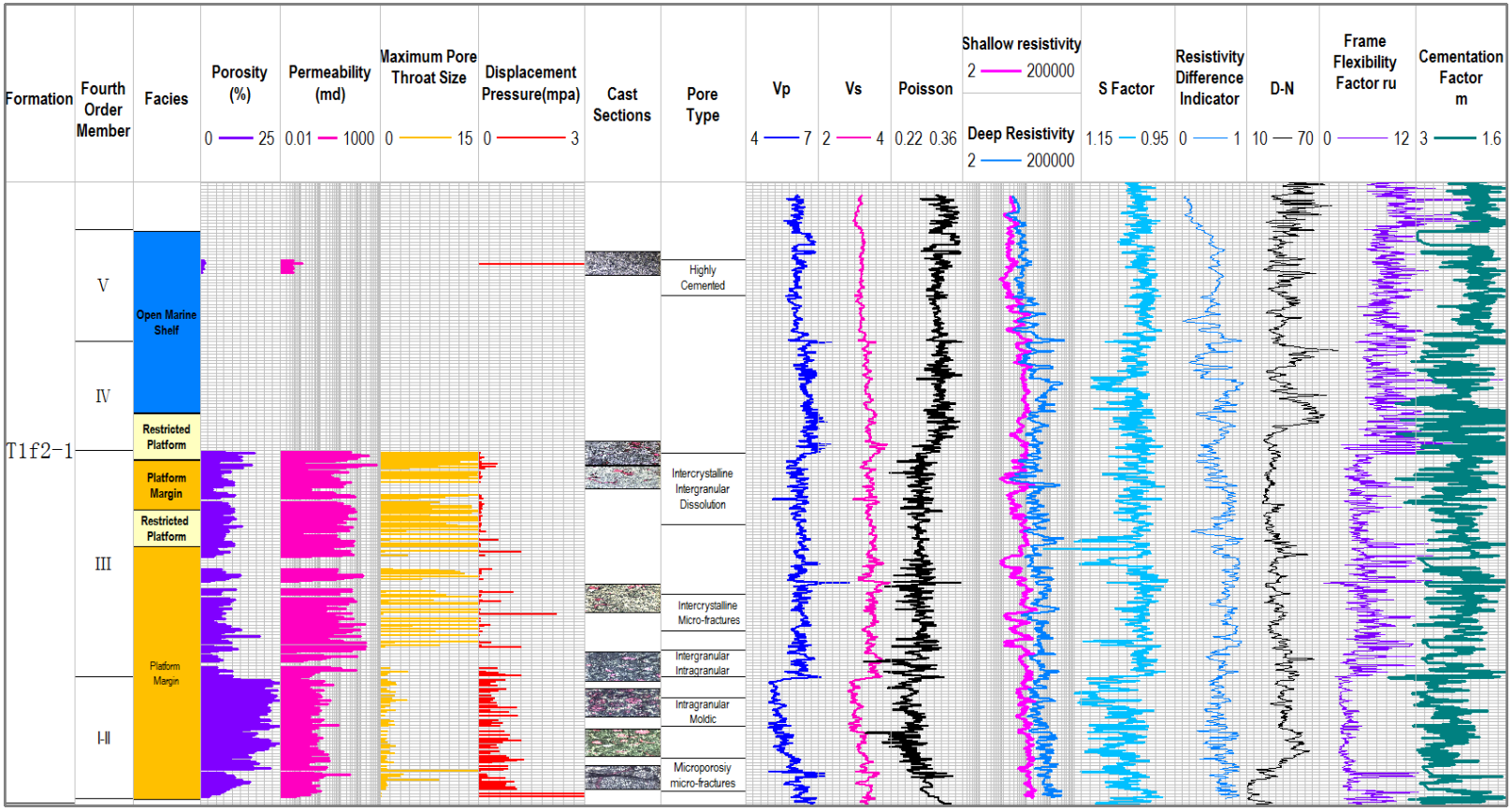

Figure A-25 Pore type evaluation of Well 1, by the five methods mentioned in Chapter II. The core measured porosity, permeability, pore throat size, and displacement pressure are also illustrated.

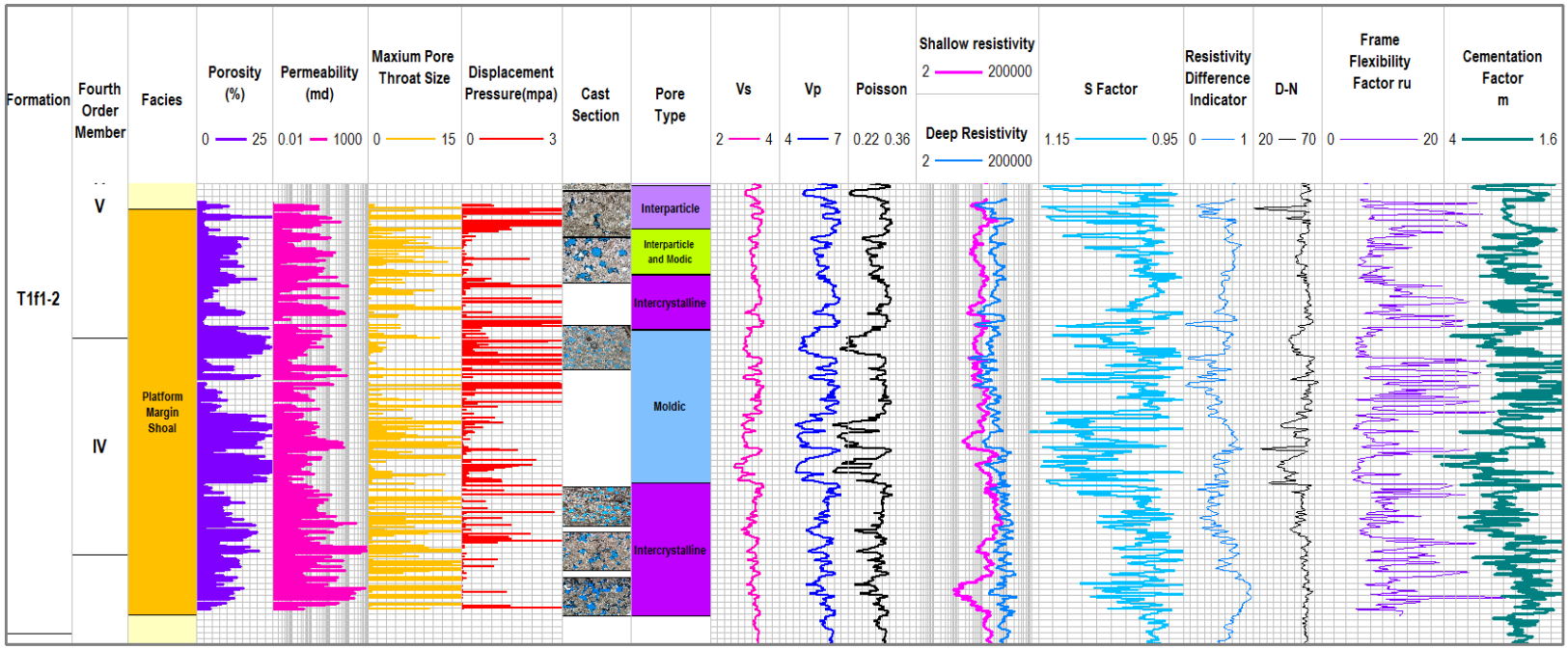

Figure A-26 Pore type evaluation of Well 3, by the five methods mentioned in Chapter II. The core measured porosity, permeability, pore throat size, and displacement pressure are also illustrated.

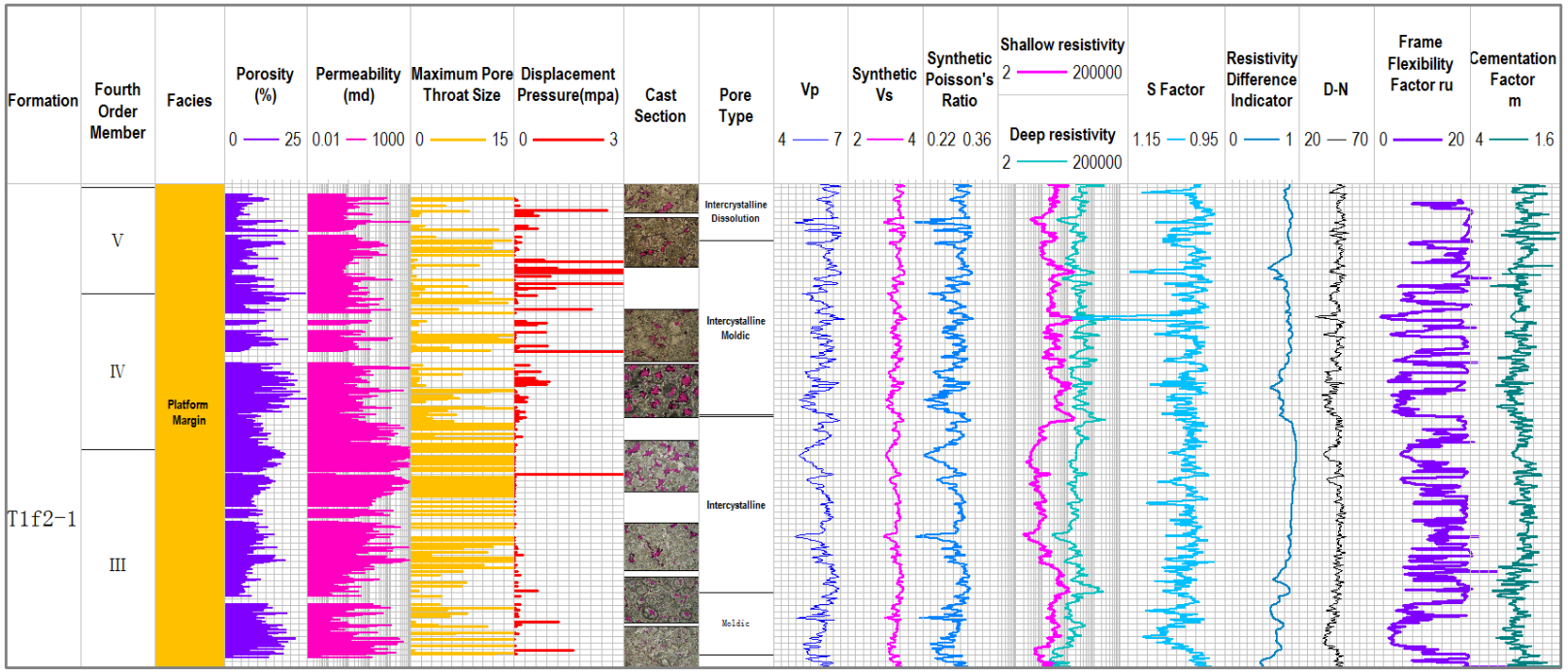

Figure A-27 Pore type evaluation of Well 4, by the five methods mentioned in Chapter II. The core measured porosity, permeability, pore throat size, and displacement pressure are also illustrated.

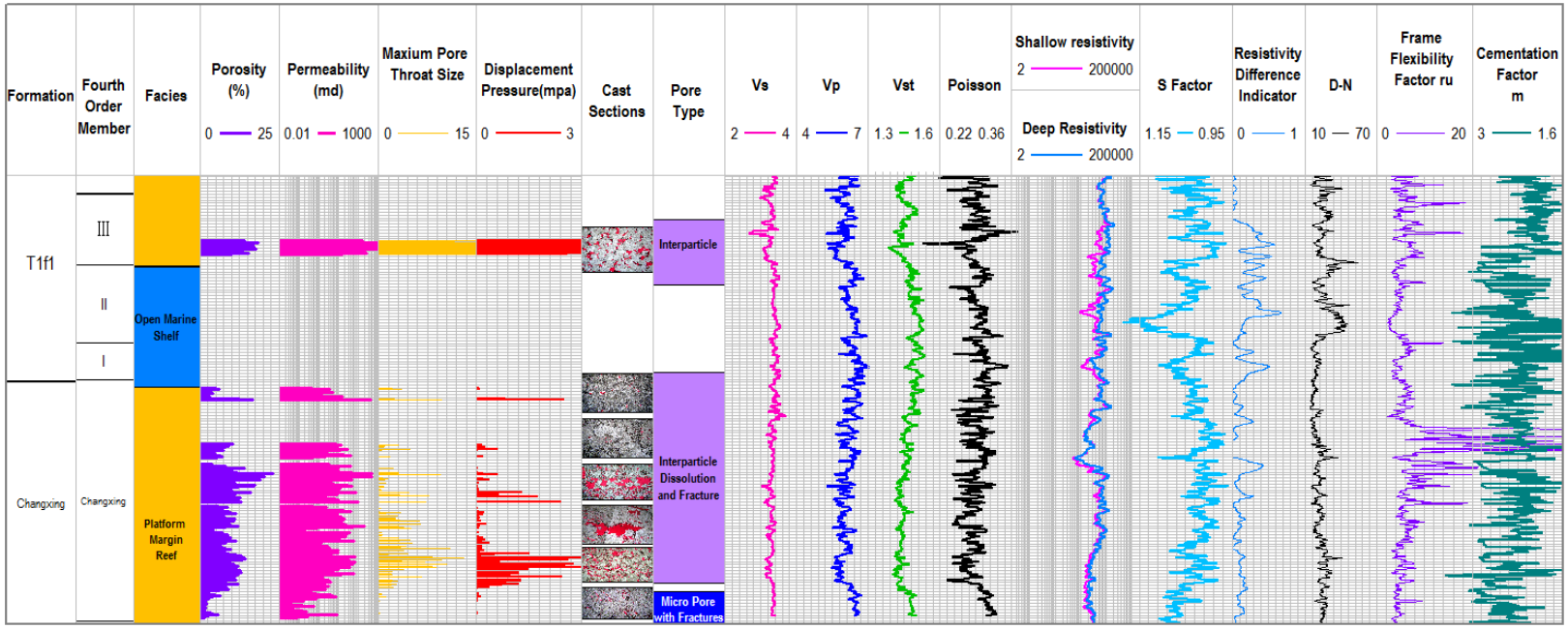

Figure A-28 Pore type evaluation an additional cored well near Well 1, by the five methods mentioned in Chapter II. The core measured porosity, permeability, pore throat size, and displacement pressure are also illustrated.

APPENDIX F

PORE STRUCTURE AND SEA LEVEL CORRELATION

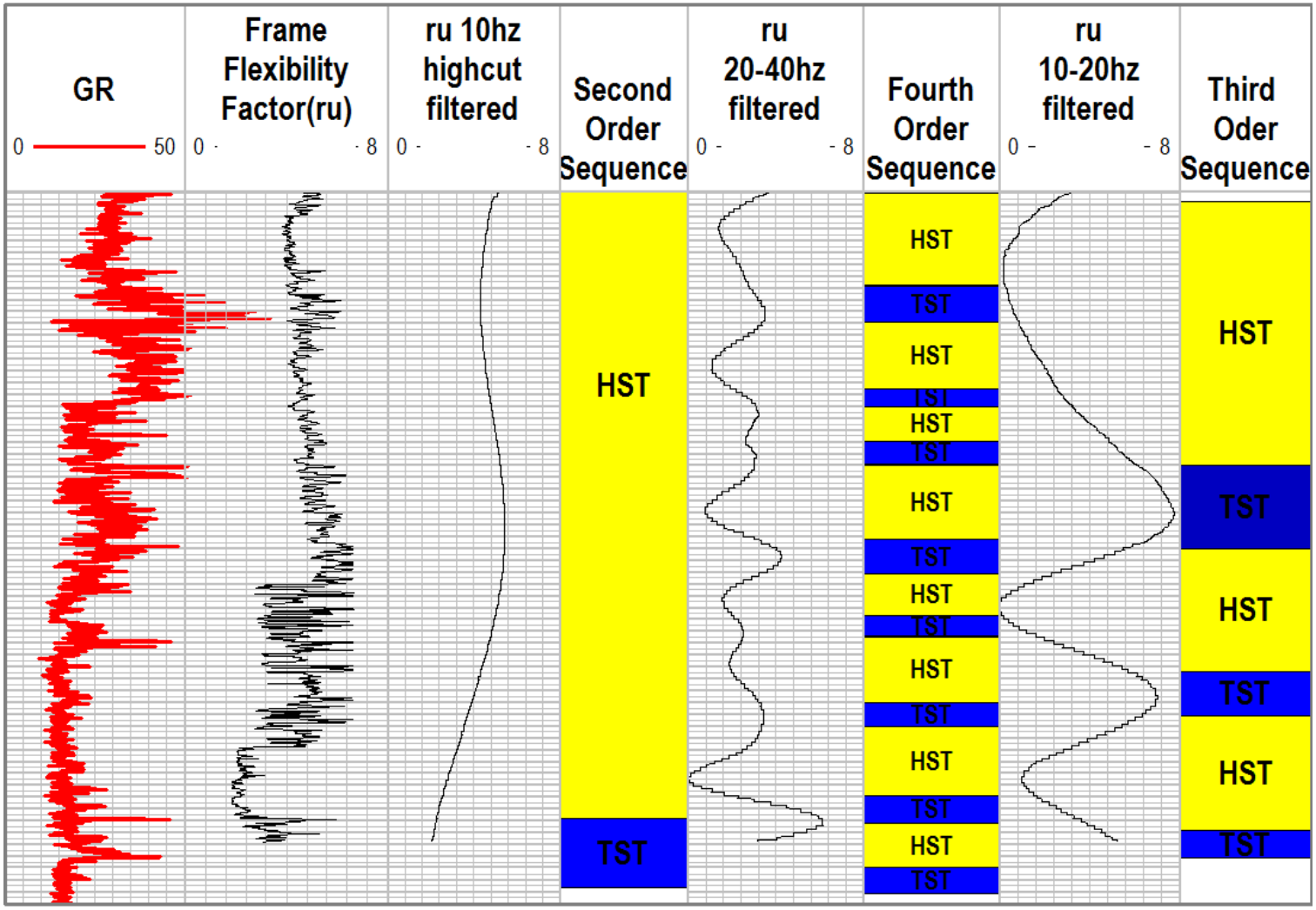

Figure A-29 The application of Frame Flexibility Factor for sea level prediction, Well 1. GR is also shown for comparison.

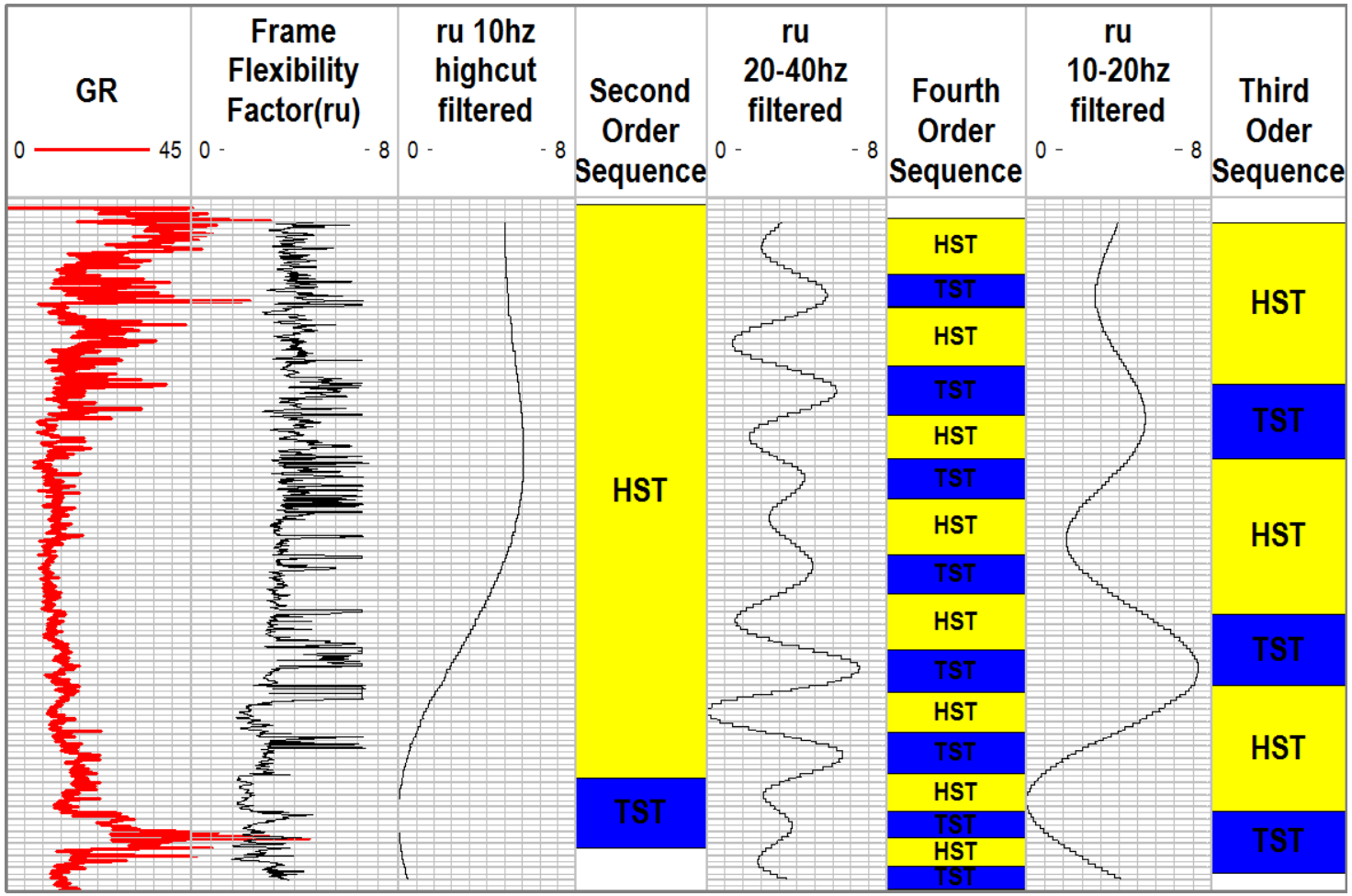

Figure A-30 The application of Frame Flexibility Factor for sea level prediction, Well 2. GR is also shown for comparison.

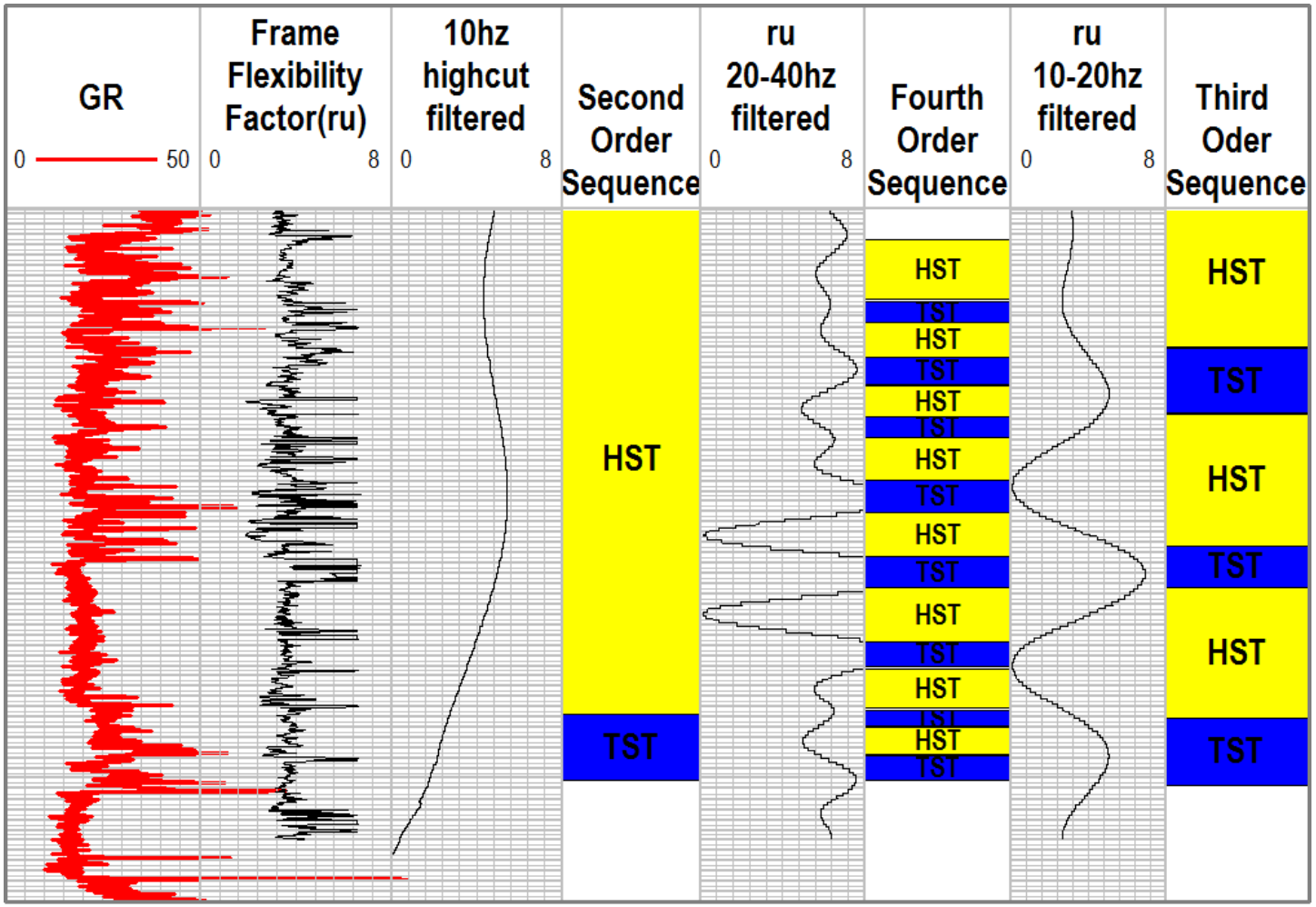

Figure A-31 The application of Frame Flexibility Factor for sea level prediction, Well 3. GR is also shown for comparison.

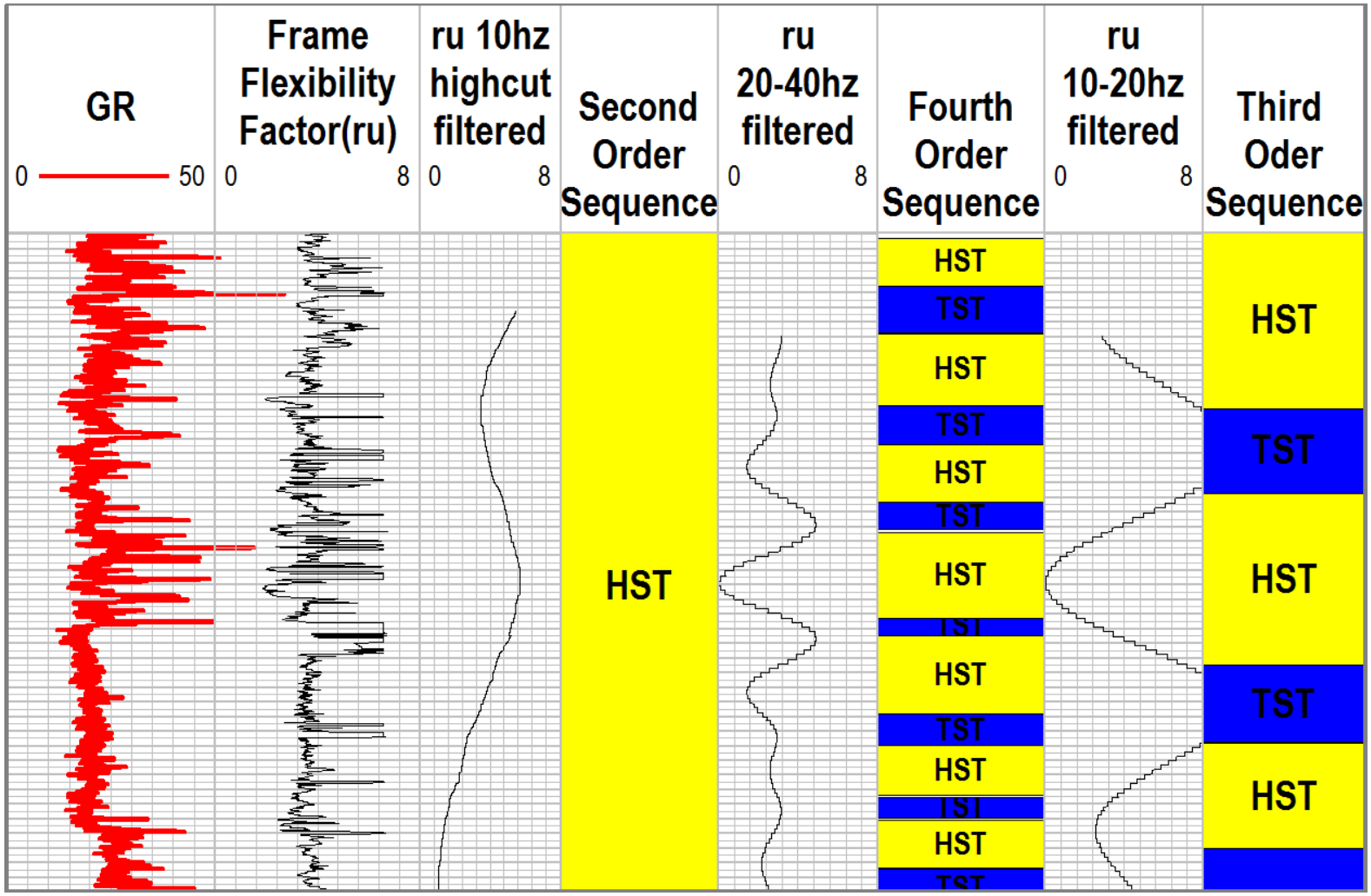

Figure A-32 The application of Frame Flexibility Factor for sea level prediction, Well 4. GR is also shown for comparison.

APPENDIX G

SEISMIC WELL TIE

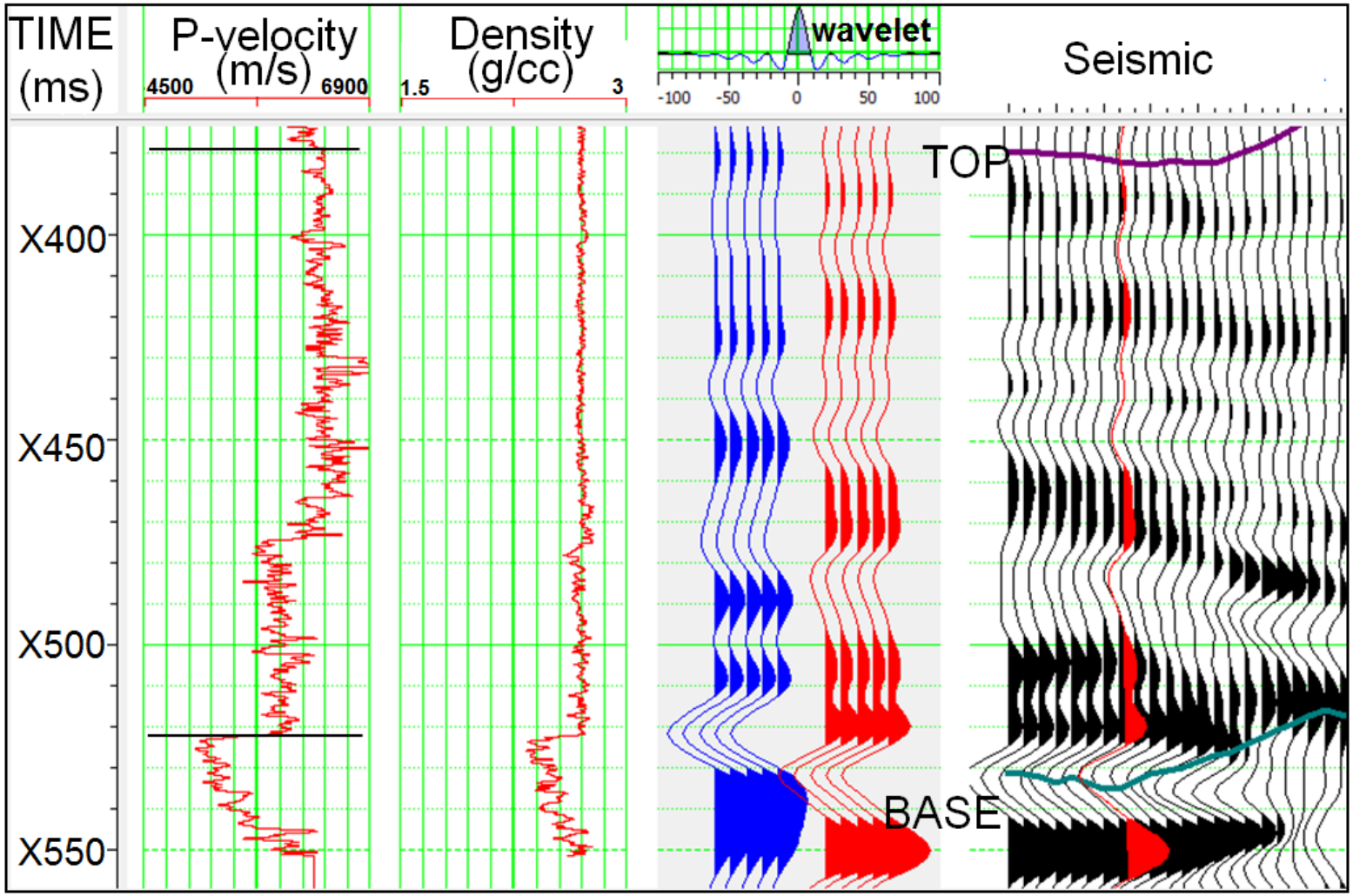

Figure A-33 Seismic well tie for Well 1.

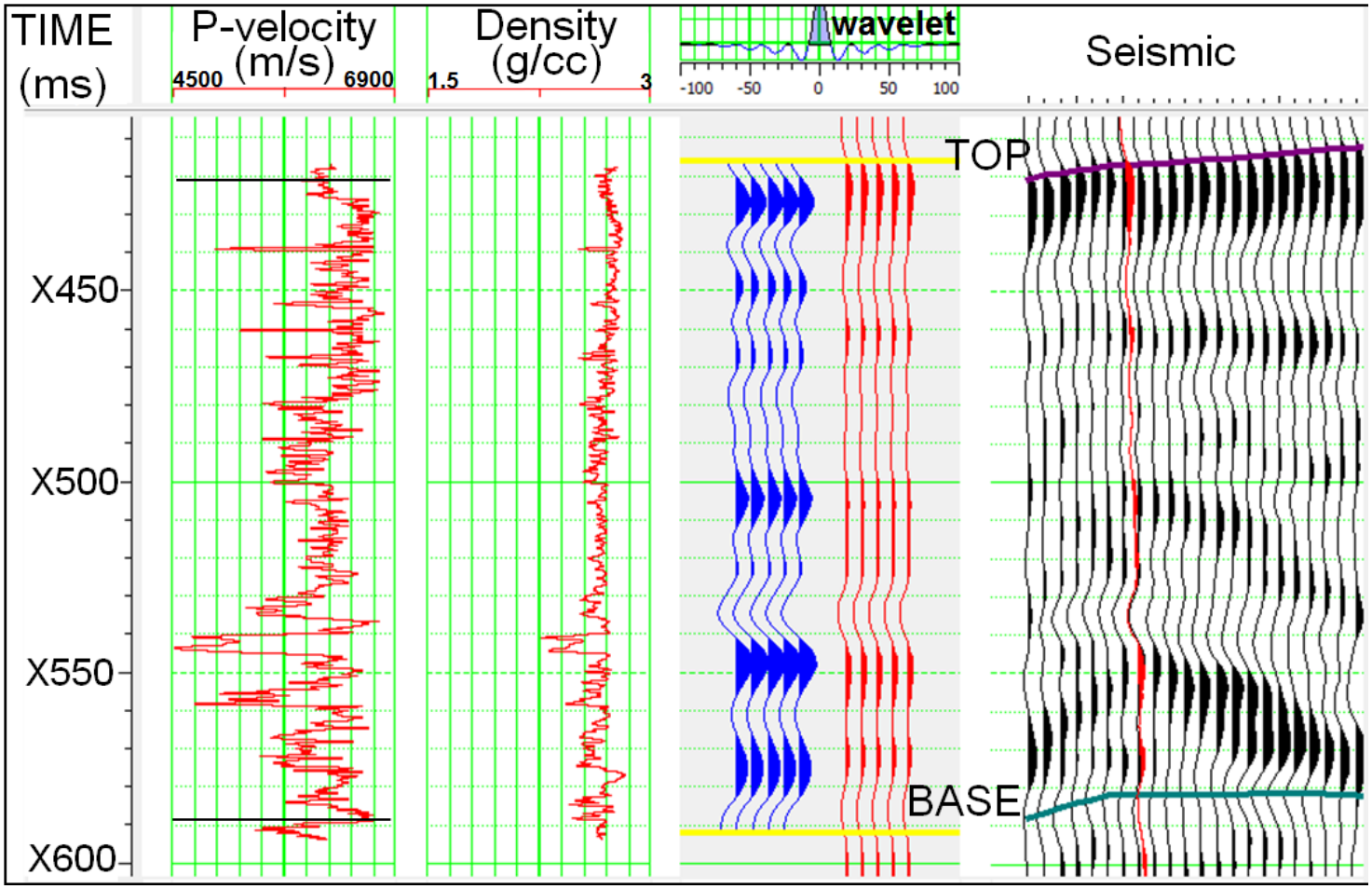

Figure A-33 Seismic well tie for Well 2.

APPENDIX H

RESERVOIR PREDICTION USING RESISTIVITY, SONIC LOGS AND SYNTHETIC MODELING IN CARBONATE ROCKS: A CASE STUDY OF LITTLE CEDAR CREEK FIELD, ONSHORE ALABAMA

Synopsis

Pore structures in carbonate rocks can strongly affect reservoir properties and seismic AVO response. In this report, cementation factor "*m*" in Archie's law, derived from resistivity and density logs, is effective to describe the pore structure variation, and explain the permeability heterogeneity in a microbial carbonate formation onshore Alabama. From log and core analysis, the dominant pore type is micropores, where $1 < m < 1.9$; the dominant pore types are intercrystalline and intergranular, where $1.9 < m < 2.1$; and vuggy pores are prevalent, where $2.1 < m < 3$. Integrated study of *m* and a rock physics model shows cementation factor can be used to estimate shear wave velocity, which is essential to model the Amplitude Versus Offset (AVO) response of pore structure. The synthetic seismic for the gas saturated thrombolite unit, dominated by vuggy/intercrystalline pores, shows abnormal amplitude increase near critical fraction followed by a sudden decrease in amplitude. The synthetic seismic for the gas saturated grainstone unit, dominated by moldic/intergranular pores, shows increasing amplitude near the critical fraction followed by a sudden decrease in amplitude. The synthetic seismic for the water saturated mudstone with microporosity shows a slight decrease and a sudden increase in amplitude near the critical fraction. The offset of critical fraction increases from thrombolite to grainstone and mudstone. The results can be used to direct

AVO prediction of pore structure and permeability in microbial carbonate reservoirs when pre-stack data is available.

Introduction

Pore structures in carbonate rocks can strongly affect reservoir properties such resistivity and sonic velocity. Formation evaluation needs to take into account the pore structure effect on the measurements such as resistivity log. The resistivity log widely used in prediction of hydrocarbon saturation, water saturation and capillary pressure (Archie, 1942, 1952). In carbonate rocks, the resistivity log can also be used to study the influence of pore structure on permeability. Changes in pore size, shape, and connectivity of the pores can greatly modify both the current flow and fluid flow even if saturation, wettability, and temperature remain spatially constant. The cementation factor "*m*" in Archie's law has a strong dependence on the shape of grains and pores, so named as "shape factor" (Salem and Chilingarian, 1999). A range of *m* value from 1.8 to 4 and relates the percentage of separate-vug porosity in total porosity to "*m*" variation (Lucia, 1983). Simple large pores such as vuggy, moldic pores have higher resistivity and cementation factor while intricate small pores such as micropores have much lower values (Verwer et al., 2011). In carbonate rocks, the *m* value for intergranular or intercrystalline pore systems is 2, 1.4 for fractures, 2.4 for vuggy pores 2.4, and greater than 3 for moldic pores (Deveton, 1999).

In thrombolytic carbonate rocks where large vugs can be connected or separated, permeability can vary greatly at constant porosity and is hard to predict even when there

is a good understanding of lithofacies and pore types. However, permeability has a good relationship with cementation factor from laboratory measurements (Verwer et al., 2011). It has been reported that samples with higher permeability have higher cementation factors for a given porosity (Verwer et al., 2011).

Similarly, sonic logs are used to study the pore structures in carbonate rocks due to the strong influence of pore structure on sonic wave propagation. A comparison of sonic-porosity and neutron-porosity often is used as secondary porosity index (SPI) in the field. SPI values can indicate the presence of vugs and fractures (Schlumberger, 1991). Some studies show that SPI is mainly influenced by pore geometry and doesn't have to be secondary porosity. The velocity-deviation log was created for predicting of pore type and permeability (Anselmetti and Eberli, 1999). It is observed that at a given porosity, velocity can differ widely due to pore type variation. The velocity-deviation log is calculated by comparing the velocity from real sonic logs with the velocity from Wyllie's time-average equation. Considering that Wyllie's equation simply averaged the acoustic behavior of the solid and fluid phases, the velocity model was improved by introducing pore shape and distribution of the solid phases in a quantitative approach to the solid-phase term of the equation (Salen and Castagna, 2004). A velocity model based on extended Biot theory (Biot, 1962a, 1962b) was derived to quantitatively describe the pore structure effect on velocity (Sun, 2000).

Although resistivity and velocity are affected by pore structure similarly as shown in Archie's equation and Sun's rock physics model, the correlation between

resistivity and velocity for pore type prediction needs much to be improved. A correlation of Archie's cementation factor and aspect ratio to the ratio of spherical pores to bulk porosity was reported and established the connection between resistivity and sonic velocity (Brie et al., 1985). In his derivation, he provides a link between Kuster-Tokoz and Maxwell-Garnet theoretical models to describe the acoustic and electric effects of including near-spherical pores in a host medium.

In addition to resistivity and sonic logs, amplitude variation with offset (AVO) analysis may be feasible to detect pore structure variations in carbonate rocks. In this case, the effects of pore structure on wave propagation are much stronger than the fluid, and the variation of pore structure is on a scale comparable to the seismic wavelength (Sun, 2004). In Sun (2004) synthetic model, AVO for detection of fluid is only possible for microporosity rocks. For moldic rocks or mixtures of rocks with micro-, interparticle, and moldic porosities, it will be difficult to distinguish water from gas using AVO analysis. Instead, different pore types show different AVO characteristics. The synthetic AVO modeling is useful to avoid the pitfall in fluid detection from seismic amplitude. However, the modeling needs an input of shear wave velocity, which is often limited in access in the field data.

Cementation factor "*m"* derived from resistivity and density logs acquired in a microbial carbonate formation onshore Alabama is investigated to relate its large variations to pore type and permeability heterogeneity. The dataset is from the Smackover Formation, Little Cedar Creek Field. We first examine the deviation of

cementation factor *m* from a value of 2. The *m* value of 2 is chosen because it corresponds to the rock frame with intergranular and intercrystalline porosity, which is the basis for Archie's law and Wyllie's average equation. We then correlate the *m* deviation log with velocity deviation log and permeability measured on the core to verify its potential for helping to locate high permeability zones in the field. Afterward, cementation factor m will be used as a pore structure indicator in a rock physics model to estimate shear wave velocity, considering the significant effect of pore structure on velocity. The estimated velocity will be further integrated to model the AVO response of the studied carbonate reservoirs. Compared to the previous studies in the Smackover Formation of Little Cedar Creek Field studying depositional models and related facies (e.g. Mancini et al., 2006, 2008; Heydari and Baria, 2006; Ridgway, 2010), this study attempt to understand the petrophysical and seismic responses to the depositional variation. The applied approach may be used to assist reservoir management in other fields producing from microbialites (e.g., Green River Formation and offshore Brazil).

Method

Pore structure index from resistivity log

We used cementation factor *m* from Archie's law (Archie, 1952) to quantify the pore type change and associated permeability behaviors in the Smackover Formation. Cementation factor *m* is calculated using deep-investigation resistivity log (R_t), apparent water saturation (R_{wa}) and density derived porosity logs (ϕ), based on the following equations:

$$FF = \frac{Rt}{R_{wa}} \tag{1}$$

$$m = \frac{\log \frac{a}{FF}}{\log \phi} \tag{2}$$

where a is assumed to be 1, FF is formation factor. Density-derived porosity is further checked and corrected against core measurements where applicable. It is noted that the value of a is not always 1 as it also varies following the variations in pore structure. However, the influence of pore structure on a is much smaller than m in the studied formation.

Based on Eqs. 1-2, cementation factor m is estimated at log scale. We then introduce a cementation factor deviation log (Δm) by comparing the value of m to a value of 2, which usually represents a rock frame with intergranular and intercrystalline pores (Dullien, 1992). The concept of cementation factor deviation is similar to velocity deviation log introduced by Anselmetti and Eberli (1999), which is used as a tool for predicting of pore type and permeability. The deviation of velocity is made by comparing the sonic log velocity with the velocity calculated using the time average equation of Wyllie (1956):

$$\frac{1}{V} = \frac{1-\phi}{Vm} + \frac{1}{Vf} \tag{3}$$

where the velocity of the matrix (V_m) and water (V_f) is taken to 6530 m/s and 1500m/s for this study, respectively. Similar to velocity deviation log, cementation deviation log can be used to correlate the pore structure change to permeability.

Pore structure index guided shear wave estimation

In the studied field, shear wave velocity log is not available and is estimated using Sun's (2000) rock physics model. The rock physics model and defined elastic parameters, termed the frame flexibility factors (γ, γ_μ), are used as proxies for pore structure classification (Sun, 2000, 2004).

$$V_p = \sqrt{\frac{K + \frac{4}{3}\mu}{\rho}} \tag{4}$$

$$V_s = \sqrt{\frac{\mu}{\rho}} \tag{5}$$

$$K_d = K_s(1-\phi)^{\gamma} \tag{6}$$

$$\mu_d = \mu_s(1-\phi)^{\gamma_\mu} \tag{7}$$

For the studied reservoir rock, we assume that

$$K = K_d \tag{8}$$

$$\mu = \mu_d \tag{9}$$

K and μ, K_d and μ_d, K_s and μ_s are total, dry frame, solid matrix bulk modulus and shear modulus, respectively; γ, γ_μ are frame flexibility factors. In the equations, porosity (ϕ) is also derived from density (ρ).

Based on Eqs. 4-9, shear wave velocity can be estimated as shown in Eq. 10.

$$V_s = \frac{V_p}{\sqrt{(1-\phi)^{\gamma-\gamma_\mu}\frac{K_s}{\mu_s}}} \tag{10}$$

$$f = (1-\phi)^{\gamma-\gamma_\mu} \tag{11}$$

The derivation of V_s requires the input of variable f which is closely related to the pore structure. When porosity increases or the pore connectivity increases, rocks become more susceptible to shear deformation than volumetric change. Both will result in lowered f value. For instance, connected vuggy pores are much easier to deform than isolated moldic porosity. As porosity and pore connectivity are the two most important factors deciding the permeability behaviors, permeability can, in turn, infer the relatively magnitude of f. We use cementation factor m deviation log as a proxy for permeability, thus estimate f as shown in Eq. 12. The assumption is verified using the well log data from another field where Vs is available and will be discussed in Results.

$$\Delta m = cf \tag{12}$$

f is a function of pore structure shown in Eq. 11, c is a constant for a specific rock type. The value of c will be discussed in Results.

Pore structure AVO modeling

With known V_p, V_s, ρ, AVO modeling is conducted at different offsets using Hampson-Russell Software based on Zoeppritz equations (Zoeppritz, 1919). The effect of pore type on AVO response will be discussed in the results.

Field Data

Little Cedar Creek Field (LCCF), onshore Alabama (Figure A-34), is an oil field with limited gas production. Since 1994, the cumulative production is 20 million bbl of oil and condensate, and 19 million mcf of gas (Tonietto, 2014). The producing reservoirs (Figure A-34) are low-energy microbial thrombolite and oolitic grainstone of the Smackover Formation. The oolitic grainstone was deposited in a high-energy, near-shore environment on a carbonate ramp (Ahr 1973, Mancini and Benson, 1980). The ramp was created during sea level regression on the northeastern Gulf of Mexico platform, which was also characterized as several marginal extensional basins created after the early Triassic breakup of Pangea (Stanley, 2005). Following that, the Jurassic Smackover Formation was deposited within these basins. The deposition was compartmentalized by a series of structural highs (Heydari and Baria 2006). Pre-Jurassic salt tectonics resulted in variations of topography (Ahr, 1973).

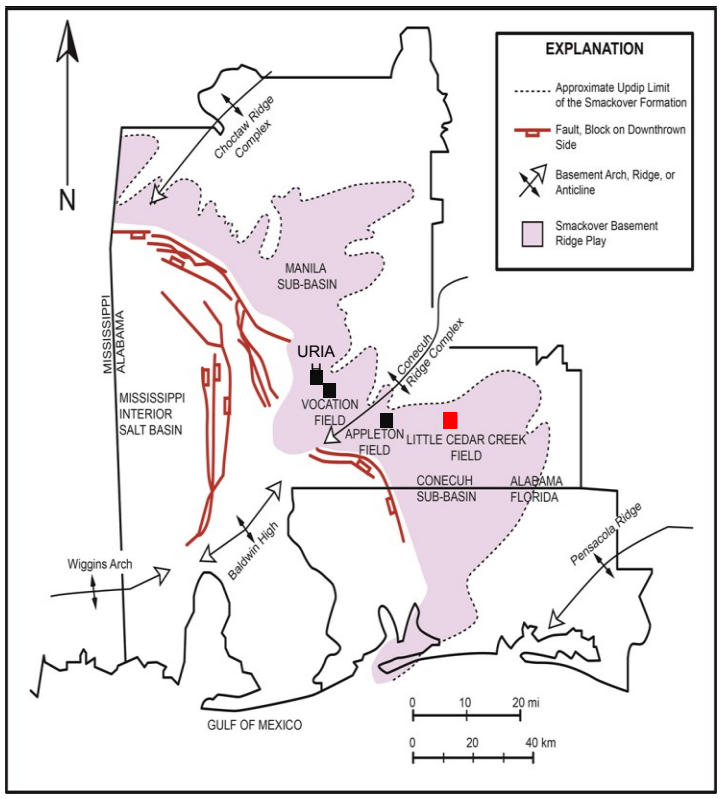

Figure A-34 Regional structure map of Gulf coastal plain, with information on the location of Little Cedar Creek Field and the distribution of Smackover Formation (modified from Tonietto, 2014).

The post-rift deposition within the Gulf coastal plain is greatly affected by the Later Jurassic and Early Cretaceous transgression-regressive (T-R) sequences (Figure A-35). The Smackover formation is deposited within one of the sequences, and is sub-divided into the lower transgressive system tract (TST) and upper highstand system tract (HST). Five major facies were formed following the sea level change. Transgressive lime-mudstone, microbial thrombolite, and microbially influenced packstone were deposited successively during the TST, following sea level rise. The maximum flooding zone is characterized by subtidal lime-mudstone / wackestone and condensed section.

Nearshore peloid/ooid grainstone and peritidal mudstone/dolostone have deposited afterward during HST when sea level dropped (Mancini et al., 1990). Thrombolites with a clotted, mottled and nodular texture, and rare domal and branching structures, was deposited in nearshore, shallow subtidal paleoenvironments along the up-dip margin of Smackover Formation deposition (Mancini et al. 2008).

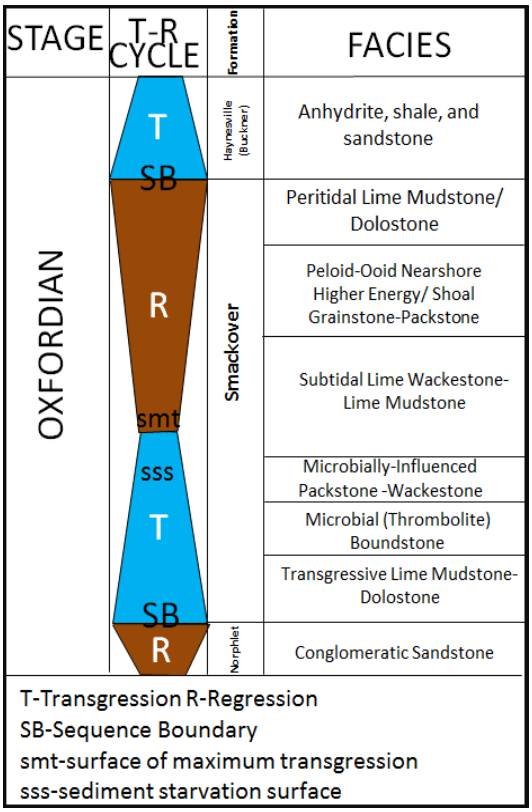

Figure A-35 Sequence stratigraphy of Smackover Formation in Little Cedar Creek Field-Alabama (modified from Mancini et al., 2008).

The dominant pore types varied significantly (Figure A-36). Vugs are mainly located in thrombolite facies developed during transgression and part of grainstone facies developed during regressions. Microporosity is mostly found in transgressive mudstone and wackestone units at the end of transgression. Most of the grainstone unit consists of moldic pores generated by the dissolution of ooids after exposure. Petrophysical properties vary significantly within the thrombolite with porosity varying from 3 to 19% and permeability varying from less than 1 to 100 md, locally as much as 500 md (Tonietto, 2014). Dolomitization is limited and often occurs within the thrombolite facies to the southern portion of the field. The porosity for these intercrystalline pores varies between 10 to 21 %, and permeability varies between 150 to 850 md. As it changed some of the vugs into sucrosic intercrystalline pores, the permeability is greatly improved from tens of md to hundreds of md. In comparison, most of the grainstone unit consists of moldic pores generated by the dissolution of ooids. The porosity is good, ranging from 5 to 32%. However, permeability is poor, varying from 1 to 10 md (Tonietto, 2014). Facies mapping helped interpret pore types, characterize pore structure, and find the reservoir zones. The limited amount of dolomitization and good preservation of depositional rock fabrics make it an excellent place to study the effect of depositional rock texture on petrophysical properties.

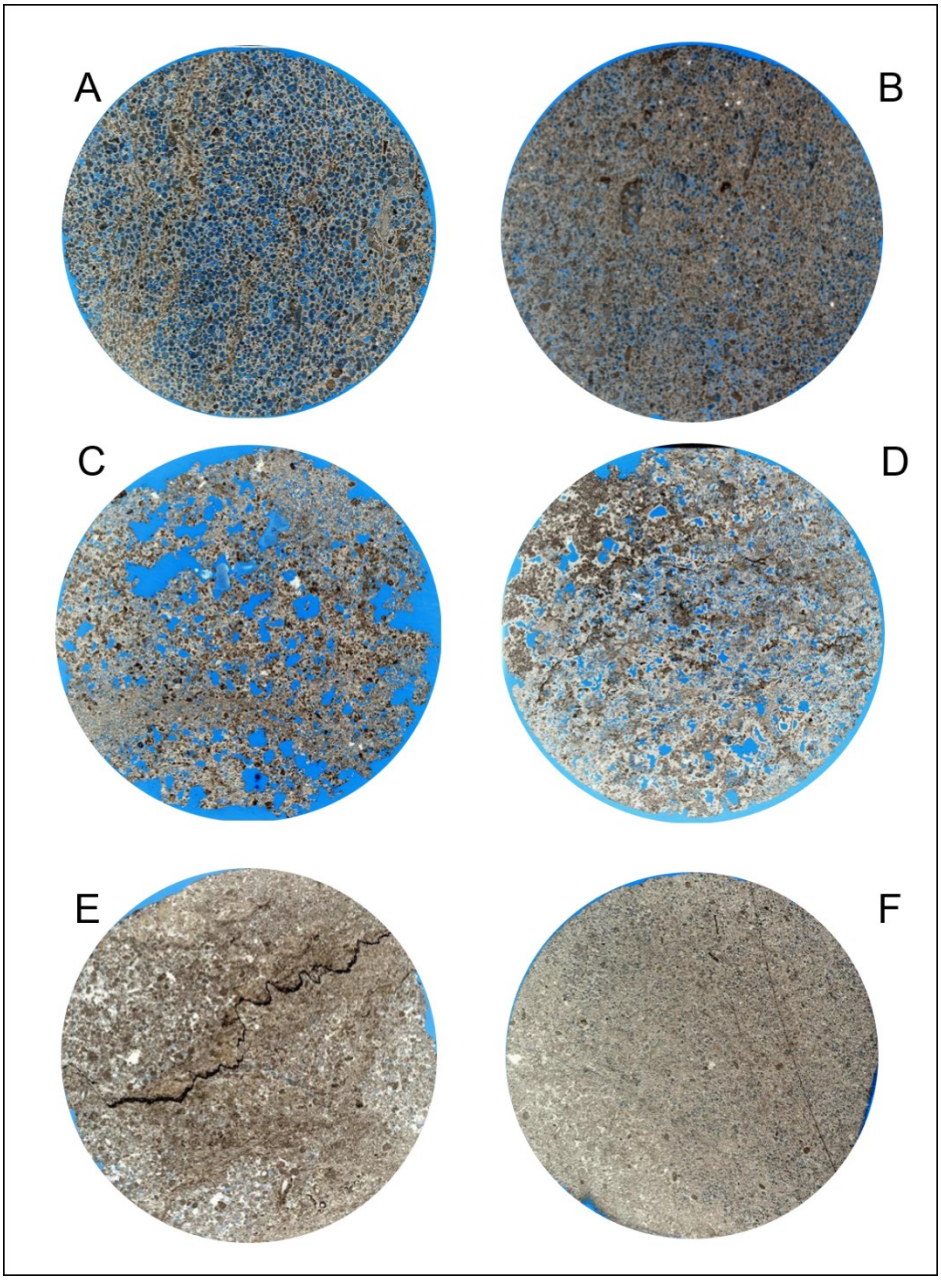

Figure A-36 images of scanned thin sections from 1 in (2.5 cm) diameter plugs. The dominant features observed are moldic porosity (A, B), large vuggy porosity (C), intercrystalline and vuggy porosity (D), stylolite and micro porosity (E), highly cemented grainstone (F).

Conventional logging data from 81 wells are used in this work. Out of the 81 wells, 27 wells have core data, and a few wells have special core analysis data. There is no shear log information from the wells. Therefore, shear wave velocity is estimated and then applied for seismic AVO modeling. The well used the most in this paper is from a dry hole with 70 ft of core measurements such as porosity, permeability, thin sections, and core descriptions. Unfortunately, seismic reflection data (Handford and Baria, 2007) are not available for this study.

Results

Pore type estimation

As shown in Figure A-36, the studied Smackover Formation has diverse pore types, which can significant affect rock properties. Figures A-37 and A-38 show the cross plots of *FF* and V_p against corrected density porosity. For a given porosity, both *FF* and V_p show large variations. Since the formation is relatively thin, in-situ pressure and temperature are considered to be constant, the variations in *FF* and V_p are caused by changes in pore structures. Cementation factor (*m*) from Archie's law shows clear trends when used to study the scattered cross plots of formation factor (*FF*) and sonic velocity (V_p) versus porosity due to its close relationship with reservoir pore structure.

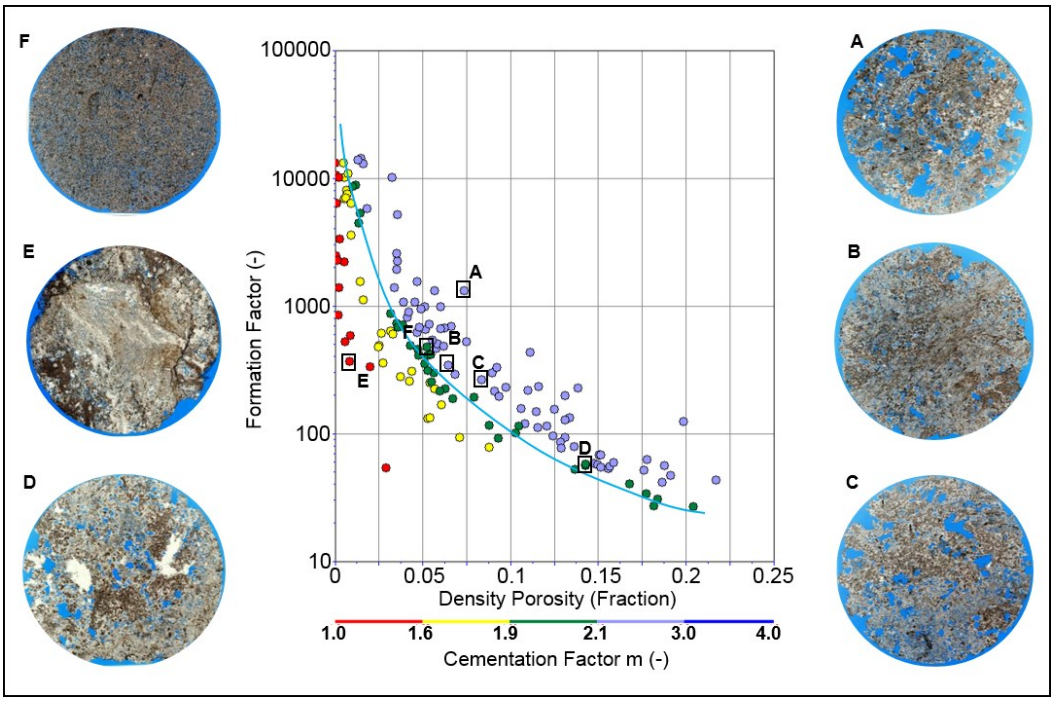

Figure A-37 A plot of Formation Factor (*FF*) and corrected density porosity with cementation factor m being the color indicator. The large scatters at a constant porosity is caused by pore structure which is related to m value. The green line shows the relation between *FF* and porosity when m is 2. Scanned thin sections from 1 in (2.5 cm) diameter plugs for the selected samples are also shown.

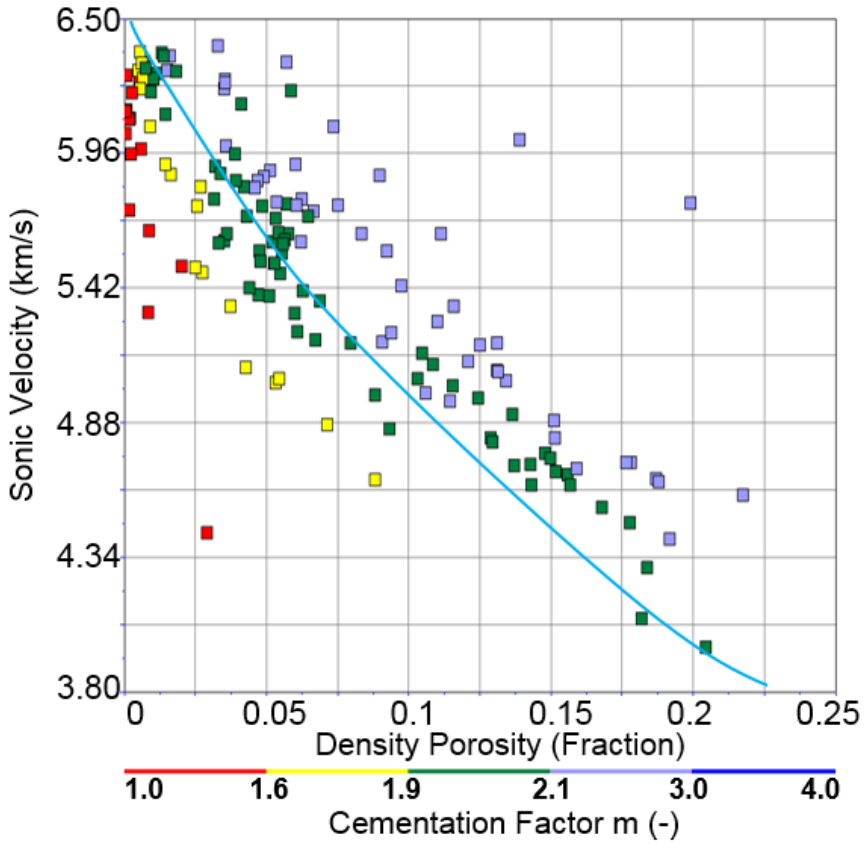

Figure A-38 A plot of P-velocity and corrected density porosity with the cementation factor being the color indicator. The scatters in velocity is caused by pore structure variation quantified by cementation factor. The blue line shows the Wyllie's equation estimated velocity.

For $m < 1.9$, *FF* and sonic velocity are low at a constant porosity as the pore type is dominated by microporosity. Micropores with larger pore numbers at a given porosity may result in a better continuity for conducting electrical current and lower resistivity, while their relatively compliant rock mechanics lower the velocity. Controversially, micropores restrict fluid flow with increased capillary actions, compared with larger pores at a given porosity. When $1.9 < m < 2.1$, the dominant pore type is interparticle or

intercrystalline porosity. The interparticle pores in grainstone often occur with moldic porosity while intercrystalline porosity in thrombolite units is due to partial dolomitization. When 2.1< *m* <3, the dominant pore type is vugs widely distributed in thrombolite, which could be connected or isolated. Compared with the microporosity at a given porosity, large vugs have a relatively lower number of pores and result in reduced flow paths for electrical charge and higher resistivity. However, the permeability of these vugs for fluid can be quite good where vugs are connected with large pore throat as shown in Figure A-36. For the very low porosity zone (< 2%), the *FF* and sonic velocity can be very high, and *m* can be larger than 3 because the rock is highly cemented and rigid.

Permeability evaluation

Carbonate pore type variation can significantly affect the permeability by changing the pore throat size and connectivity. Cementation factor as a pore structure indicator can be used to evaluate permeability. Figure A-39 and Figure A-40 show that the moldic grainstone with a high cementation factor has a relatively lower permeability. Thrombolite with a lower cementation factor has higher permeability. Mudstone with microporosity being the dominant pore type show the lowest cementation factor and lowest permeability. However, when fractures are developed in the mudstone, the permeability could be higher. It is noted that although most of the rocks from the same facies has a similar range of value for *m*, *m* can be quite variable within the same facies such as thrombolite.

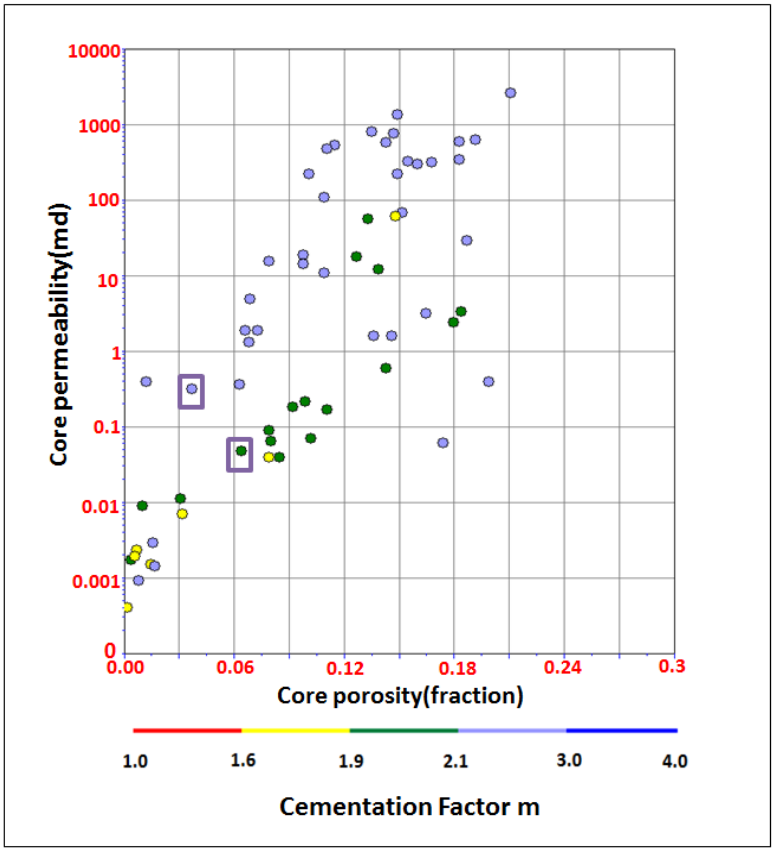

Figure A-39 Semi-log plot of air permeability against porosity from core measurement. Cementation factor is the color indicator. Higher cementation factor displays higher permeability than the ones withstr lower cementation fator. The two blocks are data with thin sections shown in Figure A-40.

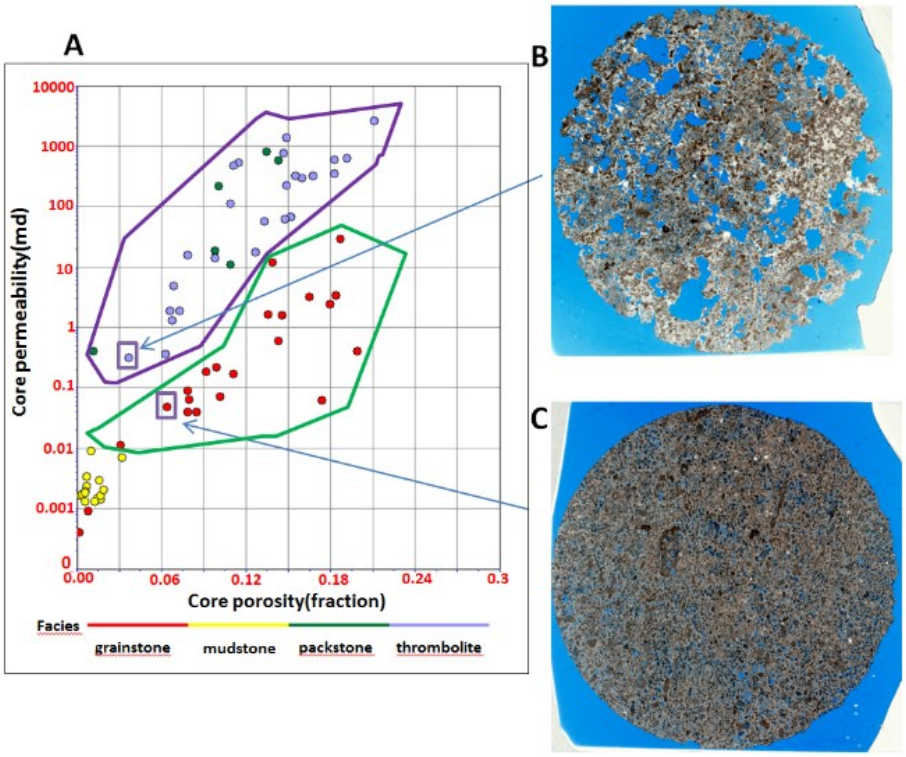

Figure A-40 (A) Semi-log plot of air permeability against porosity from core measurements. The color is facies indicated with the purple dots representing microbial thrombolite, red representing oomodic grainstone, yellow representing mudstone. The most permeable zone for this well is in thrombolite unit. (B) Thin section of thrombolite at 11589.8ft. (C) Thin section of the oolitic grainstone at 11561ft.

In the studied field, the oolitic grainstone and thrombolite units are the two major reservoirs. However, the reservoir quality differs depending on the connectivity of moldic pores in grainstone and vugs in thrombolites. The thrombolite facies has relatively large connected vuggy porosity, resulting in a higher *m* value and higher permeability than the grainstone unit. Therefore, the cementation factor deviation log can be used similarly to velocity deviation log to identify permeable zones (Figure A-41). The velocity deviation and cementation factor deviation agree very well. Both of

them have similar trends with permeability. Especially, high permeability zones can be correlated with positive m and V_p deviation logs. The m deviation is as high as 0.9 with an average of 0.4 for the two zones. However, the deviation logs only provide a qualitative way to distinguish high permeable zones from less productive zones and cannot be applied to seismic. To understand the seismic responses of different pore types, AVO modeling is applied using the estimated shear wave velocity log.

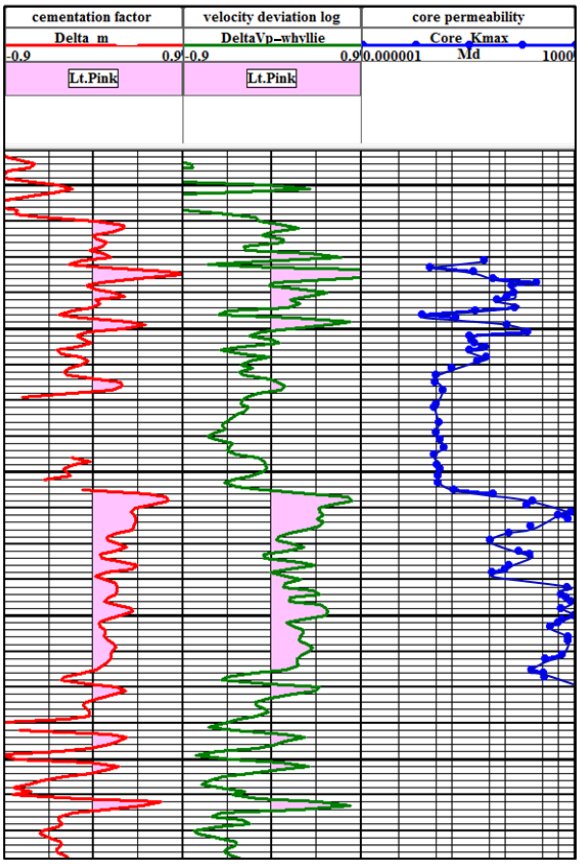

Figure A-41 Log template showing cementation factor deviation curve, velocity deviation curve, and permeability curve. The predicted high permeability zone is indicated by pink color.

Shear wave estimation

In this study, the effect of cementation factor m on resistivity in Archie's law is mathematically similar to the influence of a predefined frame flexibility factors γ and γ_μ on velocity in Sun's rock physics model (Sun, 2004). The application of frame flexibility factors for pore type prediction is limited in this field due to insufficient shear wave velocity information. However, with given pore type information, this rock physics model can be used to estimate the shear wave velocity, which is needed to study the elastic properties of the rock as well as for synthetic seismic modeling. As outlined in the Methods, m is used to classify the pore types and to obtain the solution to Eq. 11 by searching for the c value in Eq. 12. A well from Puguang gas field with shear velocity log is studied first to test the assumed relationship between Δm and f in Eq. 12. This well has two distinctive pore types, namely intergranular and dissolution porosity. Figure A-42 shows the cross plot of Δm against f. The color indicates depth, where colder colored samples are from interparticle pores, and warm colored samples are from dissolution pores. Thus, for the rock samples dominated by intergranular porosity, c is found to be around 0.5, while for the ones dominated by dissolution porosity, c is around 2.5. Considering that the dominant pore types of Smackover Formation in LCCF is related to dissolution porosity, such as moldic porosity in upper oolitic grainstone unit and vuggy porosity in the lower thrombolite unit, c is expected to be a constant around 2.5 for this study. To testify this assumption, we apply different c values to the studied wells in LCCF and observe the correlation between core permeability and the calculated values for the two frame flexibility factors γ and γ_μ (Figure A-43). Theoretically, γ and γ_μ are a

good indicator of pore type (e.g. Dou, 2011; Adesokan and Sun, 2014; Zhang, 2014). The ratio of γ and γ_μ is commonly considered as constant. The variation of both parameters should be similar and correlate with pore type variation. In this study, the permeability variation strongly agrees with the pore type variation, thus, should correspond to the variation of both factors. We assume that when the permeability variation agrees with γ and γ_μ variations, the estimated shear wave velocity is trustable. Based on this assumption, when c is 2.5, γ and γ_μ matches the core permeability the best for the studied Smackover Formation. We will apply the estimated synthetic shear wave velocity from Eqs. 10-12 where c is 2.5 to further model the AVO responses of the studied reservoir.

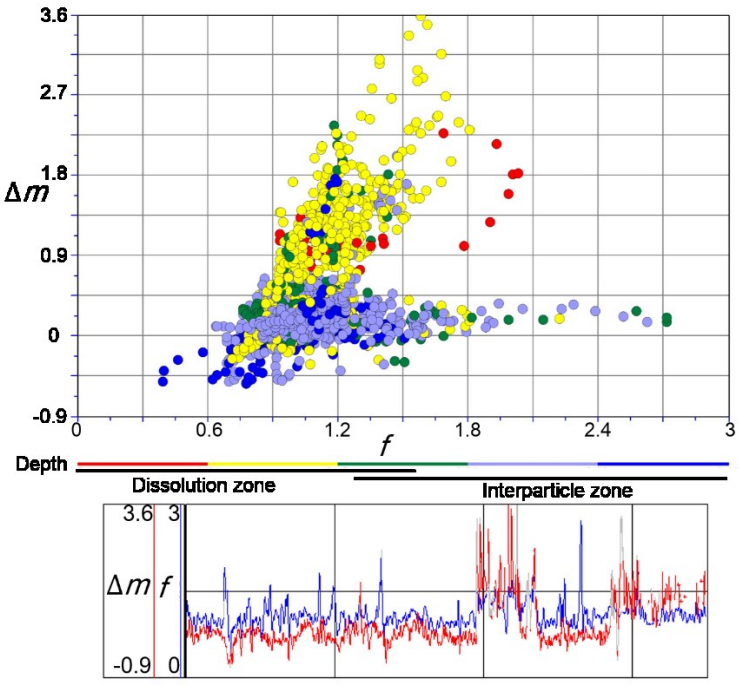

Figure A-42 Crossplot of cementation factor m against the calculated f factor from Eq. 11 using the well log data from another field.

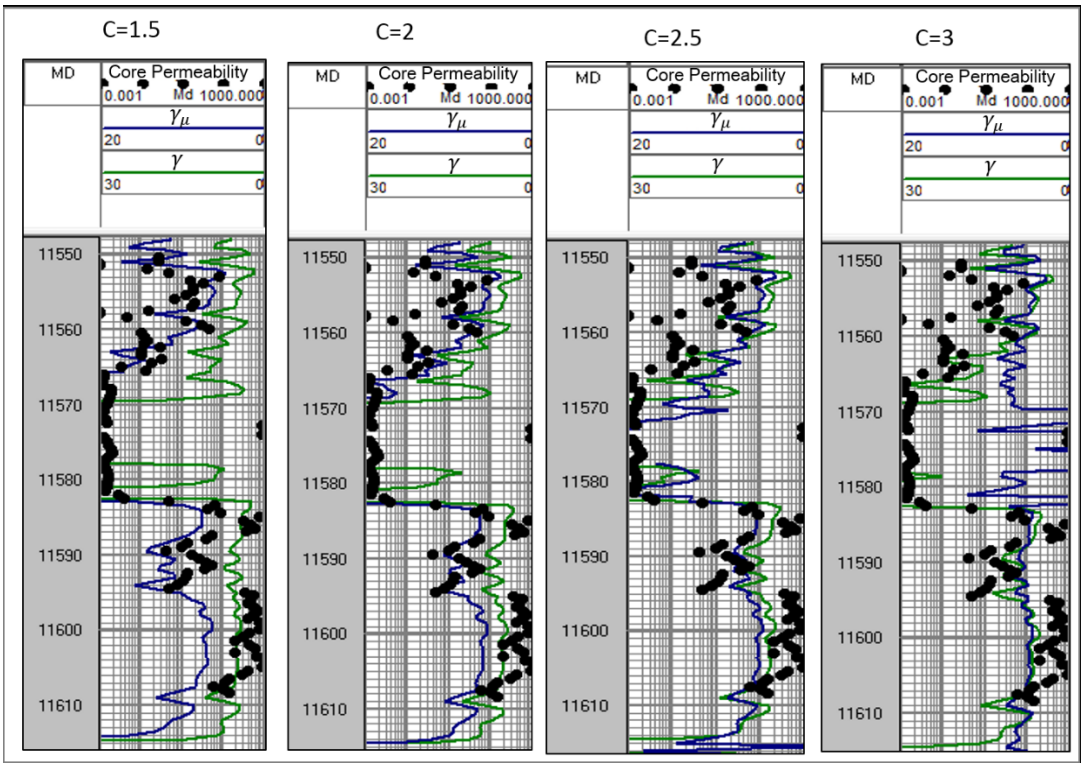

Figure A-43 Comparison of core permeability with the calculated frame flexibility factors based on different C value respectively for Little Cedar Creek Field.

AVO modeling

Seismic forward modeling is often necessary to assist better seismic interpretation and inversion. Amplitude Versus Offset (AVO) analysis is widely used to predict fluid type. However, in carbonate rocks with complex rock texture, the AVO responses for the fluid are often disguised due to the strong influence of pore type on seismic wave propagation. The conventional AVO classification may not be applicable for carbonate reservoirs. Figure A-44 shows the AVO responses of different pore types from Sun (2004). AVO for fluid detection in oil saturated carbonate reservoirs is extremely difficult due to the strong influence of pore structure on seismic wave

propagation (Sun, 2004). However, there are distinctive features on AVO for different pore types. Figure A-45 shows the synthetic AVO modeling using the well log data from this study. Agreeing with Sun (2004), the synthetic seismic for the thrombolite unit, dominated by vuggy/intercrystalline pores, shows abnormal amplitude increase near critical fraction followed by a sudden decrease in amplitude. The synthetic seismic for the grainstone unit, dominated by moldic/intergranular pores, shows a slight increase in amplitude near the critical angle followed by a sudden decrease in amplitude. The critical angle for the oolitic grainstone unit is larger compared to the thrombolite. The synthetic seismic for mudstone with microporosity shows complete reversed polarity with no critical angle of refraction. The results can be used to direct AVO prediction of pore structure and high permeability zones when pre-stack data is available.

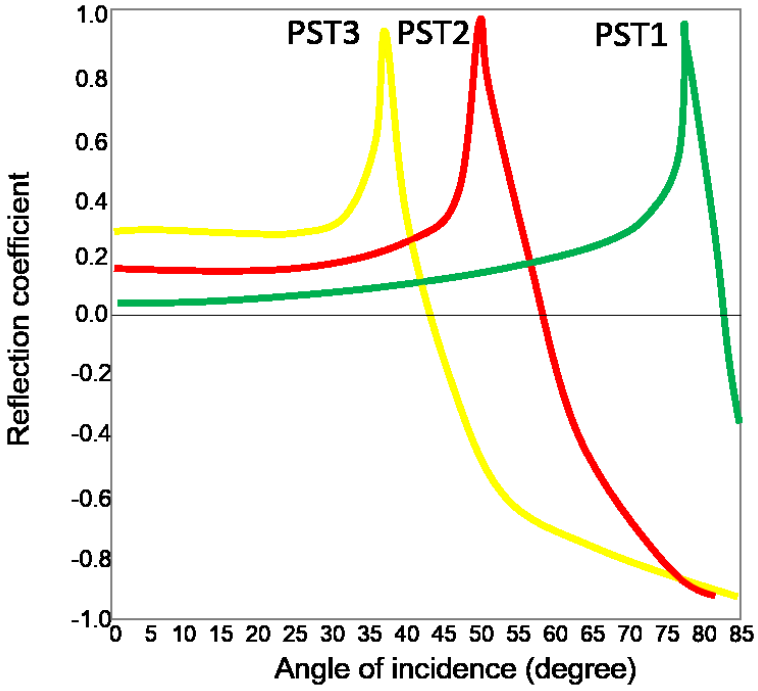

Figure A-44 Synthetic modeling of P-wave reflection for a shale/limestone interface for water saturated rocks dominated by three different pore types (modified from Sun, 2004). PST1 is dominated by microporosity, PST2 represents moldic rocks with or without vugs , PST3 is from a mixture of interparticle and vuggy porosity.

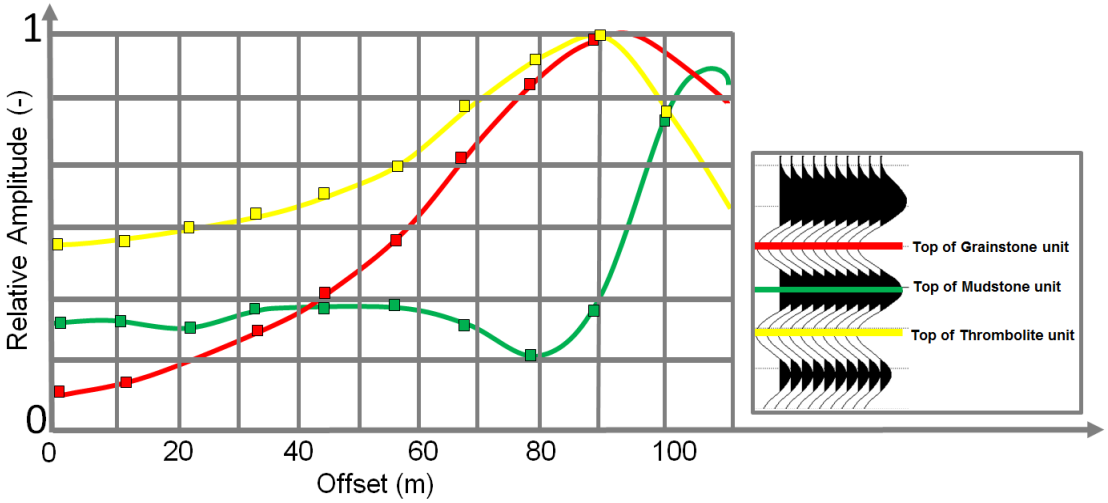

Figure A-45 Synthetic modeling of P-wave reflection for the top of grainstone unit (red), top of mudstone unit (green), and top of thrombolite unit (yellow) respectively. The grainstone and thrombolite are reservoirs while mudstone is non-reservoir.

Future application

Carbonate pore structure is controlled by depositional facies and diagenesis. Thus the influence of diagenesis in the pore system can be evaluated through the analysis of pore types. In this study, we find that cementation factor *m* is effective to estimate pore type, thus can be further applied to diagnose diagenesis. For instance, the prediction of intercrystalline pores in the lower thrombolite unit can be used to predict the intensity of dolomitization and the prediction of moldic pores and intergranular pores in the upper grainstone unit can be used to predict the intensity of meteoric dissolution and cementation.

Conclusions

Facies characterization assists in locating the reservoir rocks. However, it alone cannot predict the permeability and reservoir performance of the rock. The concept of cementation factor *m* deviation introduced in this paper can be used to better locating high permeable zones using resistivity method. The *m* deviation agrees well with the velocity deviation. Both of them have a similar trend with permeability. Considering the similar impact of pore structure on resistivity and sonic velocity, m is further applied to estimate shear wave velocity and predict the AVO responses of the reservoirs. The results show that different pore types display distinctive AVO features and fluid detection using conventional AVO classification is extremely difficult.